Influence of Viscoelasticity on the Displacement of Capillary Entrapments

Dissertation

zur

Erlangung des Grades

des Doktors der Naturwissenschaften

der Naturwissenschaftlich-Technischen Fakultät

der Universität des Saarlandes

von

Pegah Shakeri

Saarbrücken

2023

Declaration

I hereby declare that the dissertation entitled "Influence of Viscoelasticity on the Displacement of Capillary Entrapments" which I have submitted for the degree of Doctor of Natural Science at Saarland University is a record of work carried out by me under the supervision of Prof. Dr. Seemann. I further declare that the work reported in this dissertation has not been submitted and will not be submitted, either in part or in full, for the award of any other degree or diploma in this institute or any other institute or university. This is to certify that the printed version is equivalent to the submitted electronic one. I am aware of the fact that a misstatement may have serious legal consequences. I also agree that my thesis can be sent and stored anonymously for plagiarism purposes. I know that my thesis may not be corrected if the declaration is not issued.

Place: Saarbrücken

Date: March 7, 2023   **Pegah Shakeri**

Tag des Kolloquiums: 06.03.2023

Dekan: Prof. Dr. Ludger Santan

Mitglieder des Prüfungsausschusses:

Vorsitzender: Prof. Dr. Rolf Pelster

Gutacher:

Prof. Dr. Ralf Seemann

Prof. Dr. Christian Wagner

Prof. Dr. Stephan Herminghaus

Akademischer Mitarbeiter: Hendrik Hähl

Kurzzusammenfassung

Wenn Polymerlösungen als Verdrängungsmittel verwendet werden, z.B. beim "Polymerfluten", wurde bereits nachgewiesen, dass die Viskoelastizität von Polymerlösungen die Verdrängungsprozesse beeinflusst. Es gibt jedoch keine klare Erklärung dafür, welche Rolle die Viskoelastizität bei der Verdrängung auf der Mikrometerskala spielt und wie sie die mikroskopische Verdrängungseffizienz in porösen Medien verbessert.

In dieser Dissertation wird ein möglicher Mechanismus für die Verdrängung von Kapillareinschlüssen unter dem ausschließlichen Einfluss von elastischen Spannungen in der verdrängenden Flüssigkeit vorgestellt. Das verwendete mikrofluidische Modellsystem, das aus zwei Serpentinen-Kanälen besteht, die in der Mitte durch einen Kanal verbunden sind, wurde so gestaltet, dass es einen einzelnen Poreneinschluss simuliert. Die Serpentinen-Kanäle sind besonders wichtig, um die gewundene Natur der Strömung in porösen Medien zu imitieren. Direkte experimentelle Beobachtungen in diesem Modellsystem zeigen, dass die Grenzfläche zwischen der eingeschlossenen Phase und der viskoelastischen Verdrängungsphase oberhalb einer kritischen Scherrate instabil wird, was schließlich zur vollständigen Entleerung der eingeschlossenen Phase führt. Die Analyse des geschwindigkeitsabhängigen Strömungsverhaltens der Polymerlösung im Serpentinen-Kanal mittels µPIV zeigt, dass der Ursprung dieser Grenzflächenfluktuationen die Geschwindigkeitsschwankungen aufgrund von rein elastischen Instabilitäten und stark elastischen sekundären Strömungsstrukturen sind. Daraus lässt sich schließen, dass diese elastizitätsbedingten Instabilitäten die Verschiebung des kapillaren Einschlusses in den porösen Medien verursachen.

Abstract

It is already evident that the viscoelastic nature of polymer solutions affects the displacement processes when such fluids are used as displacing fluids, for example in polymer flooding. However, a clear explanation of how exactly viscoelasticity plays a role at the microscale and enhances microscopic displacement efficiency in porous media is still lacking.

In this dissertation, a possible mechanism of displacing capillary entrapment under the sole influence of elastic stresses is presented. A model system consisting of two serpentine channels connected in the middle by a capillary channel has been designed to represent a single pore entrapment. The serpentine channel is particularly important to mimic the tortuous nature of flow in porous media. Direct experimental observations in this model system show that the interface between the entrapped phase and the viscoelastic polymer solution used as the displacing phase becomes unstable above a certain shear rate, eventually leading to the complete removal of the entrapped phase.

The results of Particle Image Velocimetry experiments of the polymer flow in the serpentine channel show that the origin of these interfacial fluctuations is the velocity fluctuations due to purely elastic instabilities and strong elastic secondary flow structure.

To the brave women of Iran

Acknowledgment

I would like to express my sincere gratitude to Prof. Dr. Ralf Seemann for giving me the opportunity to pursue a PhD under his supervision. Thank you for granting me the freedom and confidence to follow my curiosity and passion. I thank Prof. Dr. Stephan Herminghaus and Max Planck Institute for Dynamics and Self-Organization for funding this PhD project. I appreciate Dr. Michael Jung for all the support and valuable discussions that have improved my critical thinking. Especial thanks to Dr. Martin Brinkman, whose contributions formed the foundation of this project. Sevde and Khalil I really enjoyed the time we spent together here and the friendship we made. I would also like to thank all my former and current colleagues especially Dr. Weiwei Li, Navid, Mahsa and Shima. Special thanks to Mrs. Judith Rech and Mrs. Monika Schuck for their administrative and technical help during my Ph.D. process.

Most importantly, I would like to thank my family for their love and support. Mom and dad, you are my heroes, my best friends, and my biggest support. Elham, you are the best sister one could ever have. Thank you all for always encouraging me to follow my dreams and for giving me the confidence that everything can be achieved with the right amount of effort. Even though I am far away from you, my heart beats for you, and I am so proud and grateful to have you. I would also like to thank Josée and Christian, for always being so kind to me and making me feel that I am a member of your family and feel at home in Germany. And last but not least, to the love of my life, my Christoph. Thank you for supporting me and always being patient even with my (sometimes!) unbearable moods. I know no matter how difficult life can get, I have you by my side and that is all that matters.

TABLE OF CONTENTS

CHAPTER 1

Introduction

Viscoelastic fluids are ubiquitous. From polymer melts to the most vital fluids in the human body, they all belong to this category of complex fluids. The presence of microstructures like polymers, particles and proteins in such fluids leads to material properties that result in unique flow behavior and transport dynamics. As the name suggests, viscoelastic fluids exhibit mechanical behavior intermediate between elastic solids and viscous liquids. Which behavior dominates, depends on the timescale of the motion, i.e., velocity. The popular children's play dough Silly Putty, made of silicone polymers, is an excellent example to understand the velocity dependence of viscoelastic behavior. It bounces back like an elastic solid when it is given a hard blow, but flows like a liquid when left at rest. If you have ever prepared a cake batter with a hand mixer, you have probably witnessed another unique feature of viscoelastic fluids. When mixing Newtonian liquid ingredients such as milk, oil, or syrup, the liquid is thrown away from the mixing blades by centrifugal force and flows outward toward the walls of the bowl, as expected according to Newton's first law. Once the flour, which contains a naturally occurring protein polymer called gluten, is added, the mixture flows in the opposite direction compared to the previous step, and the resulting batter unexpectedly climbs up the mixing blades. This peculiar rod-climbing effect, known as the Weissenberg effect, indicates that during the rotational motion of a viscoelastic fluid, an inward counterforce acts upon and outweighs the centrifugal force. This force or the corresponding stress in viscoelastic fluids is called the first normal stress difference and has an important impact on the flow behavior of such fluids, specially in curved geometries. Such geometries are of significant relevance for industrial and biological applications of viscoelastic fluids. Giesekus first discovered in 1966 that the flow of viscoelastic fluids confined in the gap between two rotating cylinders, i.e., in a Taylor-Couette geometry, becomes unstable due to the high first normal stress difference, even in the absence of inertia [1]. This unstable flow, known as purely elastic unstable or turbulent flow, has potential advantages and disadvantages in various viscoelastic fluid applications. In polymer processing and extrusion, for instance, the occurrence of purely elastic instabilities results in undesir-

able rough surfaces. On the other hand, such instabilities improve mixing efficiency and heat transfer in the creeping flow regime, providing technical advantages in industrial and biological applications of viscoelastic fluids.

High molecular weight, water-soluble polymers with strong viscoelasticity have long been successfully used in the petroleum and agricultural industries as viscosity mediators for enhanced oil recovery and soil remediation. In addition to increasing viscosity and thus improving the macro scale displacement efficiency, these polymers can also alter flow properties at the microscale due to their unique mechanical properties, i.e., viscoelasticity. However, when and how exactly viscoelasticity can improve microscopic displacement efficiency is still an unsolved puzzle to researchers. To resolve this problem, it is necessary to understand what viscoelasticity is and under what circumstances it can contribute to the removal of oil entrapment or contamination from capillary pores in a porous medium.

In this dissertation, various aspects of the microscale flow of viscoelastic polymer solutions are investigated to provide an explanation for improving microscopic displacement efficiency by such flows in porous media. A unique but simple microfluidic model system has been used, which consists of two symmetrical serpentine channels to mimic the tortuous nature of flow in a porous medium, connected by a capillary channel that serves as a single pore (capillary confinement). The symmetry between the two main serpentine channels allowed to eliminate the effects of viscous stresses and to study exclusively the effects of elasticity of semi-dilute polymer solutions on the displacement of capillary entrapment. Direct observations of the displacement processes in this model system indicated strong fluctuations of the interface between the trapped phase and the polymer solution in the serpentine channel above a certain shear rate, which eventually led to the complete removal of the trapped phase once the shear rate was further increased. Further quantitative analysis of the experimental data confirmed that the origin of these fluctuations is related to the occurrence of purely elastic instability in the polymer flow. Since in the semi-dilute regime, the polymer coils are close and thus strongly interact with each other, we have developed a suitable scaling to predict the onset of purely elastic instability with respect to the non-linear shear-dependent rheological properties of such solutions. A comprehensive characterization of the emerged turbulent polymer flow provided a clear insight into the source of the observed interface functions, namely the development of strong unsteady secondary flow structures. Finally, experiments investigating displacement processes by polymer solutions in a microfluidic porous medium consisting of randomly distributed disk arrays in a channel showed very similar results. The interfaces became unstable, resulting in the defragmentation and eventual release of the trapped phase. Although the rather complex flow geometry in this case does not allow decoupling of the effects of elasticity and viscosity,

similar mechanisms as in single pore geometry can be invoked due to the dominance of curved flow paths. In fact, the occurrence of purely elastic instability and strong secondary flows are responsible for interfacial fluctuation and removal of entrapments in porous media.

CHAPTER 2

Overview and Connectivity

This cumulative dissertation is based on four original publications, three of which have been published in peer-reviewed scientific journals, and the fourth one being under preparation at the time of submission. The original motivation behind these studies was to explore and explain the mechanism of capillary displacement by viscoelastic polymer solutions in porous media.

The publication by **Shakeri et al.** in *AIP Physics of Fluids* **2021** investigates the displacement of a capillary entrapment by various viscoelastic polymer solutions with different degree of elasticity in a microfluidic model system. The model system was designed to resemble capillary entrapment as well as the tortuous nature of flow paths in porous media. This unique model system allows the study of elasticity exclusively by eliminating the contribution of the viscosity of the fluid. The results of this study show the occurrence of an unstable flow of the polymer solutions accompanied by an increase in flow resistance even in the absence of inertial forces. This unstable flow leads to the fluctuation of the oil-polymer solution interface. Once these fluctuations are strong enough, they provide the necessary force to overcome the capillary forces and displace the capillary entrapment.

Providing a universal scaling to predict the onset of purely elastic instability with respect to the fluid's rheological properties and the geometrical properties of the flow channel is the focus of the second publication **Shakeri et al.** in *APS PHYSICAL RE-VIEW E* **2022**. In this work, the shear dependency of the rheological properties of semi-dilute entangled polymer solutions was added to the Pakdel and McKinley criterion to provide a realistic scaling of the onset of purely elastic instability in such polymer solutions.

In the publication **Shakeri et al.** in *AIP Physics of Fluids* **2022** flow of a semi-dilute entangled polymer solution with the aim of providing a full characterization was experimentally investigated. An important outcome of this work was that elastic secondary flow structures highly contribute to the total kinetic energy of the system. Looking back at the initial observation of the displacement process in the single pore geometry in light of these latter findings, it can be concluded that the additional flow resistance

and interface fluctuations observed in the capillary entrapment removal experiments are largely caused by such unsteady secondary flow structures.

Finally, a series of experiments were conducted in a porous model system to utilize the observations and findings from previous studies to explain the fluid displacement mechanisms by viscoelastic polymer solutions in porous media. The results of these experiments have been reported and discussed in **Jung et al. in *Frontiers in Physics 2022***. Similar to the experiments with single entrapment, i.e., the first publication, the interfaces between the oil entrapments and the viscoelastic invading fluid become unstable above a certain flow rate and once the fluctuations were strong enough, the oil entrapments were fragmented and eventually completely removed.

The structure of this thesis is as follows:

- In the **Chapter: Background and Theory**, the process of displacing capillary entrapments in porous media, relevant fundamentals of polymer physics, the rheological properties of polymer solutions, and their flow are discussed, with an emphasis on the relationship between the fluid properties and the corresponding flow features.

- In the **Chapter: Materials and Methods**, a general description of the experimental equipment, methods, and experimental procedures is presented, while the corresponding details can be found in the methods section of the publications in A–D.

- In the **Chapter: Results and Discussion**, the main results and findings of the attached publications in **Appendices A–D**, are discussed.

- In the **Chapter: Summary and Outlook** a summary of the presented study and an outlook for future research are provided.

CHAPTER 3

Background and Theory

Every oil reservoir undergoes three production phases during its life cycle. The first phase is primary production, where the reservoir is naturally depleted due to its pressure. However, over time, the reservoir pressure decreases and the secondary production phase begins. In this phase, an immiscible fluid, usually water, is injected into the reservoir to create the pressure needed for further production. After a period of time, the secondary recovery method also becomes ineffective, and most of the injected water is recovered in the production wells, while much of the oil remains trapped in the porous rock due to capillary forces [2, 3]. Depending on the wettability of the rock surface, the oil may be trapped as large ganglia in large pores in a water-wet rock Fig. 3.1 (a), spread as a thin film in an oil-wet rock Fig. 3.1 (b), or in an intermediate form in a mixed-wet rock Fig. 3.1 (c)[4, 5]. A wide range of tertiary or enhanced oil recovery (EOR) methods have been established in the petroleum industry over the years, most of which are aimed at recovering the fraction of oil in the reservoir that has been bypassed by secondary recovery methods, as well as improving the microscopic displacement efficiency by displacing capillary entrapments. To remove capillary entrapments, viscous forces must overcome capillary forces, thus increasing the viscosity of the displacing phase can improve displacement efficiency, especially in non-wet systems where the capillary threshold is small [2]. Polymer flooding is an established EOR method that uses polymers to increase the viscosity of the displacing fluid to improve oil recovery by reducing the mobility ratio between the displacement phase and the reservoir oil. Early application of polymer flooding in practice dates back to six decades ago, but it is still considered as one of the most efficient and reliable chemical EOR techniques in the petroleum industry [2]. For a long time, the general consensus among petroleum engineers was that polymer flooding solely improves volumetric displacement efficiency by invading the highly permeable zones and fractures in the reservoir rock that were previously bypassed by water flooding, and has no impact on the oil residual saturation in the matrix. However, several field production results [6–9] as well as experimental [10–14] and numerical studies [15–18] indicated otherwise, reporting surprisingly lower residual oil saturation after polymer flooding. Since the capillary threshold can be
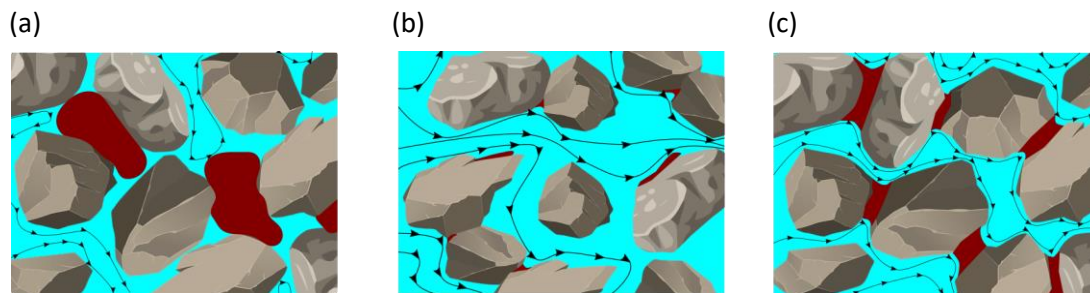
Fig. 3.1 Sketch of various forms of oil entrapments in porous media with different wettabilities. (a) Non-wet surface, large oil ganglia with relatively small capillary threshold are entrapped in the larger pores. (b) Wet-surface, oil is spread as a thin film on the surface and in small pores with a high capillary threshold. (c) Mixed-wet, an intermediate configuration between wet and non-wet. Oil ganglia are entrapped in intermediate pores and are in contact with more than one active path line.

significant, especially in mixed wet and wet systems, and the increased viscosity during polymer flooding is not sufficient to overcome it, other mechanisms must be responsible for these observations [19, 20]. Although several studies suggest that the improved microscopic displacement efficiency during polymer flooding is due to the viscoelastic nature of the fluid, the exact mechanism is not yet agreed upon [21–23]. While some researchers have linked the improved efficiency to the observed increased apparent viscosity, relating it to the extensional viscosity of the polymer solutions [24–26], others have pinpointed the occurrence of so called purely elastic instabilities as the possible cause [27–33]. The latter group argues that the unsteady flow induces fluctuations in the fluid-fluid interface between the viscoelastic invading fluid and the trapped oil ganglia [22, 34–36], resulting in the breakup of large ganglia into smaller droplets and ultimately the complete removal of the trapped oil [37]. Further displacement experiments using polymers with different molecular weights imply that the onset of displacement mainly depends on the intensity of the fluctuations rather than the absolute value of the apparent viscosity [22, 34, 38]. Other displacement mechanisms such as strip-off of oil films attached to pore walls caused by an apparent slip length [39, 40], reducing the effective permeability of porous media by polymer retention [41, 42], as well as droplet breakup [43, 44], and pulling effects [45, 46] originating from normal stress differences that remove oil from dead ends have also been reported in the literature.

The geometric features of flow paths in porous media play a crucial role in enhancing the viscoelasticity of polymer solutions and triggering instabilities. The tortuous structure of porous media, for instance, enforces both shear and extension, which can elongate the polymers and consequently alter the flow and cause instabilities, especially at large Weissenberg numbers (ratio of elastic to viscous forces) where elasticity dominates [18–20]. As a result, displacement processes in natural porous media are affected by some if not by all the listed mechanisms, yet it remains an open question which,
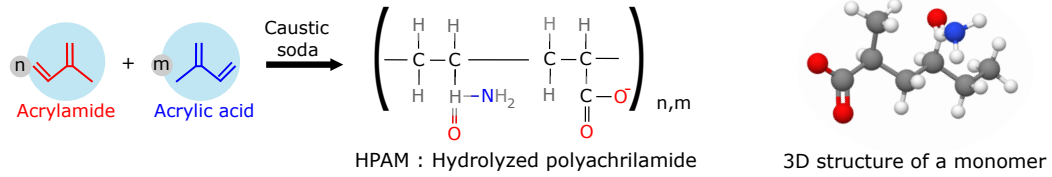
Fig. 3.2 Polymerization process of hydrolyzed polyacrylamide based on acrylamide and acrylic acid co-polymyers, in the presence of Caustic soda (NaOH), and 3D structure of a monomer unit.

mechanism prevails to (re-) mobilize capillary entrapments.

The following sections of this chapter discuss the rheological as well as flow properties of polymer solutions relevant for understanding the potential effects of viscoelasticity on the displacement process in porous media.

3.1 Polymer Solutions and Concentration Regimes

Polymers are giant macromolecules formed by covalent bonding of a large number of elementary units (monomers) through a process called polymerization [47]. Carbohydrates, lipids, proteins, and nucleic acids (DNA and RNA) are among the best-known natural and biological polymers [48]. We are also surrounded by synthetic polymers such as rubber, plastics, resins, and adhesives in our living environments. As already mentioned, one of the unique applications of synthetic polymers is in enhanced oil recovery and soil remediation, where polymers are added to increase the viscosity contrast between the displacing and displaced phases [4, 49, 50]. This results in an improved mobility ratio, i.e., more homogeneous and less fingering at the front during the displacement process [4]. The polymers used for this purpose are usually high molecular weight, water-soluble substances such as hydrolyzed polyacrylamides (HPAM), xanthan gum and schizophyllan [51–53]. The HPAM family, a semi-random flexible chain copolymer of $\sim 70\%$ acrylamide and $\sim 30\%$ acrylic acid, is most commonly used due to its cost-effectiveness and proven performance [2, 54]. The degree of hydrolysis affects certain physical properties of polymers such as adsorption, shear and thermal stability, and salt sensitivity [2, 55–57]. The polymerization process and molecular structure of HPAM polymers are shown in Fig. 3.2.

HPAM polymers in an aqueous solution and at equilibrium acquire a flexible spherical conformation to preserve their minimum energy [58]. The radius of gyration, which is an estimate of the size of the polymer coils in solution, corresponds to the radius of this imaginary enclosing sphere and is defined as [58]:

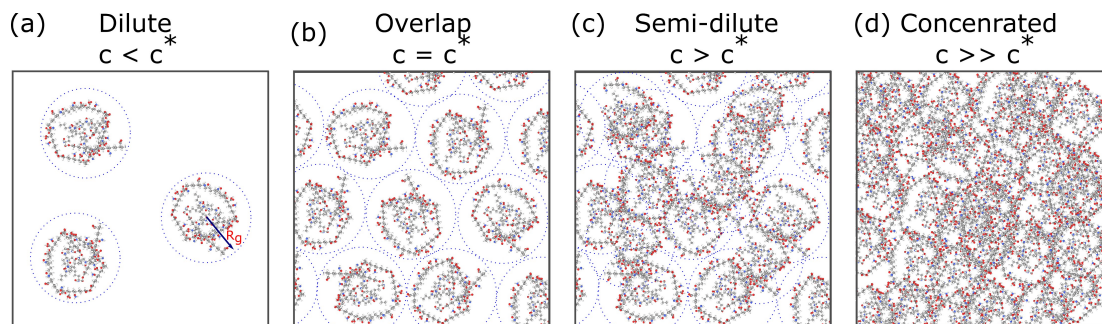$$R_g = \sqrt[3]{\frac{M_W}{\frac{4}{3}\pi N_A c^*}} \tag{3.1}$$

Fig. 3.3 Sketch of polymer coils in the solution at various concentration regimes. R_g and c_* are the radius of gyration and overlap concentration, respectively.

where M_W is the molecular weight, c^* is the overlap concentration and N_A is the Avogadro constant. The overlap concentration, i.e., the concentration at which the polymers nearly overlap, is proportional to the reciprocal of intrinsic viscosity and is defined as $c^* \approx 1/[\eta]$. For the definition of different types of viscosity, see section 3.2.1. The intrinsic viscosity $[\eta]$ relates directly to the molecular size of the polymer and is defined as the limit of the reduced viscosity as the concentration of polymer tends to zero, i.e., $[\eta] = \lim_{c \to 0} \frac{\eta - \eta_s}{c\eta_s}$, where η, η_s and c are solution viscosity, solvent viscosity and polymer concentration, respectively [47]. The intrinsic viscosity, $[\eta]$, and thus overlap concentration, c^*, are experimentally determined using Huggins–Kreamer method [59, 60]. Polymer solutions are categorized in three regimes with respect to the overlap concentration c^*. These concentration regimes are namely dilute, semi-dilute and concentrated [61]. Fig.3.3 shows a schematic demonstration of polymers at different concentration regimes. In the dilute regime, where there are only a few coils with a large distance between them, the polymers interact solely with the solvent molecules. As their number increases and the coils come closer to each other, they start to interact with each other. In the semi-dilute regime, polymers start to entangle either internally, i.e, self entangled, or with neighboring polymers whereas concentrated solutions and melts are characterized by severe entanglements and dense polymer phases. The dynamics and flow behavior of polymers strongly depends on the molecular weight and concentration of the polymer [62, 63]. Moreover, since HPAM are poly-electrolytes, they interact quite strongly with ions in the solution and the radius of gyration of the coils and thus properties of the solutions strongly depends on the type and concentration of the salts in the solution as well [64].

3.2 Rheology of Polymer Solutions

The term "rheology" comes from the ancient Greek terms "$\varrho\acute{\varepsilon}\omega$ (rhéō)" and "$\lambda o\gamma\iota\alpha$ (-logia)" which literally translates as the study of the flow. However, rheology is not just about the flow per se. It deals mainly with the flow and deformation of a substance,

in particular with the relationship between the deformation of a fluid element and the stresses exerted on it, also with respect to time [65]. Unlike ideally elastic or viscous materials, viscoelastic fluids exhibit a complex and usually nonlinear stress-strain relationship, and thus their dynamic behavior can be intricate [66].

In this section, rheological properties of viscoelastic polymer solutions are briefly explained.

3.2.1 Viscosity

Dynamic viscosity, also referred to as absolute viscosity, usually refers to non-Newtonian fluids and indicates the internal flow resistance and energy dissipation during continuous deformation, i.e., flow [67]. In polymeric fluids, the interaction between the polymers with each other and with the solvent molecules increases the flow resistance and energy dissipation, hence polymers are considered as efficient viscosifiers [2]. The viscosity of a polymer solution depends on the size, number and conformation of the polymer molecule in it, i.e., larger molecules with higher molecular weights are usually associated with a higher solution viscosity [3, 50]. Unlike Newtonian fluids, where stress and strain are linearly related and thus viscosity is a material constant, the polymer conformation and hence the viscosity of the solutions depends strongly on the shear rate, especially above the overlap concentration [68]. At rest or very low shear rates, the polymers remain in the coiled conformation, and the solution exhibits a constant viscosity. However, above a critical shear rate the polymers start to uncoil and align with the flow direction and as a result the flow resistance, i.e., viscosity, is reduced. This behavior is known as shear thinning [69]. The shear viscosity of polymer solutions is commonly measured with a rheometer in a steady rotation test, either in stress or in a strain-controlled mode [70]. Even though for polymer solutions the relationship between stress and strain is no longer linear and cannot be described by a single constant, it is still appropriate to represent the shear dependent viscosity function as [65]:

$$\eta(\dot{\gamma}) \equiv \tau/\dot{\gamma} \tag{3.2}$$

where τ is shear stress and $\dot{\gamma}$ is shear rate. The shear dependent viscosity function, $\eta(\dot{\gamma})$, of semi-dilute polymer solutions is best described by the Carrueau–Yasuda model [69], which is a power decay with two constant plateaus at the extreme ranges of the shear rate:

$$\eta(\dot{\gamma}) - \eta_\infty = (\eta_0 - \eta_\infty)[1 + (\Lambda\dot{\gamma})^a]^{\frac{n-1}{a}} \tag{3.3}$$

Here η_0 and η_∞ are the zero-shear viscosity and viscosity at infinite shear rates, Λ is a characteristic time, n is the power law exponent associated with the degree of shear
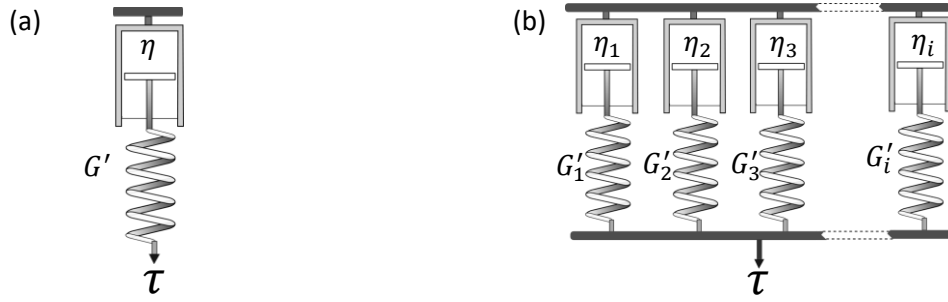
Fig. 3.4 (a) Sketch of one Maxwell element for a viscoelastic liquid, consisting of one Hookian spring attached to one Newtonian dashpot in series. (b) Generalized Maxwell model consisting of multiple parallel Maxwell elements.

thinning, and a is a transition control factor.

3.2.2 Viscoelasticity

As the term viscoelastic suggests, it is a class of material property which show an intermediate behavior between elastic solid and viscous fluid, depending on the timescale of the motion [68]. In such materials, the deformation caused by a constant load has two components: first, an immediate deformation related to elasticity, and second, a delayed deformation related to viscosity [66]. After unloading, retarded reformation occurs either partially or completely. To understand viscoelastic behavior, we must first know how an elastic and a viscous substance behave. When an ideally elastic material is slightly deformed, it tends to return to the original configuration as soon as the stress is removed. This means that the deformation energy acting on an ideally elastic body during a shear process is stored and can be fully recovered without loss when the load is removed [61]. This behavior is described via Hook's law:

$$\tau = G\gamma \tag{3.4}$$

where τ, G and γ are shear stress, shear or rigidity modulus, and strain (deformation), respectively. In contrast, in ideally viscous material, the energy is entirely dissipated and after unloading, the material remains deformed to the same extent as at the end of the loading phase [61]. This behavior is described via Newton's law:

$$\tau = -\eta\dot{\gamma} \tag{3.5}$$

James C. Maxwell, in 1868, proposed the first constitutive relationship between stress and strain and the corresponding mathematical fundamentals of a viscoelastic fluid [71]. This model in fact represents a viscoelastic fluid with a linear Hooke's spring connected in series with a Newtonian dashpot. A schematic representation of

a Maxwell element is shown in Fig. 3.4 (a). The total strain (deformation) of the viscoelastic material is determined as:

$$\gamma_{total} = \gamma_{spring} + \gamma_{dashpot} \tag{3.6}$$

The spring acts exactly like a metal spring according to Hook's law with a shear modulus G, instantly stretching under stress while the piston, immersed in the dashpot filled with a Newtonian fluid of viscosity η, moves at a rate proportional to the stress, obeying Newtons's law. Thus,

$$\tau = \frac{\eta}{G}\left(\frac{\partial \tau}{\partial t}\right) + \eta\dot{\gamma} \tag{3.7}$$

Equation 3.7 is reduced to Newton's law for a steady flow, Eq. 3.5, where the variation of the shear stress with time is negligible. On the other hand, if the stress changes rapidly with time, τ is negligible compared to $\frac{\partial \tau}{\partial t}$, and Eq. 3.7 is reduced to the constitutive equation of a Hookian solid, Eq. 3.4. In this model, $\frac{\eta}{G}$ is a constant with the dimension of time and is denoted as the relaxation time λ, thus Eq. 3.7 for $\tau(t)$ can be written as:

$$
\begin{aligned}
\tau(t) &= \int_{-\infty}^{t} \left\{ \frac{\eta}{\lambda^2} \exp\left[-\left(t-t'\right)/\lambda\right] \right\} \gamma\left(t,t'\right) \mathrm{d}t' \\
&= \int_{-\infty}^{t} M\left(t,t'\right) \gamma\left(t,t'\right) \mathrm{d}t'
\end{aligned}
\tag{3.8}
$$

where $M(t,t')$ is the memory function, incorporating the idea that stress at the current time is a function of the immediate past, with the most recent past having the greatest impact [66]. The Maxwell model is the simplest viscoelastic model among a wide class of constitutive relationships for viscoelastic fluids that does not consider the shear dependence of the rheological properties, and is thus suitable only for very dilute polymer solutions in the linear viscoelastic range [72]. To represent a realistic behavior of polymer solutions, especially in the semi-dilute range where both viscosity and relaxation time depend on shear rate, a generalized modification of the Maxwell model including a spectrum of relaxation times is required [67]. In the generalized Maxwell model, a viscoelastic fluid is described by a series of Maxwell elements connected in parallel with different G_i and η_i, as shown in 3.4 (b). According to the principle of L. Boltzmann superposition [73], the memory function for a superposition of n Maxwell elements in Eq. 3.8 can be written as:

$$M\left(t-t'\right) = \sum_{i=1}^{N} \frac{G_i}{\lambda_i} \exp\left(-\frac{t-t'}{\lambda_i}\right) \tag{3.9}$$

where G_i and λ_i are the elastic modulus and viscosity of the ith element.

The characterization of viscoelastic fluids is of great practical importance since the behavior of such fluids is directly related to the "viscous" and "elastic" response obtained during the unsteady flow of such fluids. The dynamic behavior of such fluids is mostly examined via small amplitude oscillatory tests [61], where a sinusoidal deformation or stress is imposed to the fluid, e.g., $\tau(t) = \tau_0 sin(\omega t)$ in stress-controlled mode, and the corresponding response of the fluid in the form of sinusoidal stress or deformation is captured, e.g. $\gamma(t) = \gamma_0 sin(\omega t + \delta)$. Figure. 3.5 shows an illustration of the concept of oscillatory shear flow. The phase shift, δ, varies in the range of 0 to $\frac{\pi}{2}$ and indicates whether the fluid behaves ideally viscous ($\delta = \frac{\pi}{2}$), ideally elastic ($\delta = 0$) or viscoelastic ($0 < \delta < \frac{\pi}{2}$) [70]. Analogous to the steady-state shear of viscoelastic fluids, the ratio of stress to strain during a dynamic test is defined as the complex shear modulus, $G^* = \tau(t)/\gamma(t)$. G^* is defined in the complex domain and can be decomposed into a real part (elastic or storage modulus, G') and an imaginary part (viscous or loss, G''), i.e., $G^* = G' + iG''$, and thus characterizes the overall viscoelastic behavior [61]. The small amplitude oscillatory sweep tests are usually performed in two ways: Amplitude sweep test to determine the range of linear viscoelastic behavior and frequency sweep test to determine the longest relaxation time or relaxation spectrum of the viscoelastic polymer solutions [70].

The (generalized) Maxwell model is widely used for analysis and interpretation of the small amplitude oscillatory sweep tests, which provide important information about the dynamic properties of polymer solutions in the linear viscoelastic range. The frequency dependence of G' and G'' with respect to the generalized Maxwell models is defined as:

$$G'(\omega) = \sum_{k=1}^{N} G_k \frac{(\lambda_k \cdot \omega)^2}{1 + (\lambda_k \cdot \omega)^2} \tag{3.10}$$

$$G''(\omega) = \sum_{k=1}^{N} G_k \frac{\lambda_k \cdot \omega}{1 + (\lambda_k \cdot \omega)^2} \tag{3.11}$$

where N is the number of Maxwell elements, and λ_k and $G_k = \eta_k/\lambda_k$ are the relaxation time and the corresponding shear modulus of the kth element, respectively.

The largest relaxation time is commonly used as a characteristic timescale to evaluate the degree of elasticity of the polymer solutions. However, polymer solutions in the semi-diluted regime exhibit strongly shear-dependent relaxation times. Therefore, it is more reasonable to select a relaxation time that corresponds to the range of the applied shear rate for this aim [74]. In a flow with a characteristic shear rate of $\dot{\gamma}$ or a characteristic frequency ω, two dimensionless numbers can be defined to estimate how dominant the elastic stresses are. These two dimensionless numbers, which are widely used to characterize viscoelastic flows, represent the ratio of elastic forces to viscous
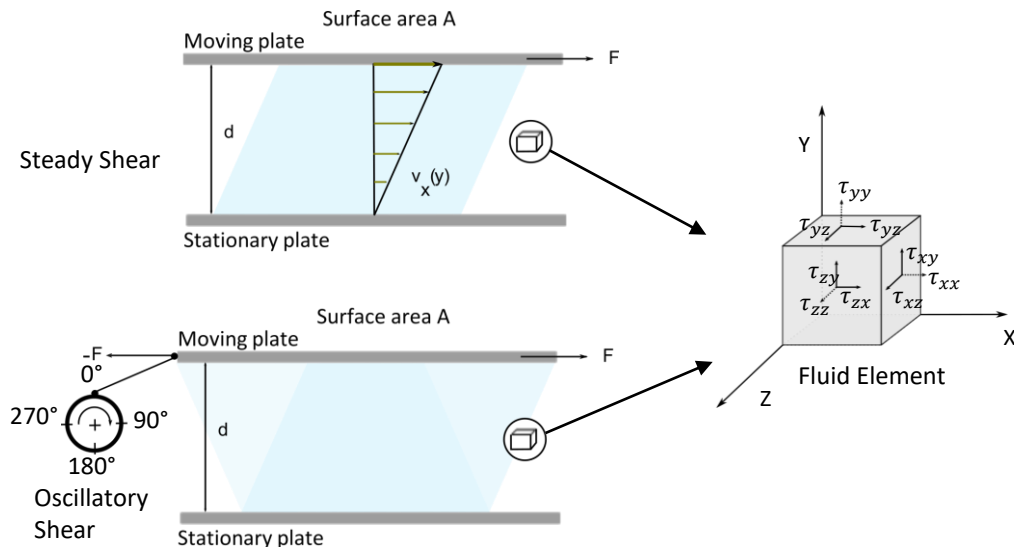
Fig. 3.5 Schematic representation of a unidirectional simple shear flow (top left) and oscillatory shear flow (bottom left). F is the force exerted on the moving plate, A is the surface area, and d is the distance between the top and bottom plate. $v_x(y)$ is the velocity component in the flow direction at any vertical location y. The stress components exerted on faces of a 3D volume element (right).

forces during flow and are referred to as the Deborah number and the Weissenberg number [75]. The Deborah number is defined as the ratio between the fluid relaxation time and the characteristic flow time (reciprocal of the characteristic frequency), $De = \lambda \omega$. The Deborah number represents the transient nature of the flow relative to the timescale of the fluid [76]. If the De number is small, implying that the observation timescale is large, the material responds like a fluid, and if the De number is large, the material exhibits a solid-like behavior. From this point of view, there is no fundamental difference between solids and fluids; it is just a matter of observation timescale. The concept behind the Weissenberg number as an indicator of elasticity becomes clear when considering its original definition by K. Weissenberg as the so-called "recoverable strain" or the ratio of elastic to viscous forces defined as $Wi = \lambda \dot{\gamma}$ [75, 77]. Similar to the De number, the higher the Wi-number, the more elastic is the response of the material.

3.2.3 Elastic Stress and Normal Stress Differences

The normal stress difference is a unique feature of viscoelastic fluids, which is responsible for important flow phenomena such as the Weissenberg effect [65] and purely elastic instability in curvilinear flows [78, 79]. To understand what this stress difference is and how it is generated, we need to look at stress and strain distribution in a three-dimensional fluid element during flow. Fig. 3.5 is a schematic demonstration of a simple shear flow of a fluid, where a constant force F is exerted on the top plate with

surface area A in x-direction. The fluid between the two plates moves in a stratified manner with a linear velocity profile $v_x(y) = v_X y/d$, where v_X is the maximum velocity at the top plate and $v_x(y = 0) = 0$ at the bottom (stationary) plate, due to the no-slip boundary condition. The shear rate in this case is defined as $\dot{\gamma}_{xy} := \frac{dv_x(y)}{dy} = \frac{v_X}{d}$ and is constant. According to Newton's law, Eq. 3.5 can be written as:

$$\tau_{xy} = \frac{F}{A} = \eta \dot{\gamma}_{xy} \tag{3.12}$$

In a three-dimensional shear flow, two shear and one normal stress components are acting on each face of a three-dimensional fluid element, as shown in Fig. 3.5. Thus, a three-dimensional **total stress tensor**, Π can be written as follows [66]:

$$\Pi = \begin{bmatrix} \Pi_{xx} & \Pi_{xy} & \Pi_{xz} \\ \Pi_{yx} & \Pi_{yy} & \Pi_{yz} \\ \Pi_{zx} & \Pi_{zy} & \Pi_{zz} \end{bmatrix}$$

The total stress tensor Π can be decomposed into an isotropic part (thermodynamic pressure, p) and a "deviatoric" part known as the extra stress tensor, τ, defined as:

$$\Pi = -p\mathbf{I} + \tau \tag{3.13}$$

The deviatoric part $\tau = \tau(V, \nabla V, etc.)$, known as the constitutive equation, is defined based on the fluid and can be substituted into Eq. 3.13 and subsequently in the flow equation. For instance, for an incompressible Newtonian fluid, the deviatoric part of the total stress tensor is symmetric and traceless, i.e., $tr(\tau) = \sum_{i=0}^{n} \tau_{ii} = \tau_{xx} + \tau_{yy} + \tau_{zz} = 0$ and the symmetry of τ imposes that $\tau = \tau^T$, thus, $\tau_{ij} = \tau_{ji}$ [67, 72]. Each off-diagonal component in the x-plane is linearly related to the rate of deformation of the tensor components. Thus:

$$\begin{aligned} \tau_{xx} &= -2\eta \frac{\partial \mathbf{V}_x}{\partial x}, \\ \tau_{xy} &= -\eta \left(\frac{\partial \mathbf{V}_x}{\partial y} + \frac{\partial \mathbf{V}_y}{\partial x} \right), \\ \tau_{xz} &= -\eta \left(\frac{\partial \mathbf{V}_x}{\partial z} + \frac{\partial \mathbf{V}_z}{\partial x} \right). \end{aligned} \tag{3.14}$$

A similar set of equations can be written for the y and z planes as well. The three-dimensional stress distribution in Newtonian fluids is in general isotropic, i.e., $\tau_{xx} = \tau_{yy} = \tau_{zz}$. In simple shear flow, the velocity is constant in the flow direction, $\frac{\partial \mathbf{V}_x}{\partial x} = 0$, and varies only in the perpendicular direction, thus $\tau_{xx} = \tau_{yy} = \tau_{zz} = 0$ [65]. In viscoelastic polymer solutions, however, the stress-strain relationship is nonlinear. Moreover, the stress distribution is anisotropic due to anisotropic deformation caused

by different polymers' conformation during flow [78]. As a result, two sets of non-zero normal stress differences appear in viscoelastic fluid flow:

$$N_1 = \tau_{xx} - \tau_{yy} \tag{3.15}$$

$$N_2 = \tau_{yy} - \tau_{zz} \tag{3.16}$$

N_1 and N_2 are known as first and second normal stress differences and are both functions of shear rate. Several unique behaviors, such as the die swell in extrusion flow [80], rod climbing or Weissenberg effect [65], purely elastic instability [78, 81], and secondary flow patterns in curved flows [82] are induced by normal stress differences in viscoelastic polymer flows.

3.2.4 Viscoelastic Constitutive Models

The deviatoric part of the total stress tensor in equation 3.13, is defined based on the stress-strain relationship corresponding to the fluid behavior described by the constitutive fluid model. The choice of an appropriate and representative fluid model is thus necessary for numerical modeling and evaluation of experimental fluid flow. There are two general types of viscoelastic fluid models, i.e., differential models and integral models [73]. Even though the integral approach is more accurate, the differential models are most commonly employed as they are relatively easier to use. Among the long list of existing differential models, Oldroyd type (Maxwell, Oldroyd-B, White–Metzner), FENE type, Phan-Thien Tanner (PTT), and Giesekus are widely used [65, 66, 83, 84]. Which model to choose to describe a viscoelastic fluid depends not only on the rheological properties of the fluid, but also on the flow geometry. For example, the shear-thinning viscosity and the non-quadratic first normal stress difference of polymer solutions in the semi-dilute regime could be represented by either the PTT, the Giesekus or the White–Metzner (WM) model. The WM constitutive model expresses a fairly simple non-linear viscoelastic fluid of polymer solutions in the semi-dilute and entangled regime with strong shear thinning [85]. It is also straightforward to select material parameters based on the experimentally measured first normal stress difference and viscosity for this model. Thus, for interpreting the flow behavior of a highly shear-thinning fluid in a serpentine channel where the flow is mainly shear-dominated, WM is an appropriate choice and is therefore used in this work.

Despite having different scopes and approaches, all of these models have a common principle, inspired by Maxwell's interpretation of a viscoelastic fluid, in which the extra stress tensor in Eq. 3.13 is decomposed into two components as:

$$\tau = \tau_1 + \tau_2 \tag{3.17}$$

where τ_1 and τ_2 are extra stress components corresponding to the elastic and viscous components of the viscoelastic fluid, respectively. The viscous part is defined as $\tau_2 = 2\eta_2 \mathbf{D}$, where $\mathbf{D}$ is the deformation tensor, $\boldsymbol{D} = \frac{1}{2}\left[\nabla V + \nabla V^T\right]$, and η_2 is the corresponding viscosity. The elastic part, τ_1, is calculated from a differential equation or an algebraic equation with a state variable (configuration tensor) obeying a differential equation [73]. For example, the White-Metzner (WM) fluid model [86] computes τ_1 in the following form:

$$\tau_1 + \lambda\left(\dot{\gamma}\right) \overset{\triangledown}{\tau}_1 = 2\,\eta_1\left(\dot{\gamma}\right)\mathbf{D} \tag{3.18}$$

where η_1 is the corresponding viscosity, and $\lambda\left(\dot{\gamma}\right)$ is the shear dependent relaxation time calculated as:

$$\lambda(\dot{\gamma}) = N_1/2(\eta(\dot{\gamma}) - \eta_\infty)\dot{\gamma}^2 \tag{3.19}$$

here $\dot{\gamma}$ is the second invariant of deformation tensor and is defined as $\dot{\gamma} = \sqrt{2\,tr(\mathbf{D}^2)}$. The term $\eta(\dot{\gamma})$ is the total viscosity of the viscoelastic fluid, i.e., $\eta = \eta_1 + \eta_2$, which for a shear-thinning fluid is usually described by Eq. 3.3. The upper convected time derivative, $\overset{\triangledown}{\tau}_1$, is calculated as:

$$\begin{aligned}
\overset{\triangledown}{\tau}_1 &= \frac{D\tau_1}{Dt} - \left[\tau_1 \cdot \nabla \mathbf{v} + (\nabla \mathbf{v})^T \cdot \tau_1\right], \\
\frac{D\tau_1}{Dt} &= \frac{\partial \tau_1}{\partial t} + \mathbf{v} \cdot \nabla \boldsymbol{\tau}_1
\end{aligned} \tag{3.20}$$

As will be explained in the next section, these constitutive equations are implemented in the flow equations to account for the time-dependent behavior and elasticity of polymer solutions and to reliably predict the stress distribution during flow.

3.3 Influence of Viscoelasticity on the Flow

Since non-Newtonian fluids are fundamentally different from Newtonian fluids, it is important to understand how their properties can modify the flow. This can be evaluated by implementing the representative constitutive equations into the flow equations, i.e., the conservation of mass and momentum [5]. In the following, we will explain where does the viscoelasticity of the polymer solutions impacts these fundamental equations.

3.3.1 Mass Conservation

The principle of mass conservation states that the mass in an arbitrary control volume as shown in Fig 3.6 is conserved at all times, i.e., the mass flow entering the control
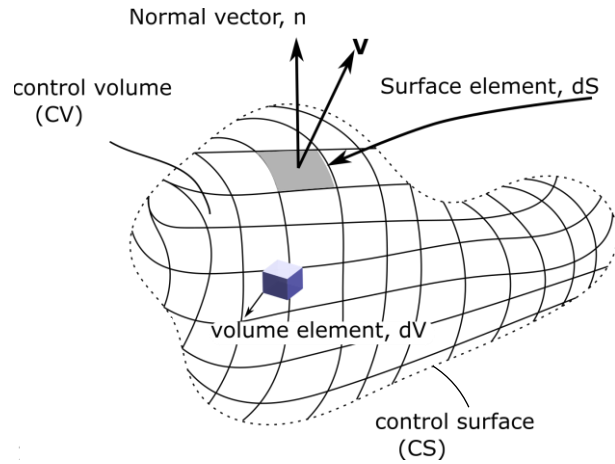
Fig. 3.6 Sketch of a fluid control volume CV and relevant components such as control surface CS, volume element dv, and surface element dS for deriving mass and momentum conservation equations.

volume $\dot{m}_{\text{in}}$ is equal to the mass flow leaving the control volume $\dot{m}_{\text{out}}$ [87]:

$$\frac{dm_{\text{CV}}}{dt} = \dot{m}_{\text{in}} - \dot{m}_{\text{out}} = 0 \tag{3.21}$$

thus, the integral form of the mass conservation is written as follows:

$$\frac{d}{dt} \int_{CV} \rho \cdot dV = - \oint_{CS} \rho \cdot \mathbf{V} \cdot \mathbf{n} dS = 0 \tag{3.22}$$

where ρ is the fluid density, dV is a volume element, n is the normal outward unit vector, dS is a surface area element, and $\mathbf{V}$ is the velocity vector of arbitrary direction, Fig. 3.6. According to the Gauss's Theorem [67]:

$$\oint_{CS} \rho \cdot \mathbf{V} \cdot \mathbf{n} dS = \int_{CV} \nabla(\rho \mathbf{V}) dV \tag{3.23}$$

Thus Eq. 3.22 is reduced to the following form:

$$\int_{CV} \left(\frac{\partial \rho}{\partial t} + \nabla(\rho \mathbf{V}) \right) dV = 0 \tag{3.24}$$

which results in the general form of the *Continuity Equation*:

$$\frac{\partial \rho}{\partial t} + \nabla(\rho \mathbf{V}) = 0 \tag{3.25}$$

As seen, viscoelasticity has no effect on the continuity equation. Therefore, it is sometimes sufficient to implement the shear-dependent viscosity of polymer solutions into

the generalized Newtonian fluid models when only the velocity distribution or its derivatives such as shear rate or deformation tensor are of interest. However, as will be discussed in the next section, the predictions of the stress tensor in this case are not entirely accurate because viscoelasticity has a significant impact on the conservation of momentum.

3.3.2 Momentum Conservation

The principle of momentum conservation is in fact the Newton's second law of motion [88]:

$$\sum f_{(i)} = ma = \frac{d(mv)}{dt} \tag{3.26}$$

where m is mass, a is acceleration, and v is velocity. The momentum balance has three components, which are momentum flow due to convection, advection (by molecular forces), and body forces:

$$\frac{d}{dt} \int_{CV} \rho \mathbf{v} dV = - \oint_{CS} (\hat{\mathbf{n}} \cdot \mathbf{v}) \rho \mathbf{v} dS + \oint_{CS} \hat{\mathbf{n}} \cdot \mathbf{\Pi} dS + \int_{CV} \rho \mathbf{g} dV \tag{3.27}$$

considering a differential surface element dS, as shown in Fig. 3.6, and following Gauss's theorem the momentum flow by convection, i.e., the first term in the RHS of Eq. 3.27 for the control volume, is written as:

$$- \oint_{CS} (\hat{\mathbf{n}} \cdot \mathbf{v}) \rho \mathbf{v} dS = \int_{CV} \nabla \cdot (\rho \mathbf{v} \mathbf{v}) dV \tag{3.28}$$

The second contribution, i.e., momentum transfer by advection is related to the molecular forces, originating from the collisions or interactions among polymer molecules and is computed as [66, 88]:

$$\oint_{CS} \hat{\mathbf{n}} \cdot \mathbf{\Pi} dS = \int_{CV} \nabla \cdot \mathbf{\Pi} dV \tag{3.29}$$

Thus, keeping the last term, which corresponds to the contribution of the body forces, as is and substituting the Eq. 3.28 and Eq. 3.29 into Eq. 3.27, the general form of the momentum equation is obtained as:

$$\rho \left(\frac{\partial \mathbf{v}}{\partial t} + \mathbf{v} \cdot \nabla \mathbf{v} \right) = -\nabla p + \nabla \cdot \tau + \rho \mathbf{g} \tag{3.30}$$

where τ is computed from the constitutive equation, e.g., for a White-Metzner fluid, by inserting Eq. 3.17, Eq. 3.18, and Eq. 3.20 into Eq. 3.30. As can be expected, unlike
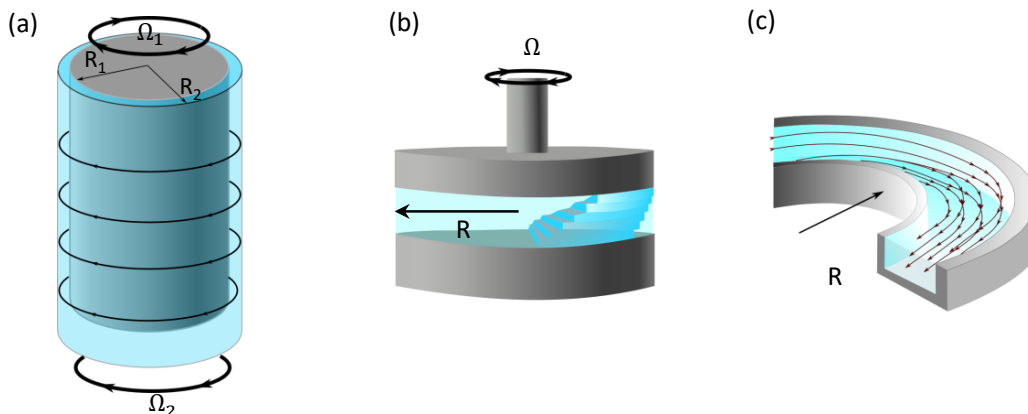
Fig. 3.7 A few examples of shear flow with curved streamline. (a) Taylor–Couette cell, (b) plate-plate geometry, and (c) serpentine channel. R is the radius of curvature of the flow geometry and Ω is the angular velocity.

for Newtonian fluids, where the relationship between stress and strain is linear, the constitutive equation, and hence the momentum equation for viscoelastic fluids can be highly nonlinear and complex.

3.3.3 Elasticity Induced Instabilities

To understand how the viscoelastic nature of polymers causes instabilities when flowing in curved geometries, a description of the behavior of polymers at the molecular level is required. Figure 3.8 (a) depicts the behavior of individual polymers under such flow conditions. At high Weissenberg numbers, the polymers are anisotropically stretched due to the shear gradients, i.e., the polymers are pulled towards the inner wall due to the stronger curvature of the streamlines and higher shear rate at this region. This anisotropic deformation of the polymers leads to an anisotropic distribution of the elastic stresses, and thus to normal stress differences. Under these conditions, a slight perturbation of the flow leads to a deformation of the streamlines, as shown in Fig. 3.8 (b) with solid streamlines. As a result, the gradient of the shear rate is also disturbed (discrepancy between the solid and dashed streamlines in Fig. 3.8 (b)), causing some fluid elements to move slightly outward while others move inward. The effective force pulling the fluid elements inward therefore increases, while the effective force on the fluid elements moving outward decreases. This effect is thus strongly self-amplifying, which means that the flow is unstable when the forces are large enough [78]. In a serpentine channel, the situation is even more complicated because the curvature alters in sign as the flow progresses, and the polymer stream exiting one half-curve enters the next with the opposite curvature. The unstable and chaotic motion of the polymers is reflected in the flow by the appearance of an unstable flow that resembles inertial turbulent flow features, i.e., increased flow resistance and fluctuating flow properties, but
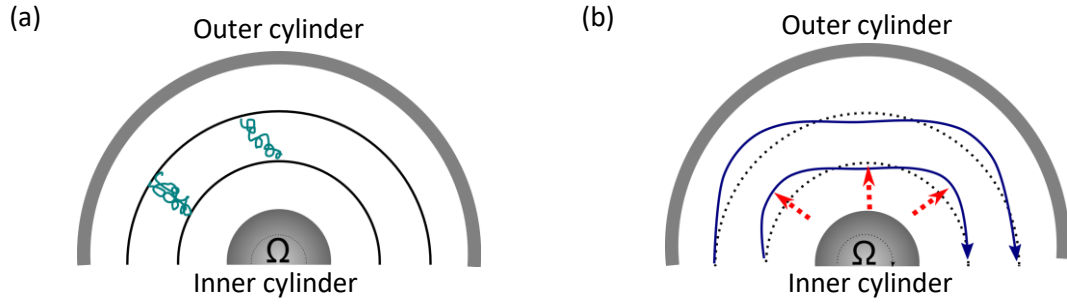
Fig. 3.8 (a) Demonstration of anisotropic stretching and deformation of polymers as they are pulled into regions of higher streamline curvature and higher shear rate, (b) deformation of streamline as a result of perturbation caused by polymer's anisotropic deformation. The solid lines show deformed streamlines with respect to the intrinsic curvature of the channel, shown by dashed lines. The arrows indicate the direction in which polymers are pulled. Adapted and redrawn from [78].

with fundamental differences in its underlying mechanism. In other words, unlike inertial turbulence, the energy cascade is not the mechanism behind, and the elasticity of the polymer solution is the sole cause of instabilities in the flow [89].

Therefore, such instabilities are referred to as "purely elastic instabilities" [81]. Such instabilities have been reported in other shear flows with curved streamlines such as in plate-plate geometry and in serpentine channels [33, 89–93] [Fig. 3.7]. Both geometric factors and fluid properties are expected to contribute to the onset and intensity of purely elastic instability in curved geometries, i.e., the larger the Weissenberg number and the stronger the curvature of the streamlines, at lower shear rates the instability is likely to occur.

One of the most fundamental studies on the scaling of the onset of pure elastic instability in curved geometries was carried out by Pakdel and Mckinley [92]. They have shown that based on the Buckingham theorem approach, the occurrence of pure elastic instability can be scaled by a dimensionless number containing all the components that govern elastic instability, namely geometric factors, and anisotropic elastic normal stresses. The well-known criterion of Pakdeland MacKinley is expressed in its most general form as follows:

$$\frac{\ell}{\mathscr{R}} \frac{|N_1|}{|\tau|} > M^2 \tag{3.31}$$

here $\ell = U\lambda$ is the length scale whereas U is the typical velocity along the flow and λ, is the polymer the longest relaxation time, $\mathscr{R}$ is the typical radius of curvature, N_1 is the first normal stress difference and τ is the shear stress. In this context, M, which is a constant value for dilute polymer solutions with constant viscosity and relaxation time, indicates a lower threshold above which instability initiates. However, the application of this criterion in its original form to semi-dilute entangled polymer solutions with nonlinear rheological properties is inaccurate because the assumption of a con-
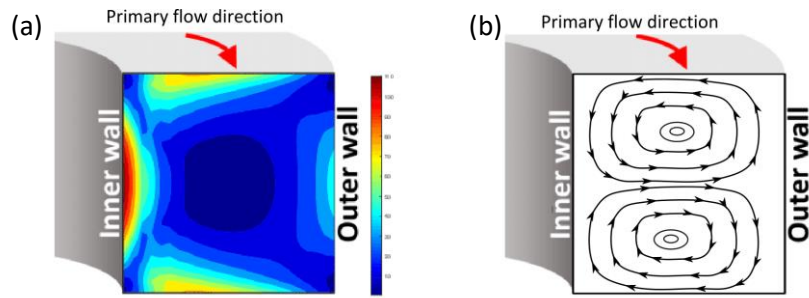
Fig. 3.9 Cross-section view of flow in a serpentine channel, adapted from [94]. (a) Counter-rotating vortices perpendicular to the main flow, (b) normalized first normal stress difference distribution, with the highest values located near the inner wall.

stant relaxation time is not valid. To address this issue, a more realistic representation of the rheological properties of such polymer solutions can be included in the original criterion in the framework of a suitable constitutive model such as the White-Metzner model (see Appendix B).

The flow of viscoelastic polymer solutions in curved geometries is accompanied by the emergence of a first normal stress difference gradient between the wall with the higher curvature and the opposite wall in the direction perpendicular to the main flow, Fig. 3.9(a) [82, 94]. This gives rise to the development of secondary flow structures in the form of counter-rotating vortices, known in fluid mechanics as Dean vortices, Fig. 3.9(b). Although such secondary flows are relatively weak compared to the main flow, they contribute significantly to the total kinetic energy of the system [95] and substantially improve the mixing capacity and heat transfer during the flow [11, 53]. As shown and discussed in Appendices A and C, such secondary flows contribute significantly to the enhancement of interfacial fluctuations and the removal of capillary entrapments as well.

CHAPTER 4

Materials and Methods

This chapter is divided into two main sections. In the first part, the rheological measurement methods used to characterize the viscoelastic polymer solutions are discussed. The second part describes the experimental setups, methods, and procedures employed to investigate the flow of the viscoelastic polymer solutions at the microscale together with their potential effects on the displacement of the capillary entrapment.

4.1 Polymer Solutions and Rheological Characterization

4.1.1 Preparation of Polymer Solutions

The Flopaam polymers used in this study, which are typically used for enhanced oil recovery, are usually supplied as water-soluble dry powders. In enhanced oil recovery, these solutions must be prepared with a suitable salinity and ionic strength to match the formation water. This is because natural porous media contain different types of clay minerals and any change in ionic composition and ionic strength will result in fine migration and a reduction in permeability [96]. Nevertheless, since these polymers have a negatively charged carboxylate group on their backbone, they are very sensitive to salts [97]. In particular, divalent ions such as Ca^{2+} strongly impair the rheological properties and reduce the elasticity of the resulting solutions. Therefore, only a minimal amount of salt was used in this work to achieve the highest possible elasticity in our studies. As recommended by the American Petroleum Institute (API) practice for the evaluation of polymer solutions [98], first, a highly concentrated stock solution with a polymer concentration of 5000 ppm was prepared in a low salinity "brine solution" of ultrapure water containing 1000 ppm NaCl and 10 ppm $CaCl_2$. Especially in the case of high molecular weight polymers, it is very important to avoid vigorous mixing, as this can lead to mechanical degradation of the polymers in the solution. The desired concentration was then achieved by diluting the stock solution with a brine having a similar salt concentration. To avoid degradation of the polymer solutions, the diluted solutions were freshly prepared every three days and the respective stock solution was renewed every four weeks.
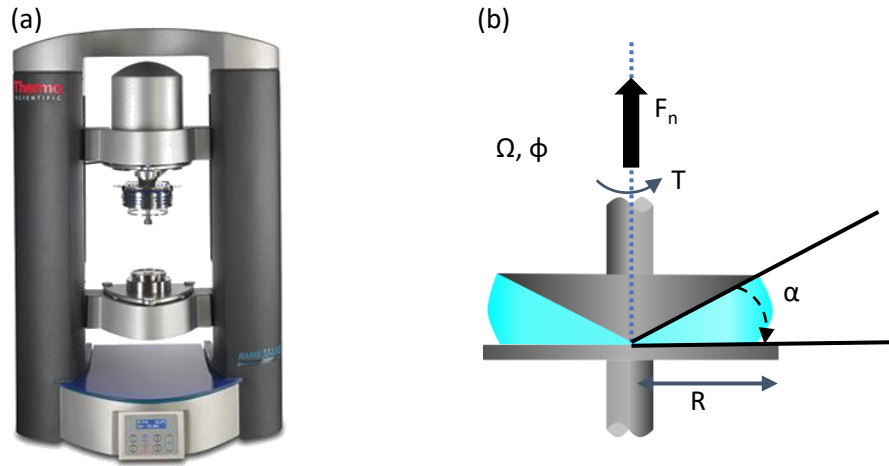
Fig. 4.1 (a) An example of a rotational rheometer (HAAKE MARS 4, Thermo Scientific). (b) Sketch of a cone-plate measuring geometry. The dimensions of the cone used for the measurements of this work were $\alpha = 1°$ and $R = 30mm$.

4.1.2   Rotational Rheometry

To measure various parameters that characterize the shear flow and rheological properties of the polymer solutions a rotational HAAKE MARS 4 rheometer (Thermo Scientific) has been used, is shown in Fig. 4.1(a). Different types of measurement geometries have been developed for rotational rheometers, such as cup-plate or Couette cell, parallel-plate, and cone-plate. The cone-plate geometry is particularly suitable for rheological measurements of shear-thinning polymer solutions used in this study because the small cone angle (usually $\alpha < 4°$) in such measuring geometries ensures that the shear rate is constant over the entire shear gap [99]. A schematic illustration of such geometry is shown in Fig. 4.1(b).

Depending on the measuring mode, either angular velocity Ω or torque T is applied and the corresponding response of the sample is measured. A third transducer is implemented in the rheometer, which measures the thrust force F_n in the axial direction exerted by the sample in the measuring gap on the upper cone. These values are converted to rheological equivalents, shear stress τ, shear rate $\dot{\gamma}$ and first normal stress difference N_1, as follows:

$$\tau = \frac{3T}{2\pi R^3} \tag{4.1}$$

$$\dot{\gamma} = \frac{\Omega}{\tan \alpha} \tag{4.2}$$

$$N_1 = \frac{2F_n}{\pi R^2} \tag{4.3}$$

where R and α are the cone radius and angle, respectively [Fig. 4.1(b)].
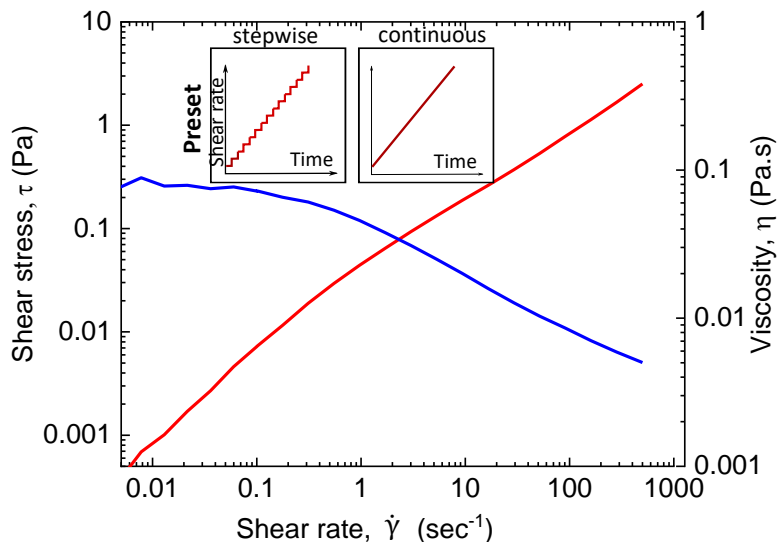
Fig. 4.2 Exemplary plot of the shear viscosity of a 2000 ppm 3630 Flopaam solution using determined via steady shear test.

Two main deformation regimes are possible when using a rotational rheometer: steady shear by imposing a constant rotational speed or torque to obtain flow curves, or oscillatory shear by imposing harmonic oscillations to measure the viscoelastic properties of materials.

4.1.2.1   Steady Shear Test

In the steady shear test, the applied shear rate is either continuously or gradually ramped up, cf. inset the of Fig. 4.2. The corresponding shear stress is measured, and the shear viscosity of the sample is calculated as the ratio of the shear stress to the shear rate at each applied shear rate. An example plot of the shear viscosity of a 2000 ppm 3630 HPAM solution measured with a HAAKE MARS rheometer (Thermo Scientific) and a cone-plate geometry with 1° cone angle is shown in Fig. 4.2

An important application of the shear viscosity values obtained by a steady shear test is to estimate the intrinsic viscosity and thus overlap concentration using the Huggins-Kraemer method [59, 60, 100]. According to the Huggins equation, the specific viscosity, η_{sp}, is related to the intrinsic viscosity, $[\eta]$, by an equation of the following form:

$$\frac{\eta_{sp}}{c} = [\eta] + K_H[\eta]^2 c \qquad (4.4)$$

In this context $\eta_{sp} = (\eta_{solution} - \eta_{solvent})/\eta_{solvent}$, whereas $\eta_{solution}$ is the zero shear viscosity of the polymer solution at the concentration c, and $\eta_{solvent}$ is the viscosity of the pure solvent.

Similarly, according to the Kraemer equation, the natural logarithm of the relative
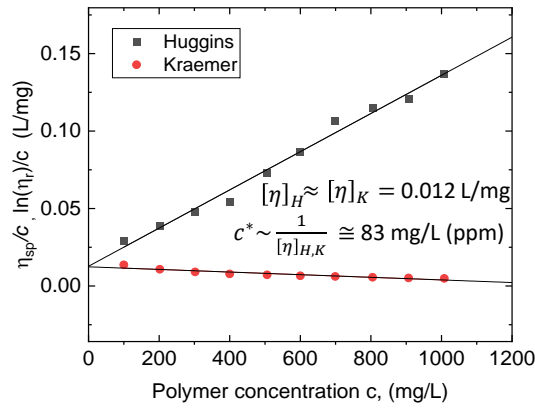
Fig. 4.3 An exemplary illustration of the implementation of the Huggins-Kreamer method for estimating the overlap concentration of 3630 Flopaam polymers in an aqueous solution containing 1000 ppm NaCl and 100 ppm CaCl$_2$ as solvent.

viscosity, $\eta_r = \eta_{solution}/\eta_{solvent}$, is related to the intrinsic viscosity, $[\eta]$, as follows:

$$\frac{ln(\eta_r)}{c} = \ln[\eta] - K_K[\eta]^2 c \tag{4.5}$$

The values K_H and K_K are constants that contain information about hydrodynamic and thermodynamic interactions between the polymer coils in solution [59]. Following Eqs. 4.4 and 4.5, plotting η_{sp}/c and $ln(\eta_r)/c$ as a function of concentration, extrapolated to zero concentration, gives the intrinsic viscosity, $[\eta]_H$ and $[\eta]_K$, respectively. The overlap concentration of the polymer, c^*, is then approximated as the reciprocal of the intrinsic viscosity, i.e., $c^* \approx \frac{1}{[\eta]_{H,K}}$. Figure 4.3 shows an exemplary illustration of the implementation of the Huggins-Kraemer method for 3630 Flopaam aqueous polymer solutions in a solvent containing 1000 ppm NaCl and 100 ppm CaCl$_2$. Further details of the rheological measurements and shear viscosity plots of polymers with different concentrations and molecular weight, as well as overlap concentrations of other polymers used in this dissertation, can be found in the Supplementary Material section of Appendix A.

As already mentioned earlier in section 3.2.3, the shear flow of viscoelastic fluids is accompanied by the storage of elastic (recoverable) deformations and the generation of normal stress differences. The first normal stress difference, as a function of shear rate, is also obtained via the steady shear test and by converting the simultaneously measured thrust normal force during shear, F_n, to the stress exerted on the cone via Eq. 4.3. The measured normal force is influenced by the inertia contribution, which can be significant at high shear rates or for measuring geometries with large diameters. Thus, a correction for inertia effects is often necessary [101, 102]. The correction is done by adding the inertia contribution, ΔF, to the measured normal forces. This value
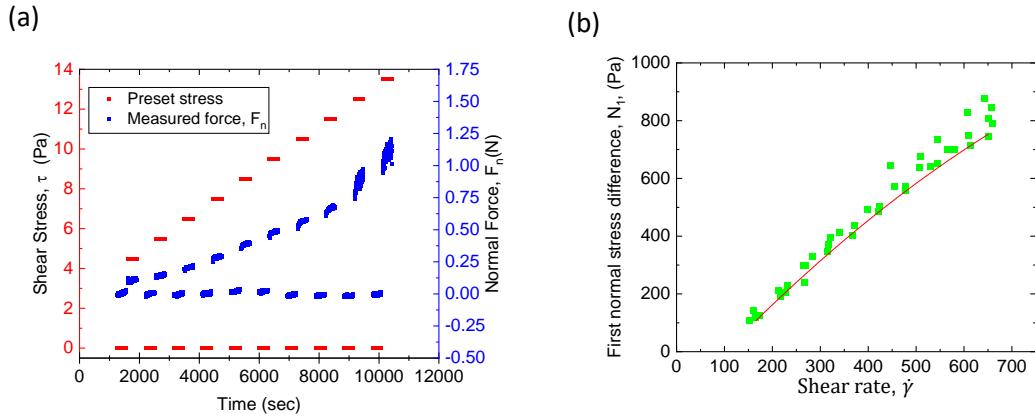
Fig. 4.4 (a) The stepwise applied steady shear stress and the corresponding measured thrust normal force. (b) The first normal stress difference computed from the measured normal forces as a function of shear rate.

is calculated as [103, 104]:

$$\Delta F = \frac{3}{40}\pi\rho\omega^2 R^4 \tag{4.6}$$

where ρ is the fluid density, ω is the angular frequency of the rotation and R is the radius of the cone geometry. To protect the edges of the sample fluid in the gap between the cone and plate, it is helpful to surround it with an immiscible fluid such as oil (often referred to as a "drowned edge"). Figure 4.4(a) shows the protocol developed based on a stepwise steady shear test in stress-controlled mode to accurately estimate the first normal stress difference of the polymer solutions used in this work. To correct for sample relaxation and force transducer drift, the normal force gauge is reset after each shear step, followed by a rest period and a second gauge reset. The force measured at each shear step is then corrected for inertia effects. The first normal stress difference values, $N_1(\dot{\gamma})$, are calculated from the measured normal force values using Eq. 4.3. Despite all precautions and corrections, the measured values at very high shear rates exhibit a high measurement error, which is most likely due to unstable sample edges and the inevitable influence of inertia. Moreover, at very low shear rates, the normal force values are close to the measurement accuracy of the force transducer and are therefore not very precise. The N_1 values as a function of shear rate for a 2000 ppm 3630 Flopaam solution are shown in Fig. 4.4(b). More details and further experimental measurements can be found in Appendix A.

4.1.2.2 Small Amplitude Oscillatory Shear Tests

The dynamic rheological behavior of viscoelastic fluids is studied by periodic deformations, i.e., the measuring geometry oscillates with a small amplitude around the axis of rotation instead of moving continuously in one direction. Therefore, the measured
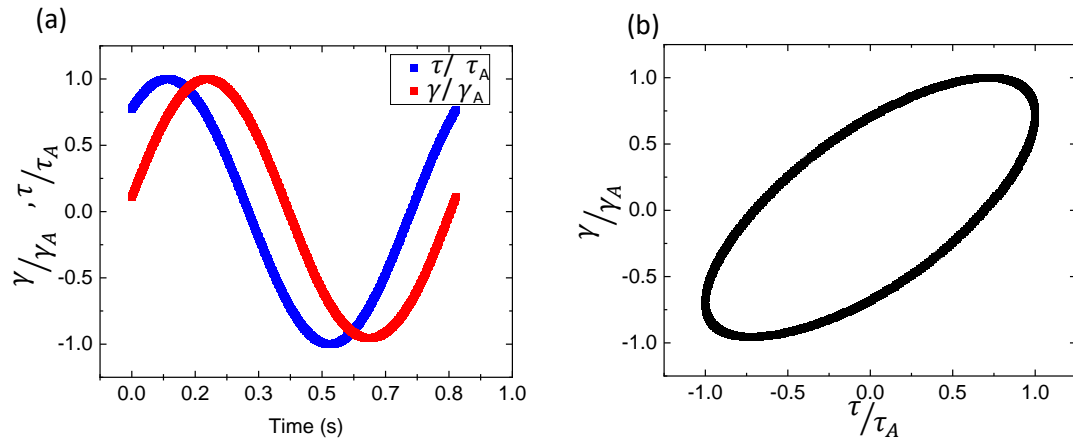
Fig. 4.5 (a) An example of an oscillatory stress and strain function as a function of time for a 2000 ppm 3630 Flopaam solution. (b) The corresponding Lissajous diagram. The shift phase angle of with $\delta \approx 45°$ and the tilted ellipsoidal shape of the Lissajous diagram indicates a linear viscoelastic behavior.

values contain information about both viscous response and stiffness (elasticity) of the sample. The rheological properties obtained from oscillatory tests are implemented directly into the constitutive model to simulate or evaluate the flow. Since these models are developed based on linear viscoelastic behavior, it is important to perform the oscillatory tests with a small amplitude to ensure that the fluid response is captured within a linear viscoelastic range.

These tests are performed in either stress or strain-controlled mode. In strain-controlled mode, a sinusoidal deformation function in the form of $\gamma(t) = \gamma_A \sin \omega t$ is applied to the sample, and the stress response is recorded in the form of a sinusoidal function $\tau(t) = \tau_A \sin \omega t$, while in stress-controlled mode, stress is applied and strain is measured. The ratio between the stress and strain is referred to as the complex shear modulus, $G^* = \tau(t)/\gamma(t)$. As explained in Section 3.2.2, the storage modulus G' is the real part of G^* and represents the elastic response of the fluid, while the loss modulus G'' is the imaginary part and represents the viscous response of the fluid. Figure 4.5(a) shows the applied deformation and the corresponding measured stress response for a 2000 ppm 3630 Flopaam solution as a function of time. The phase shift angle of $\delta \approx 45°$ is an indication of linear viscoelastic behavior. The tilted ellipsoidal shape of the Lissajous diagram plotted in Fig. 4.5(b) further confirms this behavior.

The oscillatory tests are performed in two major ways. One option is the deformation amplitude sweep test in which the deformation amplitude varies while the frequency is kept constant (usually $\omega = 10 \, rad/s$). These tests are carried out solely to determine the limit of the linear viscoelastic range (LVR). An illustrative plot of the deformation sweep test for a 2000 ppm 3630 Flopaam solution is shown in Fig. 4.6(a). The end of the LVR range is marked as the deformation at which G' deviates from the
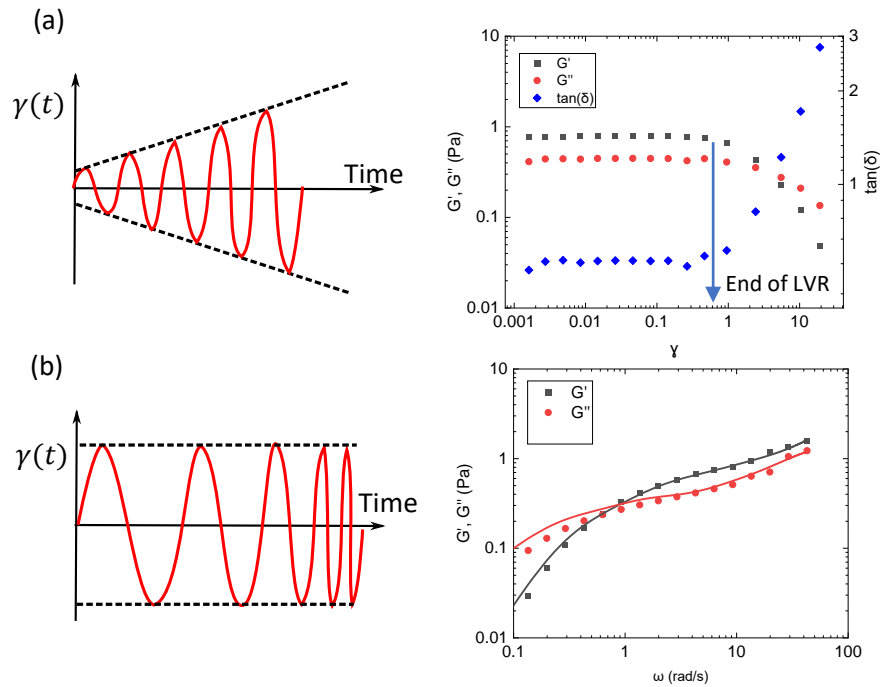
Fig. 4.6 (a) Illustration of a deformation-controlled amplitude sweep test (left) and an example of a measurement result at a frequency of $\omega = 10\ rad/s$. (b) Illustration of a deformation-controlled frequency sweep test (left) and an example of a measurement result at a constant deformation of $\gamma = 0.1$. The solid line is a fit to a 5-element Maxwell model, see Sec. 3.2.2. The fluid used for these measurements was a 2000 ppm 3630 Flopaam.

initial constant plateau by at least 5% [70]. The second type of oscillatory test is the frequency sweep test, where the amplitude is constant, and the frequency usually varies in the range of $\omega = 0.1$ to $100\ rad/s$. A suitable amplitude is selected within the LVR, which is determined by the amplitude sweep test. Frequency sweep tests are performed to investigate the time-dependent deformation behavior of the fluids, e.g., to obtain relaxation times and shear moduli of the viscoelastic polymer solutions. Frequency sweep test results are interpreted within the framework of the generalized Maxwell model, as described in section 3.2.2. An exemplary plot of the frequency sweep test for a 2000 ppm 3630 Flopaam solution is shown in Fig. 4.6(b). The time-dependent behavior of this highly viscoelastic polymer solution can be deduced from G' and G'' diagrams as a function of frequency. The values of G'' are larger than G' at low frequencies, indicating a viscous behavior, while the relationship is reversed at higher frequencies, indicating an elastic behavior.

4.2   Microfluidic Setup and Procedure

The main technique used in this dissertation is based on microscopy observations of flow in microfluidic channels. The microfluidic approach is particularly advantageous
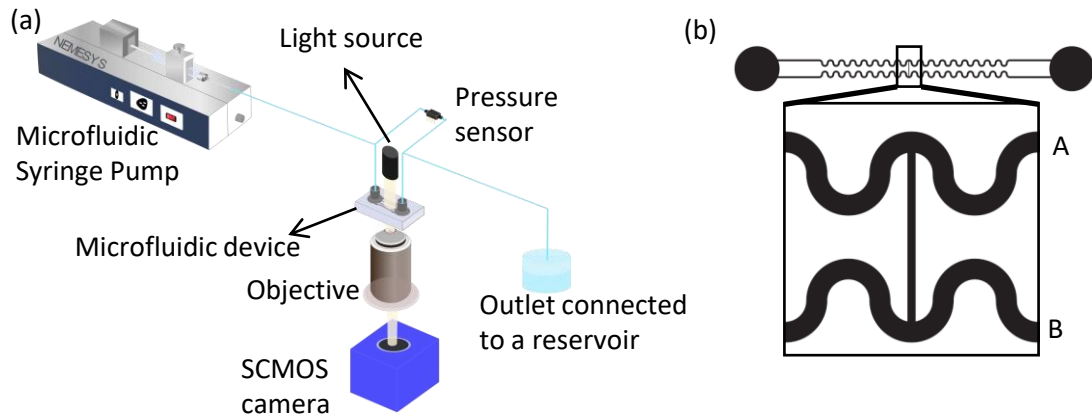
Fig. 4.7 (a) Schematic representation of the microfluidic setup, (b) sketch of the microfluidic geometry used to study the effect of elastic stresses on displacing capillary entrapments.

for the study of viscoelastic flows, since the small dimensions of the flow channels allow high elasticity and hence Weissenbeg numbers to be achieved, while inertia and thus Reynolds numbers remain minimal. A sketch of different components of the experimental setup is shown in Fig. 4.7(a). A microfluidic geometry consisting of two symmetric serpentine channels connected in the middle by a capillary channel, Fig. 4.7(b), was designed to represent a capillary entrapment in a porous medium in a controlled and simplified manner. The serpentine channels were designed to be long enough so that the side channel in the center is far away and not affected by the inlet and outlet of the flow geometry. In addition, the side channel was placed in the center for symmetry. The symmetry of the design allows for eliminating the effect of viscous stresses thus studying the mechanism of displacement of capillary entrapment solely by elastic stresses. The microfluidic devices were fabricated by the double-molding method described in Sec. 4.2.1.

4.2.1   Soft-Lithography and Microfluidic Device

Various methods have been developed to fabricate microfluidic channels in the literature, among which a variant of soft lithography [105–107] has been used in this work. In this method, first, the desired geometry is designed in 2D using high-precision design software such as AutoCAD software. The design is then printed on a transparent photomask with a resolution of approximately $5\,\mu$m. Next in the cleanroom, a negative photoresist (SU-8, MicroChem) is spin-coated onto a silicon wafer with a suitable thickness depending on the desired height of the microfluidic channel that shall be produced from this photoresist structure. The spin-coated silicon wafer is then soft-baked on a hot plate. The duration of soft baking should be adjusted according to the used SU-8 technical data sheet depending on the desired height as well. Next, the photomask is aligned on the SU-8 coated and baked silicon wafer and placed under UV exposure.
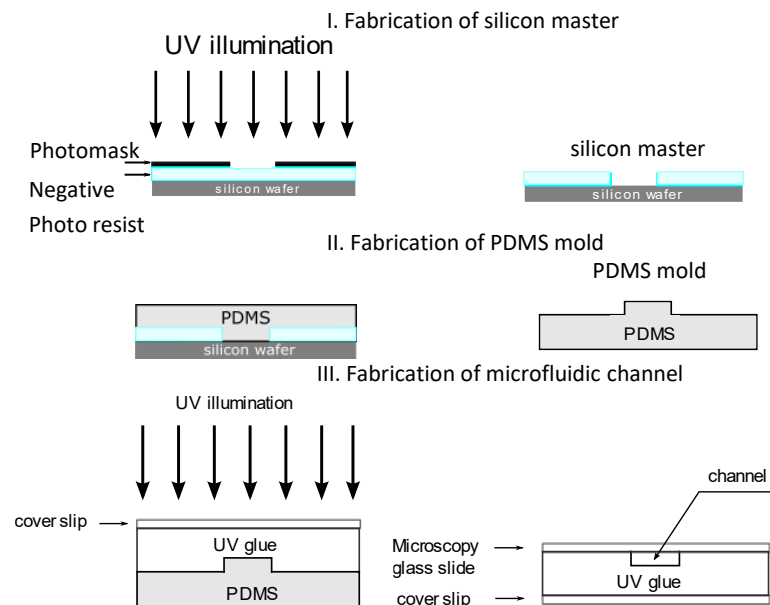
Fig. 4.8 Schematic demonstration of soft lithography for preparation of the silicon master and double-molding method for fabricating microfluidic devices with UV adhesives.

As a result, the parts of the photoresist exposed to the UV light are cross-linked. The silicon wafer is then submerged into a developer solution (MR-dev 600, MicroChem) to remove the remains of the non-crosslinked photoresist. In the final step, the silicon wafer is hard-baked at a temperature of more than 120 °C to further harden the cross-linked photoresist layer and prevent cracking.

The final microfluidic channels are fabricated using a double molding process developed by Bartolo et. al. [108]. In this method, an intermediate polydimethylsiloxane (PDMS) mold is first prepared from the silicon master, and then the microfluidic channel is replicated from this PDMS mold using UV adhesive (NOA 83H, Norland optical adhesives). The UV adhesive is spread on the PDMS mold and covered with a coverslip. After 10 minutes of curing under UV light, the adhesive/coverslip is carefully detached from the PDMS mold and bonded to a glass slide in which two holes are drilled to serve as the inlet and outlet of the channel via plastic connectors (upchurch nanoport N-333). Further details on the soft lithography process and the fabrication of the devices used in the studies presented in this dissertation can be found in the methods section of the appendix A.

4.2.2 Optical Microscopy and Experimental Procedure

As an experimental procedure, the microfluidic device was first saturated with oil, and then displacing fluids were injected in volumetric flow rate controlled mode via a pulsation-free syringe pump (neMESYS, Cetoni GmbH). During this initial injection process oil remains trapped in the side channel and the interfaces between the oil and
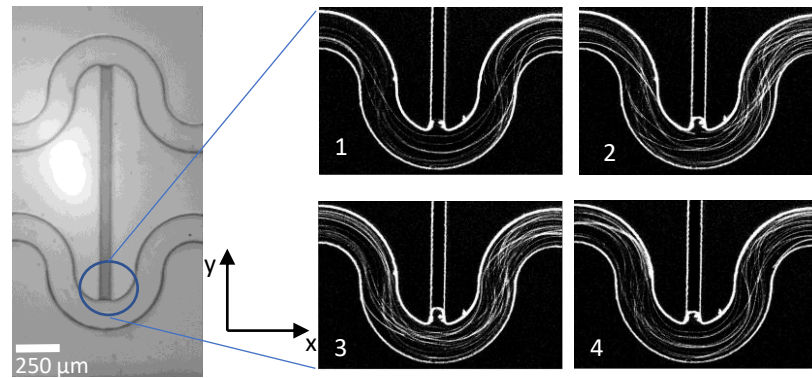
Fig. 4.9 Monitoring and recording the fluctuations of the interface between the entrapped oil and the polymer solution in the main channel at $Wi \approx 45$. A sequence of snapshots clearly shows the random fluctuation of the interface.

the injected fluid were closely inspected using high-speed imaging with a 16-bit sC-MOS camera (PCO Panda 4.2) attached to an inverted microscope. A snapshot of the microfluidic geometry is shown in Fig. 4.9, where the oil is trapped in the side channel and the serpentine channels are filled with the polymer solution. To visualize the flow paths in the serpentine channel, the polymer solutions were seeded with fluorescent particles. The fluorescent particles in the flow field are excited with a light of a certain wavelength and emit a light corresponding to their specific emission wavelength. The signal emitted by the tracer particles is isolated from the illuminated laser light via a filter cube that passes only a narrow wavelength band corresponding to the emitted light. This light is then captured by a camera attached to the epifluorescence microscope. By setting a long exposure time on the order of hundreds of milliseconds, depending on the flow velocity, the continuous flow paths can be visualized. Details of the flow path visualization experiments can be found in Appendix A. A board-mounted differential pressure sensor (26PCSeries, Honeywell) was installed between the inlet and outlet of the microfluidic device to determine the flow resistance during the experimental procedure.

After setting up the microfluidic device and setup, the experiments were conducted by stepwise increasing the flow rate at the inlet until the side channel was fully evacuated. In the case of the Newtonian reference fluid, the experiment was continued until the pressure drop exceeded the range of the pressure sensor. The random fluctuations of the interface at high Weissenberg numbers are evident when comparing successive snapshots in Fig. 4.9. The acquired images were segmented, and the temporal changes in the position of the interface (in the y-direction) were extracted for further analysis of the drainage process and characterization fluctuations, cf. Appendix A .
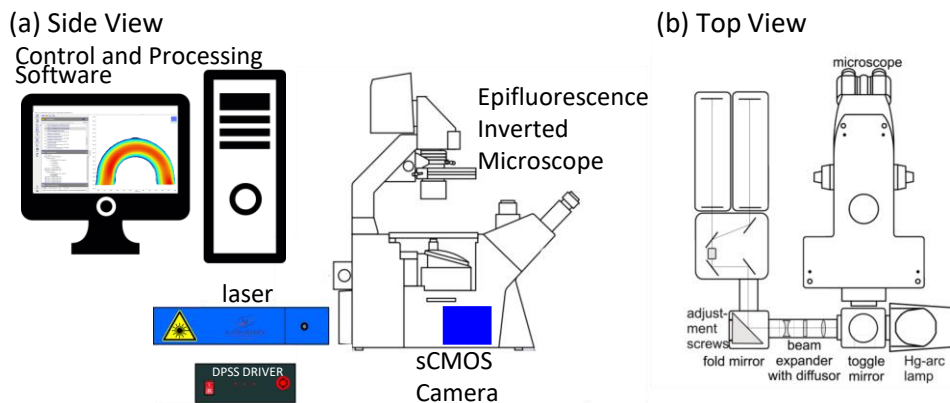
Fig. 4.10 Schematic illustration of the components of the μPIV setups.

4.2.3 Micro– Particle Image Velocimetry (μPIV)

To understand the origin of the interfacial fluctuations observed with optical microscopy, and the corresponding increased pressure drop, clear comprehension of the polymer flow in the serpentine channel has been obtained via Micro Particle Image Velocimetry (μPIV). μPIV has been developed as a non-invasive optical method to quantify and study the flow of fluids on a microscale with resolved length scales ranging from 10^{-4} to 10^{-7} m [109]. In this technique, micron-sized fluorescent particles are introduced into the fluid to monitor its motion and track its flow. The foundation of μPIV goes back to the particle streak velocimetry experiments described by Taylor and Yeung [110] and Brody et al. [111] (also cf. Fig. 4.9). The μPIV technique in its current form, which is widely used in microfluidics, was first introduced by Santiago et al. [112–114]. They used epifluorescent illumination to capture discrete particle images of fluorescent particles and developed correlation methods for calculating the velocity of the particles and thus the fluid with a spatial resolution of less than 10 μm. Extensive reviews on this topic have been published by Sinton [115] and Wereley and Meinhart [109], and more recently by Etminan et. al. [109].

In general, a μPIV system comprises several principal components: seeding, illumination, acquisition, calibration, image evaluation and processing, and post-processing. A schematic representation of the μPIV setup used in this work is shown in Fig 4.10. The fluid of interest is seeded with fluorescent particles that are assumed to follow the flow of the fluid. Therefore, it is very important to carefully select the size of the particles so that they are not too small to be affected by the browning motion or too large to affect the flow [116]. Polystyrene (PS) particles with a density of $\rho = 1.05 \ g/cm^3$ and a refractive index of 1.59 in the range of 0.3 to $2 \ \mu m$ in diameter are the most commonly used particles for μPIV as they have been proven to follow the motion of the fluid without delay or altering the flow field [117]. Such particles are supplied as a dispersion in a solution containing surfactants; however, the concentration used for μPIV is so low
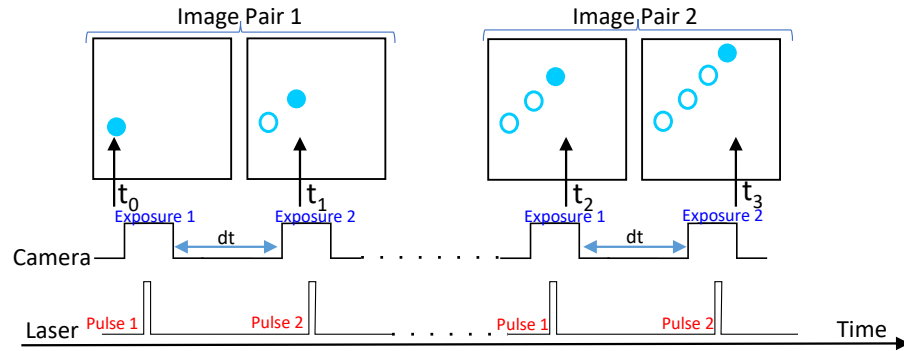
Fig. 4.11 Schematic illustration of particle tracking with single exposure and single frame imaging, and particle image velocimetry with double frame imaging.

that the amount of surfactants is insufficient to change the interfacial properties of the carrier fluid.

In contrast to macro PIV, where a two-dimensional light sheet is used for illumination, in μPIV, it is desirable to illuminate the entire test section with a volume of light, hence in volume illumination mode. This is mainly due to the lack of optical access with significant diffraction in light sheet forming optics [118]. For this purpose, a pulsed DPSS laser with a wavelength corresponding to the excitation wavelength of the tracer particles is used. The laser is expanded and directed into an inverted epifluorescence microscope. The objective directs the laser beam onto the microfluidic device. Similar to the flow path visualization experiments explained in Sec. 4.2.2, the fluorescent particles in the flow field absorb the excitation light and emit a light corresponding to their specific emission wavelength. The emitted signal reaches the camera attached to the epifluorescence microscopy after going through a filter cube that passes only a narrow wavelength band. The exact details and description of the μPIV setup used in this dissertation can be found in Appendix C.

Depending on the optical system including the microscope and the objective, there are two ways to visualize the flow. One option is to use an optical system that has a depth of correlation that exceeds the depth of the flow being measured, which has the advantage that all particles in the optical system's field of view are well-focused. However, the main disadvantage of this method is that no depth information is preserved, and the velocity fields obtained represent an average over the depth of the flow. The second option is to use an optical system whose depth of correlation is smaller than the flow height. The optical system allows focusing on particles that are within the depth of correlation of the imaging system, while the out-of-focus particles mainly contribute to the background noise. For this method, it is very important to accurately determine the depth of field, or more precisely, the correlation depth in order to resolve the velocity field with respect to the channel's height [119]. To improve the reliability of velocity fields obtained with μPIV, it is important to reduce background noise and improve the
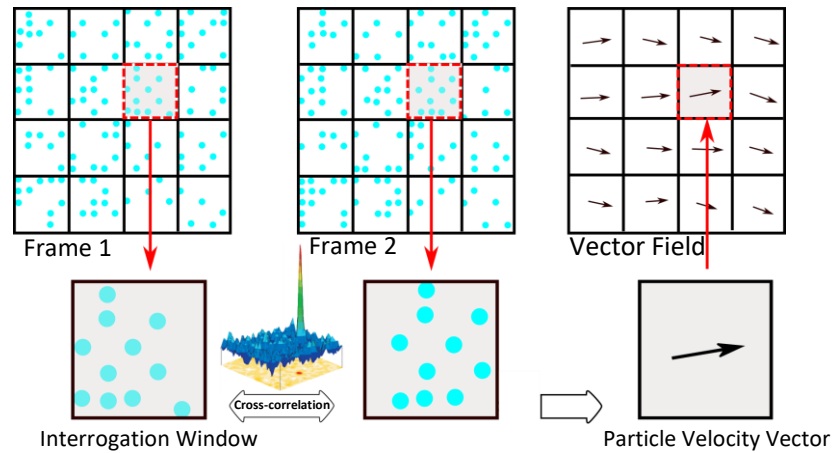
Fig. 4.12 Schematic illustration of the division of the field of view into interrogation windows in μPIV. The velocity vector field is acquired by cross-correlation of the particle motion between two successive images.

signal-to-noise ratio by adding an optimized particle concentration to the flow [113].

In the image acquisition process, two consecutive frames are captured from the moving particles with a small-time difference dt. The laser pulsation is synchronized with the camera exposure so that a short pulse is fired for each exposure time corresponding to each frame of the image pair. Figure 4.11 shows a schematic diagram of the double shutter double frame scheme. These two frames are divided into equally spaced regions called interrogation windows. Each interrogation window in the first frame is cross-correlated with the corresponding window in the second frame to determine the most probable local displacement and hence velocity vector [120]. A schematic demonstration of splitting the image field into interrogation windows and generating the velocity vector field by cross-correlation is shown in Fig. 4.12. Details on image acquisition and processing, as well as the cross-correlation approach implemented in this dissertation, can be found in Appendix C. The final temporally-spatially resolved velocity fields are used for further investigation of flow properties.

CHAPTER 5

Results and Discussion

Viscoelasticity and purely elastic instability have been implicated in several studies as possible reasons for the improvement of microscopic efficiency in polymer flooding. However, an exact mechanism and a clear explanation of how viscoelasticity affects the displacement process are still lacking. In this chapter, a mechanism of displacement under the sole influence of the elasticity of the polymer solutions is proposed and discussed in light of the direct observation and analysis of the experimental results of the viscoelastic polymer flow that are attached in the appendices A-D.

5.1 Effect of Viscoelasticity on Displacing Capillary Entrapment

When it comes to viscoelastic fluids, the flow even in the simplest microfluidic model porous media, such as the regular or irregular distribution of disks in a channel, is rather complex. This complexity does not allow disentangling the impact of the fluid's elasticity from its viscous component on the efficiency of the displacement process. To tackle this problem, a simple but robust model system consisting of two symmetric serpentine channels interconnected in the middle by a capillary channel was developed. The publication by **Shakeri et al. in *AIP Physics of Fluids* 2021** (appendix A) presents the results of a series of experiments performed to investigate the impact of viscoelasticity of semi-dilute polymer solutions on the displacement of a capillary entrapment in such a microfluidic channel. A snapshot of the microfluidic channel used in this work is shown in Fig. 5.1(a), This model system serves as a single capillary entrapment and represents the main features of flow in porous media, i.e., tortuosity. Consideration of a tortuous flow geometry is particularly important because the polymers therein are subjected to both shear and elongation, resulting in an anisotropic distribution of elastic stresses and thus inducing elastic instabilities. Due to the symmetry between channels A and B in Fig. 5.1(a), the viscous pressure at both ends of the capillary entrapment is the same and thus cancels out. This allows studying exclusively the effects of elastic stresses on the displacement mechanism. Direct observation and quantitative expression of the deviation of the interface position from a reference central line (dashed line in Fig. 5.1(a)), δY, show that strong fluctuations in the interface occur with increasing
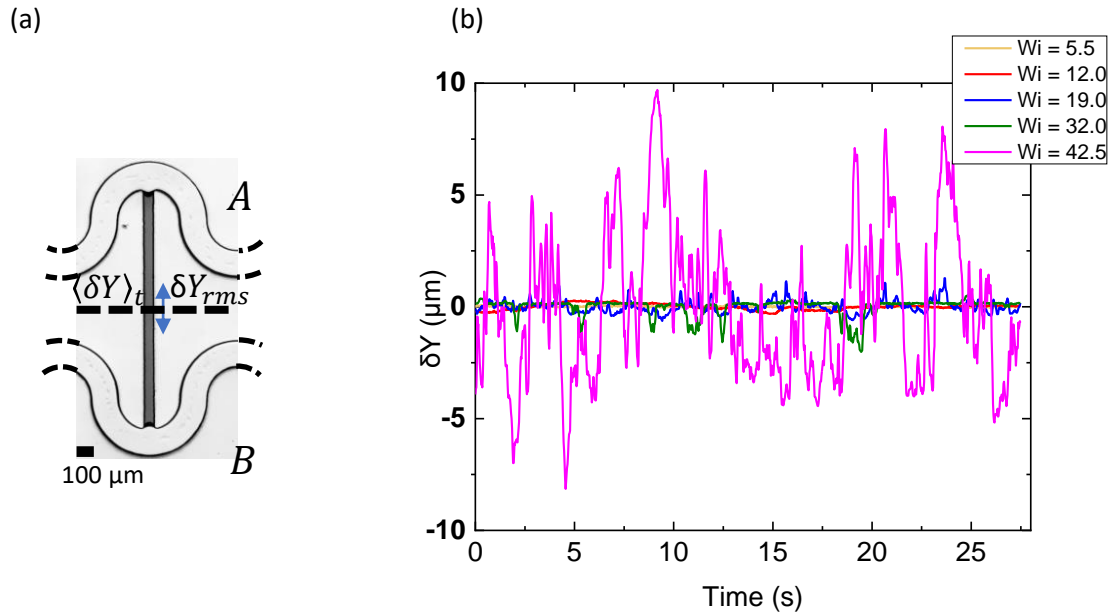
Fig. 5.1 (a) A snapshot of microfluidic geometry. δY is the instantaneous deviation of
the center of the oil column from the fixed central dashed line indicating the interface
fluctuation. $\langle \delta Y \rangle_t$ and $\langle \delta Y \rangle_{rms}$ are the time average and root mean square of δY, respectively. (b) The temporal changes of δY at different Weissenberg numbers.

flow rate and thus with increasing Weissenberg number. The simultaneously measured
pressure drop across the channel during polymer injection also indicates a sudden in-
crease, confirming the emergence of turbulent flow above a critical shear rate, cf. Fig. 2
in Appendix A. At sufficiently high Weissenberg numbers, a fully developed and highly
random turbulent flow is formed. The corresponding power spectral density analysis of
the interfacial fluctuations (Fig. 7 in Appendix A) shows a large exponent, indicating
that the fluctuations contain a wide range of intensities and are of pure elastic nature.
Once the polymer flow reaches this state of turbulence at both interfaces of the trapped
oil in the side channel, an instantaneous pressure difference between the two ends of
the capillary entrapment occurs that is high enough to overcome the capillary threshold
and release the oil.

A comparison of the experimental results of polymer solutions with different molec-
ular weights and concentrations shows that, regardless of the degree of elasticity of the
polymer solutions, a certain degree of turbulence and thus fluctuation intensity is re-
quired to overcome the capillary threshold and remove oil entrapment, cf. Fig. 5 in Ap-
pendix A. From this study, it can be concluded that purely elastic instability is respon-
sible for the improved microscopic displacement efficiency associated with viscoelastic
polymer flooding.

5.2   Scaling of the Onset of Purely Elastic Instability

An important step in the evaluation and interpretation of the experimental results for different polymer solutions discussed in Sec. 5.1, is the scaling of the onset of purely elastic instability with respect to a uniform and comparable framework. Since the used polymer solutions are in the semi-dilute regime, i.e., in a concentration regime where the polymers interact with each other, and thus the rheological and dynamic properties of the fluid are strongly affected by the shear rate, developing a proper scaling law is essential. A suitable scaling factor allows the evaluation and interpretation of the experimental results for different polymer solutions with respect to a uniform and comparable framework. Traditionally, the Pakdel and McKinley criterion is used to scale the onset of elastic instability in curved flow geometries [121]. In the original form of this criterion, it is assumed that the relaxation time is constant and equal to the longest relaxation time of the polymers. This assumption is not valid for semi-dilute regime and leads to a delayed prediction of the onset of elastic instability for such solutions. In the publication by **Shakeri et al. in *APS PHYSICAL REVIEW E* 2022**, the shear dependence of the rheological properties of the polymer solutions in the context of the White–Metzner constitutive fluid model is incorporated in the Pakdeland McKinley criterion, resulting in a criterion of the following form:

$$C\sqrt{\frac{N_1\left(\dot{\gamma}_{\text{crit}}\right)}{G_0}} \approx M_{\text{crit}} \tag{5.1}$$

where C is a geometry factor computed as $C = (WH)/(64\pi R^2)$ for a serpentine channel with rectangular cross-section with a height of H and width of W. In this approach the value of $N_1(\dot{\gamma})$ is experimentally measured (cf. Fig. S3 in Appendix B), using the protocol described in Sec. 4.4. The critical shear rate at the onset of pure elastic instability is determined as the shear rate at which the flow resistance increases and the reduced viscosity (the ratio of apparent viscosity to bulk viscosity measured with a rheometer) deviates from unity, cf. Fig. 1(b) in the appendix B. The discrete relaxation time spectrum and the corresponding shear moduli are obtained by fitting the experimentally measured G' and G" plots (cf. Fig.S4 in Appendix B) to a 5-element Maxwell model using a frequency sweep test. By using the value of $N_1(\dot{\gamma}_{crit})$, i.e., the intensity of the first normal stress difference at the onset of purely elastic instability, and G_0, the largest shear modulus corresponding to the smallest relaxation time, the degree of elasticity of the polymer solutions at the onset of instability is taken into account.

To evaluate the adjusted criterion for scaling the onset of pure elastic instability of semi-dilute polymer solutions, the flow of 15 polymer solutions with three different molecular weights in a single serpentine channel was studied. Polymer concentra-
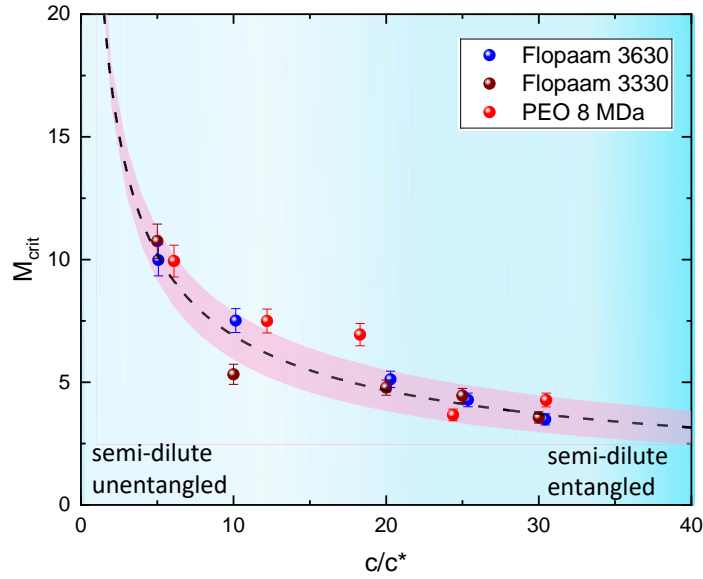
Fig. 5.2 Threshold value M_{crit} calculated from Eq. 5.1 as function of c/c^* for three different polymer solutions in the semi-dilute regime. The dashed curve is a power-law fit $M_{crit} = A\,(c/c^*)^{-b}$, where $A = (25.28 \pm 3.87)$ and $b = (0.56 \pm 0.05)$. The pink area corresponds to the standard error of the fitting parameters.

tions were varied in the range of $5\times$ to $30\times$ their corresponding overlap concentration. Plotting the corresponding M_{crit} as a function of normalized concentrations, Fig. 5.2, exhibits a universal master curve independent of the type and concentration of the polymer solutions. Therefore, the criterion proposed in Eq. 5.1 is successfully evaluated to determine the onset of pure elastic instability of polymer solutions in the semi-dilute regime.

5.3 Characterization of Elastic Turbulent flow in a Serpentine Channel

To gain a clear insight into the mechanism behind the enhanced capillary displacement at the pore level, a thorough investigation of viscoelastic microflow is of great importance. The publication by **Shakeri et al. in *AIP Physics of Fluids* 2022**, Appendix C, addresses the questions of how the elasticity of the polymers affects the flow in the semi-dilute regime and what the characteristics of the resulting flow are. The results of this work provide a comprehensive description of statistical, spectral, and structural properties of the semi-dilute entangled polymer flow in a serpentine channel, i.e., mixed type flow including regions of both shear and elongation, with curved streamlines. The direct flow investigations using μPIV and the analysis of the extracted velocity fields suggest the presence of a highly anisotropic, non-homogeneous, and unstable flow above a critical Weissenberg number. The plot of the power spectral density of the velocity fluctuations, cf. Fig.7 in Appendix C, shows a relatively smaller expo-
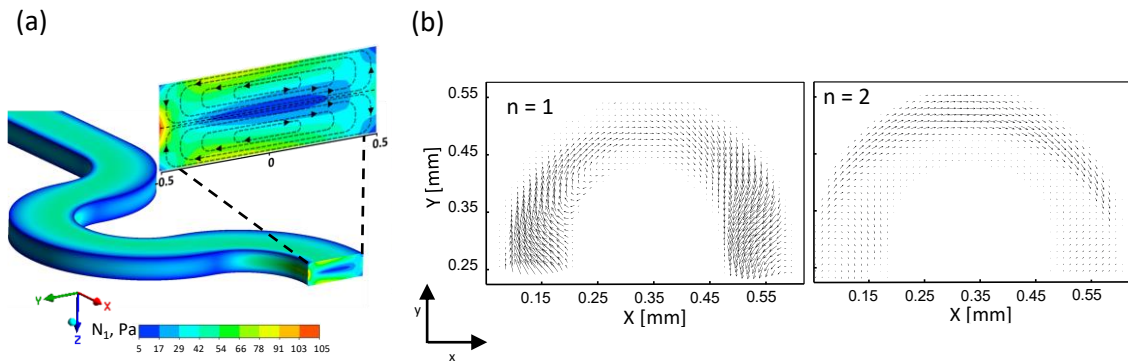
Fig. 5.3 (a) Distribution of the first normal stress difference N_1 within a vertical cross-section of the serpentine channel obtained via CFD simulations (Wi $\approx$ 5.4). (b) Secondary flow structures at two successive highest energy levels (n = 1, 2) obtained from µPIV by POD analysis (Wi $\approx$ 45).

nent compared to the corresponding value of a dilute polymer solution. This implies a limited range of the excited scales in the purely elastic turbulent flow of a semi-dilute entangled polymer solution, which can be due to the limitation of polymer motion in space and entanglement above the overlap concentration. A numerical method called proper orthogonal decomposition (POD) was applied to extract the flow structures from the velocity fields obtained via µPIV. The results of this method directly demonstrate the activity of purely elastic secondary flows in a serpentine geometry. These secondary flows which are governed by the gradient of N_1 in the cross-flow direction are shown in Fig. 5.3.

An important outcome of this study is that secondary flow structures highly contribute to the total kinetic energy of the system, cf. Fig. 8 and Fig. 9 in Appendix C. Looking back at the initial observation of the displacement process in the single pore geometry in light of these latter findings, it can be concluded that the additional flow resistance and increased pressure drop observed in the capillary entrapment removal experiments are largely caused by such a secondary flow structure. Thus, secondary flow plays an important role in inducing interfacial fluctuations and provides the force to overcome the capillary threshold.

5.4 Viscoelastic micro-flow in Porous Media

In an attempt to apply the findings from the previous studies to explore and explain the influence of viscoelasticity on displacement processes in more complex geometries, a series of experiments were conducted in a simple microfluidic model porous medium. The results of these experiments have been reported and discussed in **Jung et al. submitted to *Frontiers in Physics* 2022**, Appendix D. The porous medium used in this work is a microfluidic channel filled with arrays of randomly distributed circular posts
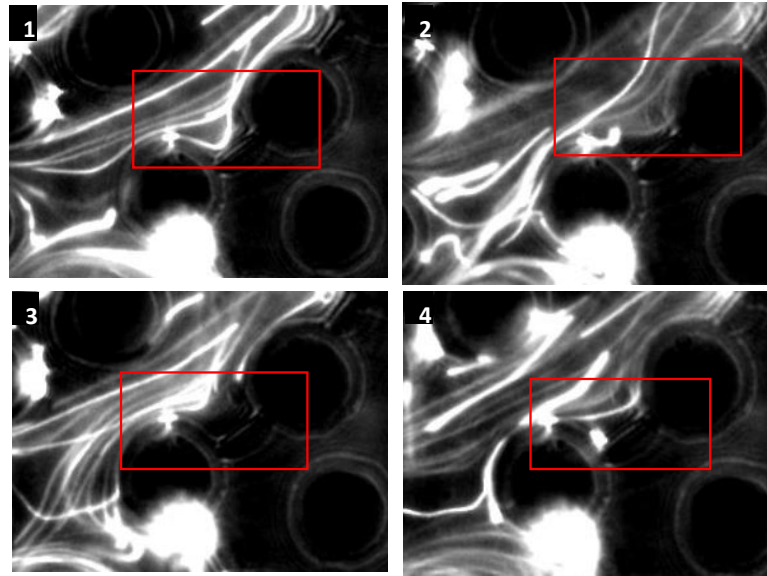
Fig. 5.4 The intense fluctuations of the interface between the trapped oil and a polymer solution containing 2000 ppm Flopaam 3630 in the porous medium. Successive images are taken with a 200 ms time difference between them.

with 30% packing density. The posts have a diameter of $d \approx 0.032\,$mm, a height of $h_1 \approx 0.030\,$mm and an average center-to-center distance of $(0.027 \pm 0.013)\,$mm. As mentioned earlier, the flow in such geometry is already quite complex, and it is not easy to disentangle the effects of elasticity and viscosity. To approach this problem, different displacing fluids were considered to separately evaluate the effects of each component, namely viscosity, shear thinning, and elasticity of the fluid. The working fluids include Newtonian fluids, i.e. water, a high-viscosity glycerin solution, an inelastic shear-thinning polymer solution (Xanthan gum), and a viscoelastic polymer solution (Flopaam), similar to the previous studies. In separate experiments, the fluids were injected into the initially oil-saturated microfluidic porous medium at a constant flow rate in the capillary-dominated regime. The polymer solutions were designed to have the same shear-thinning viscosity, while the viscosity of the glycerin solution matched the viscosity of the polymer solutions at the typical shear in the porous medium corresponding to the applied flow rates. By comparing the performance of these fluids in terms of displacement patterns, the size distribution of remaining capillary inclusions, and residual oil saturation, the contribution of elasticity can be elucidated. A comparison of the performance of high viscose glycerin solution with water shows that increasing the viscosity and thus the capillary number leads to a more efficient displacement process, both in terms of improving the mobility ratio and reducing the residual saturation. However, a comparison of the results of the inelastic polymer solution with the glycerin solution indicates that the inelastic polymer solution showed more fingers on the invading front and the final residual saturation was relatively higher than that of glycerin. This is due to

the highly shear-thinning viscosity of the polymer solution used and the random distribution of the pore geometry, which leads to a variation in the apparent in-situ viscosity of the polymer. Therefore, the possibility that the increased capillary number associated with the increased viscosity of the polymer solution per se improves the displacement process is excluded. In the case of the highly viscoelastic displacement fluid, the initial front shape looks very similar to the inelastic Xanthan gum. The unique distinction, however, is that the interfaces between the oil entrapments and the viscoelastic invading fluid become unstable after some time. A close-up view of the interface between an oil entrapment and polymer solution in the porous media is shown in Fig. 5.4. The time sequence of the flow path lines clearly shows unstable fluctuations at the interface as well as crossing path lines, indicating semi-three-dimensional effects caused by the unstable flow. This eventually led to the fragmentation and reconfiguration of the remaining oil entrapments and their removal from the porous medium. The final residual saturation was lower compared to the inelastic polymer solution with similar shear viscosity, proving that the occurrence of elastic instability in such fluids at sufficiently large flow rates has an auxiliary effect on the displacement process. The final size distribution of the remaining oil showed a relatively smaller average size in the case of the viscoelastic fluid even compared to the high viscosity glycerin solution, indicating that in the case of viscoelastic fluids, breakup and demobilization of entrapments occur and even a higher capillary threshold can be overcome.

The origin of the observed unstable flow in the porous medium can be deduced from our findings from a single capillary experiment (see Appendix A). Since the flow paths in such a porous medium inherently have the same characteristics as a serpentine channel, namely being curved and exhibiting a mixed flow type, it can be concluded that the anisotropic stress distribution causes purely elastic instability. Moreover, the tortuous nature of the pathways can cause a strong gradient of N_1 in the cross-flow direction, leading to the development of secondary flow structures. Such unstable structures cause interfacial fluctuations that exert the force necessary to overcome the capillary threshold and to break up and release the capillary entrapments.

CHAPTER 6

Summary and Outlook

The goal of this dissertation was to provide clear insight into one of the most controversial topics in the field of fluid flow in porous media, namely the microscale mechanism of capillary displacement by viscoelastic fluids.

Since even the simplest porous medium is still too complex to gain a basic understanding of viscoelastic microflow, a simple microfluidic geometry was designed to capture the most important features of such geometries, i.e., a capillary entrapment and curved flow pathways via serpentine channels. Direct visual observations in this simplified single-entrapment geometry indicated the occurrence of an unstable flow accompanied by an increase in the flow resistance of the polymer solutions above a critical shear rate. Since the inertia was negligible, this unstable flow was caused exclusively by elastic forces. Under the influence of this unstable flow, the interface between the entrapped oil and the polymer solution became unstable, and once the fluctuations were strong enough, the entrapped oil was completely released.

Since the polymer solutions used in polymer flooding for enhanced oil recovery are in the semi-dilute regime, our studies also focused on these concentrations. However, predicting and scaling the onset of elastic instability in this regime required further investigation. Therefore, we incorporated the rheological properties of such solutions into the existing scaling approaches and developed a criterion that represents a realistic account of the fluid's properties. Applying the obtained criterion to a variety of different polymer solutions with different molecular weights confirmed the reliability of the proposed scaling adjustments. This scaling approach can be further extended to account for more complex geometric properties in future studies to provide a universal framework for the comparison and scaling of purely elastic instability, independent of the geometric and fluid properties.

µPIV experiments of a semi-dilute entangled polymer solution flow in a serpentine channel showed that above a critical shear rate, highly non-homogeneous turbulent flow occurs. Compared to the turbulent flow of a dilute polymer solution, the range of excited velocity fluctuations was relatively narrower, which can be attributed to the entanglement of the polymers in the semi-dilute regime and the resulting restriction on

the free movement of the polymers. Analysis of the μPIV results using the proper orthogonal decomposition method (POD) showed strong secondary flow structures, which contribute strongly to the kinetic energy of the system. It could be concluded that the increased flow resistance observed above the critical flow rate in terms of an increased pressure drop and hence increased apparent viscosity is influenced by these secondary flows. Investigating the evolution of the secondary flows with respect to the main flow from such analyses and comparing it with the corresponding numerical predictions and their contribution to the additional pressure difference will be future research goals.

With the understanding gained from viscoelastic flow in the simplified geometry, we carried out experiments in a microfluidic porous medium consisting of a random distribution of circular posts. It was observed that similar to the displacement of a single entrapment, fluctuations at the interface between the oil entrapments and the viscoelastic fluid caused their reconfiguration and eventual removal. A comparison of these results with the displacement of oil with an inelastic polymer solution of similar shear-thinning viscosity confirmed that the additional displacement in the case of the viscoelastic polymer solution is solely due to the occurrence of unstable flow at high shear rates due to the elasticity of the fluid. Since in such porous media the flow paths are strongly curved, it could be concluded that the amplification of the first normal stress difference and its gradient in the cross-flow direction can also induce a strong secondary flow here. These secondary flow structures contribute to the increase of the flow resistance as well as the intensity of the interfacial fluctuations, which leads to an improved microscopic displacement efficiency in porous media.

The results presented in this dissertation and all the possible future experiments will further improve the understanding of viscoelastic microflow and capillary displacement in porous media and can certainly pave the way for further numerical and theoretical studies.

REFERENCES

[1] Hanswalter Giesekus. Zur stabilität von strömungen viskoelastischer flüssigkeiten. *Rheologica Acta*, 5(3):239–252, 1966.

[2] Kenneth S Sorbie. *Polymer-improved oil recovery*. Springer Science and Business Media, 2013.

[3] James Sheng. *Modern chemical enhanced oil recovery: theory and practice*. Gulf Professional Publishing, 2010.

[4] Don W Green and G Paul Willhite. Enhanced oil recovery. 2018.

[5] Larry W Lake. Enhanced oil recovery. 1989.

[6] Eric Delamaide, Philippe Corlay, and Wang Demin. Daqing oil field: The success of two pilots initiates first extension of polymer injection in a giant oil field. In *SPE/DOE Improved Oil Recovery Symposium*. OnePetro, 1994.

[7] Dongmei Wang, Huanzhong Dong, Changsen Lv, Xiaofei Fu, and Jun Nie. Review of practical experience by polymer flooding at daqing. *SPE Reservoir Evaluation and Engineering*, 12(03):470–476, 2009.

[8] Demin Wang, Jiecheng Cheng, Junzheng Wu, and Gang Wang. Experiences learned after production of more than 300 million barrels of oil by polymer flooding in daqing oil field. In *SPE annual technical conference and exhibition*. OnePetro, 2002.

[9] Y Du and L Guan. Field-scale polymer flooding: lessons learnt and experiences gained during past 40 years. In *SPE International Petroleum Conference in Mexico*. OnePetro, 2004.

[10] Zhen Zhang, Jiachun Li, and Jifu Zhou. Microscopic roles of "viscoelasticity" in hpma polymer flooding for eor. *Transport in porous media*, 86(1):199–214, 2011.

[11] Peter Mitchell. Microfluidics—downsizing large-scale biology. *Nature biotechnology*, 19(8):717–721, 2001.

[12] Demin Wang, Jiecheng Cheng, Qingyan Yang, Gong Wenchao, Li Qun, and Fuming Chen. Viscous-elastic polymer can increase microscale displacement efficiency in cores. In *SPE annual technical conference and exhibition*. OnePetro, 2000.

[13] Ahmed M Shehata, Ahmed Ghatas, Mahmoud Kamel, Ahmed Aly, and Ahmed Hassan. Overview of polymer flooding (eor) in north africa fields–elements of designing a new polymer/surfactant flood offshore (case study). In *North Africa Technical Conference and Exhibition*. OnePetro, 2012.

[14] Mojdeh Delshad, Do Hoon Kim, Oluwaseun Adedeji Magbagbeola, Chun Huh, Gary Arnold Pope, and Farhad Tarahhom. Mechanistic interpretation and utilization of viscoelastic behavior of polymer solutions for improved polymer-flood efficiency. In *SPE Symposium on Improved Oil Recovery*. OnePetro, 2008.

[15] Li-juan Zhang and Xiang-an Yue. Mechanism for viscoelastic polymer solution percolating through porous media. *Journal of Hydrodynamics*, 19(2):241–248, 2007.

[16] R Haas and F Durst. Viscoelastic flow of dilute polymer solutions in regularly packed beds. In *Progress and Trends in Rheology*, pages 212–217. Springer, 1982.

[17] Xian-Qing Han, Wei-Ying Wang, and Ying Xu. The viscoelastic behavior of hpam solutions in porous media and it's effects on displacement efficiency. In *International Meeting on Petroleum Engineering*. OnePetro, 1995.

[18] Yoshihiro Masuda, Ke-Chin Tang, Masashi Miyazawa, and Shoichi Tanaka. 1d simulation of polymer flooding including the viscoelastic effect of polymer solution. *SPE Reservoir Engineering*, 7(02):247–252, 1992.

[19] S De, P Krishnan, J Van Der Schaaf, JAM Kuipers, EAJF Peters, and JT Padding. Viscoelastic effects on residual oil distribution in flows through pillared microchannels. *Journal of colloid and interface science*, 510:262–271, 2018.

[20] RE Hincapie, A Rock, J Wegner, and L Ganzer. Oil mobilization by viscoelastic flow instabilities effects during polymer eor: A pore-scale visualization approach. In *SPE Latin America and Caribbean Petroleum Engineering Conference*. OnePetro, 2017.

[21] T. S. Urbissinova, J. J. Trivedi, and E. Kuru. Effect of elasticity during viscoelastic polymer flooding: A possible mechanism of increasing the sweep efficiency. *Journal of Canadian Petroleum Technology*, 49(12):49–56, 2010. ISSN 00219487. doi: 10.2118/133471-PA.

[22] Andrew Clarke, Andrew M. Howe, Jonathan Mitchell, John Staniland, and Laurence A. Hawkes. How viscoelastic-polymer flooding enhances displacement efficiency. *SPE Journal*, 21(03):0675–0687, 2016. ISSN 1086-055X. doi: 10.2118/174654-PA. URL http://www.onepetro.org/doi/10.2118/174654-PA.

[23] Alexander Rock, Rafael E. Hincapie, Muhammad Tahir, Nils Langanke, and Leonhard Ganzer. On the role of polymer viscoelasticity in enhanced oil recovery: Extensive laboratory data and review. *Polymers*, 12(10):1–43, 2020. ISSN 20734360. doi: 10.3390/polym12102276.

[24] Adeline Dupas, Isabelle Henaut, David Rousseau, Philippe Poulain, Rene Tabary, J-F Argillier, and Thierry Aubry. Impact of polymer mechanical degradation on shear and extensional viscosities: towards better injectivity forecasts in polymer flooding operations. In *SPE international symposium on oilfield chemistry*. OnePetro, 2013. doi: 10.2118/164083-MS. URL https://doi.org/10.2118/164083-MS. SPE-164083-MS.

[25] M. S. Azad and J. J. Trivedi. Quantification of the Viscoelastic Effects During Polymer Flooding: A Critical Review. *SPE Journal*, 24(06):2731–2757, 07 2019. ISSN 1086-055X. doi: 10.2118/195687-PA. URL https://doi.org/10.2118/195687-PA.

[26] Madhar S. Azad and Japan J. Trivedi. Extensional Effects during Viscoelastic Polymer Flooding: Understanding Unresolved Challenges. *SPE Journal*, 25 (04):1827–1841, 08 2020. ISSN 1086-055X. doi: 10.2118/201112-PA. URL https://doi.org/10.2118/201112-PA.

[27] E. S. Shaqfeh. Purely elastic instabilities in viscometric flows. *Annual Review of Fluid Mechanics*, 28(1):129–185, 1996. ISSN 00664189. doi: 10.1146/annurev.fluid.28.1.129.

[28] A. Groisman and V. Steinberg. Elastic turbulence in a polymer solution flow. *Nature*, 405(6782):53–55, May 2000. ISSN 0028-0836. doi: 10.1038/35011019. URL http://www.nature.com/articles/35011019.

[29] Alexander Groisman and Victor Steinberg. Elastic turbulence in curvilinear flows of polymer solutions. *New Journal of Physics*, 6, 2004. ISSN 13672630. doi: 10.1088/1367-2630/6/1/029.

[30] Durgesh Kawale, Esteban Marques, Pacelli L.J. Zitha, Michiel T. Kreutzer, William R. Rossen, and Pouyan E. Boukany. Elastic instabilities during the

flow of hydrolyzed polyacrylamide solution in porous media: effect of pore-shape and salt. *Soft Matter*, 13(4):765–775, 2017. ISSN 17446848. doi: 10.1039/c6sm02199a.

[31] Pegah Shakeri, Michael Jung, and Ralf Seemann. Effect of elastic instability on mobilization of capillary entrapments. *Physics of Fluids*, 33(11):113102, 2021. doi: 10.1063/5.0071556. URL https://doi.org/10.1063/5.0071556.

[32] Christopher A. Browne and Sujit S. Datta. Elastic turbulence generates anomalous flow resistance in porous media. *Science Advances*, 7(45):eabj2619, 2021. doi: 10.1126/sciadv.abj2619. URL https://www.science.org/doi/abs/10.1126/sciadv.abj2619.

[33] Sujit S. Datta, Arezoo M. Ardekani, Paulo E. Arratia, Antony N. Beris, Irmgard Bischofberger, Jens G. Eggers, J. Esteban López-Aguilar, Suzanne M. Fielding, Anna Frishman, Michael D. Graham, Jeffrey S. Guasto, Simon J. Haward, Sarah Hormozi, Gareth H. McKinley, Robert J. Poole, Alexander Morozov, V. Shankar, Eric S. G. Shaqfeh, Amy Q. Shen, Holger Stark, Victor Steinberg, Ganesh Subramanian, and Howard A. Stone. Perspectives on viscoelastic flow instabilities and elastic turbulence, 2021.

[34] Andrew Clarke, Andrew M Howe, Jonathan Mitchell, John Staniland, Laurence Hawkes, and Katherine Leeper. Mechanism of anomalously increased oil displacement with aqueous viscoelastic polymer solutions. *Soft matter*, 11(18):3536–41, Apr 2015. ISSN 1744-6848. doi: 10.1039/c5sm00064e. URL http://pubs.rsc.org/en/content/articlehtml/2015/sm/c5sm00064e.

[35] Jonathan Mitchell, Kyle Lyons, Andrew M. Howe, and Andrew Clarke. Viscoelastic polymer flows and elastic turbulence in three-dimensional porous structures. *Soft Matter*, 12(2):460–468, 2016. ISSN 1744-683X. doi: 10.1039/C5SM01749A. URL http://xlink.rsc.org/?DOI=C5SM01749A.

[36] Chiyu Xie, Ke Xu, Kishore Mohanty, Moran Wang, and Matthew T Balhoff. Nonwetting droplet oscillation and displacement by viscoelastic fluids. *Physical Review Fluids*, 5(6):063301, Jun 2020. ISSN 2469-990X. doi: 10.1103/PhysRevFluids.5.063301. URL https://link.aps.org/doi/10.1103/PhysRevFluids.5.063301.

[37] S. De, P. Krishnan, J. van der Schaaf, J.A.M. Kuipers, E.A.J.F. Peters, and J.T. Padding. Viscoelastic effects on residual oil distribution in flows

through pillared microchannels. *Journal of Colloid and Interface Science*, 510 (September):262–271, Jan 2018. ISSN 00219797. doi: 10.1016/j.jcis.2017. 09.069. URL `http://linkinghub.elsevier.com/retrieve/pii/ S0021979717311013`.

[38] Andrew M. Howe, Andrew Clarke, and Daniel Giernalczyk. Flow of concentrated viscoelastic polymer solutions in porous media: Effect of mw and concentration on elastic turbulence onset in various geometries. *Soft Matter*, 11 (32):6419–6431, 2015. ISSN 17446848. doi: 10.1039/c5sm01042j. URL `http://dx.doi.org/10.1039/C5SM01042J`.

[39] Julien Beaumont, Hugues Bodiguel, and Annie Colin. Drainage in two-dimensional porous media with polymer solutions. *Soft Matter*, 9(42): 10174–10185, 2013. ISSN 1744683X. doi: 10.1039/c3sm51480c.

[40] Bing Wei, Laura Romero-Zerón, and Denis Rodrigue. Oil displacement mechanisms of viscoelastic polymers in enhanced oil recovery (eor): a review. *Journal of Petroleum Exploration and Production Technology*, 4(2):113–121, 2014. ISSN 21900566. doi: 10.1007/s13202-013-0087-5.

[41] Eseosa M. Ekanem, Maja Rücker, Sherifat Yesufu-Rufai, Catherine Spurin, Nicholas Ooi, Apostolos Georgiadis, Steffen Berg, and Paul F. Luckham. Novel adsorption mechanisms identified for polymer retention in carbonate rocks. *JCIS Open*, 4:100026, 2021. ISSN 2666-934X. doi: https://doi.org/10.1016/j.jciso. 2021.100026. URL `https://www.sciencedirect.com/science/ article/pii/S2666934X21000258`.

[42] Shijie Zhu, Shilun Zhang, Xinsheng Xue, Jian Zhang, Jiangen Xu, and Zhezhi Liu. Influencing factors for effective establishment of residual resistance factor of polymer solution in porous media. *Journal of Polymer Research*, 29(5):1–10, 2022. doi: https://doi.org/10.1007/s10965-022-03066-7.

[43] Lijuan Zhang, Xiang'an Yue, and Fenqiao Guo. Micro-mechanisms of residual oil mobilization by viscoelastic fluids. *Petroleum Science*, 5(1):56–61, Feb 2008. ISSN 1672-5107. doi: 10.1007/s12182-008-0009-1. URL `http://link. springer.com/10.1007/s12182-008-0009-1`.

[44] Nicolle M Lima, Jorge Avendaño, and Marcio S Carvalho. Effect of viscoelasticity on oil displacement in a microfluidic porous medium. *Journal of the Brazilian Society of Mechanical Sciences and Engineering*, 44(4):1–10, 2022. doi: https://doi.org/10.1007/s40430-022-03435-9.

[45] Demin Wang, Gang Wang, Wenxiang Wu, Huifen Xia, and Hongjun Yin. The influence of viscoelasticity on displacement efficiency–from micro to macro scale. In *SPE Annual Technical Conference and Exhibition*. Society of Petroleum Engineers, Apr 2007. doi: 10.2118/109016-MS. URL http://www.onepetro.org/doi/10.2118/109016-MS.

[46] Jing Cun Fan, Feng Chao Wang, Jie Chen, Yin Bo Zhu, De Tang Lu, He Liu, and Heng An Wu. Molecular mechanism of viscoelastic polymer enhanced oil recovery in nanopores. *Royal Society Open Science*, 5(6), 2018. ISSN 20545703. doi: 10.1098/rsos.180076.

[47] Michael Rubinstein and Ralph H Colby. *Polymer physics*, volume 23. Oxford University Press New York, 2003.

[48] Michael Niaounakis. *Biopolymers: processing and products*. William Andrew, 2014.

[49] Arne Stavland, HC Jonsbråten, Arild Lohne, Arild Moen, and Nils Harald Giske. Polymer flooding–flow properties in porous media versus rheological parameters. In *SPE EUROPEC/EAGE Annual Conference and Exhibition*. OnePetro, 2010.

[50] Shuang Cindy Cao, Bate Bate, Jong Wan Hu, and Jongwon Jung. Engineering behavior and characteristics of water-soluble polymers: implication on soil remediation and enhanced oil recovery. *Sustainability*, 8(3):205, 2016.

[51] AZ Abidin, T Puspasari, and WA Nugroho. Polymers for enhanced oil recovery technology. *Procedia Chemistry*, 4:11–16, 2012.

[52] DAZ Wever, F Picchioni, and AA Broekhuis. Polymers for enhanced oil recovery: a paradigm for structure–property relationship in aqueous solution. *Progress in polymer science*, 36(11):1558–1628, 2011.

[53] Chia-Yen Lee, Chin-Lung Chang, Yao-Nan Wang, and Lung-Ming Fu. Microfluidic mixing: a review. *International journal of molecular sciences*, 12(5):3263–3287, 2011.

[54] Antoine Thomas. *Essentials of polymer flooding technique*. John Wiley and Sons, 2019.

[55] David Levitt and Gary Arnold Pope. Selection and screening of polymers for enhanced-oil recovery. In *SPE symposium on improved oil recovery*. OnePetro, 2008.

[56] N Gaillard, B Giovannetti, T Leblanc, A Thomas, O Braun, and C Favero. Selection of customized polymers to enhance oil recovery from high temperature reservoirs. In *SPE Latin American and Caribbean petroleum engineering conference*. OnePetro, 2015.

[57] Stephane Jouenne. Polymer flooding in high temperature, high salinity conditions: Selection of polymer type and polymer chemistry, thermal stability. *Journal of Petroleum Science and Engineering*, 195:107545, 2020.

[58] Gert R Strobl and Gert R Strobl. *The physics of polymers*, volume 2. Springer, 1997.

[59] Maurice L Huggins. The viscosity of dilute solutions of long-chain molecules. iv. dependence on concentration. *Journal of the American Chemical Society*, 64 (11):2716–2718, 1942.

[60] Elmer O Kraemer. Molecular weights of celluloses and cellulose derivates. *Industrial and Engineering Chemistry*, 30(10):1200–1203, 1938.

[61] GI Menon, J Murali Krishnan, A Deshpande, and PBS Kumar. Rheology of complex fluids. 2010.

[62] William W Graessley. The entanglement concept in polymer rheology. *The entanglement concept in polymer rheology*, pages 1–179, 1974.

[63] Roger S Porter and Julian F Johnson. The effect of molecular weight and distribution on polymer rheology near the entanglement region. *Transactions of the Society of Rheology*, 7(1):241–252, 1963.

[64] A Ait-Kadi, PJ Carreau, and G Chauveteau. Rheological properties of partially hydrolyzed polyacrylamide solutions. *Journal of Rheology*, 31(7):537–561, 1987.

[65] Faith A Morrison et al. *Understanding rheology*, volume 1. Oxford university press New York, 2001.

[66] Nhan Phan-Thien and Nam Mai-Duy. *Understanding viscoelasticity: an introduction to rheology*. Springer, 2013.

[67] R Byron Bird et al. *Dynamics of polymeric liquids.-*. Wiley, 1977.

[68] John Ferry. *Viscoelastic properties of polymers*. John Wiley, 1980.

[69] Frans L Muller and John F Davidson. Rheology of shear thinning polymer solutions. *Industrial and engineering chemistry research*, 33(10):2364–2367, 1994.

[70] Thomas G Mezger. *The rheology handbook: for users of rotational and oscillatory rheometers*. Vincentz Network GmbH Co KG, 2006.

[71] James Clerk Maxwell. *The Scientific Letters and Papers of James Clerk Maxwell: Volume 1, 1846-1862*, volume 1. CUP Archive, 1990.

[72] R Byron Bird and John M Wiest. Constitutive equations for polymeric liquids. *Annual review of fluid mechanics*, 27(1):169–193, 1995.

[73] Richard Christensen. *Theory of viscoelasticity: an introduction*. Elsevier, 2012.

[74] Pegah Shakeri, Michael Jung, and Ralf Seemann. Scaling purely elastic instability of strongly shear thinning polymer solutions. *Phys. Rev. E*, 105: L052501, May 2022. doi: 10.1103/PhysRevE.105.L052501. URL `https://link.aps.org/doi/10.1103/PhysRevE.105.L052501`.

[75] RJ Poole. The deborah and weissenberg numbers. 53(2):32–39, 2012.

[76] RR Huilgol. On the concept of the deborah number. *Transactions of the Society of Rheology*, 19(2):297–306, 1975.

[77] Bingham Medalist Tom McLeish and Metzner Awardee Suzanne Fielding. Rheology bulletin.

[78] Alexander N Morozov and Wim van Saarloos. An introductory essay on subcritical instabilities and the transition to turbulence in visco-elastic parallel shear flows. *Physics Reports*, 447(3-6):112–143, 2007.

[79] L Pan, A Morozov, C Wagner, and PE Arratia. Nonlinear elastic instability in channel flows at low reynolds numbers. *Physical review letters*, 110(17):174502, 2013.

[80] RI Tanner. A theory of die-swell. *Journal of Polymer Science Part A-2: Polymer Physics*, 8(12):2067–2078, 1970.

[81] Ronald G Larson, Eric SG Shaqfeh, and Susan J Muller. A purely elastic instability in taylor–couette flow. *Journal of Fluid Mechanics*, 218:573–600, 1990.

[82] RJ Poole, A Lindner, and MA Alves. Viscoelastic secondary flows in serpentine channels. *Journal of Non-Newtonian Fluid Mechanics*, 201:10–16, 2013.

[83] Daniel D Joseph. *Fluid dynamics of viscoelastic liquids*, volume 84. Springer Science and Business Media, 2013.

[84] Robert G Owens and Timothy N Phillips. *Computational rheology*. World Scientific, 2002.

[85] Huan-Chang Tseng. A revisitation of white-metzner viscoelastic fluids. *Physics of Fluids*, 33(5):057115, 2021. doi: 10.1063/5.0049132. URL https://doi.org/10.1063/5.0049132.

[86] JL White and AB Metzner. Development of constitutive equations for polymeric melts and solutions. *Journal of Applied Polymer Science*, 7(5):1867–1889, 1963.

[87] Yuan-cheng Fung. A first course in continuum mechanics. *Englewood Cliffs*, 1977.

[88] Bengt Andersson, Ronnie Andersson, Love Håkansson, Mikael Mortensen, Rahman Sudiyo, and Berend Van Wachem. *Computational fluid dynamics for engineers*. Cambridge university press, 2011.

[89] Teodor Burghelea, Enrico Segre, and Victor Steinberg. Elastic turbulence in von karman swirling flow between two disks. *Physics of fluids*, 19(5):053104, 2007.

[90] J Zilz, RJ Poole, MA Alves, D Bartolo, B Levaché, and A Lindner. Geometric scaling of a purely elastic flow instability in serpentine channels. *Journal of Fluid Mechanics*, 712:203–218, 2012.

[91] Susan J Muller. Elastically-influenced instabilities in taylor-couette and other flows with curved streamlines: a review. *Korea-Australia Rheology Journal*, 20 (3):117–125, 2008.

[92] Peyman Pakdel and Gareth H McKinley. Elastic instability and curved streamlines. *Physical Review Letters*, 77(12):2459, 1996.

[93] Gareth H McKinley, Jeffrey A Byars, Robert A Brown, and Robert C Armstrong. Observations on the elastic instability in cone-and-plate and parallel-plate flows of a polyisobutylene boger fluid. *Journal of Non-Newtonian Fluid Mechanics*, 40(2):201–229, 1991.

[94] Lucie Ducloué, Laura Casanellas, Simon J Haward, Robert J Poole, Manuel A Alves, Sandra Lerouge, Amy Q Shen, and Anke Lindner. Secondary flows of viscoelastic fluids in serpentine microchannels. *Microfluidics and Nanofluidics*, 23(3):1–10, 2019.

[95] Pegah Shakeri, Michael Jung, and Ralf Seemann. Characterizing purely elastic turbulent flow of a semi-dilute entangled polymer solution in a serpentine channel. *Physics of Fluids*, 30(10):1200–1203, 2022. doi: 10.1063/5.0100419.

[96] Rizwan Muneer, M Rehan Hashmet, and Peyman Pourafshary. Fine migration control in sandstones: Surface force analysis and application of dlvo theory. *ACS omega*, 5(49):31624–31639, 2020.

[97] Abhijit Kakati, Ganesh Kumar, and Jitendra S Sangwai. Low salinity polymer flooding: effect on polymer rheology, injectivity, retention, and oil recovery efficiency. *Energy and Fuels*, 34(5):5715–5732, 2020. doi: 10.1021/acs.energyfuels.0c00393.

[98] API. Recommended practices for evaluation of polymers used in enhanced oil recovery operations. *API Recommended Practice 63 (RP63)*, 1990. URL `https://standards.globalspec.com/std/183645/APIRP63`.

[99] Fridtjov Irgens. *Rheology and non-newtonian fluids*, volume 1. Springer, 2014.

[100] Thomas G Mezger. *The rheology handbook: for users of rotational and oscillatory rheometers*. Vincentz Network GmbH and Co KG, 2006.

[101] WM Kulicke, Gabor Kiss, and Roger S Porter. Inertial normal-force corrections in rotational rheometry. *Rheologica Acta*, 16(5):568–572, 1977.

[102] Raj P Chhabra and John Francis Richardson. *Non-Newtonian flow and applied rheology: engineering applications*. Butterworth-Heinemann, 2011.

[103] Howard A Barnes, John Fletcher Hutton, and Kenneth Walters. *An introduction to rheology*, volume 3. Elsevier, 1989.

[104] Osama M Maklad, Kate McAulay, Sandra Lerouge, Dave J Adams, and Robert J Poole. A technical note on large normal-stress differences observed in a novel self-assembling functionalized dipeptide surfactant solution. *Rheologica Acta*, pages 1–14, 2022.

[105] Younan Xia and George M Whitesides. Soft lithography. *Angewandte Chemie International Edition*, 37(5):550–575, 1998.

[106] Peter Gravesen, Jens Branebjerg, and O Søndergård Jensen. Microfluidics-a review. *Journal of micromechanics and microengineering*, 3(4):168, 1993.

[107] Patrick Tabeling. *Introduction to microfluidics*. Oxford University Press on Demand, 2005.

[108] Denis Bartolo, Guillaume Degré, Philippe Nghe, and Vincent Studer. Microfluidic stickers. *Lab on a Chip*, 8(2):274–279, 2008.

[109] Steven T Wereley and Carl D Meinhart. Recent advances in micro-particle image velocimetry. *Annual review of fluid mechanics*, 42:557–576, 2010.

[110] John A Taylor and Edward S Yeung. Imaging of hydrodynamic and electrokinetic flow profiles in capillaries. *Analytical Chemistry*, 65(20):2928–2932, 1993.

[111] James P Brody, Paul Yager, Raymond E Goldstein, and Robert H Austin. Biotechnology at low reynolds numbers. *Biophysical journal*, 71(6):3430–3441, 1996.

[112] Juan G Santiago, Steve T Wereley, Carl D Meinhart, DJ Beebe, and Ronald J Adrian. A particle image velocimetry system for microfluidics. *Experiments in fluids*, 25(4):316–319, 1998.

[113] Carl D Meinhart, Steve T Wereley, and Juan G Santiago. Piv measurements of a microchannel flow. *Experiments in fluids*, 27(5):414–419, 1999.

[114] Carl D Meinhart, Steve T Wereley, and Juan G Santiago. A piv algorithm for estimating time-averaged velocity fields. *J. Fluids Eng.*, 122(2):285–289, 2000.

[115] David Sinton. Microscale flow visualization. *Microfluidics and Nanofluidics*, 1 (1):2–21, 2004.

[116] Michel Stanislas, Jerry Westerweel, and Jürgen Kompenhans. *Particle Image Velocimetry: Recent Improvements: Recent Improvements: Proceedings Of The Europiv 2 Workshop Held in Zaragoza, Spain, March 31-April 1, 2003*. Springer Science and Business Media, 2004.

[117] Ronald J Adrian and Jerry Westerweel. *Particle image velocimetry*. Number 30. Cambridge university press, 2011.

[118] CD Meinhart, ST Wereley, and MHB Gray. Volume illumination for two-dimensional particle image velocimetry. *Measurement Science and Technology*, 11(6):809, 2000.

[119] Matthias Hein, Bernhard Wieneke, and Ralf Seemann. Calculation of the weighting function and determination of the depth of correlation in micro-piv from experimental particle images. *Measurement Science and Technology*, 25(8): 084008, 2014.

[120] Amin Etminan, Yuri S Muzychka, Kevin Pope, and Baafour Nyantekyi-Kwakye. Flow visualization: state-of-the-art development of micro-particle image velocimetry. *Measurement Science and Technology*, 2022.

[121] Peyman Pakdel and Gareth H. McKinley. Elastic instability and curved streamlines. *Physical Review Letters*, 77(12):2459–2462, 1996. ISSN 10797114. doi: 10.1103/PhysRevLett.77.2459.

LIST OF PUBLICATIONS

1. P. Shakeri, M. Jung, and R. Seemann. Effect of elastic instability on mobilization of capillary entrapments. *Physics of Fluids*33.11: 113102, 2021.

2. P. Shakeri, M. Jung, and R. Seemann. Scaling purely elastic instability of strongly shear thinning polymer solutions. *Physical Review E* 105.5: L052501, 2022.

3. P. Shakeri , M. Jung , and R. Seemann. Characterizing purely elastic turbulent flow of a semi-dilute entangled polymer solution in a serpentine channel. *Physics of Fluids*, 34(7), 073112, 2022.

4. M. Jung, P. Shakeri, and R. Seemann. Effect of viscoelasticity on displacement processes in porous media *to be submitted to Frontiers in Physics*, 2022.

Appendices

Effect of elastic instability on mobilization of capillary entrapments

Authors: P. Shakeri[1,2], M. Jung[1,2], and R. Seemann[1,2]

[1]Experimental Physics, Saarland University, 66123 Saarbrücken, Germany

[2]Max Planck Institute for Dynamics and Self-Organization, 37077 Göttingen, Germany

`https://doi:10.1063/5.0071556`

Abstract:

The flow of viscoelastic polymer solutions and their use as displacing agents in porous media are important for industrial applications, such as enhanced oil recovery and soil remediation. Complexity of flow and high elasticity of conventionally used viscoelastic polymer solutions can lead to purely elastic instability in porous media. In this study, we investigate the impact of this instability on displacing capillary entrapments at low Reynolds numbers using a microfluidic approach. Our unique design consists of a single-capillary entrapment connected to two symmetric serpentine channels. This design excludes the effect of viscous forces and enables a direct focus on displacement processes driven solely by elastic forces. After the onset of purely elastic instability, an unstable base flow is observed in the serpentine channels. We discuss that the pressure fluctuations caused by this unstable flow create an instantaneous non-equilibrium state between the two ends of the capillary entrapment. This provides the driving pressure to overcome the capillary threshold pressure and eventually displace the entrapped oil. In our geometry, we observe that the displacement coincides with the emergence of a fully developed turbulent state.

Pegah Shakeri, Michael Jung and Ralf Seemann

View Online   Export Citation   CrossMark

ARTICLES YOU MAY BE INTERESTED IN

Effect of elastic instability on mobilization of capillary entrapments

View Online   Export Citation   CrossMark

Pegah Shakeri,[1,2,a)] (ID) Michael Jung,[1,2,b)] (ID) and Ralf Seemann[1,2] (ID)

AFFILIATIONS

[1]Experimental Physics, Saarland University, 66123 Saarbrücken, Germany
[2]Max Planck Institute for Dynamics and Self-Organization, 37077 Göttingen, Germany

[a)]Author to whom correspondence should be addressed: pegah.shakeri@physik.uni-saarland.de
[b)]michael.jung@physik.uni-saarland.de

ABSTRACT

The flow of viscoelastic polymer solutions and their use as displacing agents in porous media are important for industrial applications, such as enhanced oil recovery and soil remediation. The complexity of flow and high elasticity of conventionally used viscoelastic polymer solutions can lead to purely elastic instability in porous media. In this study, we investigate the impact of this instability on displacing capillary entrapments at low Reynolds numbers using a microfluidic approach. Our unique design consists of a single-capillary entrapment connected to two symmetric serpentine channels. This design excludes the effect of viscous forces and enables a direct focus on displacement processes driven solely by elastic forces. After the onset of purely elastic instability, an unstable base flow is observed in the serpentine channels. We discuss that the pressure fluctuations caused by this unstable flow create an instantaneous non-equilibrium state between the two ends of the capillary entrapment. This provides the driving pressure to overcome the capillary threshold pressure and eventually displace the entrapped oil. In our geometry, we observe that the displacement coincides with the emergence of a fully developed elastic turbulent state.

I. INTRODUCTION

The addition of high molecular weight polymers to a Newtonian solvent results in a viscoelastic fluid, i.e., a fluid with intermediate mechanical properties between viscous fluids and elastic solids. Large elastic stresses induced during the flow of viscoelastic fluids lead to purely elastic instability even in the absence of inertia, i.e., at low Reynolds numbers.[1,2] As the polymers approach their maximum capacity for alignment with the flow and reach a so-called stretched state, they exert a significant back reaction to the flow above a critical shear rate, $\dot{\gamma}_{crit}$.[3] In other words, purely elastic instability occurs when the polymer relaxation time exceeds its transit time and elastic stresses are no longer fully dissipated.[4] The excessive elastic stresses elicit an unstable base flow. This unstable flow resembles inertia-induced hydrodynamic turbulent flow below the dissipation scale (Kolmogorov length), which is known as the "Batchelor regime."[5,6] This regime is characterized by spatially smooth, temporary random instabilities that cover a wide range of frequencies.[5,7,8] This is reflected as a power-law decay $\sim f^{-\beta}$ of the power spectral density (PSD) of kinetic energy with a characteristic exponent $\beta > 3$.[2,7,9–13] The occurrence of purely elastic instability during the flow of viscoelastic fluids in various geometries has been extensively studied in the literature.[2,7,14–17] Elastic instability is known to improve the efficiency of heat transfer[18–22] and microfluidic mixing.[23–26] Recently, it has been observed in enhancement oil recovery that purely elastic instability might play a crucial role in capillary entrapments (ganglia) displacement in porous media.[27–29]

Several experimental and numerical studies have focused on basic designs to study the microscopic behavior of viscoelastic fluids and elastic instability in porous media. A few basic geometries are commonly considered to mimic porous media flow characteristics at the microscale including straight channels embedded with uniform or randomized post arrays;[30–40] a single pore formed by four disks;[41,42] and converging and diverging channels.[43–45] All of these geometries have a curved streamline component in common. In fact, the streamline curvature of viscoelastic fluid flows can amplify the normal stress differences that lead to unstable flow.[17,46–48]

Purely elastic instability in porous media is commonly associated with increased flow resistance, i.e., an increased apparent viscosity even at low Reynolds numbers.[7,14,49–52] However, this increased apparent viscosity is not *per se* large enough to explain the improved

displacement efficiency of capillary entrapments in porous media. Displacement experiments performed using polymers with different molecular weights suggest that the mobilization of capillary entrapments is in fact caused by the unstable nature of flow.[27,49,53] The unstable flow induces fluctuations of the fluid–fluid interface in between the viscoelastic invading fluid and the trapped oil ganglia.[53–56] These fluctuations can lead to breakup of large ganglia into smaller droplets and eventually complete removal of the trapped defending phase.[57]

In this study, we use a microfluidic approach to investigate the mechanism by which a single-capillary entrapment is displaced by viscoelastic polymer solutions in the semi-dilute regime. We use serpentine channels with constant cross section to mimic the shear-dominated, curved (tortuous) nature of flow in porous media. We focus on the underlying elasticity-induced phenomena to establish a link with the displacement of capillary entrapment. To exclude inertial effects and evaluate the observations as purely elasticity-induced effects, we conduct microfluidic experiments at small Reynolds numbers $Re < \mathcal{O}(10^0)$ in the creeping flow regime. This paper is structured as follows: the methods utilized including the experimental setup, sample preparation, and fundamentals of the relevant fluid model are described in Sec. II; in Sec. III, we provide rheological characterizations of the polymer solutions and present and discuss the results of the microfluidic experiments; and we conclude the paper in Sec. IV.

II. METHODS

A. Microfluidic geometry

The microfluidic geometry employed in this work consisted of two identical serpentine channels of width $w_{mc} = 0.125$ mm that were connected by a perpendicular side channel of width $w_{sc} = 0.05$ mm and length $l_{sc} = 1$ mm [Fig. 1(a)]. The inner and outer radii of curvature of the serpentine channels were $r_i = 0.125$ mm and $r_o = 0.25$ mm, respectively. The height h of the microfluidic channels was approximately 0.045 mm. Serpentine channels were ideally suited for mimicking tortuous flow in porous media, whereas the perpendicular side channel provided the possibility of capillary entrapment of the oil phase. This geometry resembled a capillary entrapment between two grains, where fluid interfaces are in contact with more than one active pathway of the invading phase [Fig. 1(b)]. Together with a common inlet and outlet, the symmetry of serpentine channels provided an equal viscous pressure at both ends of the side channel. Hence, our microfluidic geometry served as a model system that isolated the effect of elastic stresses on the fluid–fluid interfaces and consequently on the mechanism of oil displacement from the side channel.
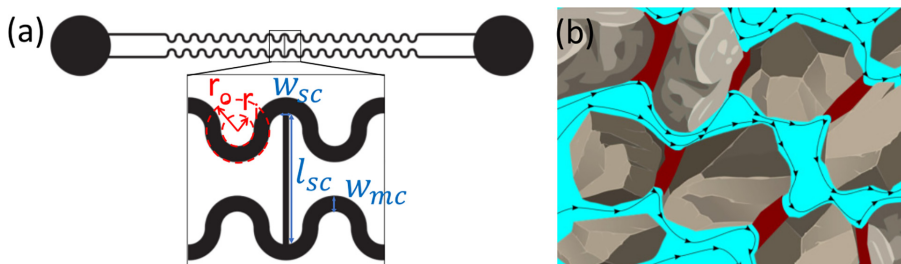
B. Experimental protocol

The microfluidic devices were fabricated following a standard soft-lithographic procedure.[58] The positive master for microfluidic device production was fabricated via standard photolithographic protocols: a SU-8 (Kayaku Advanced Materials, Inc.) layer was spin coated onto a silicon wafer and then exposed to UV light through a transparent photomask. A negative of such a master was replicated in polydimethylsiloxane (PDMS, Sylgard 184 Dow Corning). The final microfluidic device was molded from this PDMS replicate using the stiff, oil resistant photo-reactive resin NOA 83H (Norland optical adhesives). The devices were sealed with a microscopy glass slide and sandwiched with a coverslip to further increase the sample stability and avoid deformation of the channel at higher pressures. Such deformations are a typical problem among conventionally used PDMS devices.[15] The inlet of the microfluidic device was connected to a high-precision, pulsation-free syringe pump (neMESYS, Cetoni GmbH) that enabled fluid injection at a controlled volumetric flow rate. The outlet was connected to a liquid reservoir at the same height as the microfluidic device to avoid gravitational counter pressure. A board-mounted differential pressure sensor (26PC series, Honeywell) was installed between the inlet and outlet of the microfluidic device to measure the hydrodynamic pressure drop inside the microfluidic channel. Prior to the measurements, the pressure sensor was calibrated using a pressure-controlled pump (MFCS-EZ, Fluigent). The microfluidic device was placed on an inverted MeF3 microscope (Reichert-Jung) illuminated by a light-emitting diode (LED) light source in transmission and images were captured using a 16 Bit-sCMOS camera (PCO Panda 4.2) at a frame rate of 40 fps and a pixel resolution of (2048 × 2048) pixels. The microfluidic experiments were conducted at room temperature of $(20 \pm 1)\,°C$. The microfluidic geometry was initially fully saturated with dodecane. Subsequently, dodecane was flushed out of the main channels by the respective invading phase at the lowest applied flow rate of $0.5\,\mu$ l/min but remained entrapped in the side channel. For each set of experiments, the flow rate of the invading phase was gradually increased in steps of $0.5\,\mu$l/min until it reached a critical flow rate where fluctuation of the fluid–fluid interface could be detected. The flow rate was increased further in steps of $1.0\,\mu$l/min until complete desaturation of the side channel. To ensure a fully developed steady-state flow while recording fluid-fluid interface fluctuations, we used the simultaneously measured pressure signal as a reference and started recording at each flow rate after the pressure reached a stable plateau.

C. Preparation and physical properties of working fluids

We used viscoelastic aqueous solutions that contained 1000 ppm (0.1 w%) or 2000 ppm (0.2 w%) of partially hydrolyzed polyacrylamide

FIG. 1. Sketches of the microfluidic geometry (a) and a typical oil entrapment in a porous medium (b).
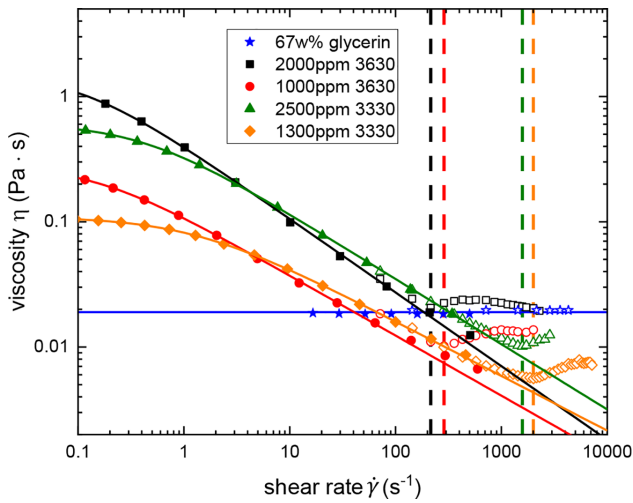
FIG. 2. The (shear) viscosity $\eta(\dot{\gamma})$ measured using a rheometer (filled symbols) and apparent viscosities calculated from *in situ* pressure measurements (open symbols). Lines are fits to the Carreau–Yasuda model. Dashed lines indicate the critical shear rates $\dot{\gamma}_{crit}$, where the viscosities calculated from *in situ* pressure measurements deviate from the bulk values.

(HPAM) Flopaam 3630 (SNF Floerger) and 1300 ppm (0.13 w%) or 2500 ppm (0.25 w%) Flopaam 3330 (SNF Floerger) as invading fluids in our microfluidic experiments. The molecular weights of the HPAM polymers Flopaam 3630 and 3330 are (18.7 ± 2.0) and (6.5 ± 2.0) MDa, respectively, according to the manufacturer. The concentrations of the respective polymer solutions were adjusted to provide similar shear viscosities despite their different degrees of elasticity (Figs. 2 and 3). Following a standard protocol,[59] we initially prepared a stock solution with 5000 ppm of the appropriate polymer in a "brine" solution composed of ultrapure water with 1000 ppm NaCl and 100 ppm CaCl₂. The stock solution was filtered to avoid the presence of any undissolved polymer or salt particles and subsequently diluted to the desired concentration by adding

brine solution. To avoid degradation of the polymer solutions, the diluted solutions were renewed every three days and the respective stock solution every four weeks. By applying the Huggins–Kraemer method[60] using rotational shear rate ramp measurement results (data not shown), we determined the critical overlap concentrations to be $c_{3630}^* \approx 82$ ppm and $c_{3330}^* \approx 137$ ppm and the corresponding radii of gyration to be $Rg_{3630} \approx 441$ nm and $Rg_{3330} \approx 266$ nm for Flopaam 3630 and Flopaam 3330, respectively. Because the polymer concentrations used in our microfluidic experiments were at least ten times greater than c^*, we could safely presume to be in the semi-dilute regime. A characteristic exponent of 3/2 calculated by scaling the respective zero-shear viscosity as a function of the polymer concentration (data not shown) confirmed that we remained in the entangled regime for all utilized polymer solutions.[61] As a Newtonian reference case, an aqueous glycerin solution was prepared by adding 67 w% glycerin (Grüssing GmbH) to ultrapure water. The defending phase in all experiments was dodecane (Merck) with a constant dynamic viscosity $\eta_{dodecane} = 1.4$ mPa·s. First, dodecane was filtered three times in a column of aluminum oxide powder (Al₂O₃, Sigma Aldrich) to remove any potential surface-active contaminants. To increase the optical contrast of the fluids in the microfluidic setup, 0.5 w% of the non-surface-active dye oil-red-o (Sigma Aldrich) was added to the purified dodecane. For the visualization of path lines, 0.01 w% green fluorescent particles (2 μm, FluoroMax, Thermo Fisher) were added to the respective polymer solution and imaged via fluorescence microscopy. We confirmed that neither of these additives altered the physical or rheological properties of the utilized fluids. We measured densities of $\rho_P = (1.00 \pm 0.01)$ g/cm³ and $\rho_G = (1.18 \pm 0.01)$ g/cm³, respectively, for the aqueous polymer and glycerin solutions using a pycnometer. The respective interfacial tensions against dodecane were determined to be $\sigma_P = (50 \pm 1)$ mN/m and $\sigma_G = (32 \pm 1)$ mN/m via the pendant drop method using a contact angle measurement device (OCA 25, DataPhysics). The advancing and receding contact angles of the aqueous polymer and glycerin solutions on glass and the NOA 83H-surface in a surrounding dodecane phase were in all cases determined to be $\theta_{adv} = (125 \pm 4)^\circ$ and $\theta_{rec} = (59 \pm 6)^\circ$, respectively, via the sessile drop needle-in method using the contact angle measurement device (OCA 25, DataPhysics).

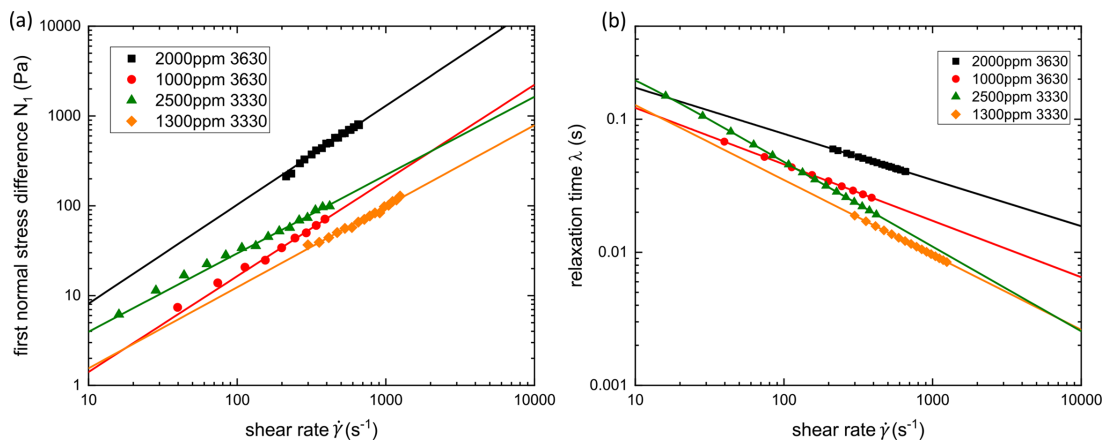**FIG. 3.** The (a) first normal stress difference N_1 and (b) relaxation time λ as functions of the shear rate $\dot{\gamma}$. The lines in figures (a) and (b) are extrapolated power-law fits of N_1 and extrapolated Carreau fits of λ.

D. Viscoelastic fluid model

A representative fluid model was needed to describe the specific rheological properties of our viscoelastic polymer solutions in the semi-dilute regime and to provide quantitative interpretation of the experimental results. The general approach of describing viscoelastic fluids is to include viscoelastic properties via a total stress tensor $\mathbf{T} = \mathbf{T_1} + \mathbf{T_2}$, where the index "1" identifies a viscoelastic component and the index "2" a purely viscous component.[62] After defining a total viscosity $\eta = \eta_1 + \eta_2$ and a deformation rate tensor $\mathbf{D} = 1/2(\nabla\mathbf{u} + [\nabla\mathbf{u}]^\mathrm{T})$ derived from the velocity tensor $\mathbf{u}$, we can estimate the solvent contribution to the total stress in a viscoelastic solution, i.e., the stress response that corresponds to the flow at vanishing degrees of elasticity, as $\mathbf{T_2} = 2\eta_2\mathbf{D}$. The viscoelastic contribution $\mathbf{T_1}$ is defined for each type of viscoelastic fluid model. In this work, we used the White–Metzner fluid constitutive model[63–65] as a representative framework for our polymer solutions. We chose this model because it is suitable for describing the non-quadratic first normal stress difference $N_1(\dot\gamma)$ and the strong shear thinning viscosities of the HPAM solutions used in our experiments.[66–68] The White–Metzner fluid model computes $\mathbf{T_1}$ from

$$\mathbf{T_1} + \lambda\, \overset{\triangledown}{\mathbf{T_1}} = 2\,\eta_1(\dot\gamma)\,\mathbf{D}, \qquad (1)$$

where λ and η_1 are the relaxation time and the viscosity of the polymer contribution, respectively; $\overset{\triangledown}{\mathbf{T_1}}$ is the upper convected time derivative; and $\dot\gamma$ is the shear rate [defined as $\dot\gamma = \sqrt{2\,tr(\mathbf{D^2})}$] that can be calculated from the velocity field and the rate of deformation tensor $\mathbf{D}$.[69]

To represent the shear-dependent total viscosities $\eta(\dot\gamma)$ of the HPAM solutions, we applied the Carreau–Yasuda model, which is commonly utilized for this type of polymer,[67] i.e.,

$$\eta(\dot\gamma) - \eta_\infty = (\eta_0 - \eta_\infty)\left[1 + (\Lambda\dot\gamma)^a\right]^{\frac{n-1}{a}}. \qquad (2)$$

Here, η_0 and η_∞ are the zero-shear viscosity and viscosity at infinite shear rates, respectively; Λ is the characteristic time; n is the power-law exponent associated with the degree of shear thinning; and a is a transition control factor.

The shear-dependent relaxation time $\lambda(\dot\gamma)$ is calculated from the shear viscosity, $\eta(\dot\gamma)$, and the first normal stress difference, N_1, as follows:

$$\lambda(\dot\gamma) = N_1/2[\eta(\dot\gamma) - \eta_0]\dot\gamma^2. \qquad (3)$$

The shear-dependent behavior of the relaxation time is described by the Careau model with λ_0 as the longest relaxation time as follows:

$$\lambda(\dot\gamma) = \frac{\lambda_0}{\left[1 + (\Lambda\dot\gamma)^2\right]^{\frac{n-1}{2}}}. \qquad (4)$$

III. RESULTS AND DISCUSSION

With our microfluidic experiments, we sought to understand the role of the elasticity of a viscoelastic polymer solution in the enhanced mobilization of capillary entrapments in porous media. To understand the effects of rheological properties on the flow and displacement processes, we first characterized our polymer solutions.

A. Rheological characterization

The polymer solutions selected in this work are known to exhibit strong shear rate dependence in the semi-dilute regime with regard to both the viscosity and relaxation time. To characterize their rheological properties, we conducted a set of rheological measurements to determine the shear-dependent viscosity $\eta(\dot\gamma)$) (Fig. 2) and first normal stress difference $N_1(\dot\gamma)$ [Fig. 3(a)] using a Haake Mars 40 rheometer. Further details on the experimental measurement protocols can be found in the Appendix as well as the results of the frequency sweep tests.

The viscosity measurements in Fig. 2 are fitted to the Carreau model according to Eq. (2). The fitting parameters are summarized in Table I. The value of η_∞ was set to zero in all four fits. The shear-dependent relaxation time $\lambda(\dot\gamma)$, plotted in Fig. 3(b), is calculated according to Eq. (3) using the viscosity data $\eta(\dot\gamma)$ (Fig. 2) and the first normal stress difference N_1 [Fig. 3(a)]. The relaxation time $\lambda(\dot\gamma)$ is fitted to the Carreau model [Eq. (4)]. The maximum relaxation times are $\lambda_0 \approx 1.2$ s (2000 ppm 3630), $\lambda_0 \approx 1.2$ s (1000 ppm 3630), $\lambda_0 \approx 0.4$ s (2500 ppm 3330), and $\lambda_0 \approx 0.5$ s (1300 ppm 3330).

B. Interfacial fluctuations and mobilization of capillary entrapment

The unique design of our microfluidic geometry [Fig. 1(a)] and high spatiotemporal optical resolution enabled us to focus on the interactions between the flow in the serpentine channel and the fluid–fluid interface of oil entrapped at the side channel, as depicted in Fig. 4(a) (Multimedia view). To this end, fluid–fluid interface time series were captured at various shear rates. The shear rate in serpentine channels is approximated by $\dot\gamma = 4Q/(\pi r^3)$ with the equivalent radius $r = \sqrt{(w_{mc} h)/\pi}$,[70] where w_{mc} and h are the width and height of the serpentine channels, respectively. The saturation S of the oil in the side channel and the fluctuating motion of the fluid–fluid interface could be acquired from the recorded time series. The saturation S was defined as the area of the oil column at the end of each step, normalized by the area of the oil column in the first step. Desaturation was initiated once the fluid–fluid interface was depinned from the edges of the side channel and $S < 1$. Interfacial motion was described quantitatively based on the motion of the center of mass, $\delta\mathrm{Y}$, of the entrapped

TABLE I. Fitting parameters of the Carreau–Yasuda model for viscosity: η_0 is the zero-shear viscosity; Λ is the characteristic time; a is a transition control factor; and n is the power-law exponent associated with the degree of shear thinning.

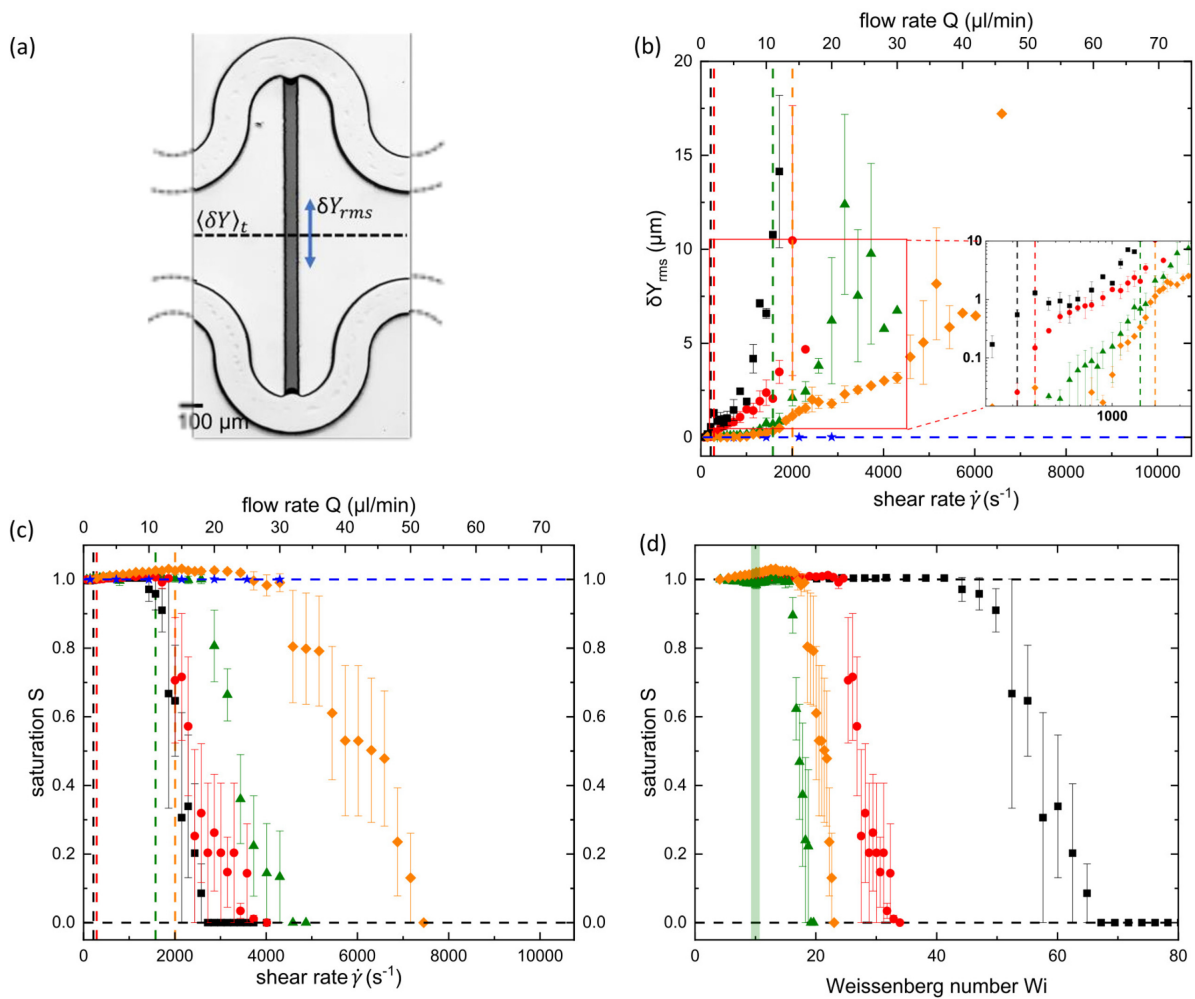| Polymer	η_0 (Pa·s)	Λ (s)	a	n
2000 ppm 3630	1.535 ± 0.011	9.45 ± 0.81	1.07 ± 0.05	0.41 ± 0.02
1000 ppm 3630	0.284 ± 0.004	6.89 ± 0.32	1.03 ± 0.06	0.52 ± 0.01
2500 ppm 3330	0.612 ± 0.003	2.43 ± 0.16	0.99 ± 0.06	0.48 ± 0.01
1300 ppm 3330	0.109 ± 0.001	0.81 ± 0.03	0.90 ± 0.02	0.56 ± 0.01

FIG. 4. (a) Optical image of microfluidic geometry. (b) Root-mean square (rms) of δY_{rms} The inset shows a magnified view of the initial values above $\delta Y_{rms} \approx 0.015\,\mu m$ (marked by the red box). [(c) and (d)] Remaining oil saturation S in the side channel as a function of the applied flow at various (c) shear rates and (d) Weissenberg numbers. The vertical dashed lines in figures (b) and (c) as well as the green area in figure (d) indicate the onset of purely elastic instability. The symbols in figures (b)–(d) represent the experimental data for 67 w% glycerin ($\star$), 2000 ppm Flopaam 3630 (■), 1000 ppm Flopaam 3630 (●), 2500 ppm Flopaam 3330 (▲), and 1300 ppm Flopaam 3330 (◆). Multimedia view: https://doi.org/10.1063/5.0071556.1

oil column. To quantify the strength of interfacial motion, we calculated the root mean square δY_{rms} for each shear rate and plotted the results in Fig. 4(b). As shown in the inset of Fig. 4(b), for $\delta Y_{rms} > 0.015\,\mu m$ (i.e., for δY_{rms} values exceeding the noise level of the experimental setup), optically visible motion of the fluid–fluid interface that increases with the shear rate is clearly detectable. At the lowest applied shear rate of $\dot{\gamma} \approx 72\ \text{s}^{-1}$, the fluid–fluid interface is stationary for all utilized invading fluids. When glycerin solution is the invading phase, the fluid–fluid interface remains stationary across the full range of applied shear rates. Despite the rather high glycerin solution viscosity, no oil displacement is observed from the side channel [Fig. 4(c)]. However, when a viscoelastic polymer solution is the invading phase, the fluid–fluid interface begins to wobble above a certain shear rate. The intensity of this wobbling motion increases

monotonically as the shear rate increases further. The higher the polymer molecular weight and concentration, i.e., the higher the degree of elasticity, the smaller the corresponding shear rate at which wobbling is initially detected. Eventually, the displacement of the entrapped oil phase from the side channel is initiated for all utilized polymer solutions when the fluid–fluid interface fluctuations are sufficiently intense [Fig. 4(c)]. As with the onset of interfacial fluctuations, the higher the elasticity of the polymer solution, the lower the critical shear rate at which displacement initiates. The large values of δY_{rms} and their respective error bars after the onset of displacement stem from the fact that two different types of motions contribute to δY_{rms} at this stage. These motions are the fluctuation of the fluid–fluid interface that is already visible at lower flow rates and the back-and-forth motion of the remaining oil column in the side channel that contributes at larger flow rates.

The dashed vertical lines in Figs. 4(b) and 4(c) correspond to the critical shear rates $\dot{\gamma}_{crit}$ that indicate the onset of increased flow resistance, as determined from the deviation of the apparent viscosity from the bulk shear viscosity in Fig. 2. Here, the apparent viscosity of each invading fluid is estimated from pressure drop measurements made between the inlet and outlet of the microfluidic device, $\bar{P}_{in-out}$, using the Hagen–Poiseuille equation for channels with rectangular cross sections. Because the maximum Reynolds number in our experiments is on the order of $Re \sim \mathcal{O}(10^0)$, potential inertial contributions to the observed increase in flow resistance can be neglected safely and it can be associated with so-called purely elastic instability at low Reynolds numbers.[14,50]

For the two Flopaam 3330 solutions, the wobbling motion starts at shear rates well below $\dot{\gamma}_{crit}$ [Fig. 4(b)]. This suggests that these initial fluctuations may have different physical origins than the purely elastic instability. The onset of elastic instability appears at similar critical Weissenberg numbers (the ratio of elastic and viscous forces) $Wi_{crit} = \lambda(\dot{\gamma}_{crit})\,\dot{\gamma}_{crit}$, as noted in Table II. This suggests that a certain ratio of elastic to viscous forces must be achieved in a given geometry to initiate purely elastic instability, independent of the molecular weight and polymer concentration. However, the desaturation curves plotted as functions of the Weissenberg number in Fig. 4(d) do not collapse, and no consistent Weissenberg number can be assigned to the onset of displacement. In particular, the respective onsets of displacement for the two polymer solutions that include Flopaam 3630 (high molecular weight) are shifted remarkably toward higher Weissenberg numbers than the two Flopaam 3330 solutions. These observations imply a more complex displacement mechanism with respect to the elasticity of the invading fluids.

Because there is no displacement in the case of a fully laminar flow of the glycerin solution, during the entire range of the experiments, it is evident that the magnitude of pressure, $\bar{P}_{in-out}$, cannot drive displacement. Indeed, the displacement mechanism can be explained with respect to the fluctuating component of pressure, $P'(t)$, in serpentine channels. These fluctuations occur because of the unstable nature of viscoelastic flow driven by the elasticity-induced instability at high shear rates. At any position in the channel, the instantaneous pressure, $P(t)$, can be treated as $P(t) = \langle P \rangle_t + P'(t)$, where $\langle P \rangle_t$ is the time-averaged steady-state mean value of the pressure at this position. Due to a common inlet and outlet and the symmetry of our microfluidic geometry, $\langle P \rangle_t$ cancels out, leaving the difference in fluctuating pressure components between both ends of the side channel to overcome the capillary pressure that traps the oil in place. Because there is no direct access to the local instantaneous pressure, $P(t)$, in our experimental setup, $P'(t)$ cannot be evaluated

TABLE II. Overview of the experimentally preset flow rate Q_{crit}, the approximate shear rate $\dot{\gamma}_{crit}$, and the Weissenberg number Wi_{crit} at the onset of purely elastic instability. The specified error margins are determined based on the nominal precision of the microfluidic pump and rheometer, as well as dimensional uncertainty within the microfluidic device.

Polymer	Q_{crit} (µl/min)	$\dot{\gamma}_{crit}$ (s^{-1})	Wi_{crit}
2000 ppm 3630	1.5 ± 0.2	215 ± 30	12.8 ± 2.9
1000 ppm 3630	2.0 ± 0.2	287 ± 21	11.2 ± 1.8
2500 ppm 3330	11.0 ± 0.2	1576 ± 139	13.0 ± 0.1
1300 ppm 3330	14.0 ± 0.2	2006 ± 192	13.0 ± 0.1

directly. Instead, we can hypothesize that the local pressure fluctuations correlate directly with the corresponding time averaged steady-state mean pressure, i.e., $P'(t) \propto \langle P \rangle_t$. Assuming a constant pressure gradient along the microfluidic geometry, $\langle P \rangle_t$ can be assessed directly from the experimentally measured pressure difference $\bar{P}_{in-out}$. Furthermore, the fluctuating component, $P'(t)$, is reflected directly by the intensity of the observed interfacial fluctuations. Our hypothesis is supported by the fact that the intensity of interfacial fluctuations increases in proportion with the average pressure difference between the inlet and outlet, $\bar{P}_{in-out}$, of the microfluidic geometry [Fig. 5(a)]. Hence, we can consider $\bar{P}_{in-out}$ as a measure of $\langle P \rangle_t$ and the δY_{rms} values as a measure of pressure fluctuation intensities at both ends of the side channel. The plot of saturation as a function of $\bar{P}_{in-out}$ shown in Fig. 5(b) shows that the remaining saturations of all invading polymer solutions collapse into a single curve and displacement of the entrapment occurs within a narrow pressure range (indicated by the red area in Fig. 5). A comparison of the data shown in Figs. 4(b) and 4(c) indicates that the displacement starts at a fluctuation intensity larger than $\delta Y_{rms} \approx 3\,\mu m$, as shown via the dashed lines in Fig. 5(a) and in the inset of Fig. 5(b), respectively. In fact, as indicated in the inset of Fig. 5(b), when saturation is plotted as a function of δY_{rms}, the displacement starts at similar fluctuation intensities $\delta Y_{rms} \approx 3\,\mu m$, i.e., in a similar range of pressure fluctuations, regardless of the polymer concentration and molecular weight. It can therefore be concluded that due to the unstable nature of the flow, the pressure fluctuations provide the pressure required to overcome the capillary threshold of the entrapment once they are strong enough.

C. Elasticity-induced phenomena in serpentine channels

To illustrate the underlying elasticity-induced flow features that cause the observed unstable flow and motion of the fluid–fluid interface, we visualized flow path lines by adding fluorescent particles to the invading polymer phase. Figure 6 (Multimedia view) shows the viscoelastic flow path lines for 2500 ppm Flopaam 3330, as visualized using fluorescence imaging. At $\dot{\gamma} \approx 143\,s^{-1} < \dot{\gamma}_{crit}$ in Fig. 6(a), we observe a laminar flow, in which the flow path lines follow the curvature of the channel. At increased $\dot{\gamma}$ but below $\dot{\gamma}_{crit} \approx 1576\,s^{-1}$, in Figs. 6(b) and 6(c), the path lines become slightly asymmetric with reference to a central vertical line. At this stage, visible but mild fluid–fluid interface fluctuations occur [Fig. 6(c)]. After the onset of purely elastic instability, $\dot{\gamma} > \dot{\gamma}_{crit}$, the base flow exhibits characteristics of turbulent flow such as chaotic motion of fluorescent particles and semi-3D effects in the form of crossing path lines [Figs. 6(d)–6(f)]. With further increase in $\dot{\gamma}$, the intensity of the turbulent flow is amplified and accompanied by eventual displacement of oil from the side channel [Figs. 6(e) and 6(f)]. As indicated in Fig. 6(f), no steady path line is established in the perpendicular side channel and only random particle motion is observed temporarily. The latter observation confirms the presence of an instantaneous pressure difference between the two ends of the side channel.

Figure 7(a) illustrates an example PSD analysis of δY extracted from the optical images of 2500 ppm Flopaam 3330. We observe a rather flat plateau at the lowest shear rate $\dot{\gamma} \approx 72\,s^{-1}$ s, where the fluid–fluid interface remains stationary. At $\dot{\gamma} \approx 716\,s^{-1}$, i.e., below $\dot{\gamma}_{crit}$, the PSD curve continues to be a rather flat plateau even though interfacial fluctuations are detected optically at this shear rate
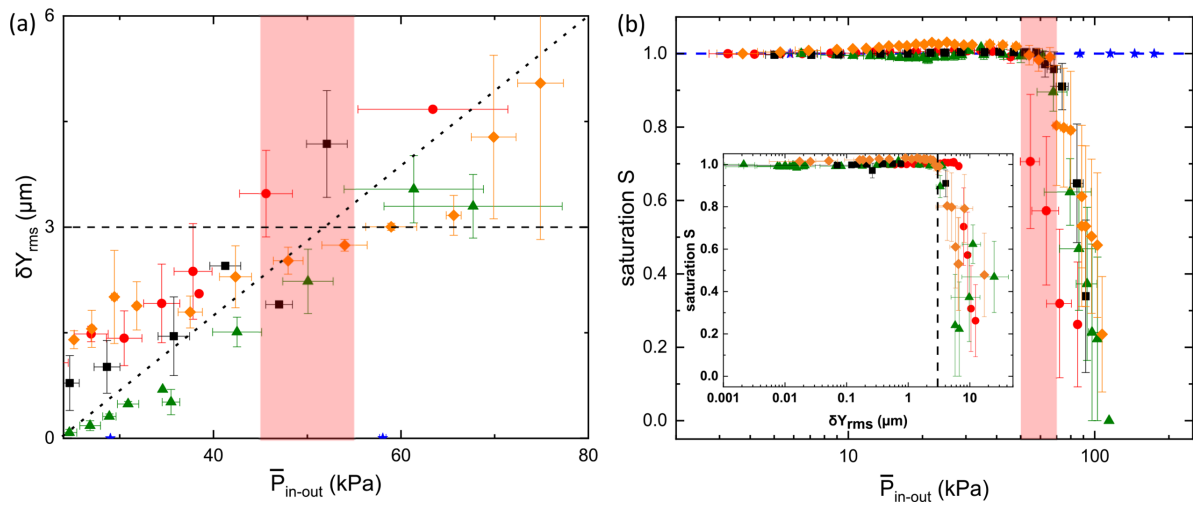
FIG. 5. (a) The fluctuation intensity δY_{rms} and (b) remaining oil saturation S as functions of the measured pressure difference $\bar{P}_{in-out}$. The inset in figure (b) shows the saturation S as function of δY_{rms}. The horizontal dashed lines in figure (a) and the inset in figure (b) indicate $\delta Y_{rms} \approx 3\,\mu m$, where we observe the onset of displacement in Fig.4(b). The red areas in figures (a) and (b) refer to the pressure ranges associated with the onset of displacement. The symbols in figures (a) and (b) represent the experimental data for 67 w% glycerin (★), 2000 ppm Flopaam 3630 (■), 1000 ppm Flopaam 3630 (●), 2500 ppm Flopaam 3330 (▲), and 1300 ppm Flopaam 3330 (◆).

[Fig. 4(b)]. This suggests an additional phenomenon induced by polymer solution elasticity prior to the onset of purely elastic instability. At further increased shear rates, close to $\dot{\gamma}_{crit} \approx 1576\ s^{-1}$ and above, power-law decay is observed with an exponent $\beta > 3$. In general, at shear rates above the respective critical values for the various polymer types and concentrations, power-law decay with an exponent within $3.3 \leq \beta \leq 3.8$ is detected in Figs. 7(b)–7(d). This is also in agreement with the exponent $\beta \approx 3.4$ reported by Mitchell et al.,[54] who performed a similar analysis. Based on this, we can conclude that above the respective values of $\dot{\gamma}_{crit}$, as identified in Fig. 2, the characteristic

features of purely elastic instability are indeed reflected in the observed fluctuating motion of the fluid–fluid interface.

The observed interfacial fluctuations, out of plane particle motion, and slight flow path line asymmetry in Fig. 6(c) prior to the onset of purely elastic instability (more visible for Flopaam 3330) may be associated with elastic secondary flows, i.e., flows in the cross-stream direction that are much weaker than the flow in the main flow direction.[16,71,72] These types of secondary flows result from a difference between the curvatures of inner and outer bends of the serpentine channel, where the gradient of the first normal stress difference N_1 arises [Fig. 8(a)]. Consequently, the so-called "Hoop stress" emerges and drives the viscoelastic fluid toward inner bends at the top and bottom of the serpentine channel, where N_1 is the largest. The fluid is then pushed back to the outer part of the serpentine channel at the center plane to complete the formation of counter-rotating vortices in the out-of-plane cross section of the channel, as indicated by the dashed contours of potential secondary flow vortices in Fig. 8(a). Values of N_1 as a function of the normalized lateral distance along the dashed central line in Fig. 8(a) are shown in Fig. 8(b). As indicated in this figure, the N_1 difference between the inner and outer bends is continuously increased by increasing the shear rate, respectively, the Weissenberg number. However, due to the difficulty of solving the flow equation including the White–Metzger fluid model after the onset of purely elastic instability, the computational fluid dynamics (CFD) simulations are limited to low Weissenberg numbers. The out-of-plane moving particles, and thus the path lines deformed in the direction of flow toward the inner bend in the consecutive stacks of images observed experimentally in Figs. 6(b) and 6(c), are consistent with the direction of counter-rotating secondary flow vortices in the upper half of the channel [Fig. 8(a)] with the assumption that the focal plane of the objective is set slightly above the midplane with respect to the z-direction. Therefore, we can conclude that the visible but mild fluctuations of the fluid–fluid interfaces in Fig. 4(b) and the deviations from the laminar path lines in Fig. 6(c) occur because of the secondary flows. Such elastic secondary flows are present for all
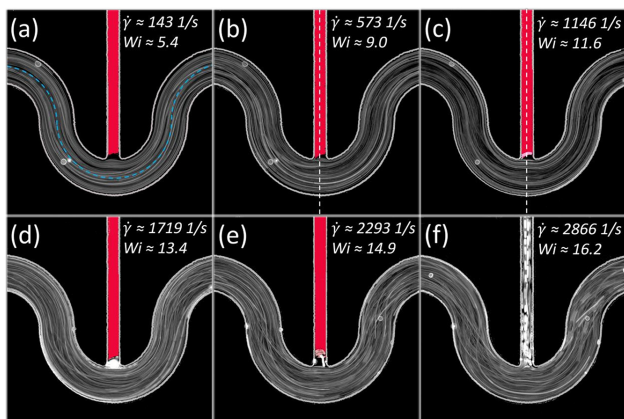
FIG. 6. [(a)–(f)] Stacks of 32 consecutive path line images of flow in the serpentine channel. The fluid is 2500 ppm Flopaam 3330 and the images are obtained via fluorescence microscopy. The flow direction is from left to right. The dashed blue line in figure (a) is a guide for the eye and marks the radius of curvature of the serpentine channel. The white vertical dashed lines in figures (b) and (c) are references for symmetry. The entrapped oil phase is colored red artificially for easier identification. The pink area in figures (c)–(e) indicates the moving fluid–fluid interface. Multimedia view: https://doi.org/10.1063/5.0071556.2

33, 113102-7
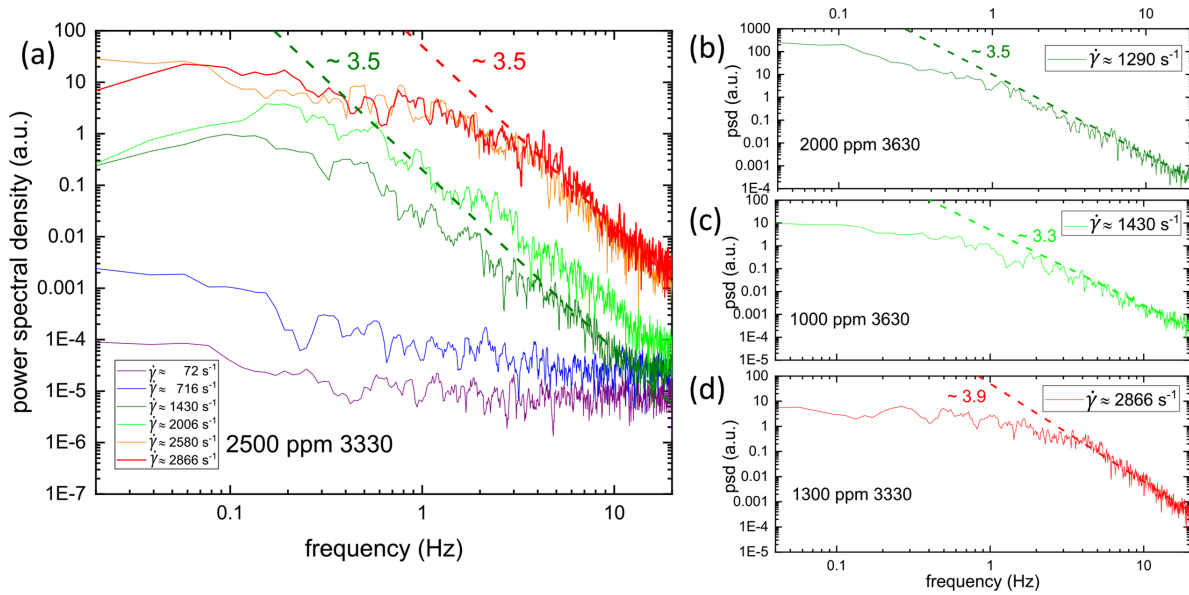
FIG. 7. PSD analysis of vertical fluctuation of the center position δY of (a) 2500 ppm Flopaam 3330 for various shear rates above and below the critical shear rate; (b) 2000 ppm Flopaam 3630; (c) 1000 ppm Flopaam 3630; and (d) 1300 ppm Flopaam 3330. The shear rates in figures (b)–(d) are selected to ensure that the flow is safely above the onset of purely elastic instability $\dot{\gamma}_{crit}$.

applied shear rates in the case of viscoelastic flow and their strength intensifies as the Weissenberg number increases.[17]

To study the evolution of flow toward a fully developed elastic turbulent state, the experimentally measured pressure drops were normalized using the corresponding values of a laminar reference flow and plotted as functions of the shear rate $\dot{\gamma}$ in Figs. 9(a) and 9(b) and as a function of the Weissenberg number Wi in Fig. 9(c). The pressure drops of the corresponding laminar reference flows were calculated using CFD simulations of imaginary fluids with the same shear

thinning properties as the polymer solutions defined by the Carreau–Yasuda model, i.e., with no elastic component attributed to the total stress tensor. The normalized pressure is close to unity at lower shear rates, respectively, at $Wi < Wi_{crit}$. This verifies the laminar-flow regime at this stage. A steep monotonic increase is observed for all solutions above the onset of purely elastic instability. After this onset, the normalized pressure follows a convex shape in the case of Flopaam 3630 and a concave shape in the case of Flopaam 3330. The curve flattens slowly at the highest applied shear rates for all
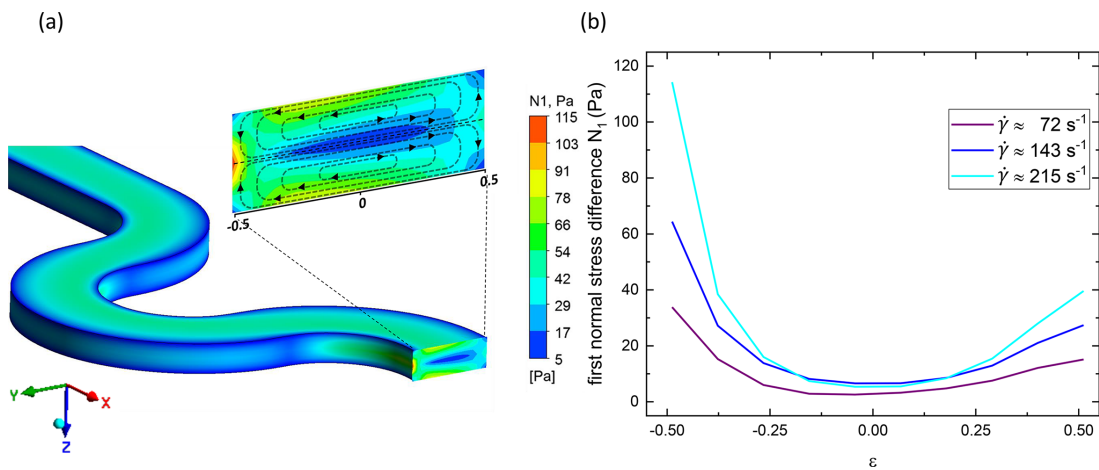
FIG. 8. (a) Sample distribution of the first normal stress difference N_1 within a vertical cross section of the serpentine channel obtained via CFD simulations using the White–Metzner model for 2500 ppm Flopaam 3330 at $\dot{\gamma} \approx 143 \, s^{-1}$ and corresponding $Wi \approx 5.4$. The contours of potential secondary flow vortices are indicated by dashed lines, which are intended as guides to the eye. (b) N_1 at the central line of the cross section for increasing shear rates $\dot{\gamma} \approx 72 \, s^{-1}$ s ($Wi \approx 4.2$), $\dot{\gamma} \approx 143 \, s^{-1}$ ($Wi \approx 5.4$), and $\dot{\gamma} \approx 215 \, s^{-1}$ ($Wi \approx 6.3$).
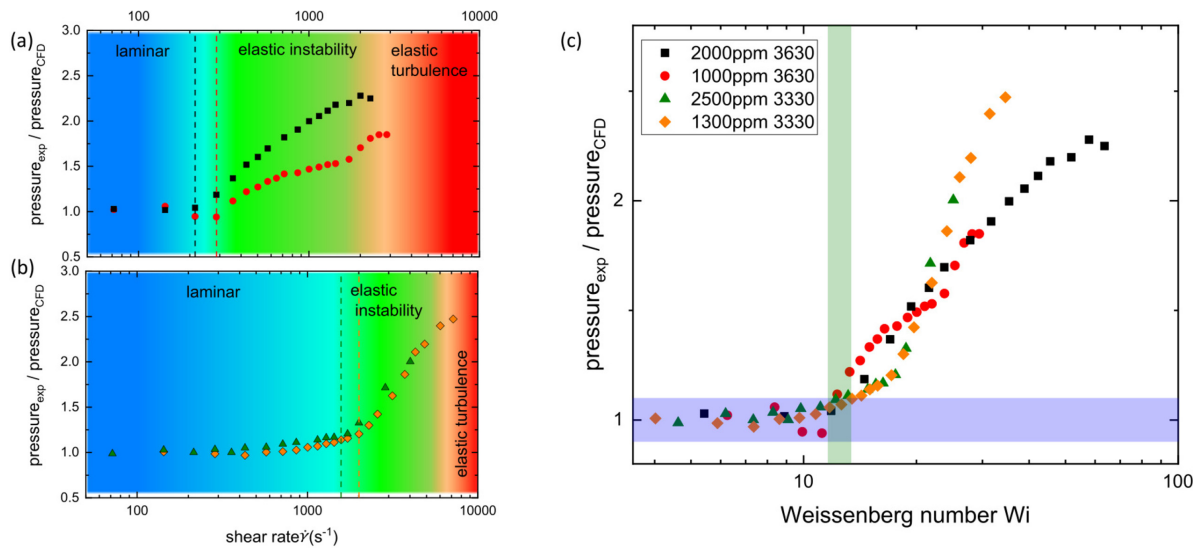
FIG. 9. The ratio of experimentally measured pressures to the computed steady-state pressure drops of imaginary fluids with the same shear thinning properties, as defined by the Carreau–Yasuda model. Evolution of flow from a laminar to a fully developed turbulent regime for the polymers (a) Flopaam 3630 and (b) Flopaam 3330 as function of the shear rate, and Weissenberg number (c). The symbols in figure (a) represent data for 2000 ppm Flopaam 3630 (■), and 1000 ppm Flopaam 3630 (●), while the symbols in (b) represent 2500 ppm Flopaam 3330 (▲), and 1300 ppm Flopaam 3330 (◆). The horizontal rectangle indicates the laminar regime, the vertical rectangle marks the onset of purely elastic instabilities.

the polymer solutions [Figs. 9(a) and 9(b)]. The latter behavior is interpreted in the literature as an indication of transition toward a fully developed turbulent regime.[7,16,73] The different curvatures of the evolving normalized pressures after the onset of purely elastic instability can be explained with respect to the relaxation time, i.e., degree of elasticity of polymer coils in the solutions. Larger polymer coils, i.e., Flopaam 3630, are more elastic and therefore stretch more easily during flow. This leads to an immediate and steep increase in normalized pressure, after the onset of purely elastic instability. Higher elasticity of polymers in the solution also leads to a fully developed turbulent state already at lower shear rates [Figs. 9(a) and 9(b)]. In the case of Flopaam 3630, the transition from laminar to fully developed turbulence occurs in the range of $\dot{\gamma} \approx 200$ s^{-1} to $\dot{\gamma} \approx 2000$ s^{-1}, whereas transition for Flopaam 3330 occurs between $\dot{\gamma} \approx 2000$ s^{-1} and $\dot{\gamma} \approx 6000$ s^{-1}. Comparing these shear rates to the shear rate range where we detect displacement of the capillary entrapment in our geometry, in Fig. 4(d), we note that the displacement coincides with transition toward the fully developed turbulent regime.

IV. CONCLUSION AND OUTLOOK

A single-entrapment microfluidic geometry was designed based on serpentine channels to mimic the essential features of flow in porous media, i.e., shear-dominated tortuous pathways. The unique microfluidic geometry and high optical and temporal resolution of our experiments allowed us to focus on the displacement of capillary entrapments (exclusively) by elastic stresses. We confirmed that the presence of purely elastic instabilities is reflected by the statistics of the interfacial fluctuations. Based on the power spectral density analysis, a characteristic exponent $\beta \approx 3.5$ was detected for shear rates that exceeded the onset of elastic instability. This led us to conclude that the mild interfacial fluctuations observed prior to the onset of purely

elastic instability have a different origin and could be attributed to secondary flows induced by the gradient of the first normal stress difference due to the curvature of the serpentine channel. It was evident that a certain fluctuation intensity is required to overcome the capillary pressure threshold and initiate desaturation. The results of our experiments confirmed that displacement of the capillary entrapment is governed primarily by the randomness of base flow that arises from elastic instability. The results of our research show that, in our specific design, the displacement coincides with transition toward a fully developed turbulent regime regardless of the polymer molecular weight and concentration.

Displacement processes in actual porous media are more complex. Flow asymmetry in randomized porous media and heterogeneous pore-throat distributions lead to a wide range of capillary entrapment sizes as well as broad distributions of *in situ* flow velocities. This produces non-uniform viscous pressure fields. Therefore, a synergic effect of different elasticity-induced phenomena coupled with viscous forces can be expected to contribute to the mobilization of capillary entrapments. Thus, decoupling of these components requires further in-depth investigation into more complex model systems.

AUTHOR DECLARATIONS
Conflict of Interest

The authors have no conflicts of interest to disclose.

DATA AVAILABILITY

The data that support the findings of this study are available from the corresponding author upon reasonable request.

APPENDIX: RHEOLOGY PROTOCOLS

1. Rotational test

Shear viscosity of all polymer solutions and dynamic viscosity of the glycerin solution as shown in Fig. 2 of the main text were determined through a steady shear step test applying a standard protocol in stress-controlled mode using HAAKE MARS 40 rheometer and 60 mm cone plate geometry with 1° angle. To avoid air bubbles when placing the respective fluids between the cone and plate, we placed a small droplet at the tip of the cone to create a wetting film when bringing the cone and plate in contact. The temperature was set to $(20 \pm 0.2)^\circ$ C for all measurements to match the lab temperature.

2. First normal stress difference

The measurements of the first normal stress difference N_1 are shown in Fig. 10(a). At each step, first the normal force value is set
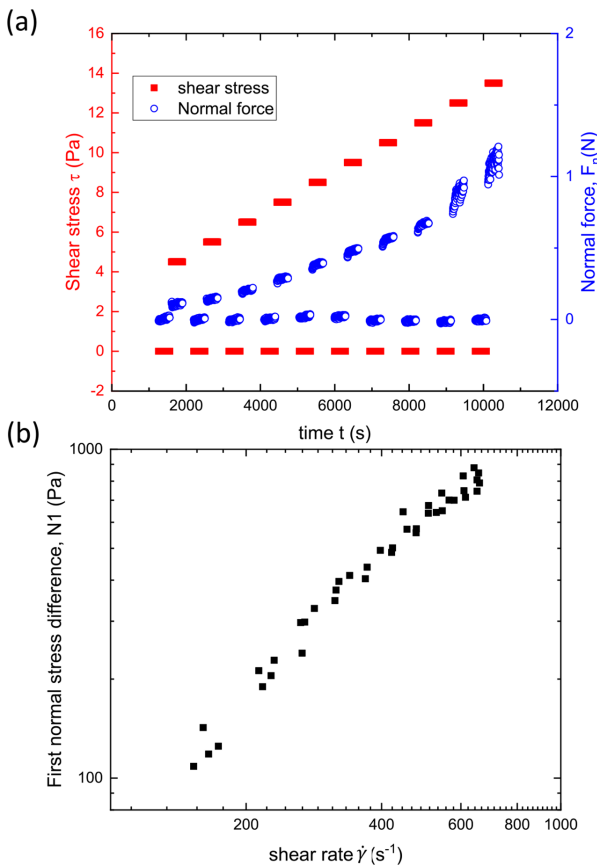

FIG. 11. Frequency sweep test for the utilized polymer solutions: 2000 ppm Flopaam 3630 (■), 1000 ppm Flopaam 3630 (●), 2500 ppm Flopaam 3330 (▲), and 1300 ppm Flopaam 3330 (◆). Filled symbols represent the storage modulus G' and open symbols represent the loss modulus G''.

to zero. To account for the drift caused by relaxation of the solution as well as the force measuring sensor in the device, the measuring geometry stays for 300 s at rest, followed by a constant rotation at fixed applied stress for 300 s. The respective polymer solution in the measuring geometry was surrounded by mineral oil to avoid inertial instabilities at the edges at higher rotation rates. The normal force values measured by the rheometer were corrected for inertia, $N_{inertia} = -0.075\pi\rho\Omega^2 R^4$, and drift and converted to the first normal stress difference using $N_{1corr} = \frac{2F_n}{\pi R^2}$ in which F_n is the normal force measured by the rheometer; Ω, ρ, and R are the angular rotation, density, and the radius of the measuring geometry, respectively. An exemplary plot (four times repetitions) of first normal stress difference as a function of shear rate for 2000 ppm Flopaam 3630 is shown in Fig. 10(b).

3. Frequency sweep test

The small amplitude frequency sweep tests were performed using a standard protocol in stress-controlled mode. The stress amplitude was acquired priorly from a deformation amplitude sweep test to be safely in the linear viscoelastic range. To ensure minimum measurement error, the duration of measurements at each point was automatically adjusted based on the frequency. The results are shown in Fig. 11.

FIG. 10. Exemplary normal force measurement for 2000 ppm Flopaam 3630 (a) and corresponding first normal stress differences N_1 (b).

REFERENCES

[1]A. Groisman and V. Steinberg, "Mechanism of elastic instability in Couette flow of polymer solutions: Experiment," Phys. Fluids **10**, 2451–2463 (1998).

[2]V. Steinberg, "Elastic turbulence: An experimental view on inertialess random flow," Annu. Rev. Fluid Mech. **53**, 27–58 (2021).

[3]T. Burghelea, E. Segre, and V. Steinberg, "Elastic turbulence in von Karman swirling flow between two disks," Phys. Fluids **19**, 053104 (2007).

[4]Y. Jun and V. Steinberg, "Elastic turbulence in a curvilinear channel flow," Phys. Rev. E **84**, 056325 (2011).

[5]T. Burghelea, E. Segre, and V. Steinberg, "Validity of the Taylor hypothesis in a random spatially smooth flow," Phys. Fluids **17**, 103101 (2005).

[6]J. Davoudi and J. Schumacher, "Stretching of polymers around the Kolmogorov scale in a turbulent shear flow," Phys. Fluids **18**, 025103 (2006).

[7]A. Groisman and V. Steinberg, "Elastic turbulence in curvilinear flows of polymer solutions," New J. Phys. **6**, 29 (2004).

[8]Y. Jun and V. Steinberg, "Polymer concentration and properties of elastic turbulence in a von Karman swirling flow," Phys. Rev. Fluids **2**, 103301 (2017).

[9]A. Fouxon and V. Lebedev, "Spectra of turbulence in dilute polymer solutions," Phys. Fluids **15**, 2060–2072 (2003).

[10]A. Groisman and V. Steinberg, "Stretching of polymers in a random three-dimensional flow," Phys. Rev. Lett. **86**, 934–937 (2001).

[11]Y. Jun and V. Steinberg, "Power and pressure fluctuations in elastic turbulence over a wide range of polymer concentrations," Phys. Rev. Lett. **102**, 124503 (2009).

[12]V. Steinberg, "Scaling relations in elastic turbulence," Phys. Rev. Lett. **123**, 234501 (2019).

[13]T. Watanabe and T. Gotoh, "Power-law spectra formed by stretching polymers in decaying isotropic turbulence," Phys. Fluids **26**, 035110 (2014).

[14]A. Groisman and V. Steinberg, "Elastic turbulence in a polymer solution flow," Nature **405**, 53–55 (2000).

[15]X. Shi and G. F. Christopher, "Growth of viscoelastic instabilities around linear cylinder arrays," Phys. Fluids **28**, 124102 (2016).

[16]G. Yao, J. Zhao, H. Yang, M. A. Haruna, and D. Wen, "Effects of salinity on the onset of elastic turbulence in swirling flow and curvilinear microchannels," Phys. Fluids **31**, 123106 (2019).

[17]J. Zilz, R. J. Poole, M. A. Alves, D. Bartolo, B. Levaché, and A. Lindner, "Geometric scaling of a purely elastic flow instability in serpentine channels," J. Fluid Mech. **712**, 203–218 (2012).

[18]B. Traore, C. Castelain, and T. Burghelea, "Efficient heat transfer in a regime of elastic turbulence," J. Non-Newtonian Fluid Mech. **223**, 62–76 (2015).

[19]R. Whalley, W. Abed, D. Dennis, and R. Poole, "Enhancing heat transfer at the micro-scale using elastic turbulence," Theor. Appl. Mech. Lett. **5**, 103–106 (2015).

[20]W. M. Abed, R. D. Whalley, D. J. Dennis, and R. J. Poole, "Experimental investigation of the impact of elastic turbulence on heat transfer in a serpentine channel," J. Non-Newtonian Fluid Mech. **231**, 68–78 (2016).

[21]D.-Y. Li, X.-B. Li, H.-N. Zhang, F.-C. Li, S. Qian, and S. W. Joo, "Efficient heat transfer enhancement by elastic turbulence with polymer solution in a curved microchannel," Microfluid. Nanofluid. **21**, 10 (2017).

[22]H. Yang, G. Yao, and D. Wen, "Experimental investigation on convective heat transfer of shear-thinning fluids by elastic turbulence in a serpentine channel," Exp. Therm. Fluid Sci. **112**, 109997 (2020).

[23]T. Burghelea, E. Segre, I. Bar-Joseph, A. Groisman, and V. Steinberg, "Chaotic flow and efficient mixing in a microchannel with a polymer solution," Phys. Rev. E **69**, 066305 (2004).

[24]A. Groisman and V. Steinberg, "Efficient mixing at low Reynolds numbers using polymer additives," Nature **410**, 905–908 (2001).

[25]J. A. Pathak, D. Ross, and K. B. Migler, "Elastic flow instability, curved streamlines, and mixing in microfluidic flows," Phys. Fluids **16**, 4028–4034 (2004).

[26]H. Yang, G. Yao, and D. Wen, "Efficient mixing enhancement by orthogonal injection of shear-thinning fluids in a micro serpentine channel at low Reynolds numbers," Chem. Eng. Sci. **235**, 116368 (2021).

[27]A. Clarke, A. M. Howe, J. Mitchell, J. Staniland, and L. A. Hawkes, "How viscoelastic-polymer flooding enhances displacement efficiency," SPE J. **21**, 0675–0687 (2016).

[28]A. Rock, R. E. Hincapie, J. Wegner, and L. Ganzer, "Advanced flow behavior characterization of enhanced oil recovery polymers using glass-silicon-glass micromodels that resemble porous media," in *SPE Europec Featured at EAGE Conference and Exhibition* (OnePetro, 2017).

[29]R. E. Hincapie, A. Rock, J. Wegner, and L. Ganzer, "Oil mobilization by viscoelastic flow instabilities effects during polymer EOR: A pore-scale visualization approach," in *SPE Latin America and Caribbean Petroleum Engineering Conference* (OnePetro, 2017).

[30]C. A. Browne, A. Shih, and S. S. Datta, "Pore-scale flow characterization of polymer solutions in microfluidic porous media," Small **16**, 1903944 (2020).

[31]S. De, J. A. Kuipers, E. A. Peters, and J. T. Padding, "Viscoelastic flow past mono- and bidisperse random arrays of cylinders: Flow resistance, topology and normal stress distribution," Soft Matter **13**, 9138–9146 (2017).

[32]E. Hemingway, A. Clarke, J. Pearson, and S. Fielding, "Thickening of viscoelastic flow in a model porous medium," J. Non-Newtonian Fluid Mech. **251**, 56–68 (2018).

[33]B. Khomami and L. D. Moreno, "Stability of viscoelastic flow around periodic arrays of cylinders," Rheol. Acta **36**, 367–383 (1997).

[34]B. Qin, P. F. Salipante, S. D. Hudson, and P. E. Arratia, "Flow resistance and structures in viscoelastic channel flows at low re," Phys. Rev. Lett. **123**, 194501 (2019).

[35]B. Qin and P. E. Arratia, "Characterizing elastic turbulence in channel flows at low Reynolds number," Phys. Rev. Fluids **2**, 083302 (2017).

[36]M. Kumar and A. M. Ardekani, "Elastic instabilities between two cylinders confined in a channel," Phys. Fluids **33**, 074107 (2021).

[37]S. De, J. van der Schaaf, N. G. Deen, J. A. M. Kuipers, E. A. J. F. Peters, and J. T. Padding, "Lane change in flows through pillared microchannels," Phys. Fluids **29**, 113102 (2017).

[38]S. Varchanis, C. C. Hopkins, A. Q. Shen, J. Tsamopoulos, and S. J. Haward, "Asymmetric flows of complex fluids past confined cylinders: A comprehensive numerical study with experimental validation," Phys. Fluids **32**, 053103 (2020).

[39]D. M. Walkama, N. Waisbord, and J. S. Guasto, "Disorder suppresses chaos in viscoelastic flows," Phys. Rev. Lett. **124**, 164501 (2020).

[40]C. C. Hopkins, S. J. Haward, and A. Q. Shen, "Tristability in viscoelastic flow past side-by-side microcylinders," Phys. Rev. Lett. **126**, 054501 (2021).

[41]S. De, J. A. Kuipers, E. A. Peters, and J. T. Padding, "Viscoelastic flow simulations in model porous media," Phys. Rev. Fluids **2**, 1–21 (2017).

[42]J. J. J. Gillissen, "Viscoelastic flow simulations through an array of cylinders," Phys. Rev. E **87**, 023003 (2013).

[43]E. M. Ekanem, S. Berg, S. De, A. Fadili, T. Bultreys, M. Rücker, J. Southwick, J. Crawshaw, and P. F. Luckham, "Signature of elastic turbulence of viscoelastic fluid flow in a single pore throat," Phys. Rev. E **101**, 042605 (2020).

[44]F. J. Galindo-Rosales, L. Campo-Deaño, F. T. Pinho, E. Van Bokhorst, P. J. Hamersma, M. S. Oliveira, and M. A. Alves, "Microfluidic systems for the analysis of viscoelastic fluid flow phenomena in porous media," Microfluid. Nanofluid. **12**, 485–498 (2012).

[45]M. Kumar, S. Aramideh, C. A. Browne, S. S. Datta, and A. M. Ardekani, "Numerical investigation of multistability in the unstable flow of a polymer solution through porous media," Phys. Rev. Fluids **6**, 033304 (2021).

[46]P. Pakdel and G. H. McKinley, "Elastic instability and curved streamlines," Phys. Rev. Lett. **77**, 2459–2462 (1996).

[47]G. H. McKinley, P. Pakdel, and A. Öztekin, "Rheological and geometric scaling of purely elastic flow instabilities," J. Non-Newtonian Fluid Mech. **67**, 19–47 (1996).

[48]S. S. Datta, A. M. Ardekani, P. E. Arratia, A. N. Beris, I. Bischofberger, J. G. Eggers, J. E. López-Aguilar, S. M. Fielding, A. Frishman, M. D. Graham, J. S. Guasto, S. J. Haward, S. Hormozi, G. H. McKinley, R. J. Poole, A. Morozov, V. Shankar, E. S. G. Shaqfeh, A. Q. Shen, H. Stark, V. Steinberg, G. Subramanian, and H. A. Stone, "Perspectives on viscoelastic flow instabilities and elastic turbulence," arXiv:2108.09841 [physics.flu-dyn] (2021).

[49]A. M. Howe, A. Clarke, and D. Giernalczyk, "Flow of concentrated viscoelastic polymer solutions in porous media: Effect of mw and concentration on elastic turbulence onset in various geometries," Soft Matter **11**, 6419–6431 (2015).

[50]C. A. Browne and S. S. Datta, "Elastic turbulence generates anomalous flow resistance in porous media," arXiv:2011.06036 [physics.flu-dyn] (2020).

[51]D. Kawale, E. Marques, P. L. Zitha, M. T. Kreutzer, W. R. Rossen, and P. E. Boukany, "Elastic instabilities during the flow of hydrolyzed polyacrylamide solution in porous media: Effect of pore-shape and salt," Soft Matter **13**, 765–775 (2017).

[52]E. S. Shaqfeh, "Purely elastic instabilities in viscometric flows," Annu. Rev. Fluid Mech. **28**, 129–185 (1996).

[53]A. Clarke, A. M. Howe, J. Mitchell, J. Staniland, L. Hawkes, and K. Leeper, "Mechanism of anomalously increased oil displacement with aqueous viscoelastic polymer solutions," Soft Matter **11**, 3536–3541 (2015).

[54]J. Mitchell, K. Lyons, A. M. Howe, and A. Clarke, "Viscoelastic polymer flows and elastic turbulence in three-dimensional porous structures," Soft Matter **12**, 460–468 (2016).

[55]C. Xie, K. Xu, K. Mohanty, M. Wang, and M. T. Balhoff, "Nonwetting droplet oscillation and displacement by viscoelastic fluids," Phys. Rev. Fluids **5**, 063301 (2020).

[56]M. A. Nilsson, R. Kulkarni, L. Gerberich, R. Hammond, R. Singh, E. Baumhoff, and J. P. Rothstein, "Effect of fluid rheology on enhanced oil recovery in a microfluidic sandstone device," J. Non-Newtonian Fluid Mech. **202**, 112–119 (2013).

[57]S. De, P. Krishnan, J. van der Schaaf, J. Kuipers, E. Peters, and J. Padding, "Viscoelastic effects on residual oil distribution in flows through pillared microchannels," J. Colloid Interface Sci. **510**, 262–271 (2018).

[58]Y. Xia and G. M. Whitesides, "Soft lithography," Annu. Rev. Mater. Sci. **28**, 153–184 (1998).

[59]American Petroleum Institute, *Recommended Practices for Evaluation of Polymers Used in Enhanced Oil Recovery Operations* (American Petroleum Institute, 1990), Vol. 63.

[60]T. G. Mezger, *The Rheology Handbook: For Users of Rotational and Oscillatory Rheometers* (Vincentz Network GmbH & Co KG, 2006).

[61]A. V. Dobrynin, R. H. Colby, and M. Rubinstein, "Scaling theory of polyelectrolyte solutions," Macromolecules **28**, 1859–1871 (1995).

[62]C. W. Macosko, *Rheology: Principles, Measurements and Applications* (Wiley-VCH, 1994), Vol. 86.

[63]H. A. Barnes, J. F. Hutton, and K. Walters, *An Introduction to Rheology* (Elsevier, 1989), Vol. 3.

[64]T. Burghelea and V. Bertola, *Transport Phenomena in Complex Fluids* (Springer, 2020), Vol. 598.

[65]J. L. White and A. B. Metzner, "Development of constitutive equations for polymeric melts and solutions," J. Appl. Polym. Sci. **7**, 1867–1889 (1963).

[66]H. Bodiguel, J. Beaumont, A. Machado, L. Martinie, H. Kellay, and A. Colin, "Flow enhancement due to elastic turbulence in channel flows of shear thinning fluids," Phys. Rev. Lett. **114**, 028302 (2015).

[67]A. Soulies, J. Aubril, C. Castelain, and T. Burghelea, "Characterisation of elastic turbulence in a serpentine micro-channel," Phys. Fluids **29**, 083102 (2017).

[68]L. Casanellas, M. A. Alves, R. J. Poole, S. Lerouge, and A. Lindner, "The stabilizing effect of shear thinning on the onset of purely elastic instabilities in serpentine microflows," Soft Matter **12**, 6167–6175 (2016).

[69]ANSYS, *ANSYS Polyflow User's Guide* (ANSYS Inc., 2020).

[70]Y. Son, "Determination of shear viscosity and shear rate from pressure drop and flow rate relationship in a rectangular channel," Polymer **48**, 632–637 (2007).

[71]L. Ducloué, L. Casanellas, S. J. Haward, R. J. Poole, M. A. Alves, S. Lerouge, A. Q. Shen, and A. Lindner, "Secondary flows of viscoelastic fluids in serpentine microchannels," Microfluid. Nanofluid. **23**, 33 (2019).

[72]R. Poole, A. Lindner, and M. Alves, "Viscoelastic secondary flows in serpentine channels," J. Non-Newtonian Fluid Mech. **201**, 10–16 (2013).

[73]B. A. Schiamberg, L. T. Shereda, H. Hu, and R. G. Larson, "Transitional pathway to elastic turbulence in torsional, parallel-plate flow of a polymer solution," J. Fluid Mech. **554**, 191–216 (2006).

Scaling purely elastic instability of strongly shear thinning polymer solutionss

Authors: P. Shakeri[1,2], M. Jung[1,2], and R. Seemann[1,2]

[1]Experimental Physics, Saarland University, 66123 Saarbrücken,Germany

[2]Max Planck Institute for Dynamics and Self-Organization, 37077 Göttingen, Germany

–

Author contributions:

Fabrication of microfluidic devices, preparation of working fluids, and rheological characterization were conducted by P. Shakeri and M. Jung. Experiments were designed, performed, and analyzed by P. Shakeri and M. Jung. The article was written by P. Shakeri, M. Jung, and R. Seemann. The research was directed by R. Seemann.

Abstract:

The flow of viscoelastic polymer solutions in curved channels exhibits instability caused by the elastic nature of polymers even at low Reynolds numbers. However, scaling of the onset of this purely elastic instability in semi-dilute polymer solutions has not been previously reported. Here we experimentally investigate the flow of highly elastic polymer solutions above their overlap concentrations using pressure measurements and particle image velocimetry. We demonstrate that the onset of instability can be scaled by including shear dependent rheological properties of the polymer solutions in the nonlinear stability analysis. As a result, a universal criterion is provided for scaling the onset of purely elastic instability in the semi-dilute regime regardless of the type and concentration of the polymer.

Scaling purely elastic instability of strongly shear thinning polymer solutions

Pegah Shakeri ●,[*,†] Michael Jung ●,[*,‡] and Ralf Seemann ●
Experimental Physics, Saarland University, 66123 Saarbrücken, Germany
and Max Planck Institute for Dynamics and Self-Organization, 37077 Göttingen, Germany

Flow of viscoelastic polymer solutions in curved channels exhibits instability caused by the elastic nature of polymers even at low Reynolds numbers. However, scaling of the onset of this purely elastic instability in semidilute polymer solutions has not been previously reported. Here we experimentally investigate the flow of highly elastic polymer solutions above their overlap concentrations using pressure measurements and particle image velocimetry. We demonstrate that the onset of instability can be scaled by including shear dependent rheological properties of the polymer solutions in the nonlinear stability analysis. As a result, a universal criterion as function of normalized polymer concentration is provided for scaling the onset of purely elastic instability in the semidilute regime regardless of the type and molecular weight of the polymer.

Purely elastic instability is a well-known phenomenon occurring during the flow of viscoelastic polymer solutions and melts at vanishing Reynolds numbers Re. This instability can be attributed to nonlinear elastic stresses, arising from the stretching and relaxing of flexible polymers, which do not fully dissipate beyond a critical shear rate [1–6]. The occurrence of purely elastic instability can be beneficial for practical applications such as microfluidic mixing, heat transfer, and mobilization of capillary entrapments [7–9]. However, in multiple processes in food and cosmetics industry [10,11], as well as polymer extrusion [12], the occurrence of purely elastic instability is undesirable. Therefore, it is crucial to estimate the conditions under which the purely elastic instability occurs, in terms of the rheology of the fluid and the geometrical properties of the flow.

Polymers are inherently nonuniformly stretched during flow, resulting in an anisotropic distribution of three-dimensional stresses. The difference between the stress component in the flow direction and the stress component in the transverse direction is called the first normal stress difference N_1. In curved geometries when N_1 becomes substantially larger than the shear stress τ, elastic stresses dominate, and polymers are pulled toward regions with higher streamline curvature [4,9]. As a result, the laminar flow paths are disturbed and the polymers are spatially and temporally subjected to different shear rates. Consequently, the polymers

repeatedly store and release elastic stresses during flow, which leads to the emergence of an unstable flow above a certain threshold. Pakdel and McKinley observed that in a curved geometry the onset of this instability can be scaled with respect to the ratio of the first normal stress difference N_1 to the shear stress τ and the curvature of the streamline [13,14]. Thus, the criteria for scaling the onset of pure elastic instability can be formulated as in Eq. (1) [4]:

$$\sqrt{\frac{l}{\mathcal{R}} \frac{|N_1|}{|\tau|}} \geqslant M_{\text{crit}}, \tag{1}$$

where l is a characteristic length scale and $\mathcal{R}$ is the radius of streamline curvature. Since, for a given geometry, the onset of instability is governed merely by the stress ratio, M_{crit} can be considered as a critical stress factor. However, it is essential to notice that this approach does not provide a universal numerical value for M_{crit}, but rather describes how the onset of nonlinearity scales with respect to the rheological and geometrical properties [15]. The value of M_{crit} depends on the type and concentration of the polymer and salt in the solution, as well as on the type of solvent, and is commonly in the range of 1 to 6 [4,16].

This scaling is often used for polymer solutions in the dilute regime, i.e., for polymer concentrations below the overlap concentration c^*, in which the viscosity η, and the relaxation time λ can be assumed to be independent on the shear rate $\dot{\gamma}$. Here, the ratio of $|N_1|$ to $|\tau|$ is linearly dependent on the shear rate, and the characteristic length can be estimated by $l = U\,\lambda_0$, where U is the average flow velocity and λ_0 is the longest polymer relaxation time [4,16–20]. However, above the overlap concentration c^* the polymer behavior during flow is more complicated. Both $\eta(\dot{\gamma})$ and $\lambda(\dot{\gamma})$ show significant nonlinear dependency on the shear rate [21,22]. Using the longest polymer relaxation time λ_0 to estimate the characteristic length, as commonly done in literature [23–25], leads to unrealistically large timescales which do not represent the

---

*These authors contributed equally to this work.

†pegah.shakeri@physik.uni-saarland.de

‡michael.jung@physik.uni-saarland.de

actual dynamics of the polymers in flow in this concentration regime [25]. Moreover, unlike the dilute regime, the ratio of the first normal stress difference to the shear stress in Eq. (1) is not linearly dependent on the shear rate due to the nonquadratic dependence of N_1 on the shear rate, and the nonlinear dependence of $|\tau|$ on the shear rate. Therefore, the assumption of a constant relaxation time is not reasonable, and it is necessary to adopt a realistic approach for scaling the onset of purely elastic instability in the semidilute regime that faithfully reflects the rheological properties of the polymers.

In this paper, we present a practical scaling of the onset of purely elastic instability for strongly shear thinning, highly elastic polymer solutions in the semidilute regime. To this aim, we determine the onset of purely elastic instability of various polymer solutions in a microfluidic serpentine channel via pressure measurements and particle image velocimetry (μPIV). We scale the onset of the observed instability in our experiments by considering the White-Metzner fluid model to account for the shear dependence of the rheological properties of the polymer solutions. Applying this scaling, the onset of purely elastic instability as function of normalized polymer concentration collapses into a universal master curve independent of polymer type and molecular weight, confirming the suggested approach.

The microfluidic channel used in our experiments is fabricated from UV-curable glue NOA 83H (Norland optical adhesives) by soft lithography using standard protocols [9,26]. The microfluidic serpentine channel consisting of 33 consecutive half-loops has the total length of $l \approx 26$ mm, width of $w \approx 0.125$ mm, height of $h \approx 0.036$ mm, and an inner bend radius of curvature of $r_i \approx 0.125$ mm. The inlet of the microfluidic channel is connected to a high-precision, pulsation-free syringe pump (neMESYS, Cetoni GmbH) that enables fluid injection at a controlled volumetric flow rate. The outlet is connected to a liquid reservoir at the same height as the microfluidic device to avoid additional hydrostatic pressure difference. The hydrodynamic pressure drop ΔP inside the serpentine channel is measured by a differential pressure sensor (26PC series, Honeywell) mounted between inlet and outlet. A sketch of the microfluidic channel is provided in the inset of Fig. 1(a).

To represent a wide range of common polymer types that are prone to purely elastic instability, we use two commercial polyelectrolytes, the partially hydrolyzed polyacrylamides (HPAM, 30% hydrolysis) Flopaam 3630 ($M_{w,3630} \approx 18.7$ MDa) and Flopaam 3330 ($M_{w,3330} \approx 6.5$ MDa) dissolved in 17 mM NaCl solution as well as polyethylene oxide (PEO, $M_{w,PEO} \approx 8.0$ MDa) dissolved in ultrapure water. The sample solutions with different concentrations are prepared following standard protocols [9]. It should be mentioned that the salt concentration in case of the HPAM solutions is rather in the low-salt limit and not sufficient to screen all charges of the polyelectrolyte [27]. The densities of all utilized solutions were determined to $\varrho = (1.00 \pm 0.01)$ g/cm^3 by a pycnometer. A full rheological characterization including steady shear step measurements to determine $\eta(\dot{\gamma})$ and $N_1(\dot{\gamma})$ as well as small amplitude frequency sweep tests to determine the storage modulus $G'(\omega)$ and the loss modulus $G''(\omega)$ are performed using a rotational rheometer (HAAKE MARS 40, Thermo Scientific). The data are presented in the
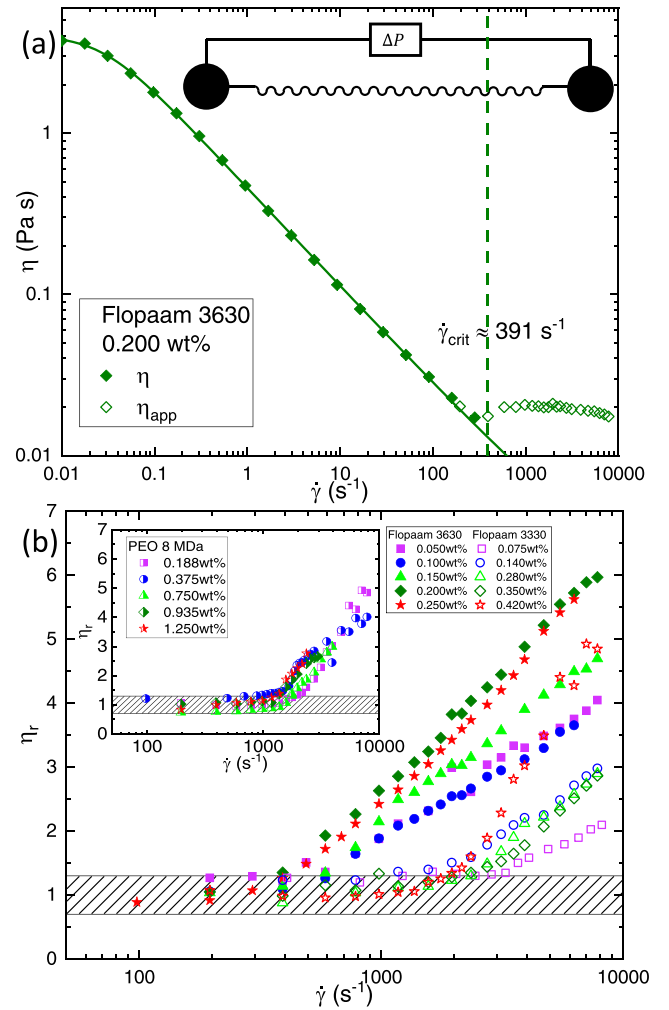
FIG. 1. (a) The shear viscosity $\eta(\dot{\gamma})$ measured using a rheometer (filled symbols) and apparent viscosity $\eta_{app}(\dot{\gamma})$ (open symbols) calculated from the pressure difference ΔP along the serpentine channel (sketch in the inset) for 0.200 wt% Flopaam 3630. The line is a fit to the Carreau-Yasuda model [Eq. (3)]. The dashed vertical line indicates the critical shear rates $\dot{\gamma}_{crit}$. (b) Reduced viscosity $\eta_r(\dot{\gamma}) = \eta_{app}(\dot{\gamma})/\eta(\dot{\gamma})$ as function of the shear rate $\dot{\gamma}$ for Flopaam 3630 and 3330. The inset shows the respective data for PEO 8MDa. The shaded area indicates the initial plateau within the experimental accuracy.

Supplemental Material (SM) [28]. The critical overlap concentrations c^* of the respective polymer types was determined using the Huggins-Kraemer method [29] to be $c^*_{3630} \approx 0.0082$ wt%, $c^*_{3330} \approx 0.0137$ wt%, and $c^*_{PEO} \approx 0.0375$ wt% in agreement with literature values [9,30,31]. To be safely in the semidilute regime for each polymer type, the concentrations are chosen to cover the range from $5 \times c^*$ to $30 \times c^*$. Comparison of the power-law exponents of the respective zero shear viscosity (data in SM [28]) as function of concentration with literature values [25,27,30,32] confirms that the polymer chains remain unentangled below $10 \times c^*$ and become entangled at higher polymer concentrations.

TABLE I. Overview of the critical shear rate $\dot{\gamma}_{\text{crit}}$, and M_{crit} at the onset of purely elastic instability for the utilized polymer solutions.

Flopaam 3630	c/c^*	$\dot{\gamma}_c$ [s^{-1}]	M_c	Flopaam 3330	c/c^*	$\dot{\gamma}_c$ [s^{-1}]	M_c	PEO 8 MDa	c/c^*	$\dot{\gamma}_c$[s^{-1}]	M_c
0.050 wt%	6	783 ± 39	9.9 ± 0.6	0.075 wt%	5	3100 ± 39	12.9 ± 0.8	0.188 wt%	5	1566 ± 39	18.3 ± 1.2
0.100 wt%	12	587 ± 39	7.5 ± 0.5	0.140 wt%	10	2741 ± 39	10.6 ± 0.7	0.375 wt%	10	1468 ± 39	6.3 ± 0.4
0.150 wt%	18	587 ± 39	6.9 ± 0.5	0.280 wt%	20	2741 ± 39	5.1 ± 0.3	0.750 wt%	20	1417 ± 39	4.8 ± 0.3
0.200 wt%	24	391 ± 39	3.7 ± 0.2	0.350 wt%	25	2349 ± 39	4.3 ± 0.3	0.938 wt%	25	1370 ± 39	4.5 ± 0.3
0.250 wt%	30	391 ± 39	4.3 ± 0.3	0.420 wt%	30	1566 ± 39	3.5 ± 0.2	1.250 wt%	30	1175 ± 39	3.6 ± 0.2

In our microfluidic experiment, we stepwise increase the flow rate and measure the corresponding pressure drop ΔP across the serpentine channel. This pressure drop can be converted to an apparent viscosity $\eta_{\text{app}}(\dot{\gamma}) = \tau(\dot{\gamma})/\dot{\gamma}$, where the shear stress in a serpentine channel is approximated by $\tau = (\Delta P\, H\, W)/[2L(W + H)]$ [33], while the shear rate is approximated by $\dot{\gamma} = 4Q/(\pi\, r^3)$ with the equivalent radius of $r = \sqrt{(W\,H)/\pi}$ [34]. It should be noted that this approximation of apparent shear rate $\dot{\gamma}$ is commonly recommended for aspect ratios $H/W \approx 1$. For smaller aspect ratios, Hartnett and Kostic [35] proposed a correction that also includes the Rabinowitch relation [36] to account for the shear thinning of polymer solution and nonparabolic velocity profile. However, we have confirmed that for the aspect ratio $H/W \approx 0.3$ used in this work, the apparent viscosity $\eta_{\text{app}}(\dot{\gamma})$ exhibits a good agreement with the bulk viscosity values (see the Supplemental Material [28]). Thus, the given approximation is reliable, and the corrections are not essential. Furthermore, it is important to note that we employ a "point-wise" method and assume that for a particular flow rate the corresponding apparent shear rate, viscosity, and relaxation time can be described by constant values.

Comparison of the apparent viscosity $\eta_{\text{app}}(\dot{\gamma})$ with the extrapolated bulk viscosity values $\eta(\dot{\gamma})$ in Fig. 1(a) reveals that above a critical shear rate, $\eta_{\text{app}}(\dot{\gamma})$ deviates from $\eta(\dot{\gamma})$. Figure 1(b) shows the reduced viscosity $\eta_r(\dot{\gamma}) = \eta_{\text{app}}(\dot{\gamma})/\eta(\dot{\gamma})$ as function of the shear rate $\dot{\gamma}$ for all studied polymer solutions. We identify the critical shear rate $\dot{\gamma}_{\text{crit}}$, listed in Table I, at the onset of instability when the reduced viscosity exceeds 1.15. For a given polymer type, $\dot{\gamma}_{\text{crit}}$ decreases only slightly with increasing concentration. These observations are in agreement with those of Howe *et al.* [30] who have reported that $\dot{\gamma}_{\text{crit}}$ is independent of polymer concentration above $c \approx 10 \times c^*$ and is inversely proportional to M_w^2.

The serpentine geometry with rectangular cross section requires the consideration of two Reynolds numbers to ensure that inertial forces are negligible throughout the geometry. For channel flows, the Reynolds number is usually defined as $\text{Re}_c = \varrho\, U\, r/\eta$ with the equivalent radius r as the characteristic length, whereas the average velocity is approximated by $U = Q/(W\,H)$. To account for centrifugal inertia in curvilinear flow, the radius of curvature of the serpentine channel r_i is used as the characteristic length and thus $\text{Re}_s = \varrho\, U\, r_i/\eta$. The maximum Reynolds numbers of our presented experiments are $\text{Re}_c \approx 1$ and $\text{Re}_s \approx 4$. Therefore, we can conclude that the contribution of inertia to the flow is negligible. To verify the purely elastic origin of the observed instability, we perform μPIV (LaVison) measurements by adding 0.05 wt% 1-μm red fluorescent particles (FluoroMax, Thermo Fisher) to the polymer solution. The particles are excited with a laser

wavelength of 532 nm. Double-frame images with short time differences (0.1 ms $< dt < 0.8$ ms), depending on the flow velocity, are recorded from the light emitted by the particles. Cross correlating these double frames, we obtain the velocity field in the serpentine channel. Figure 2(a) demonstrates the velocity fields at the middle half-bend of the serpentine channel averaged over 50 s for two different shear rates. Below the onset of purely elastic instability (left side), a laminar flow is observed whereas above the onset of purely elastic instability the velocity field (right side) deviates from a laminar flow. In the latter stage, unlike the laminar velocity profile, the maximum velocity is shifted toward the outer bend, i.e., toward the larger radius of curvature. The power spectra density of the local velocity fluctuations at the center of the middle half-bend of the serpentine channel [indicated by a (+) sign in Fig. 2(a)] are shown for four shear rates below and above the onset of flow instability in Figs. 2(b)–2(e) (further details in the Supplemental Material [28]). Indeed, the power-law decay $\sim f^{-\beta}$ with a characteristic exponent $\beta \approx 2$, in the range of 1 to 10 Hz at sufficiently high flow rates, is larger than the Kolmogorov scale of 5/3 associated with the inertial turbulence, suggesting that the mechanism of turbulence is not associated with inertia [37]. Similar exponents of β in the range of 2 to 3 have been reported in the literature for semidilute polymer solutions at highly elastic turbulent stage [23,38,39].

In order to scale the onset of the instability observed in our experiments, we require both a rheological description of the fluids as well as geometrical properties of the flow channel, as suggested by Eq. (1). The polymer solutions used in our experiments exhibit strongly shear-dependent viscosity as well as a nonquadratic first normal stress difference (data in the Supplemental Material [28]). The behavior of such polymer solutions is described based on the White-Metzner constitutive fluid model [9,19,25,40]. The basic concept of this model is to define a total stress tensor $\boldsymbol{\tau} = \boldsymbol{\tau_1} + \boldsymbol{\tau_2}$, and a total viscosity $\eta = \eta_1 + \eta_2$ that are related by the deformation rate tensor $\mathbf{D}$ [21,41,42]. The pure viscous component of the stress tensor $\boldsymbol{\tau_2}$ is defined as $\boldsymbol{\tau_2} = 2\,\eta_2\,\mathbf{D}$, where η_2 is the solvent viscosity. $\boldsymbol{\tau_1}$ is defined by

$$\boldsymbol{\tau_1} + [\eta(\dot{\gamma})/G_0]\overset{\triangledown}{\boldsymbol{\tau_1}} = 2\,\eta_1(\dot{\gamma})\,\mathbf{D}, \qquad (2)$$

where $\overset{\triangledown}{\boldsymbol{\tau_1}}$ is the upper convected time derivative. The shear rate is defined as $\dot{\gamma} = \sqrt{2\,tr(\mathbf{D}^2)}$ and the total shear stress is given by $\tau = 2\,\eta(\dot{\gamma})\,\dot{\gamma}$. The shear-dependent total viscosity of the polymer solution $\eta(\dot{\gamma})$ is described by the Carreau-Yasuda model [21,22]:

$$\eta(\dot{\gamma}) - \eta_\infty = (\eta_0 - \eta_\infty)[1 + (\Lambda\dot{\gamma})^a]^{\frac{n-1}{a}}. \qquad (3)$$
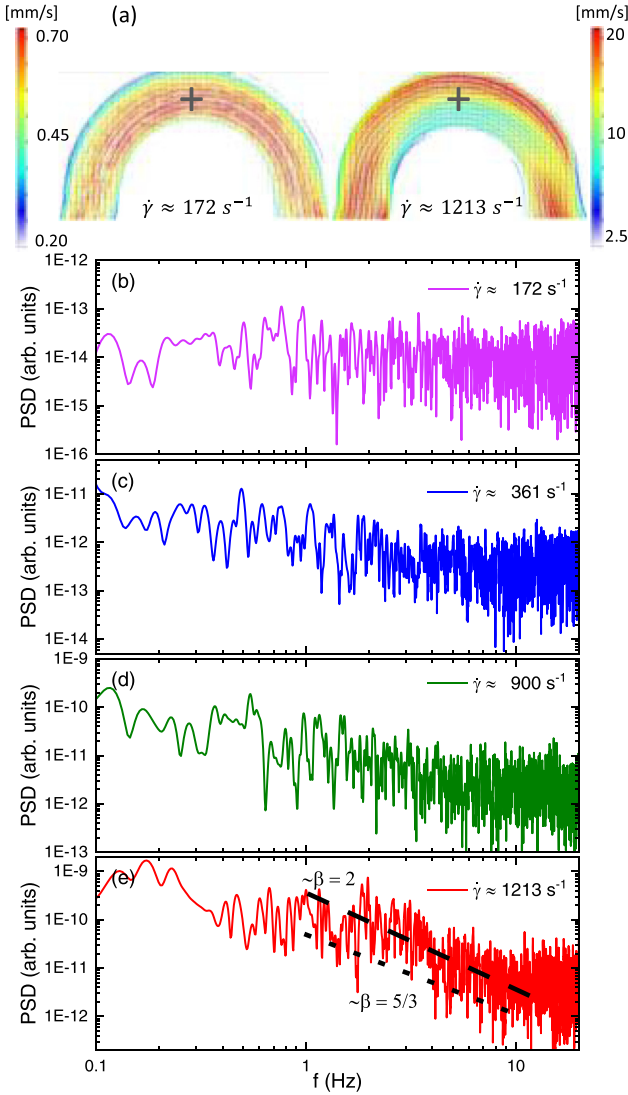
FIG. 2. (a) Time averaged velocity and streamlines obtained from μPIV for 0.200 wt% Flopaam 3630. [(b)–(e)] PSD analysis of velocity fluctuations at the center of serpentine channel indicated by a (+) sign in panel (a) for 0.200 wt% Flopaam 3630 at various shear rates below and above the critical shear rate. The dashed line indicates an exponential scaling with $\beta = 2$, and the dotted line represents the Kolmogorov scaling ($\beta = 5/3$) for comparison.

η_0 and η_∞ are the zero-shear viscosity and viscosity at infinite shear rates, Λ is a characteristic time, n is the power law exponent associated with the degree of shear thinning, and a is a transition control factor. In Eq. (2), the ratio of the shear-dependent viscosity $\eta(\dot{\gamma})$ to the shear modulus G_0 is equivalent to the relaxation time $\lambda(\dot{\gamma})$ [41,42]. The shear modulus G_0 is taken as the largest shear mode obtained from the generalized Maxwell model fitted to the small amplitude frequency sweep test results (data in the Supplemental Material [28]). This is a reasonable approximation of the shear modulus at relatively fast flows, corresponding to the range of shear rate at which purely elastic instability is observed in our experiments. To this end, $G(\omega) = G'(\omega) + iG''(\omega)$ is fitted to the frequency sweep test results with the least number of

relaxation elements required for a proper fit (typically $N = 4$), where $G'(\omega)$ and $G''(\omega)$ are given by Eqs. (4) and (5):

$$G'(\omega) = \sum_{k=1}^{N} G_k \frac{(\lambda_k \cdot \omega)^2}{1 + (\lambda_k \cdot \omega)^2}, \tag{4}$$

$$G''(\omega) = \sum_{k=1}^{N} G_k \frac{\lambda_k \cdot \omega}{1 + (\lambda_k \cdot \omega)^2}. \tag{5}$$

Shear modulus G in general describes the elastic component of a viscoelastic material under shear in the viscoelastic fluid model, and is defined as $G = \tau/\gamma_e$, where γ_e is the deformation of the elastic component.

In the following, we adapt the scaling of the nonlinear instability of the polymer solutions in the semidilute regime according to the White-Metzner fluid model. Since the relaxation time is shear dependent in the semidilute regime, the characteristic length nonlinearly increases with $\dot{\gamma}$ and is approximated by $l(\dot{\gamma}) = \lambda(\dot{\gamma}) U = (\eta(\dot{\gamma}) U)/G_0$. Streamlines of polymer flow in the serpentine channel obtained from μPIV generally follow the geometrical curvature of the channel [Fig. 2(a)]. Therefore, the minimum radius of the curved streamlines $\mathcal{R}$ in our experiments is approximated by the inner radius of the serpentine r_i. Thus, within the framework of the White-Metzner model, the threshold of the critical stress factor M_{crit} at the onset of purely elastic instability in Eq. (1) is approximated by

$$\sqrt{\frac{\eta(\dot{\gamma}) U}{G_0 \mathcal{R}} \frac{N_1(\dot{\gamma})}{2 \eta(\dot{\gamma}) \dot{\gamma}}} \geqslant M_{\text{crit}}. \tag{6}$$

The average velocity in the serpentine channel is expressed as $U = Q/(W H)$. Since we consider the shear rate $\dot{\gamma}$ to depend linearly on the flow rate Q and $\eta(\dot{\gamma})$ is canceled out, we approximate the critical stress factor M_{crit} by Eq. (7). As previously mentioned, according to our point-wise approach, we obtain the relevant rheological properties of the polymer solution corresponding to the apparent shear rate $\dot{\gamma}_{\text{crit}}$ at onset of purely elastic instability:

$$C \sqrt{\frac{N_1(\dot{\gamma}_{\text{crit}})}{G_0}} \approx M_{\text{crit}}. \tag{7}$$

Here, C is a geometry constant computed as $C = (W H)/(64\pi \mathcal{R}^2)$ for a serpentine channel with rectangular cross section. Equation (7) suggests that, for a given geometry, M_{crit} correlates solely with the ratio between the first normal stress difference at the onset of purely elastic instability, $N_1(\dot{\gamma}_{\text{crit}})$, and the shear modulus G_0 corresponding to the smallest relaxation mode. As explained earlier, the first normal stress difference is responsible for destabilizing the polymer flow in a curved geometry. On the other hand, the capacity of polymers to deform, i.e., their degree of elasticity is characterized by the value of the shear modulus. Therefore, the ratio of N_1 to G_0 is expected to be the decisive factor for the onset of instability.

Higher normalized concentration of a polymer solution correlates to higher degree of elasticity, and thus higher value of G_0. This means that the onset of purely elastic instability at higher normalized concentrations requires a larger N_1. Applying Eq. (7), we estimate M_{crit} for our experiments as
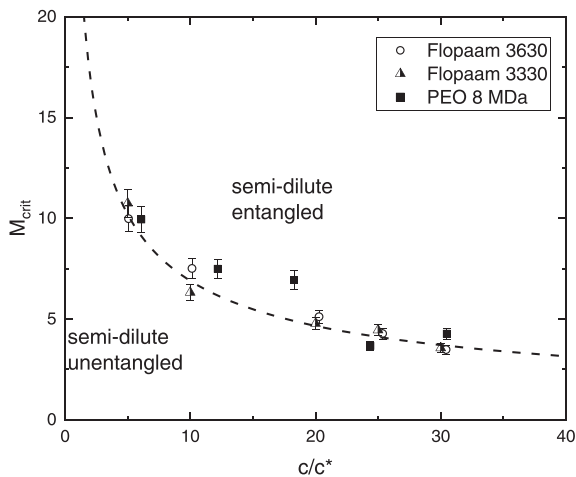
FIG. 3. Threshold value M_{crit} calculated from Eq. (7) as function of $c/c^\star$ for all utilized polymer solutions. The dashed curve is a power-law fit $M_{crit} = A\,(c/c^*)^{-b}$, where $A = (25.28 \pm 3.87)$ and $b = (0.56 \pm 0.05)$.

summarized in Table I and plotted in Fig. 3 as function of the normalized concentration c/c^* for all polymer solutions used in this work. In fact, the estimated values for M_{crit} collapse into a single master curve following a power law with an exponent of about -0.56. Qualitatively, this trend can be understood in view of the rheological differences observed in frequency sweep test between polymers below and above the entanglement concentration $10 \times c^*$. For unentangled polymer solutions, i.e., at $c/c^* < 10$ the loss modulus $G''(\omega)$ is always larger than the storage modulus $G'(\omega)$ for the entire range of frequencies [28]. This suggests that despite a significant elastic component in the fluid, viscous behavior

during flow is likely to dominate in this concentration regime, resulting in retardation of purely elastic instability. This means that purely elastic instability for $c/c^* < 10$ occurs at relatively higher shear rates, and thus M_{crit} is relatively larger. The above argument is consistent with the discussion of Morozov *et al.*, who suggest that the Pakdel and McKinley criterion should be considered as a suitable asymptotic rule that is accurate only at sufficiently large degree of elasticity [4]. Indeed, for concentrations $c/c^* > 10$, i.e., in the semidilute entangled regime where the elastic component is entirely dominant, M_{crit} approaches an asymptotic value of approximately 3.7.

In summary, we have studied the flow of semidilute polymer solutions in a geometrically well-defined serpentine channel and detected the occurrence of purely elastic instability via pressure measurement and μPIV. We have adapted the traditional scaling of the onset of purely elastic instability for polymer solutions in the semidilute regime by respecting the shear dependency of their rheological properties. As a consequence, our approach provides a realistic representation of the actual polymer behavior with respect to the flow by taking the rheological properties at the onset of instability into account. This, indeed, leads to a universal scaling as function of normalized concentration depending only on the ratio between the first normal stress difference $N_1(\dot{\gamma}_{crit})$ and the shear modulus G_0 regardless of the type of the polymer. As demonstrated, this scaling allows quantitative prediction of the onset of purely elastic instability for a wide range of high molecular weight polymer solutions.

[1] E. S. Shaqfeh, Annu. Rev. Fluid Mech. **28**, 129 (1996).

[2] A. Groisman and V. Steinberg, Nature (London) **405**, 53 (2000).

[3] T. Burghelea, E. Segre, and V. Steinberg, Phys. Rev. Lett. **96**, 214502 (2006).

[4] A. N. Morozov and W. van Saarloos, Phys. Rep. **447**, 112 (2007).

[5] V. Steinberg, Annu. Rev. Fluid Mech. **53**, 27 (2021).

[6] S. S. Datta, A. M. Ardekani, P. E. Arratia, A. N. Beris, I. Bischofberger, J. G. Eggers, J. E. López-Aguilar, S. M. Fielding, A. Frishman, M. D. Graham, J. S. Guasto, S. J. Haward, S. Hormozi, G. H. McKinley, R. J. Poole, A. Morozov, V. Shankar, E. S. G. Shaqfeh, A. Q. Shen, H. Stark *et al.*, arXiv:2108.09841.

[7] W. M. Abed, R. D. Whalley, D. J. Dennis, and R. J. Poole, J. Non-Newtonian Fluid Mech. **231**, 68 (2016).

[8] A. Groisman and V. Steinberg, Nature (London) **410**, 905 (2001).

[9] P. Shakeri, M. Jung, and R. Seemann, Phys. Fluids **33**, 113102 (2021).

[10] R. H. Ewoldt, M. T. Johnston, and L. M. Caretta, in *Complex Fluids in Biological Systems*, edited by S. Spagnolie, Biological

and Medical Physics, Biomedical Engineering (Springer, New York, NY, 2015), pp. 207–241.

[11] K. Hyun, M. Wilhelm, C. O. Klein, K. S. Cho, J. G. Nam, K. H. Ahn, S. J. Lee, R. H. Ewoldt, and G. H. McKinley, Prog. Polym. Sci. **36**, 1697 (2011).

[12] B. Meulenbroek, C. Storm, V. Bertola, C. Wagner, D. Bonn, and W. van Saarloos, Phys. Rev. Lett. **90**, 024502 (2003).

[13] P. Pakdel and G. H. McKinley, Phys. Rev. Lett. **77**, 2459 (1996).

[14] G. H. McKinley, P. Pakdel, and A. Öztekin, J. Non-Newtonian Fluid Mech. **67**, 19 (1996).

[15] S. J. Haward, G. H. McKinley, and A. Q. Shen, Sci. Rep. **6**, 33029 (2016).

[16] G. Yao, J. Zhao, H. Yang, M. A. Haruna, and D. Wen, Phys. Fluids **31**, 123106 (2019).

[17] A. Groisman and V. Steinberg, New J. Phys. **6**, 29 (2004).

[18] J. Zilz, R. J. Poole, M. A. Alves, D. Bartolo, B. Levaché, and A. Lindner, J. Fluid Mech. **712**, 203 (2012).

[19] A. Souliès, J. Aubril, C. Castelain, and T. Burghelea, Phys. Fluids **29**, 083102 (2017).

[20] L. Pan, A. Morozov, C. Wagner, and P. E. Arratia, Phys. Rev. Lett. **110**, 174502 (2013).

[21] R. B. Bird, C. F. Curtiss, R. C. Armstrong, and O. Hassager, *Dynamics of Polymeric Liquids*, 2nd ed., Kinetic Theory, Vol. 2 (Wiley-Interscience, New York, 1987).

[22] T. Burghelea and V. Bertola, *Transport Phenomena in Complex Fluids*, CISM International Centre for Mechanical Sciences (Springer, Cham, 2020), Vol. 598.

[23] Y. Jun and V. Steinberg, Phys. Rev. Lett. **102**, 124503 (2009).

[24] Y. Liu, Y. Jun, and V. Steinberg, J. Rheol. **53**, 1069 (2009).

[25] L. Casanellas, M. A. Alves, R. J. Poole, S. Lerouge, and A. Lindner, Soft Matter **12**, 6167 (2016).

[26] M. Jung, M. Brinkmann, R. Seemann, T. Hiller, M. Sanchez de La Lama, and S. Herminghaus, Phys. Rev. Fluids **1**, 074202 (2016).

[27] A. V. Dobrynin, R. H. Colby, and M. Rubinstein, Macromolecules **28**, 1859 (1995).

[28] See Supplemental Material at http://link.aps.org/supplemental/10.1103/PhysRevE.105.L052501 for rheological characterisation of the utilized polymer solutions and additional information to the μPIV measurements.

[29] T. G. Mezger, *The Rheology Handbook: For Users of Rotational and Oscillatory Rheometers* (Vincentz Network, Hannover, 2006).

[30] A. M. Howe, A. Clarke, and D. Giernalczyk, Soft Matter **11**, 6419 (2015).

[31] D. Rivero, L. M. Gouveia, A. J. Müller, and A. E. Sáez, Rheol. Acta **51**, 13 (2012).

[32] O. Arnolds, H. Buggisch, D. Sachsenheimer, and N. Willenbacher, Rheol. Acta **49**, 1207 (2010).

[33] A. Machado, H. Bodiguel, J. Beaumont, G. Clisson, and A. Colin, Biomicrofluidics **10**, 043507 (2016).

[34] Y. Son, Polymer **48**, 632 (2007).

[35] J. P. Hartnett and M. Kostic, in *Advances in Heat Transfer* (Academic Press, New York, 1989), Vol. 19, pp. 247–356.

[36] A. Collyer and D. Clegg, *Rheological Measurements* (Springer, Berlin, 1998).

[37] A. N. Kolmogorov, Proc. R. Soc. London, Ser. A **434**, 15 (1991).

[38] J. Beaumont, H. Bodiguel, and A. Colin, Soft Matter **9**, 10174 (2013).

[39] D. Kawale, E. Marques, P. L. Zitha, M. T. Kreutzer, W. R. Rossen, and P. E. Boukany, Soft Matter **13**, 765 (2017).

[40] H. Bodiguel, J. Beaumont, A. Machado, L. Martinie, H. Kellay, and A. Colin, Phys. Rev. Lett. **114**, 028302 (2015).

[41] J. L. White and A. B. Metzner, J. Appl. Polym. Sci. **7**, 1867 (1963).

[42] H.-C. Tseng, Phys. Fluids **33**, 057115 (2021).

Scaling purely elastic instability of strongly shear thinning polymer solutions
Supplemental material

Pegah Shakeri,* Michael Jung,† and Ralf Seemann

Experimental Physics, Saarland University, 66123 Saarbrücken, Germany and
Max Planck Institute for Dynamics and Self-Organization, 37077 Göttingen, Germany

(Dated: May 9, 2022)

Fitting parameter Carreau-Yasuda model for viscosity

Figure S.1 shows bulk viscosity measurements of all utilized polymer solutions obtained from steady shear step tests in stress-controlled mode using a HAAKE MARS 40 rheometer and a 60 mm cone plate geometry with an angle of 1°. To avoid air bubbles when placing the respective fluids between the cone and plate, we place a small droplet at the tip of the cone to create a wetting film when bringing the cone and plate in contact. The temperature is set to $T = (20 \pm 0.2)°C$ for all measurements to match the lab temperature where the microfluidic experiments were conducted. The data are fitted using the Carreau-Yasuda model (Eq. (3) of the main text). The fitting parameter are summarized in Table S.I.
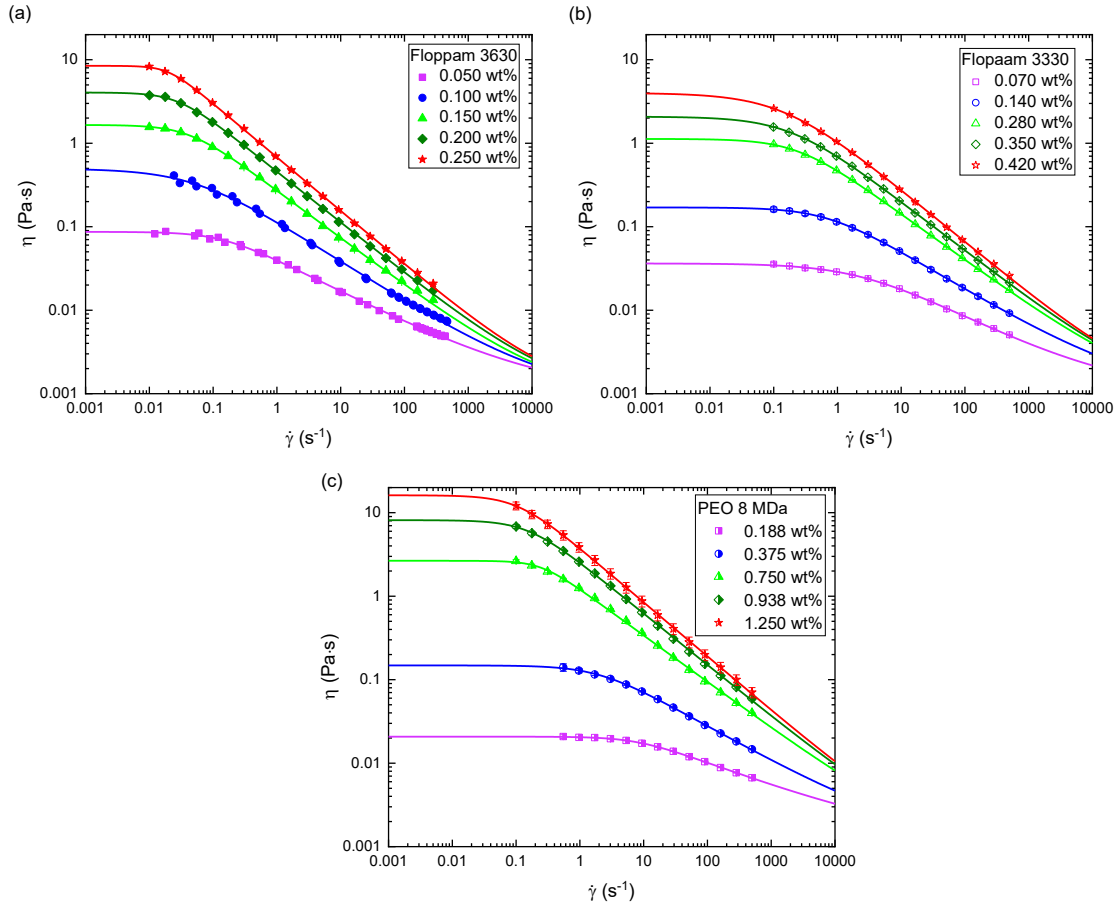

FIG. S.1: Bulk viscosity $\eta(\dot{\gamma})$ for different concentrations of (a) Flopaam 3630, (b) Flopaam 3330, and (c) PEO 8 MDa. Lines are fits to the Carreau–Yasuda model (Eq. (3) in the main text).

TABLE S.I: Fitting parameters of Carreau–Yasuda model for viscosity: η_0 is the zero-shear viscosity; Λ is a characteristic time; a is a transition control factor; and n is the power law exponent associated with the degree of shear thinning. The viscosity at infinite shear rates was set to the solvent viscosity $\eta_s = 1 \cdot 10^{-3}\,\mathrm{Pa\,s}$.

Flopaam 3630	η_0 [Pa.s]	Λ [s]	a	n
0.050 wt%	0.087 ± 0.001	7.14 ± 0.89	1.20 ± 0.17	0.60 ± 0.02
0.100 wt%	0.496 ± 0.080	18.58 ± 3.70	0.79 ± 0.24	0.51 ± 0.02
0.150 wt%	1.656 ± 0.025	23.84 ± 0.74	1.39 ± 0.09	0.43 ± 0.01
0.200 wt%	4.050 ± 0.095	35.83 ± 1.32	1.64 ± 0.15	0.39 ± 0.01
0.250 wt%	8.459 ± 0.897	50.52 ± 8.01	2.47 ± 0.92	0.36 ± 0.01
Flopaam 3330	η_0 [Pa.s]	Λ [s]	a	n
0.075 wt%	0.036 ± 0.001	0.42 ± 0.03	0.72 ± 0.04	0.59 ± 0.01
0.140 wt%	0.170 ± 0.003	1.40 ± 0.04	1.027 ± 0.05	0.54 ± 0.01
0.280 wt%	1.127 ± 0.0491	4.15 ± 0.27	1.10 ± 0.09	0.44 ± 0.01
0.350 wt%	2.081 ± 0.016	5.33 ± 0.20	0.92 ± 0.03	0.41 ± 0.01
0.420 wt%	3.998 ± 0.013	6.88 ± 0.19	0.81 ± 0.04	0.37 ± 0.01
PEO 8MDa	η_0 [Pa.s]	Λ [s]	a	n
0.188 wt%	0.021 ± 0.001	0.12 ± 0.01	1.25 ± 0.07	0.70 ± 0.01
0.375 wt%	0.148 ± 0.010	0.50 ± 0.06	1.31 ± 0.17	0.57 ± 0.01
0.750 wt%	2.655 ± 0.485	4.02 ± 1.26	1.98 ± 1.23	0.44 ± 0.01
0.938 wt%	8.139 ± 1.087	6.46 ± 1.22	1.41 ± 0.35	0.38 ± 0.01
1.250 wt%	16.166 ± 2.366	9.42 ± 1.89	1.42 ± 0.33	0.35 ± 0.01

Figure S.2 shows the power-law fits of the zero shear viscosity as function of concentration for the three polymer types. Below the overlap concentration c^*, the polymer solutions are in the dilute regime. For concentrations $c^* < c < 10 \times c^*$, the polymer solutions are in the semi-dilute unentangled regime, while for concentrations $c > 10 \times c^*$, the polymer solutions are entangled. The power-law exponents in Fig. S.2 are in agreement with literature values for polyelectrolytes in case of the two HPAM-solutions and neutral polymer in case of PEO [1–4].
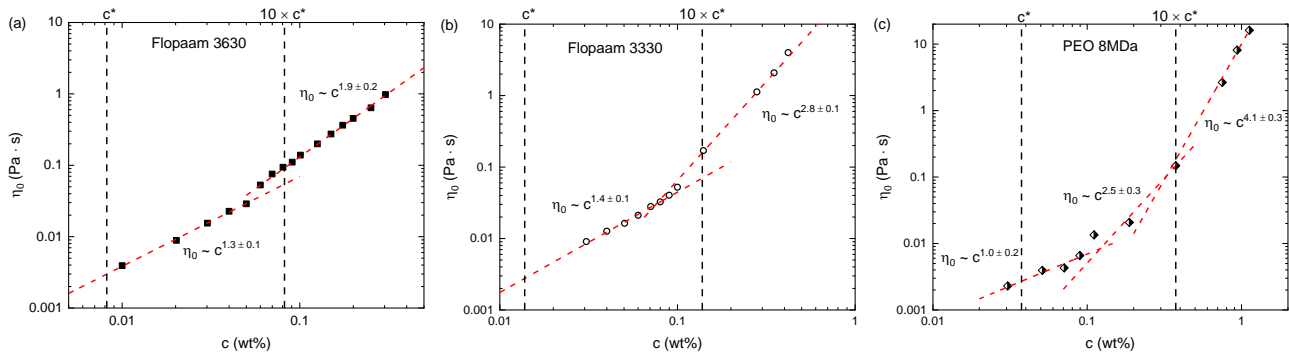

FIG. S.2: Zero-shear viscosity η_0 as function of concentrations of (a) Flopaam 3630, (b) Flopaam 3330, and (c) PEO 8 MDa. Dashed red lines are extrapolated power-law fits. Dashed vertical lines indicate the overlap concentration c^* and the entanglement concentration $10 \times c^*$.

First normal stress difference $N_1(\dot{\gamma})$

The values of the first normal stress difference N_1 and the corresponding fitting parameter are shown in Fig. S.3 and Table S.II. To account for drift due to relaxation of the solution as well as the force sensor in the rheometer, the measurement geometry remains at rest for 300 s, followed by rotation at a constant shear rate for also 300 s with a ramp from $\dot{\gamma} = 60\,s^{-1}$ to $\dot{\gamma} = 1000\,s^{-1}$. The polymer solution in the measuring geometry was surrounded by mineral oil to avoid inertia instabilities at the edges at higher rotation rates. The normal force values measured by the rheometer were corrected for inertia, $N_{inertia} = -0.075\,\pi\,\varrho\,\Omega^2\,R^4$, and drift and converted to the first normal stress difference using $N_{1,corr} = (2F_n)/(\pi R^2)$ in which F_n is the normal force measured by the rheometer. Ω, ϱ and R are respectively angular rotation, density of the polymer solution, and the radius of the measuring geometry.
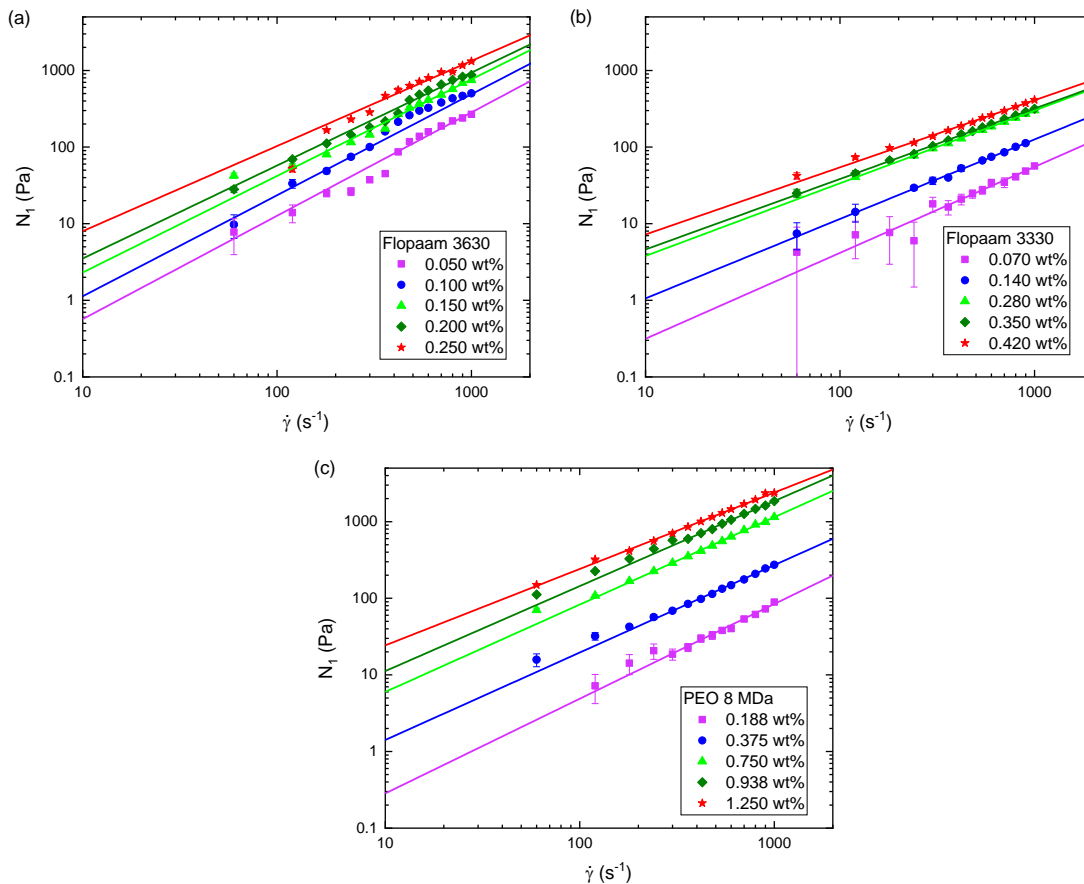
FIG. S.3: First normal stress difference $N_1(\dot{\gamma})$ for different concentrations of (a) Flopaam 3630, (b) Flopaam 3330, and (c) PEO 8 MDa. Lines are extrapolated power-law fits.

TABLE S.II: Fitting parameters of the power-law fit $A \cdot \dot{\gamma}^b$ of the first normal stress difference $N_1(\dot{\gamma})$

Flopaam 3630	A	b	Flopaam 3330	A	b	PEO 8MDa	A	b
0.050 wt%	0.025 ± 0.015	1.35 ± 0.09	0.075 wt%	0.024 ± 0.010	1.12 ± 0.01	0.188 wt%	0.016 ± 0.007	1.24 ± 0.06
0.100 wt%	0.054 ± 0.022	1.31 ± 0.07	0.140 wt%	0.097 ± 0.013	1.04 ± 0.02	0.375 wt%	0.102 ± 0.015	1.14 ± 0.02
0.150 wt%	0.126 ± 0.034	1.26 ± 0.04	0.280 wt%	0.427 ± 0.021	0.95 ± 0.01	0.750 wt%	0.434 ± 0.054	1.14 ± 0.02
0.200 wt%	0.215 ± 0.095	1.21 ± 0.07	0.350 wt%	0.555 ± 0.031	0.92 ± 0.01	0.938 wt%	0.873 ± 0.092	1.11 ± 0.02
0.250 wt%	0.619 ± 0.245	1.11 ± 0.06	0.420 wt%	0.963 ± 0.083	0.88 ± 0.01	1.250 wt%	2.445 ± 0.166	0.99 ± 0.01

Storage $G'(\omega)$ and loss modulus $G''(\omega)$

The storage modulus $G'(\omega)$ and the loss modulus $G''(\omega)$ are determined by small amplitude frequency sweep tests (SAOS) performed in the stress-controlled mode and are presented in Fig. S.4. The stress amplitude was set to 0.1 Pa, safely in the linear viscoelastic range of all solutions. The data are fitted to a multimode Maxwell model, i.e., Eq.(4) and (5) of the manuscript. The number of modes N was chosen to assure the best possible simultaneous fit to $G'(\omega)$ and $G''(\omega)$. Typically N was set to four, besides the solutions in the semi-dilute unentangled regime, where a smaller number of modes was sufficient to proper fit the data. The full list of fitting parameter is given in Table S.III.

For the utilized polymer solutions, the longest relaxation time is in the order of 10^0 s to 10^1 s, which is 1-2 orders larger than the typical traveling time of the polymers passing a serpentine bend. Therefore, we believe the smallest relaxation mode, i.e., the largest mode of the shear modulus in Table S.III to be relevant in our work. Consequently, the used G_0 in the manuscript corresponds to the largest G-value (G_1 in Table S.III) that typically corresponds to the mode with the smallest relaxation time. It should be noted that the frequency range used for the fit was carefully adjusted based on Lissajous curves of stress and strain from the raw measurement data to ensure that $G'(\omega)$ and $G''(\omega)$ correspond to the linear viscoelasticity range in which the Maxwell model is valid.
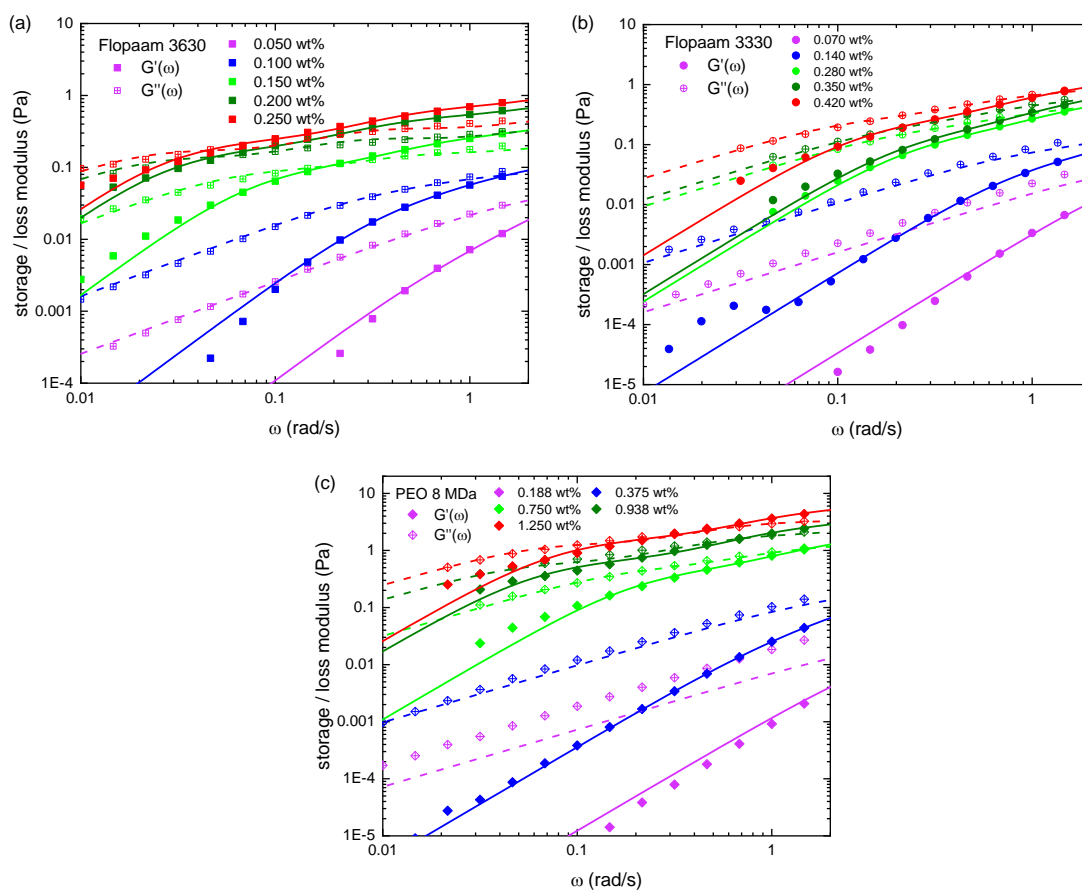

FIG. S.4: Frequency sweep test for different concentrations of (a) Flopaam 3630, (b) Flopaam 3330, and (c) PEO 8 MDa. Filled symbols represent the storage modulus $G'(\omega)$ and open symbols represent the loss modulus $G''(\omega)$. Lines are fits to the multimode Maxwell model with $N = 4$ (Eqs. (4) and (5) in the main text).

TABLE S.III: Fitting parameters of the simultaneous fit of the Maxwell model to $G'(\omega)$ and $G''(\omega)$ according to Eqs. (4) and (5) in the main text. G_k is the shear modulus corresponding to the relaxation time λ_k at the k-te mode.

Flopaam 3630	G_1 [Pa]	G_2 [Pa]	G_3 [Pa]	G_4 [Pa]	λ_1 [s]	λ_2 [s]	λ_3 [s]	λ_4 [s]
0.050 wt%	0.094 ± 0.003	0.055 ± 0.003	–	–	0.053 ± 0.004	0.345 ± 0.020	–	–
0.100 wt%	0.163 ± 0.027	0.064 ± 0.005	0.061 ± 0.010	0.034 ± 0.007	0.144 ± 0.018	0.774 ± 0.109	0.044 ± 0.034	2.512 ± 0.269
0.150 wt%	0.307 ± 0.018	0.256 ± 0.020	0.182 ± 0.019	0.099 ± 0.015	0.041 ± 0.006	0.268 ± 0.020	1.778 ± 0.337	12.834 ± 2.164
0.200 wt%	0.846 ± 0.036	0.448 ± 0.022	0.342 ± 0.020	0.176 ± 0.016	0.035 ± 0.003	0.352 ± 0.035	3.310 ± 0.385	35.314 ± 4.834
0.250 wt%	0.971 ± 0.031	0.662 ± 0.034	0.470 ± 0.031	0.232 ± 0.022	0.031 ± 0.002	0.287 ± 0.030	2.706 ± 0.339	35.369 ± 5.250
Flopaam 3330	G_1 [Pa]	G_2 [Pa]	G_3 [Pa]	G_4 [Pa]	λ_1 [s]	λ_2 [s]	λ_3 [s]	λ_4 [s]
0.075 wt%	0.075 ± 0.002	0.049 ± 0.002	–	–	0.048 ± 0.002	0.256 ± 0.009	–	–
0.140 wt%	0.241 ± 0.111	0.116 ± 0.079	0.049 ± 0.073	–	0.081 ± 0.026	0.279 ± 0.323	1.130 ± 1.099	–
0.280 wt%	1.127 ± 0.169	0.672 ± 0.034	0.374 ± 0.022	0.135 ± 0.014	0.025 ± 0.005	0.143 ± 0.012	0.702 ± 0.062	4.062 ± 0.364
0.350 wt%	1.442 ± 0.113	0.905 ± 0.047	0.489 ± 0.031	0.151 ± 0.019	0.028 ± 0.004	0.152 ± 0.013	0.744 ± 0.070	4.410 ± 0.492
0.420 wt%	1.884 ± 0.077	1.216 ± 0.065	0.666 ± 0.047	0.228 ± 0.024	0.036 ± 0.004	0.192 ± 0.018	1.017 ± 0.105	7.782 ± 0.906
PEO 8MDa	G_1 [Pa]	G_2 [Pa]	G_3 [Pa]	G_4 [Pa]	λ_1 [s]	λ_2 [s]	λ_3 [s]	λ_4 [s]
0.188 wt%	0.048 ± 0.013	0.005 ± 0.018	–	–	0.116 ± 0.040	0.351 ± 0.618	–	–
0.375 wt%	0.397 ± 0.005	0.180 ± 0.006	0.071 ± 0.005	0.009 ± 0.008	0.054 ± 0.001	0.171 ± 0.009	0.487 ± 0.064	1.187 ± 0.339
0.750 wt%	2.819 ± 0.085	1.984 ± 0.087	1.204 ± 0.076	0.432 ± 0.048	$0,021 \pm 0.001$	0.111 ± 0.009	0.639 ± 0.066	4.912 ± 0.608
0.938 wt%	5.008 ± 0.164	3.601 ± 0.169	2.141 ± 0.137	0.658 ± 0.073	0.026 ± 0.001	0.166 ± 0.015	1.221 ± 0.129	16.148 ± 2.863
1.250 wt%	8.389 ± 0.345	5.882 ± 0.293	3.943 ± 0.236	1.561 ± 0.147	0.016 ± 0.002	0.127 ± 0.012	1.031 ± 0.111	12.858 ± 1.858

Approximation of shear rate $\dot{\gamma}$

As stated in the manuscript, we use the relation $\dot{\gamma} = 4Q/(\pi \, r^3)$ with the equivalent radius of $r = \sqrt{(W \, H)/\pi}$ to approximate the shear rate in our serpentine channels with rectangular cross section ($W \approx 125 \, \mu$m, $H \approx 36 \, \mu$m) for an applied flow rate Q. Strictly speaking, this approximation is developed for Newtonian fluids and aspect ratios $H/W \approx 1$, and must be modified by a geometry factor for other aspect ratios. For non-Newtonian, in particular shear-thinning fluids, this expression must also be corrected using the Rabinowitsch correction [5] to account for the non-parabolic flow profile. Here we follow a method proposed by Son et al.[6], and show that shear rates obtained with these corrections at the aspect ratio $H/W \approx 0.3$, employed in our work, deviate less than 10% from our estimation of $\dot{\gamma}$. Son et al. combined an estimation of the shear rate for arbitrary aspect ratios proposed by Hartnett and Kostic [7] with the Rabinowitsch relation to correct for the flow profile of shear-thinning fluids. The procedure is as follows:

(a) Calculate the wall shear stress τ_w from the measured pressure difference ΔP:

$$\tau_W = (\frac{\Delta P}{2L})(\frac{W \, H}{W + H})$$

(b) Calculate the Newtonian approximation of the shear rate

$$\dot{\gamma}_a = (\frac{6Q}{W \, H^2})(1 + \frac{H}{W}) \, f^\star \, (\frac{H}{W})$$

, where $f^\star$ is a geometrical constant for rectangular ducts provided in Ref. [7].

(c) Calculate the power-law index n as slope of the curve $log(\tau_W)$ vs $log(\dot{\gamma}_a)$.

(d) Calculate the corrected wall shear rate for a rectangular duct for non-parabolic flow $\dot{\gamma}_W$:

$$\dot{\gamma}_W = \dot{\gamma}_a(\frac{2}{3})(\frac{b^\star}{f^\star} + \frac{a^\star}{f^\star}\frac{1}{n})$$

, where $a^\star$, $b^\star$, and $f^\star$ are geometrical constants for rectangular ducts provided in Ref. [7].

In Figure S.5, we show a comparison of the apparent viscosity in our serpentine channel for corrected and non-corrected approximation of the shear rate and the bulk viscosity data. We determine a discrepancy of less than 10% between the corrected and non-corrected shear rates.
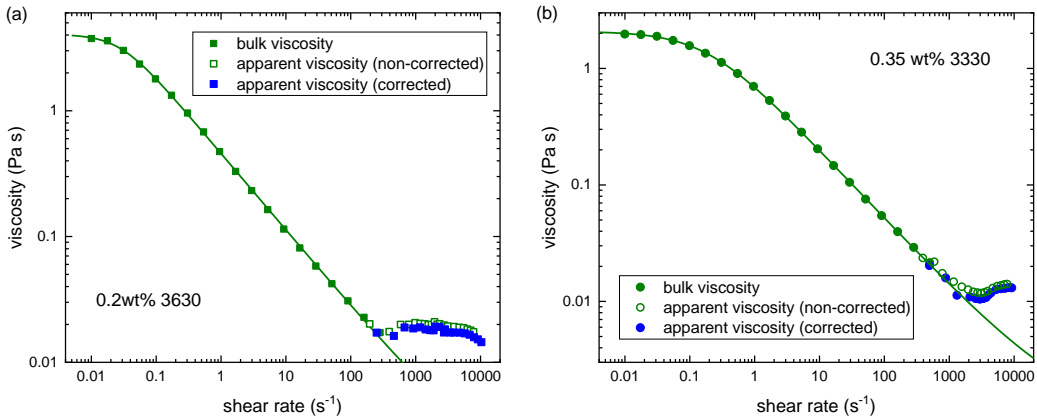

FIG. S.5: Comparison of bulk rheology data (full green symbols) for (a) $0.2 \, w\%$ Flopaam 3630 and (b) $0.35 \, w\%$ Flopaam 3330 with the apparent viscosity as used in the manuscript (open green symbols), and the apparent viscosity using correction for shear-thinning and non-parabolic flow profile (full blue symbols). Lines are fits of the Carreau-Yasuda model to the bulk rheology data.

Particle image velocimetry (μPIV)

Particle image velocimetry is performed using a μPIV setup (LaVision, Zeiss Axio Observer Z1). The polymer solutions are loaded with $1\,\mu$m red fluorescent particles (FluoroMax, Thermo Fisher) and illuminated by green laser wavelength of 532 nm. For each flow rate, a sequence of double-image is recorded using sCMOS camera (Imager CLHS, PCO) at a frequency of 42 Hz for a duration of 50 seconds. The flow velocity is estimated from the images using Davis 10 software (LaVision). The time averaged velocity $\bar{U}$ for four different flow rates at the central bend of the serpentine channel is shown on the left side of Fig. S.6. The velocity fluctuations $U'(t) = U(t) - \bar{U}$ at the center of the channel, indicated by (+) signs on the left panel, is shown on the right side of Fig. S.6.
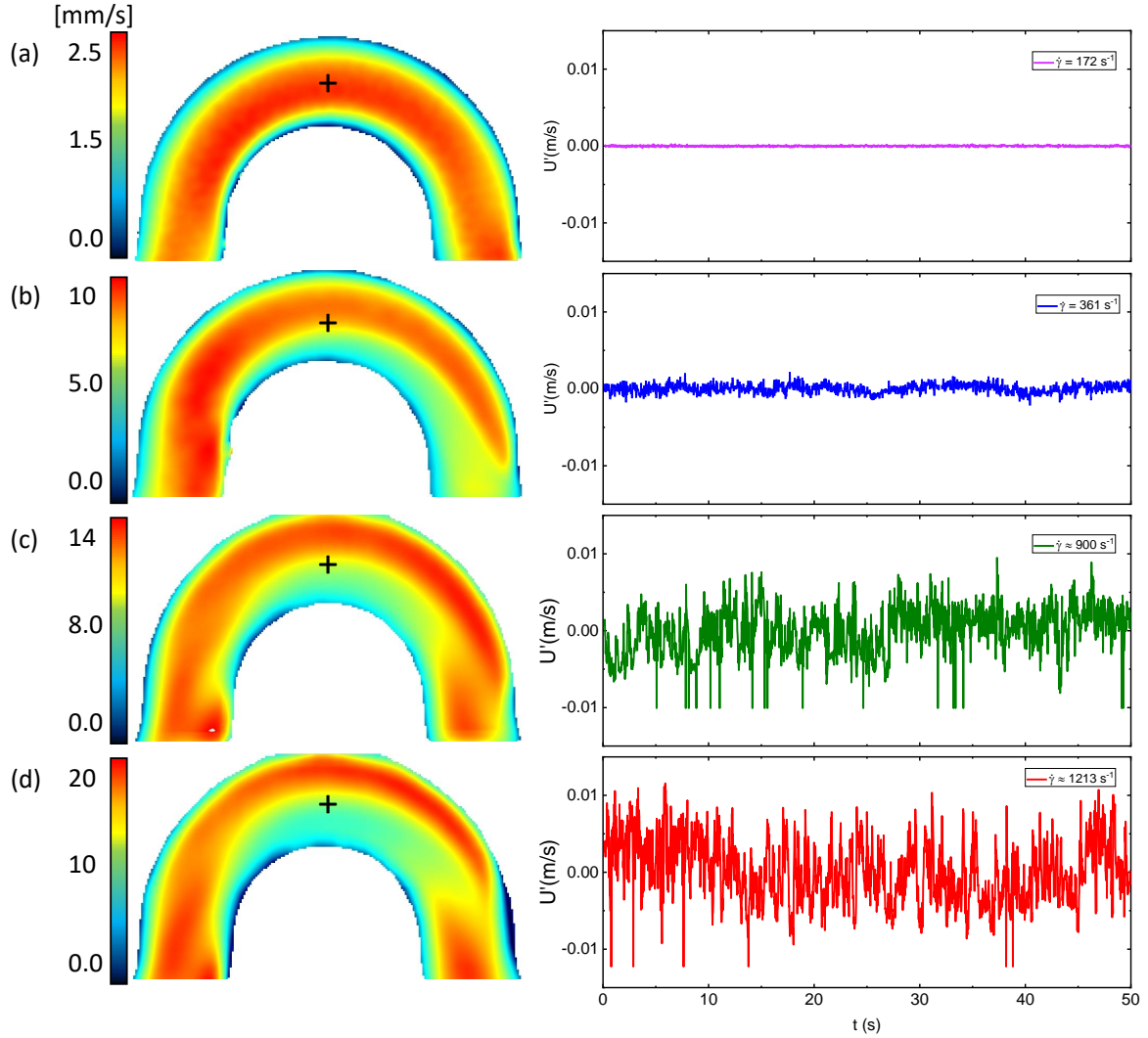
FIG. S.6: (a) - (d) Velocity field captured by μPIV for various shear rates and corresponding velocity fluctuations at the center of the middle curve as function of time t.

[1] A. V. Dobrynin, R. H. Colby, and M. Rubinstein, Macromolecules **28**, 1859–1871 (1995).

[2] A. M. Howe, A. Clarke, and D. Giernalczyk, Soft Matter **11**, 6419–6431 (2015).

[3] L. Casanellas, M. A. Alves, R. J. Poole, S. Lerouge, and A. Lindner, Soft Matter **12**, 6167–6175 (2016).

[4] O. Arnolds, H. Buggisch, D. Sachsenheimer, and N. Willenbacher, Rheologica acta **49**, 1207 (2010).

[5] A. Collyer and D. Clegg, *Rheological measurements* (Springer, 1998).

[6] Y. Son, Polymer **48**, 632–637 (2007).

[7] J. P. Hartnett and M. Kostic (Elsevier, 1989) pp. 247–356.

Characterizing purely elastic turbulent flow of a semi-dilute entangled polymer solution in a serpentine channel

Authors: P. Shakeri[1,2], M. Jung[1,2], and R. Seemann[1,2]

[1]Experimental Physics, Saarland University, 66123 Saarbrücken,Germany

[2]Max Planck Institute for Dynamics and Self-Organization, 37077 Göttingen, Germany

Author contributions:

Fabrication of microfluidic devices, preparation of working fluids, and rheological characterization were conducted by P. Shakeri. Experiments were designed, performed, and analyzed by P. Shakeri. The article was written by P. Shakeri, M.Jung, and R. Seemann. The research was directed by R. Seemann.

Abstract:

Polymer solutions in the semi-dilute regime are of considerable industrial importance. The complex rheological properties of such highly viscoelastic fluids and the complexity of their flow characteristics, especially in curved geometries, necessitate a thorough experimental characterization of the dynamics of such fluid flows. We apply statistical, spectral, and structural analyses to the experimentally obtained velocity fields of a semi-dilute entangled polymer solution in a serpentine channel to fully characterize the corresponding flow. Our results show that at high Weissenberg numbers, yet vanishing Reynolds numbers, the flow resistance is significantly increased, which indicates the emergence of a purely elastic turbulent flow. Spatial flow observations and statistical analysis of temporal flow features show that this purely elastic turbulent flow is non-homogeneous, non-Gaussian, and anisotropic at all scales. Moreover, spectral analysis indicates that compared to elastic turbulence in the dilute regime, the range of present scales of the excited fluctuations is narrower. This is partly due to the entanglement of the polymers in this concentration regime, which restricts their movement, and partly due to the mixed flow type inherent in the serpentine geometry, which can reduce the extent of polymer stretching and, thus, reduce the intensity of the fluctuations in the flow. Furthermore, proper orthogonal decomposition analysis is applied to directly ex-

tract the turbulent flow structure and reveals the activity of the counterrotating vortices associated with secondary flow, which significantly contribute to the total kinetic energy of the flow.

Pegah Shakeri, Michael Jung and Ralf Seemann

ARTICLES YOU MAY BE INTERESTED IN

Effect of elastic instability on mobilization of capillary entrapments
Physics of Fluids **33**, 113102 (2021); https://doi.org/10.1063/5.0071556

Viscoelastic effects of immiscible liquid–liquid displacement in microchannels with bends
Physics of Fluids **34**, 073111 (2022); https://doi.org/10.1063/5.0091501

Prediction of polymer extension, drag reduction, and vortex interaction in direct numerical simulation of turbulent channel flows
Physics of Fluids **34**, 073318 (2022); https://doi.org/10.1063/5.0094978

Characterizing purely elastic turbulent flow of a semi-dilute entangled polymer solution in a serpentine channel

View Online   Export Citation   CrossMark

Pegah Shakeri,[1,2,a] (iD) Michael Jung,[1,2] (iD) and Ralf Seemann[1,2] (iD)

AFFILIATIONS

[1]Experimental Physics & Center of Biophysics, Saarland University, 66123 Saarbrücken, Germany
[2]Max Planck Institute for Dynamics and Self-Organization, 37077 Göttingen, Germany

[a]Author to whom correspondence should be addressed: pegah.shakeri@physik.uni-saarland.de

ABSTRACT

Polymer solutions in the semi-dilute regime are of considerable industrial importance. The complex rheological properties of such highly viscoelastic fluids and the complexity of their flow characteristics, especially in curved geometries, necessitate a thorough experimental characterization of the dynamics of such fluid flows. We apply statistical, spectral, and structural analyses to the experimentally obtained velocity fields of a semi-dilute entangled polymer solution in a serpentine channel to fully characterize the corresponding flow. Our results show that at high Weissenberg numbers, yet vanishing Reynolds numbers, the flow resistance is significantly increased, which indicates the emergence of a purely elastic turbulent flow. Spatial flow observations and statistical analysis of temporal flow features show that this purely elastic turbulent flow is non-homogeneous, non-Gaussian, and anisotropic at all scales. Moreover, spectral analysis indicates that compared to elastic turbulence in the dilute regime, the range of present scales of the excited fluctuations is narrower. This is partly due to the entanglement of the polymers in this concentration regime, which restricts their movement, and partly due to the mixed flow type inherent in the serpentine geometry, which can reduce the extent of polymer stretching and, thus, reduce the intensity of the fluctuations in the flow. Furthermore, proper orthogonal decomposition analysis is applied to directly extract the turbulent flow structure and reveals the activity of the counter-rotating vortices associated with secondary flow, which significantly contribute to the total kinetic energy of the flow.

I. INTRODUCTION

Polymer solutions exhibit mechanical properties that are intermediate between viscous liquids and elastic solids due to the elasticity of the polymer molecules and their stretching and relaxation during flow.[1] Such viscoelastic fluids are ubiquitous in a broad range of industrial applications[2–4] and biological settings.[5–8] One of the unique features of viscoelastic fluid flows, particularly in curved flow pathways, is the appearance of an unstable state driven by nonlinear elastic stresses, even in the absence of inertial forces.[9] This phenomenon, known as purely elastic instability or purely elastic turbulence, was first discovered by Giesekus in the Taylor-Couette flow of dilute polymer solutions.[10] The occurrence of purely elastic instability can be beneficial for several industrial applications. For example, the agitation caused by the unstable flow improves mixing capacity and heat transfer.[11,12] Improving the efficiency of capillary entrapment displacement in porous media has also been proven to be related to the occurrence of

purely elastic instability during polymer flooding.[13] However, in multiple processes in the food and cosmetics industries[14,15] as well as polymer extrusion,[4] the occurrence of purely elastic instability is rather undesirable. Therefore, the importance of this phenomenon necessitates an understanding of the origin and characterization of purely elastic turbulent flows.

The origin of the purely elastic instability is related to the behavior of polymer molecules.[16–18] In fact, the counter-reaction of the elastic stress loading (deformation) and unloading (relaxation) of the polymers is reflected in the flow, resembling the characteristics of turbulent flow, such as non-parallel streamlines and chaotic fluctuation of flow properties, accompanied by a significant increase in flow resistance.[19] The polymer behavior and, thus, the induced unstable flow features strongly depend on the polymer properties such as molecular weight, size, and concentration, as well as the flow type.[20–23] In the dilute regime below the overlap concentration, the individual

polymer coils are far apart from each other and, hence, do not interact. The behavior of such polymer solutions is governed solely by the dynamics of a single polymer and its interaction with solvent molecules.[1] Although a considerable amount of research has been devoted to the numerical and experimental study of the purely elastic turbulence of dilute polymer solutions,[17,24–35] there are far fewer studies focusing on the semi-dilute entangled polymer solutions,[17,36–38] despite their industrial importance. The polymer behavior above the overlap concentration in the semi-dilute entangled regime is more complicated, as polymers strongly interact with each other and even become significantly entangled. Numerical modeling of such fluid flows in a highly turbulent state is extremely challenging due to the chaotic nature of the expected solution caused by the nonlinear rheological properties and the corresponding flow equations.[39,40] Therefore, understanding and characterizing the purely elastic instability in the semi-dilute concentration regime through experimental research are not only valuable, but essential.

Despite the highly nonlinear and random nature of elastic turbulent flows in general, they are known to be systematic and reproducible on a statistical level.[41–43] A precise and reliable statistical representation of elastic turbulence, however, requires an extensive description of temporal and spatial fluctuations of flow properties. Improvements in particle image velocimetry (PIV), both in hardware and data processing algorithms that allow high temporal and spatial resolution data acquisition, make this technique one of the most attractive and successful tools in turbulent fluid flow dynamics.[44–46] The acquired time-resolved velocity fields provide in-depth information on the turbulent flow, which can be further processed using various statistical and numerical methods to extract the stochastic turbulent features and structure. A number of studies restricted to dilute polymer solutions have already used the PIV technique to characterize the corresponding purely elastic turbulence in various geometries with curved pathways.[18,32,47,48]

Most statistical analyses of elastic turbulence are based on the flow fluctuations at fixed points either in time or in space and rely on the Taylor frozen turbulence hypothesis to relate the temporal and spatial characteristics of elastic turbulence.[18,49,50] The Taylor hypothesis suggests that in homogeneous flows, turbulent fluctuations travel downstream without changing their properties.[51] However, the global validity of this hypothesis has been experimentally and numerically questioned in the elastic turbulence of dilute polymer solutions.[27,50] To avoid the Taylor hypothesis and directly extract the spatial features and structure of turbulent flow, the proper orthogonal decomposition (POD) method was developed in the field of fluid dynamics.[52] POD is a robust order reduction method for decomposing the fluctuations in a flow field into a set of energy modes to represent them as a set of basis functions. As a result, the highly complex problem can be reduced to a simpler one by considering only the modes with the highest energy that contributes the most to the turbulent flow. The application and practical utility of POD analysis to direct numerical simulation (DNS) results of elastic turbulence of dilute polymer solutions have been demonstrated in the literature for both high[53,54] and vanishing Reynolds numbers, Re (ratio of inertial to viscous forces).[55] However, the application of POD in the analysis of experimentally acquired dynamics of an elastic turbulent flow has not yet been reported.

In this work, we investigate the flow of a semi-dilute entangled polymer solution in a microfluidic serpentine geometry using the μPIV technique with the aim of providing a comprehensive characterization of the purely elastic turbulent flow observed at relatively high Weissenberg numbers (ratio of elastic to viscous forces) yet at vanishing Reynolds numbers. In our experiments, three different stages of the flow are considered, namely, below, near, and safely above the onset of purely elastic instability, to study the evolution of the purely elastic turbulent flow. Furthermore, to evaluate the homogeneity and stream-wise dependence of the flow features at the highly turbulent stage, we compare the velocity profile and spatial flow features at five different positions in the serpentine channel. Common statistical analyses, including single-point statistics and two-point correlation, are employed to characterize purely elastic turbulent flow features of semi-dilute entangled polymer solutions in the serpentine channel. Furthermore, we directly extract the structure of purely elastic turbulent flow in the serpentine channel, for the first time to the best of our knowledge, by applying the POD method to the instantaneous velocity fields captured experimentally using μPIV.

The structure of this paper is as follows: We explain the proper orthogonal decomposition method in Sec. II and sample preparation methods, rheological properties of the fluid, and the experimental setup and procedure in Sec. III. The experimental results are presented and discussed in Sec. IV and concluded in Sec. V.

II. PROPER ORTHOGONAL DECOMPOSITION

Proper Orthogonal Decomposition (POD) also known as principal component analysis is a numerical order reduction technique that decomposes a set of instantaneous velocity fields into a set of deterministic basis functions or modes.[52,56,57] In the following, we briefly present the basic concept of this method, which is necessary to comprehend this work. Further mathematical details and application of this method in fluid dynamics of the turbulent flow can be found in the literature.[52,56,58–60] In the case of an experimentally acquired flow field with high spatial resolution, the POD method is applied using the "snapshot method."[61] As its name suggests, this method treats each velocity field obtained from μPIV as a snapshot. In each snapshot, the velocity vector is defined as $\mathbf{u} = (u, v)$ and each velocity component (scalar) is both a function of position (x, y) and time. The proper orthogonal decomposition can be applied to either component as well as to the magnitude of the velocity $|\mathbf{u}| = \sqrt{u^2 + v^2}$. The numerical analysis begins with constructing a $m \times n$ matrix, $\mathbf{U}$, from the velocity components, e.g., $u(x, y, t)$, where $m = N_t$ and $n = N_x \times N_y$, with N_t being the number of snapshots and N_x, N_y being the number of spatial vectors in x- and y-directions. In fact, each entry (u_{ij}) of the matrix $\mathbf{U}$ is the measured velocity at a point j in space at time i,

$$\mathbf{U} = \begin{bmatrix} u_{11} = u(x_1, y_1, t_1) & \cdots & u_{1n} = u(x_{N_x}, y_{N_y}, t_1)) \\ u_{21} = u(x_1, y_1, t_2) & \cdots & u_{2n} = u(x_{N_x}, y_{N_y}, t_2) \\ \vdots & \vdots & \vdots \\ u_{m1} = u(x_1, y_1, t_m) & \cdots & u_{mn} = u(x_{N_x}, y_{N_y}, t_m) \end{bmatrix}.$$

A POD decomposition of the matrix $\mathbf{U}$ aims to find a set of orthogonal vectors $[\mathbf{\Phi}^{(1)}(x, y), \mathbf{\Phi}^{(2)}(x, y), \ldots, \mathbf{\Phi}^{(N_t)}(x, y)]$ such that

$$\mathbf{U}(x, y, t) = \mathbf{U}_1(x, y, t) + \sum_{n=2}^{N_t} \mathbf{a}^{(n)}(t) \cdot \mathbf{\Phi}^{(n)}(x, y), \quad (1)$$

where $\mathbf{U}_1(x, y, t)$ represents the time averaged velocity over all N_t snapshots. $\mathbf{\Phi}^{(n)}$ are the eigenvectors of the auto-covariance matrix

$\mathbf{C} = 1/(m-1)\mathbf{U}^T\mathbf{U}$, and $\mathbf{a}^{(n)}$ are their corresponding temporal coefficients. These eigenvectors, known as *proper orthogonal modes* of the velocity fluctuations, can be viewed as the axes of an n-dimensional ellipsoid enclosing the entire data set (matrix $\mathbf{U}$) in an n-dimensional space.[62] Moreover, since the coefficients $\mathbf{a}^{(n)}$ are uncorrelated, each one can be interpreted as variations of one independent "mode" of fluctuation. The energy contribution of each mode, $[i = 1, ..., N_t]$ to the total kinetic energy (TKE), is calculated as $E_i = \lambda_i / \sum_{k=1}^{N_t} \lambda_k$, where λ_i are the corresponding eigenvalues in the descending order.

III. EXPERIMENTAL METHODS
A. Working fluid and its rheological properties

In this study, we used a viscoelastic aqueous solution containing 2000 ppm (0.2 w%) of partially hydrolyzed polyacrylamide (HPAM) Flopaam 3630 (SNF Floerger) with a molecular weight of (18.7 ± 2.0) MDa. The polymer solution was diluted following a standard protocol[13,63] from a 5000 ppm stock solution in a "brine" solution composed of ultrapure water with 1000 ppm NaCl and 100 ppm $CaCl_2$. Since HPAM polymers are widely used for enhanced oil recovery, where salt is an essential component of the injected polymer solutions, we have included the typical salt type and concentration considered in the literature.[37,38,64] As shown in our previous study,[65] the selected salt concentration is in the low salt range and does not have a significant impact on screening the negative charges of the polymers' backbone or causing transient cross-linking network. Using a pycnometer, the density of the polymer solution was determined as $\rho_P = (1.00 \pm 0.01)$ g/cm^3. Because the polymer concentration used in our microfluidic experiments was about 25 times larger than the polymer's overlap concentration of $c^*_{3630} \approx 82$ ppm, we can safely assume it to be in the semi-dilute entangled regime.[65] The shear rate, $\dot{\gamma}$, dependent viscosity, $\eta(\dot{\gamma})$, and the first normal stress difference, $N_1(\dot{\gamma})$, of the polymer solution at $(20 \pm 0.2)°$C were measured by a steady shear step test applying a standard protocol in the deformation rate-controlled mode using a HAAKE MARS 40 rheometer and a

60 mm cone plate geometry with an angle of $1°$. The rheological data are plotted in Fig. 1(a). The storage modulus, G', and loss modulus, G'', determined from small amplitude frequency sweep tests in the stress-controlled mode are plotted in Fig. 1(b). The crossover happens at the frequency of $\omega \approx (0.35 \pm 0.1)$ Hz; thus, the longest relaxation time of the polymer solution is determined as $\lambda_{max} = 1/\omega \approx (3 \pm 1)$ s. The experimental data are fitted to the multi-mode Maxwell model.[65]

B. Viscoelastic fluid model

To define the relevant dimensionless Weissenberg number and to evaluate viscoelastic flow, we need to choose a constitutive fluid model, which best represents the rheological properties of the fluid. Among all models developed for describing semi-dilute polymer solutions,[66] the White-Metzner (WM) constitutive model could best represent the strong shear-thinning and non-quadratic first normal stress difference of our polymer solution (Fig. 1). It should be noted that the WM consecutive model assumes that the second normal stress difference, N_2, is zero and does not consider extensional viscosity. In polymer melts and highly entangled polymer solutions, N_2 can be significant and is typically exerted in the opposite direction of N_1; thus, it can dampen elastic instability and suppress secondary flows in curved ducts. However, since for polymer solutions in the semi-dilute regime, as used in this work, the magnitude of N_2 is typically measured to be in the range of 1% to a maximum of 10% of N_1, we assume that N_2 can be neglected.[67] Moreover, the flow in a serpentine channel is mainly shear dominated; thus, the effect of extensional viscosity can also be safely excluded. Therefore, the choice of the WM fluid model in our case is reasonable. The basic concept of the WM model is to define a total stress tensor $\tau = \tau_1 + \tau_2$ and a total viscosity $\eta = \eta_1 + \eta_2$ that are related to the deformation rate tensor $\mathbf{D} = \frac{1}{2}(\nabla\mathbf{u} + \nabla\mathbf{u}^T)$.[9,40,68] The pure viscous component of the stress tensor τ_2 is defined as $\tau_2 = 2\eta_2\mathbf{D}$, where η_2 is the solvent viscosity. τ_1 is defined by

$$\tau_1 + \lambda(\dot{\gamma})\overset{\nabla}{\tau_1} = 2\eta_1(\dot{\gamma})\mathbf{D}, \tag{2}$$

(a)

(b)
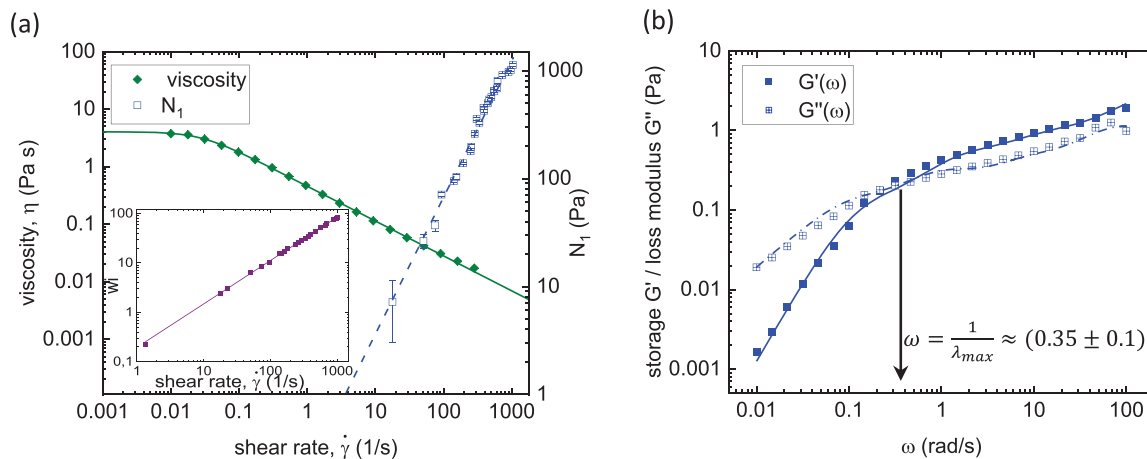
FIG. 1. (a) The (shear) viscosity $\eta(\dot{\gamma})$ (green diamonds) and first normal stress difference N_1 (□) measured using a rotational rheometer. The solid and the dashed lines are (olive green) fit to the Carreau-Yasuda model Eq. (4) and a power law (blue) $N_1(\dot{\gamma}) = (0.34 \pm 0.07)\dot{\gamma}^{(1.19 \pm 0.03)}$, respectively. The inset shows the calculated Wi (purple squares) based on Eq. (5). The solid line (purple) is a power law fit, $Wi(\dot{\gamma}) = (0.15 \pm 0.01)\dot{\gamma}^{(0.91 \pm 0.01)}$. (b) Elastic modulus G' (blue squares) and loss modulus G'' (⊞) measured via small amplitude frequency sweep test. Solid and dashed lines are corresponding fits to the multi-mode Maxwell model with four elements.

where $\overset{\triangledown}{\tau_1}$ is the upper convected time derivative and $\lambda(\dot\gamma)$ is the shear dependent relaxation time calculated as

$$\lambda(\dot\gamma) = N_1/2(\eta(\dot\gamma) - \eta_\infty)\dot\gamma^2, \tag{3}$$

where the shear rate is defined as $\dot\gamma = \sqrt{2\,tr(\mathbf{D}^2)}$. The shear dependent total viscosity of the polymer solution $\eta(\dot\gamma)$ is described by the Carreau–Yasuda model,[9,69]

$$\eta(\dot\gamma) - \eta_\infty = (\eta_0 - \eta_\infty)\left[1 + (\Lambda\dot\gamma)^a\right]^{\frac{n-1}{a}}, \tag{4}$$

where η_0 and η_∞ are the zero-shear viscosity and the viscosity at infinite shear rates, Λ is a characteristic time, n is the power law exponent associated with the degree of shear thinning, and a is a transition control factor. The Weissenberg number, Wi, which is defined as $Wi(\dot\gamma) = \lambda(\dot\gamma)\dot\gamma$, is thus calculated as

$$Wi(\dot\gamma) = N_1/2(\eta(\dot\gamma) - \eta_\infty)\dot\gamma. \tag{5}$$

Since, in our study, the Reynolds number is always safely below one, inertia forces are negligible, and the observed flow features are merely related to elastic stresses. Therefore, the Weissenberg number Wi is the relevant dimensionless number to be considered in this case. The calculated values of Wi as a function of the shear rate are plotted in the inset of Fig. 1.

C. Microfluidic geometry

The flow geometry used in all experiments was a microfluidic serpentine channel consisting of 33 consecutive half-bends with a total length of $l \approx 26$ mm, a width of $w \approx 0.125$ mm, a height of $h \approx 0.04$ mm, and an inner bend radius of $r_i \approx 0.125$ mm, see the sketch in Fig. 2. The microscale geometry allows us to achieve high Wi while keeping the Re low. It is worth mentioning that the choice of the serpentine channel as flow geometry is twofold. On the one hand, curved channels are significant for industrial and biological viscoelastic fluid flows. On the other hand, despite its simplicity, the flow type in the serpentine channel is complex and leads to intriguing phenomena in polymer dynamics and the structure of the flow.

The positive master of the microfluidic device was fabricated via standard photo lithographic protocols.[70] A negative mold was fabricated from that using Sylgard 184 (Dow Corning). In a second molding step, the final microfluidic device was made using the stiff, oil resistant, photo-reactive resin NOA 83H (Norland optical adhesives) sealed with a microscopy glass slide and sandwiched with an additional coverslip to enhance the stability and avoid deformation of the channel at higher pressures.

D. Experimental protocol and μPIV setup

The microfluidic channel described in Sec. III C was used as the flow geometry in this work. The inlet of the microfluidic device was connected to a microfluidic pressure pump (MFCS-EZ, Fluigent) that enabled fluid injection at a controlled pressure. The outlet was connected to a liquid reservoir at the same height as the microfluidic device to avoid gravitational counterpressure. The microfluidic device was placed on an epifluorescent inverted microscope (Axio observer Z1, Zeiss) equipped with a 20× air objective (Plan-Apochromat, Zeiss) with numerical aperture NA = 0.8. Fluorescent polystyrene microspheres ($\lambda_{ext} = 542$ nm $/\lambda_{emt} = 612$ nm; FlouroMax, Thermo Fisher) with a diameter of 1 μm were added to the polymer solution. The size of these particles was large enough to achieve an acceptable signal-to-noise ratio but small enough to ensure that they followed the flow with minimal delay without affecting it. The flow in the serpentine channel was illuminated with a triggered Continuous Wave (CW) laser ($\lambda = 532$ nm, LaVision), and the light from the fluorescent particles was captured via a sCMOS camera (Imager pro HS, PCO) with a resolution of ≈ 3 pixel/μm after passing through a cutoff filter to isolate the emission signal and reduce the background noise. A sketch of the μPIV setup is shown in Fig. 2(a).

To ensure that the recorded images correspond to the steady state flow and not to the transient regime, the recording was started at least 20 min after applying the pressure at the inlet. Double-frame images were captured with small-time delay dt in the range of 0.1–0.8 ms, depending on the flow velocity, to achieve a particle shift of no more than five pixels between consecutive double-frames. The imaging
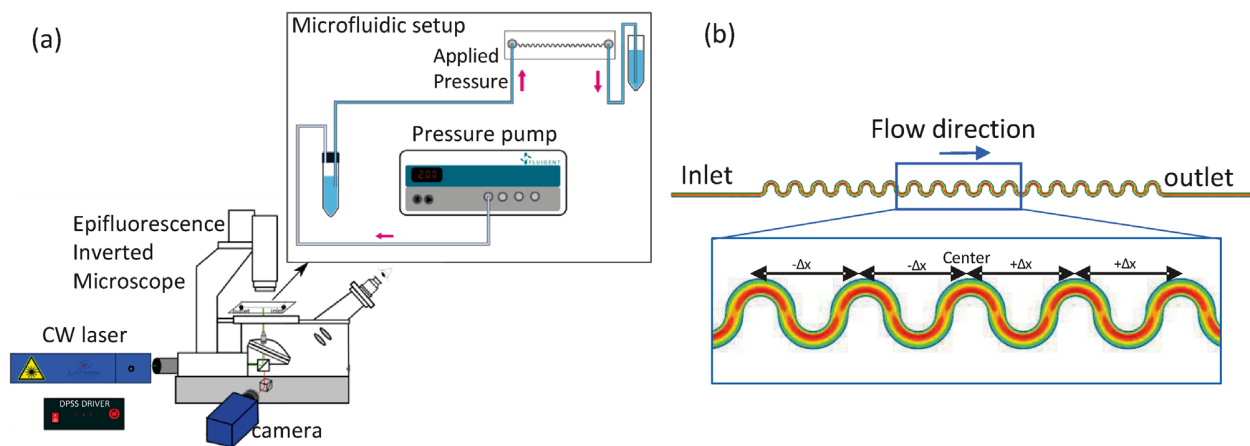

FIG. 2. (a) Sketch of the experimental setup including μPIV. (b) Sketch of the microfluidic geometry with dimensions of $w \approx 0.125$ mm, height of $h \approx 0.04$ mm, and an inner bend radius of $r_i \approx 0.125$ mm. The center corresponds to a point 13 mm downstream of the inlet and $\Delta x = 1$ mm.

frequency, based on each pair of double-frames, was set to 42 Hz for all experiments, and a sequence of 2100 double-frames, equivalent to a duration of 50 s, ≈17 times longer than the polymer's longest relaxation time, was recorded at multiple locations in the channel, i.e., at different locations along the channel by focusing on the mid-height plane of the channel [Fig. 2(b)]. The depth of correlation,[71] δz, based on the optical properties of the objective, laser wavelength, and particle size used in our experiments, is computed as $\delta z \approx 5\,\mu$m for our setup. This corresponds to roughly 12% of the channel height. All experiments were conducted at a room temperature of $(20\pm1)^\circ$C.

To compute the velocity fields from the μPIV images using a cross-correlation algorithm, the individual images of the double-frames were first divided into square areas called "interrogation windows." A multi-pass processing approach with an initial interrogation window size of (64×64) pixel, and 50% overlap to a final interrogation window size of (24×24) pixel with 75% overlap was considered to improve the accuracy of the fast Fourier transform (FFT) cross-correlation algorithm.[72] The experimental setup and the processing routine were tested with a 50 w% aqueous glycerin solution. The difference between the μPIV results of the test experiments and the corresponding computational fluid dynamic (CFD) simulation was less than 5%.

IV. RESULTS AND DISCUSSION

In the following, we present and discuss the experimental results. First, we study the transition from laminar to elastic turbulent flow and identify the onset of purely elastic instability. Then, we investigate the spatial dependence of the velocity profile on the position in the

laminar and turbulent stages of the flow. Thereafter, the purely elastic turbulent flow is characterized at different probing positions using single-point statistics in the time domain and two-point correlation analyses. Finally, we extract the flow structure at the highest turbulent stage of our system using the POD method.

A. Evolution of the purely elastic turbulent flow and flow features

1. Onset of purely elastic instability

To study the flow evolution from the laminar to turbulent state, the pressure applied at the inlet was stepwise increased, and instantaneous velocity fields were captured at the center of the serpentine channel, approximately 13 mm downstream of the channel inlet [Fig. 2(b)]. In all experiments, the microscope focus was set at the mid-height of the channel. Examples of the time-averaged velocity fields and their corresponding root-mean-square distribution at two stages of the flow, corresponding to the lowest and the highest applied inlet pressures, are shown in Fig. 3. At lower applied inlet pressure, the velocity field is laterally symmetric [Fig. 3(a)] with negligible rms values [Fig. 3(b)], indicating a laminar flow. However, the velocity field corresponding to the highest applied inlet pressure is clearly asymmetric [Fig. 3(c)], with a significant rms distribution [Fig. 3(d)].

The time averaged velocity as a function of the applied inlet pressure, respectively, Weissenberg number, at a normalized vertical position of $\varepsilon = 0$ at the center of the channel is plotted in Fig. 4(a). The shear rate in the serpentine channel is approximated by $\dot{\gamma} = 4\langle|\mathbf{u}|\rangle/r$,[65,73]
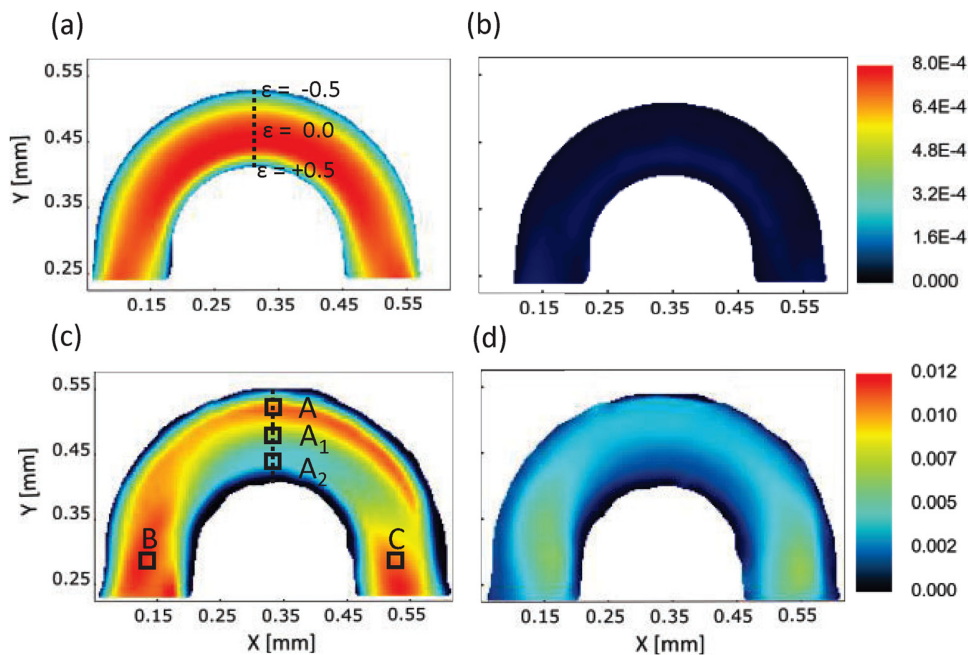
FIG. 3. (a) Time averaged velocity field at the mid-height of the channel at the central half-bend for an inlet pressure of 3.47 kPa ($Wi \approx 5 < Wi_{crit}$), $\varepsilon = (0.5w - y)/w$ is the normalized vertical position across the channel width; (b) the corresponding time averaged root mean square values of the velocity field; (c) time averaged velocity fields at the center of the serpentine channel for an inlet pressure of 56.39 kPa ($Wi \approx 45 > Wi_{crit}$). Points (A), (A₁), and (A₂) along the central vertical line at $\varepsilon = -0.3$, $\varepsilon = 0.0$, and $\varepsilon = +0.3$, respectively, and points (B) and (C) at the lateral ends of the half-bend are probing positions. Point (A) represents the region with the highest average velocity, and points (B) and (C) represent the regions with the highest rms value; and (d) the corresponding time averaged root mean square values of the velocity field.

FIG. 4. (a) Time averaged velocity and (b) the corresponding root-mean-square values at $\varepsilon = 0$ at the center of the serpen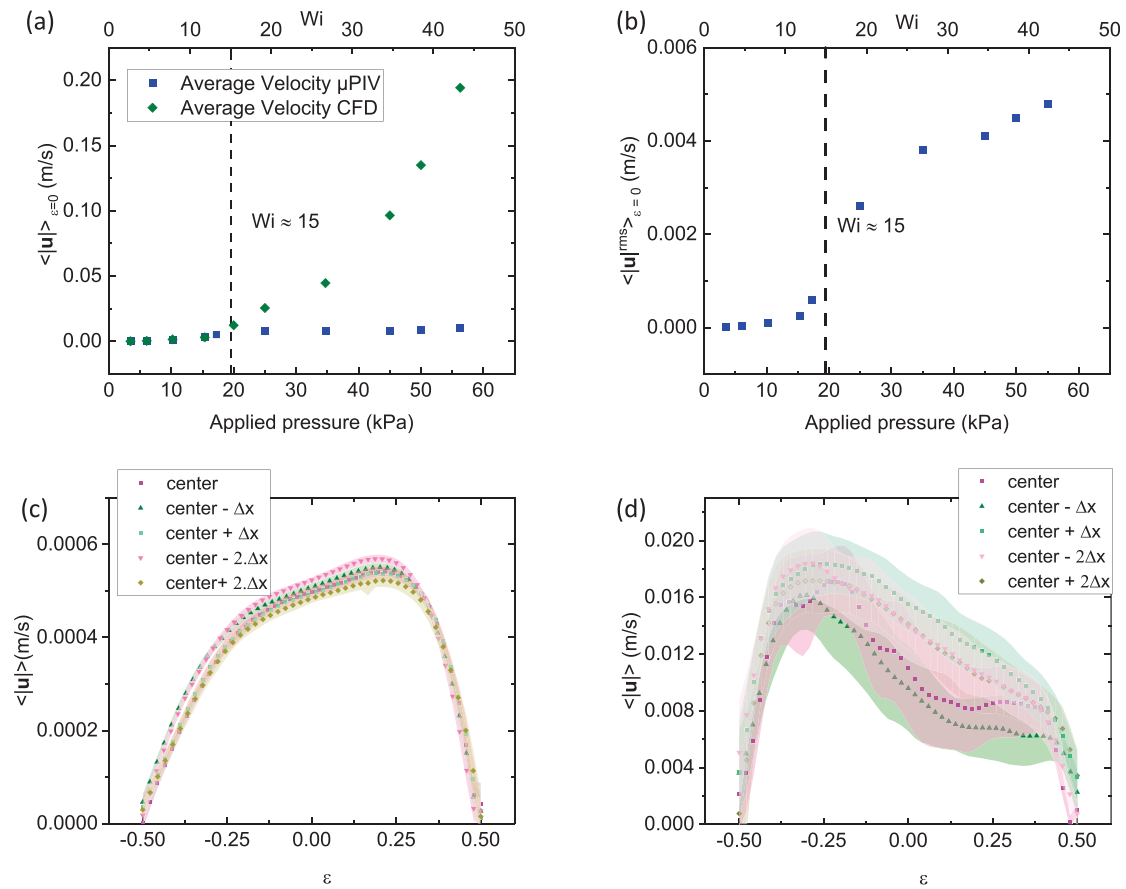tine channel as the function of applied inlet pressure (bottom axis) and corresponding Weissenberg number (Wi, top axis). (c) Time averaged velocity profiles for an inlet pressure of 3.47 kPa ($Wi \approx 5 < Wi_{crit}$), and (d) for the inlet pressure of 56.39 kPa ($Wi \approx 45 > Wi_{crit}$) at five different positions with respect to the center (($\Delta x = 1\,mm$) of the serpentine channel.

with $\langle |\mathbf{u}| \rangle$ and $r = \sqrt{(w\,h)/\pi}$ being the time-averaged velocity and the equivalent radius, respectively. The corresponding Weissenberg number is then calculated based on Eq. (5) for the approximated *in situ* shear rates.

Above a critical inlet pressure, corresponding to $Wi_{crit} \approx 15$, as shown in Fig. 4(a), the measured time averaged velocities determined at the center of the channel fall significantly below numerical values. The numerical values are predicted based on CFD simulations of an imaginary shear thinning fluid with similar Carreau–Yasuda fitting parameters but no elasticity component, using a generalized Newtonian fluid model. Moreover, the experimental root-mean-square (rms) values of the corresponding time-averaged velocities, shown in Fig. 4(b), exhibit a dramatic increase above $Wi_{crit} \approx 15$ as well. These observations indicate an increased flow resistance and large velocity fluctuations, which are characteristics of an unstable flow. To ensure that inertia is negligible throughout the geometry and does not contribute to this unstable flow, we estimate the relevant Reynolds numbers. The used serpentine geometry with the rectangular cross section requires the consideration of two Reynolds numbers. For channel flows, the Reynolds number is usually defined as $Re_c = \varrho \langle |\mathbf{u}| \rangle r/\eta$,

where the equivalent radius, r, is employed as the characteristic length. To account for centrifugal inertia in the curvilinear flow, the radius of the curvature of the serpentine channel, r_i, is used as the characteristic length, and the corresponding Re number can be, thus, expressed as $Re_s = \varrho \langle |\mathbf{u}| \rangle r_i/\eta$. The maximum Reynolds numbers in our experiments are $Re_c \approx 0.05$ and $Re_s \approx 0.16$, respectively, and we can conclude that the contribution of inertia to the flow is negligible, and the observed unstable flow is a purely elastic turbulent flow related solely to the anisotropic elastic stresses associated with the highly viscoelastic polymer solution.

2. Spatial features of purely elastic turbulent flow

After analyzing the global flow behavior for shear rates below and above the critical shear rate, we additionally aim at the analyzing dependence of the flow profile on the location in the channel, and the spatial homogeneity of the flow. To this end, we repeated the μPIV recordings at four additional positions [Fig. 2(b)], with $\pm \Delta x$, $\pm 2\Delta$ being the distance from the center, ($\Delta x = 1\,mm$, based on the periodicity of our serpentine channel) at two different stages, i.e., at $Wi < Wi_{crit}$ and $Wi > Wi_{crit}$. The velocity profiles across the channel

width along a vertical centerline in each half-bend are plotted in Figs. 4(c) and 4(d), for $Wi \approx 5 < Wi_{crit}$ and for $Wi \approx 45 > Wi_{crit}$, respectively. At $Wi < Wi_{crit}$, the polymer flow in the serpentine channel is laminar, i.e., the flow lines follow the curvature of the channel. The velocity profile at this stage is similar to that of a Newtonian fluid, which means it is skewed toward the wall with the highest curvature, i.e., at $\varepsilon = (0.5w - y)/w > 0$, where the shear rate is higher. Furthermore, velocity profiles at different locations have an identical shape, with negligible difference within the experimental error. In contrast, the velocity profiles corresponding to $Wi > Wi_{crit}$ [Fig. 4(d)] show reversed skewness and are rather shifted to the opposite wall, i.e., $\varepsilon < 0$. This deviation from a laminar flow behavior clearly points toward the presence of flow structures other than the primary streamwise flow. The structure of the flow will be discussed in Sec. IV C. The shape of the velocity profiles is rather irregular and exhibits spatial dependence, which means that the mean flow is not essentially invariant and, thus, the flow is spatially non-homogeneous.

3. Flow topology and its impact on polymer behavior and flow features

The explanation for the observed unstable, non-homogeneous flow of a semi-dilute entangled polymer solution is multifaceted due to the interdependence of fluid and flow properties. Therefore, we first require a lucid insight into the origin of the observed unstable flow, determined by the molecular behavior of the polymers, with respect to the flow geometry. As discussed in the literature,[16–18,74] the purely elastic instability in polymer solutions is driven by the dynamics of the polymers' deformation, which, in turn, is highly dependent on the flow type. In fact, Shaqfeh argues that the ratio between the vorticity and rate of deformation, i.e., the flow type in the flow geometry is a decisive factor for polymer behavior.[22] A practical dimensionless number to define the flow type is the topology factor defined as $\xi = (|\boldsymbol{D}| - |\boldsymbol{\Omega}|)/(|\boldsymbol{D}| + |\boldsymbol{\Omega}|)$, where $|\boldsymbol{D}|$ is the magnitude of the deformation rate tensor and $|\boldsymbol{\Omega}|$ is the magnitude of the vorticity tensor. Polymers exposed to different flow types deform intrinsically different. When subjected to low to moderate shear, the polymers remain in their coiled configuration and align with the flow direction at high shear rates. Extensional flow stretches the polymers, while rotational flow tends to restore them to their coiled shape.[22] The topology factor distribution calculated from experimental values at $Wi \approx 5 < Wi_{crit}$ and $Wi \approx 45 > Wi_{crit}$ is shown in Fig. 5. Below the onset of purely elastic instability, three distinguished regions of shear (green), extensional (red), and rotational (blue) are visible, alternating orderly between successive half-bends. The corresponding histogram of the topology factor distribution indicates that the flow is mainly shear dominated with defined extensional regions. This suggests that polymers remain mainly in their coiled configuration, and thus, the flow is predominantly laminar. For $Wi > Wi_{crit}$, these well-defined regions are no longer distinguishable, and the flow types are rather randomly distributed. The corresponding probability distribution indicates that the fraction of rotational (vortical) flow has increased. This random distribution of flow types combined with their impact on polymer behavior results in spatial non-homogeneity of the flow. Furthermore, the significant contribution of randomly distributed rotational flow type suggests that the purely elastic turbulent flow is anisotropic. However, as Haward et al. noted, the topology factor can be dubious
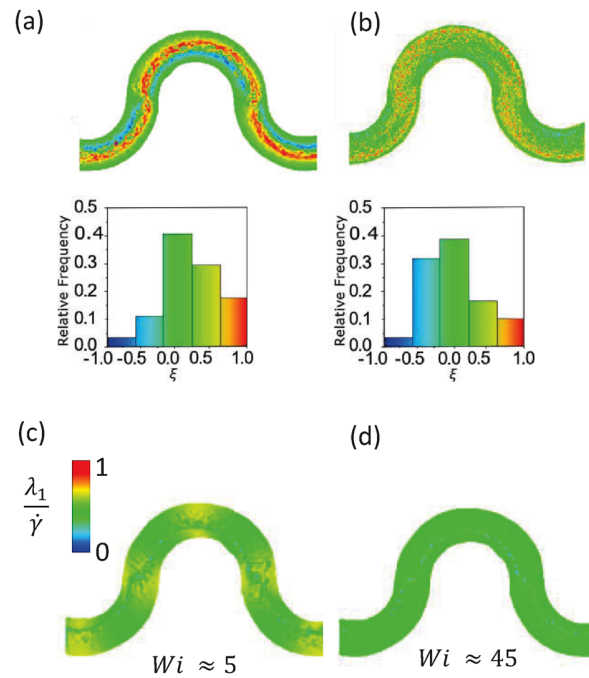

FIG. 5. Local distribution of the topology factor ξ along the serpentine channel ξ (top) and their corresponding probability distribution (bottom) at $Wi \approx 5 < Wi_{crit}$ (a) and at $Wi \approx 45 > Wi_{crit}$ (b). The value $\xi = -1.0$ (blue) indicates a pure rotational flow, $\xi = 0.0$ (green) a pure shear flow, and $\xi = 1.0$ (red) a pure extensional flow. The normalized principal strain rate $(\lambda_1/\dot{\gamma})$ at $Wi \approx 5 < Wi_{crit}$ (c) and $Wi \approx 45 > Wi_{crit}$ (d). The red color in the legend $(\lambda_1/\dot{\gamma} = 1)$ indicates strong extension.

because it does not necessarily contain information about the strength of the flow types, which is very important for the polymer behavior.[75] To this aim, the extensional flow strength is quantified in terms of the principal strain rate parameter λ_1, which is the eigenvector of the deformation rate tensor and is expressed as $\lambda_1 = \frac{1}{2}\sqrt{(D_{11} - D_{22})^2 + 4D_{12}^2}$. The normalized value of $\lambda_1/\dot{\gamma}$ is plotted in Figs. 5(c) and 5(d). As can be seen, even though distinct extensional regions are visible in the topology-factor distribution [Fig. 5(a)], the strength of the extension is quite weak [Fig. 5(c)] and even weaker at the higher Weissenberg number [Fig. 5(d)]. Thus, the flow remains shear dominated across the range of the considered Weissenberg number.

In the semi-dilute entangled regime, the complexity of the rheological properties of the fluid plays an important role in the flow properties as well. Shear thinning, for example, causes a non-parabolic velocity profile and, thus, strong transversal variation of the shear rate in the channel. This leads to different velocities and relaxation times and to different degrees of deformation and relaxation of the polymer at different points in the channel. Moreover, the deformation exerted on the polymers at a given shear rate is stored in them, due to their significant memory effect, before they relax or deform at a different shear rate. This further affects the spatial distribution of rheological properties.

As a result, the mixed and random distribution of the flow types in a serpentine channel in combination with the highly complex rheological behavior of semi-dilute entangled polymer solutions leads to a non-homogeneous and anisotropic purely elastic turbulent flow.

B. Temporal features of purely elastic turbulent flow

To characterize the temporal features of the observed purely elastic turbulent flow, we conduct point-wise analysis of the velocity fluctuations. The velocity fluctuations, $u'(x, y, t)$, are the Reynolds decomposition of the velocity in the form of $u'(x, y, t) = u(x, y, t) - \langle u(x, y) \rangle$, where $u(x, y, t)$ is the instantaneous velocity and $\langle u(x, y) \rangle$ is the time averaged velocity at any point in the 2D domain. We extract time series of velocity fluctuations at three locations along the centerline of the channel, shown as the dashed line in Fig. 3(c), namely, (A) near the outer wall with the largest radius of curvature $(\varepsilon = -0.30)$, (A_1) in the middle of the channel $(\varepsilon = 0.0)$, and (A_2) near the inner wall with the smallest radius of the curvature $(\varepsilon = +0.30)$. It should be noted that these points are chosen at the vertical centerline for convenience, since here the x and y directions correspond to the azimuthal (streamwise) and radial (transversal) directions, respectively.

1. Single-point statistics

The corresponding vertical and horizontal components of the velocity fluctuations, u'_x and u'_y, as a function of time, are shown in Figs. 6(a) and 6(b). The fluctuations in the streamwise direction, u'_x, are significantly stronger than the fluctuations in the transversal direction, u'_y. This observation, which indicates that the temporal velocity fluctuations are anisotropic, is further evident in the statistical moments of the velocity fluctuations at these points, shown in Table I.

The values of skewness, S_x and S_y, and kurtosis, K_x and K_y, at different locations suggest that the velocity fluctuations are slightly non-Gaussian. It is worth noting that the higher value of the kurtosis of the streamwise velocity fluctuations near the walls indicates that the fluctuations at these regions are intermittent, i.e., the velocity fluctuations contain a random sequence of violent bursts also known as rare events.[32] The normalized (auto)-correlation function of total velocity fluctuations at points (A), (A_1) and (A_2) computed as $r_{ij}(\tau) = \langle u'_i(t + \tau) u'_j(t) \rangle / \langle u'_i \cdot u'_j(t) \rangle$, and $i = j$, is plotted in Fig. 6(c). The corresponding characteristic time $T = \int_0^\infty r_{ii}(\tau) d\tau$ is on the order of the polymer's longest relaxation time and depends on the position of the probing point. This variation in characteristic time can be explained in view of the shear dependency of the polymer relaxation time in the semi-dilute entangled regime. Near the walls, where the shear rate is highest, the characteristic timescale is smaller than at the center where the shear rate is lower.

2. Two-point correlation

The total temporal velocity fluctuations at points (A), (B), and (C) are extracted, and two-point correlation and spectral analysis are applied to obtain further statistical information about the flow. Point (A) represents the region with the highest average velocity, and points (B) and (C) represent the regions with the highest rms value [Fig. 3(c)]. The normalized velocity fluctuations at these points are shown in Figs. 7(a)–7(c). The presence of random "bursts," an
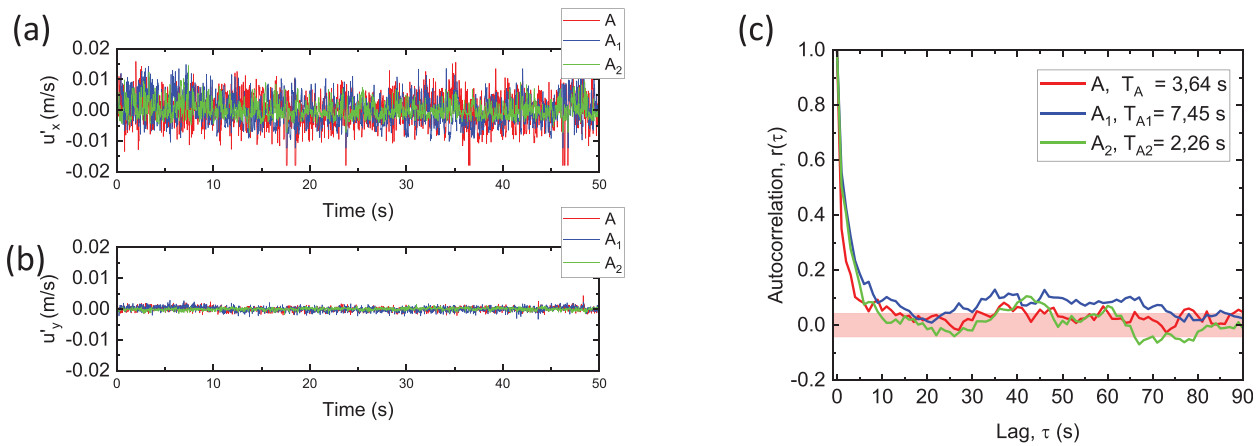
FIG. 6. Temporal fluctuations of (a) streamwise velocity component, (b) transversal velocity component, and (c) autocorrelation function of total velocity fluctuations at points (A), (A_1), and (A_2) marked in Fig. 3(b). The colored rectangle indicates the confident band.

TABLE I. First to fourth moments of velocity fluctuations at $Wi \approx 45$ above the onset of purely elastic instability at three different points (A), (A_1), and (A_2) located along the central vertical line [Fig. 3(c)]. $\langle u'_x \rangle$, $\langle u'_y \rangle$ first moment (mean), σ_x, σ_y second moment (standard deviation), S_x, S_y third moment (skewness), and K_x, K_y fourth moment (kurtosis) of, respectively, x and y components of velocity fluctuations.

Sampling location	$\langle u'_x \rangle$ (m/s)	σ_x (m/s)	S_x	K_x	$\langle u'_y \rangle$ (m/s)	σ_y (m/s)	S_y	K_y
A	3.2040×10^{-6}	0.0052	-0.4822	0.8367	3.3270×10^{-10}	7.4540×10^{-4}	-0.07308	0.43032
A_1	-4.780×10^{-8}	0.0049	0.2763	-0.2681	-1.534×10^{-10}	6.712×10^{-4}	0.1995	0.8450
A_2	-9.2708×10^{-7}	0.0027	0.8538	1.2531	7.3841×10^{-11}	4.1440×10^{-4}	-0.3780	0.4673

FIG. 7. Normalized total velocity fluctuations at (a) point (*A*), (b) point (*B*), and (c) point (*C*) marked in Fig. 3(b). *U* is the time averaged velocity at the corresponding point. Examples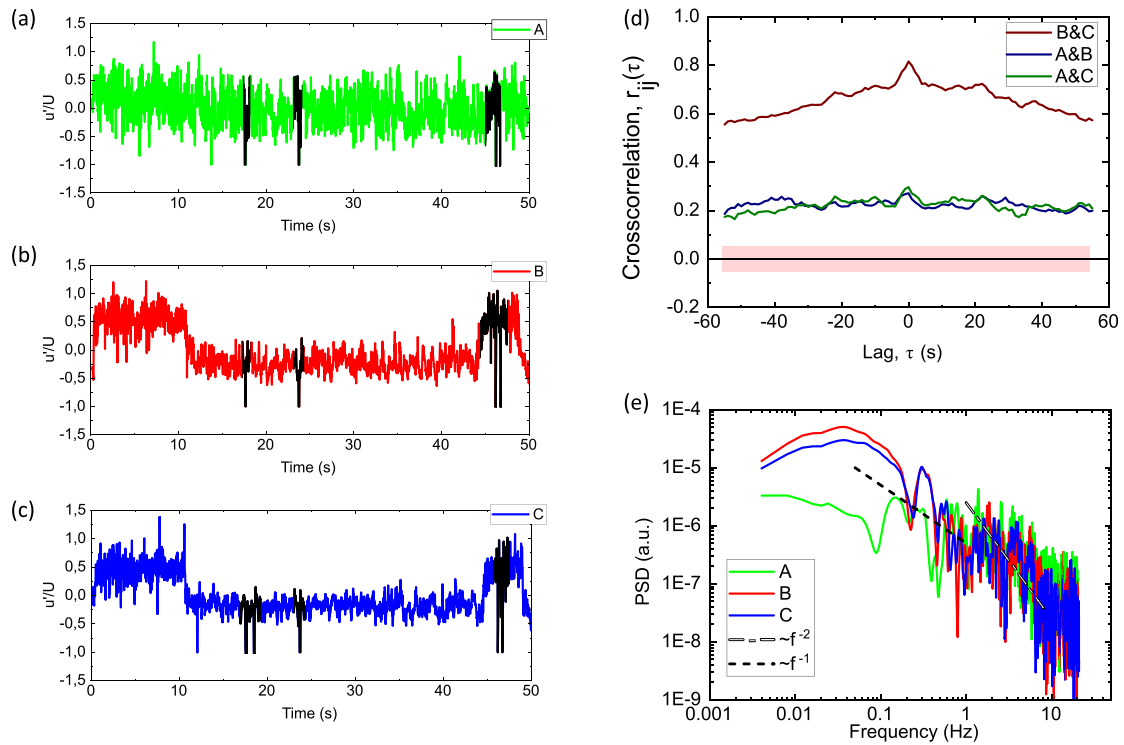 of bursts (rare events) are marked in black. (d) Cross-correlation of normalized velocity fluctuations at points (A), (B), and (C). The colored rectangle indicates the confident band. (e) Power spectral density of velocity fluctuations at points (A), (B), and (C).

indication of the intermittency of the purely elastic turbulent flow, is clearly visible in the velocity fluctuations at all positions [marked in black in Figs. 7(a)–7(c)]. The temporal fluctuations at points (B) and (C) look very similar but differ significantly from point (A). This is further evident in the cross-correlation between time series shown in Fig. 7(d). The significant correlation between points (B) and (C) with a peak at zero lag time implies that fluctuations at these points are highly correlated and synchronized. This indicates the presence of a flow structure, which will be explained in detail in the context of the POD analysis in Sec. IV C.

3. Spectral features

The power spectral densities (PSD) of velocity fluctuations at points (A), (B), and (C) are plotted in Fig. 7(e). A power decay, $\sim f^{-\beta}$, with an exponent of $\beta \approx 2$ describes the power spectral density of the velocity fluctuations in the range of 1 to 10 Hz. Similar exponents have also been reported for the PSD of velocity fluctuations ($\beta \approx 2.3$),[42] stress fluctuations ($\beta \approx 2.0$),[76] and pressure fluctuations ($\beta \approx 2.2$)[38] of semi-dilute entangled polymer solutions in curved geometries. However, at lower frequencies, the exponent is smaller than $\beta \approx 2$. The presence of two different exponents in the PSD curve of velocity fluctuations has been also reported by various researchers, but no clear reasoning for this observation has been provided so far.[38,47] We believe that in our case, the reason for the lower exponent at lower frequencies

is the presence of a large turbulent structure that is associated with the secondary flow. This is further supported by the fact that at point (B) and (C), the power corresponding to the low frequencies is larger than in point (A).

It should be noted that the observed exponent of $\beta \approx 2$ for semi-dilute polymer solutions is smaller than the corresponding exponents of $\beta > 3$ commonly reported for purely elastic turbulent flow of dilute polymer solutions.[24,42] The value of $\beta \approx 3$ is theoretically predicted for dilute polymer solutions based on the assumption of homogeneous flow, linear elasticity, and linear relaxation of the polymers, which do not apply to the semi-dilute entangled regime.[24,25,47,77] In fact, as discussed in Sec. III A, the rheological properties of polymer solutions in the semi-dilute entangled regime are shear dependent and, thus, highly nonlinear. Therefore, it is not unexpected that the exponent of the power spectral density of the velocity fluctuations appears to be different from the value for dilute polymer solutions. However, there is so far no theoretical work on the spectral features of purely elastic turbulent flow of semi-dilute entangled polymer solutions and the expected exponents for this concentration regime.

As proposed by de Gennes[78] in "Reptation Theory" and as experimentally demonstrated by Perkins *et al.*,[20] the motion of the entangled polymers is strongly restricted by the neighboring polymers as if they were confined in a tube. Therefore, due to the restricted deformation and freedom of individual polymers, their corresponding back reaction to the flow is also restricted. Furthermore, as shown in Fig. 5,

the rotational component of the flow in the serpentine channel intensifies at high Weissenberg numbers while the extensional component is weakened. This can reduce the extent of polymer stretching and, thus, dampen the corresponding velocity fluctuations.[16]

The damping and limiting of the flow fluctuations are reflected in the smaller exponent of the power decay of the velocity fluctuations, indicating that the range of excited scales in the flow is also limited.

C. Proper orthogonal decomposition of the purely elastic turbulent flow

The cross correlation of velocity fluctuations at points (B) and (C) in conjunction with the PSD analysis points toward an underlying flow structure. In fact, an interesting feature of viscoelastic flow in bend channels is the presence of a secondary flow due to hoop stress caused by the gradient of the first normal stress difference.[13,79,80] However, experimental studies have so far only been able to implicitly indicate the presence of secondary flows based on the bent streamlines in the mean flow direction.[79] As we discussed extensively so far, the turbulent flow of a semi-dilute entangled polymer solution in a serpentine channel is non-homogeneous and anisotropic on any scale. This rejects the assumption of Taylor's hypothesis, and one cannot explain spatial flow properties based on temporal statistics. Therefore, in this section, we will directly extract the secondary turbulent structure using the POD method. As discussed in Sec. II, the aim of proper orthogonal decomposition is to find a hierarchy of spatial modes, $\Phi^{(n)}$, that best describes the original stochastic flow. The energy spectrum of spatial eigenmodes, E_i, calculated at three different Weissenberg numbers above the onset of purely elastic instability is plotted in Fig. 8(a). The first mode in all cases contains the highest energy content, which at the highest stage of the turbulent flow at $Wi \approx 45$ contains almost 50% of the total kinetic energy (TKE) of the system. The first mode, in fact, represents the time averaged mean flow, and all the other modes describe the deviations from the mean flow. The energy content of the modes decays and is less than 1% of TKE for modes larger than 6. As can be seen from the cumulative energy plot in Fig. 8(b), the energy content of the lower modes is higher at higher Weissenberg numbers, i.e., where the elastic stresses are more significant. In fact, at $Wi \approx 45$,

the first 375 eigenmodes represent 90% of the TKE, while for $Wi \approx 17$, the number of eigenmodes representing 90% of the TKE is 700. This indicates that at higher Weissenberg numbers, the lower modes representing the larger scale structures gain more energy at the expense of the higher modes, which correspond to the finer structures. It can be concluded that, at higher Weissenberg numbers, only a few early modes are sufficient to describe the existing dominant flow structures in the system. Moreover, an exponent of approximately $(-11/9)$ can be fitted to the energy decay spectrum in the range of 2–40, indicated by a dashed line in Fig. 8(a). The exponent of $(-11/9)$ has been proposed by Knight and Sirovich based on dimensional arguments for the Kolmogorov inertial range in non-homogeneous turbulent flows.[81] Since, in our case, the exponent of $\beta \approx 2$ for the PSD curve of velocity fluctuations is close to the Kolmogorov scale of (5/3), the exponent of about $(-11/9)$ is not unexpected.

In order to gain insight into the dominant flow structures, the vector fields of spatial eigenmodes and their corresponding temporal coefficients of the three initial highest energy modes at $Wi \approx 45$ are illustrated in Fig. 9. It should be noted that although the 2D distribution of these modes resembles the shape of a velocity field, they do not convey the same physical meaning because eigenmodes are, in fact, dimensionless. Indeed, the instantaneous velocity field associated with each mode is computed as $\mathbf{U}^{(n)}(x, y, t) = \mathbf{a}^{(n)}(t) \cdot \mathbf{\Phi}^n(x, y)$. The spatial eigenmodes of the first mode, i.e., the mean flow, clearly indicate a strong spiral motion at the lateral sides of the half-bend [Fig. 9(a)]. This points toward the secondary flow governed by the serpentine geometry due to the change in the curvature at the inflection points, (B) and (C), affecting the streamwise mean flow.[79,82] The temporal coefficients associated with the first mode exhibit a sudden jump after a certain time, i.e., the number of snapshots. This sudden jump has also been observed in numerical simulations for viscoelastic Oldroyd-B fluids and is related to the onset of the temporal evolution of the flow.[55]

The presence of counter-rotating vortices associated with hoop stress, caused by the gradient of the first normal stress difference[13,79,80] in the serpentine channel is further evident in the spatial eigenmodes 2 and 3, which contain 5% and 3% of the TKE, respectively, as can be seen in Figs. 9(b) and 9(c).
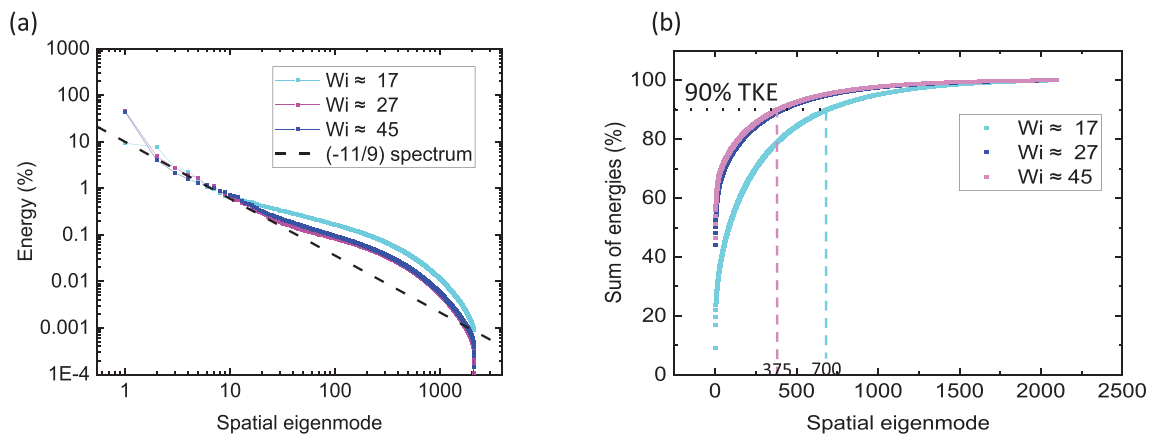
(a)

(b)

FIG. 8. (a) The energy spectrum of the spatial eigenmodes, the dashed line indicates a spectrum exponent of $(-11/9)$, and (b) the cumulative energy of the spatial eigenmodes. The total number of eigenmodes corresponding to 90% TKE is shown as dashed lines.
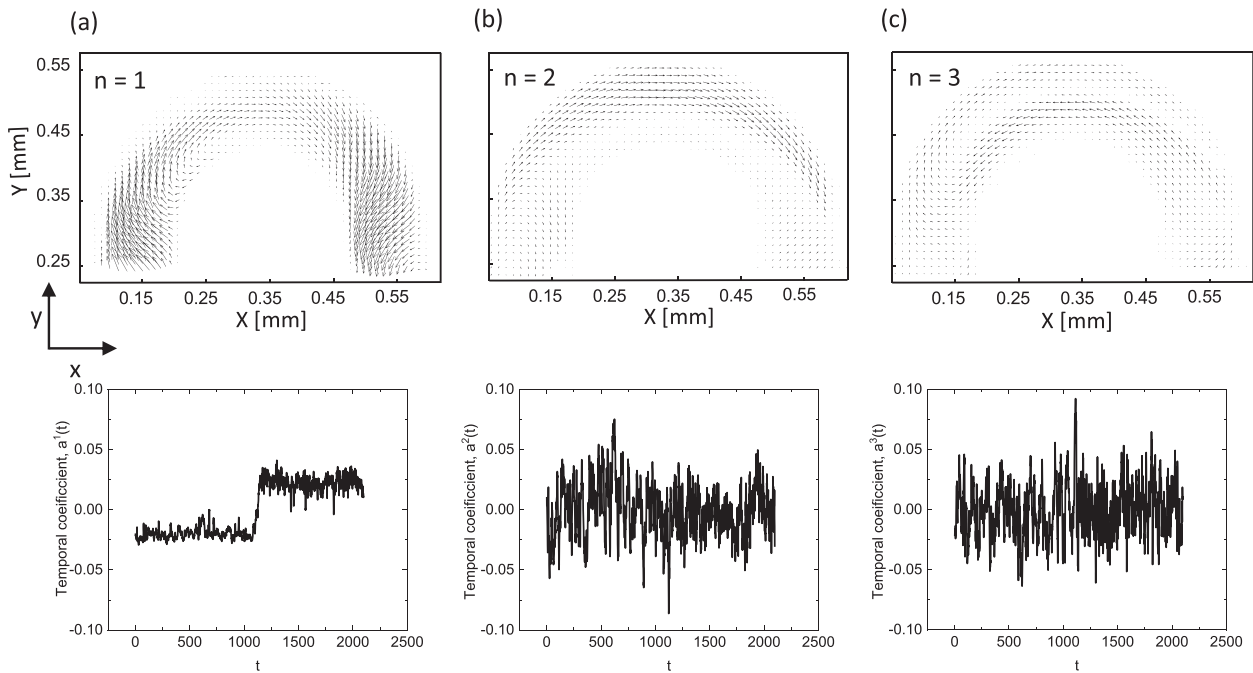
FIG. 9. The vector fields of spatial eigenmodes (top) and their corresponding temporal coefficients (bottom) at $Wi \approx 45$, t is the number of the snapshot or the vector number, for (a) mode 1, (b) mode 2, and (c) mode 3.
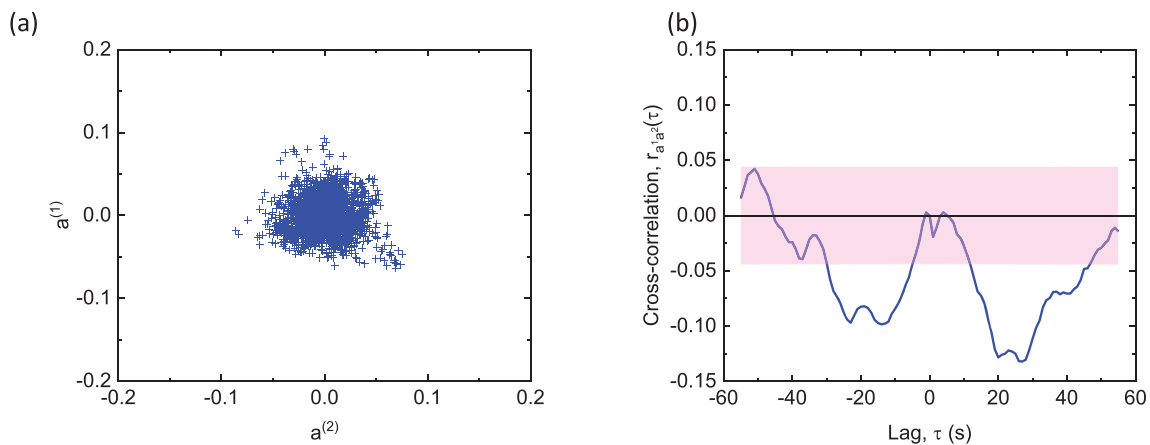
FIG. 10. (a) Phase portrait of temporal coefficients of mode 2 vs mode 3 and (b) cross correlation between temporal coefficients of mode 2 and mode 3. The colored rectangle indicates the confident band.

To clarify the correlation between modes 2 and 3, the time coefficients of these modes are plotted against each other in Fig. 10(a). As evident in the rather compact circular scattering of the temporal coefficients in the phase portrait, the temporal coefficients are strongly related, even though both seem to fluctuate rather randomly. The cross correlation of these temporal coefficients in Fig. 10(b) verifies that modes 2 and 3 are indeed anti-correlated. These observations confirm that at high Weissenberg numbers, there is a strong secondary flow in the form of counter-rotating vortices, which significantly contributes

to the total kinetic energy of the system. Therefore, we can conclude that the strong increase in the flow resistance during the flow of the polymer solution in the serpentine channel is indeed related to the activity of the secondary flow caused by the geometry and the significant first normal stress difference at high Weissenberg numbers.

V. CONCLUSION

In this work, we have performed μPIV experiments to extract spatially and temporally high-resolution velocity fields of a semi-dilute

entangled polymer solution flowing in a serpentine channel. The general flow inspections and standard single-point statistical analysis reveal the presence of a highly anisotropic non-homogeneous unstable flow above a critical Weissenberg number. The power spectral density plot decays with an exponent relatively smaller than the corresponding value of a dilute polymer solution. This indicates a limited range of excited scales in the purely elastic turbulent flow of a semi-dilute entangled polymer solution compared to the dilute regime, which is due to the limitation of polymer motion in space and entanglement above the overlap concentration. In addition, the geometry-induced mixed flow type and the strong rotation and weak extension of the flow in the turbulent state further reduce the extent of polymer stretching and, thus, reduce the range of excited scales in the turbulent flow.

The two-point correlation indicates the strong cross correlation between the fluctuations at the two lateral ends of a half-bend. This implies the presence of a strong secondary flow structure. Due to the absence of a global correlation between the velocity fluctuations, and non-homogeneity of the flow and thus invalidity of the Taylor hypothesis, we used the proper orthogonal decomposition method to gain direct insight into the structural properties of the observed purely elastic turbulent flow. The POD analysis, in fact, clearly shows a strong spiral structure in the highest energy mode and counter-rotating vortices in the two subsequent modes. This confirms the existence of a three-dimensional secondary flow driven by the geometry and the hoop stress, which originates from the gradient of the first normal stress difference in the transversal direction between the inner and outer walls.

With this first experimental characterization of the flow of a semi-dilute polymer solution, we hope to stimulate a theoretical validation of the experimentally observed features that will provide a deep insight into the flow and purely elastic turbulence in this concentration regime.

ACKNOWLEDGMENTS

AUTHOR DECLARATIONS
Conflict of Interest

The authors have no conflicts to disclose.

Author Contributions

Pegah Shakeri: Conceptualization (equal); Data curation (equal); Formal analysis (equal); Methodology (equal); Software (equal); Validation (equal); Visualization (equal); Writing – original draft (equal); Writing – review and editing (equal). **Michael Jung:** Conceptualization (equal); Investigation (equal); Methodology (equal); Supervision (equal); Validation (equal); Writing – original draft (equal); Writing – review and editing (equal). **Ralf Seemann:** Conceptualization (equal); Funding acquisition (lead); Project administration (lead); Resources (lead); Supervision (lead); Writing – original draft (equal); Writing – review and editing (equal).

DATA AVAILABILITY

The data that support the findings of this study are available from the corresponding author upon reasonable request.

REFERENCES

[1] M. Rubinstein, R. H. Colby *et al.*, *Polymer Physics* (Oxford University Press, New York, 2003), Vol. 23.

[2] K. S. Sorbie, *Polymer-Improved Oil Recovery* (Springer Science & Business Media, 2013).

[3] J. M. Dealy and K. F. Wissbrun, *Melt Rheology and Its Role in Plastics Processing: Theory and Applications* (Springer Science & Business Media, 2012).

[4] B. Meulenbroek, C. Storm, V. Bertola, C. Wagner, D. Bonn, and W. van Saarloos, "Intrinsic route to melt fracture in polymer extrusion: A weakly non-linear subcritical instability of viscoelastic Poiseuille flow," Phys. Rev. Lett. **90**, 024502 (2003).

[5] S. E. Spagnolie, *Biological and Medical Physics, Biomedical Engineering* (Springer, 2015).

[6] M. Thiébaud, Z. Shen, J. Harting, and C. Misbah, "Prediction of anomalous blood viscosity in confined shear flow," Phys. Rev. Lett. **112**, 238304 (2014).

[7] M. Levant and V. Steinberg, "Complex dynamics of compound vesicles in linear flow," Phys. Rev. Lett. **112**, 138106 (2014).

[8] S. Gulati, D. Liepmann, and S. J. Muller, "Elastic secondary flows of semidilute DNA solutions in abrupt 90° microbends," Phys. Rev. E **78**, 036314 (2008).

[9] R. B. Bird, C. F. Curtiss, R. C. Armstrong, and O. Hassager, *Dynamics of Polymeric Liquids* (Wiley-Interscience, 1987), Vol. 2.

[10] H. Giesekus, "Zur stabilität von strömungen viskoelastischer flüssigkeiten," Rheol. Acta **5**, 239 (1966).

[11] W. M. Abed, R. D. Whalley, D. J. Dennis, and R. J. Poole, "Experimental investigation of the impact of elastic turbulence on heat transfer in a serpentine channel," J. Non-Newtonian Fluid Mech. **231**, 68–78 (2016).

[12] A. Groisman and V. Steinberg, "Efficient mixing at low Reynolds numbers using polymer additives," Nature **410**, 905 (2001).

[13] P. Shakeri, M. Jung, and R. Seemann, "Effect of elastic instability on mobilization of capillary entrapments," Phys. Fluids **33**, 113102 (2021).

[14] R. H. Ewoldt, M. T. Johnston, and L. M. Caretta, *In Complex Fluids in Biological Systems* (Springer, 2015), pp. 207–241.

[15] K. Hyun, M. Wilhelm, C. O. Klein, K. S. Cho, J. G. Nam, K. H. Ahn, S. J. Lee, R. H. Ewoldt, and G. H. McKinley, "A review of nonlinear oscillatory shear tests: Analysis and application of large amplitude oscillatory shear (LAOS)," Prog. Polym. Sci. **36**, 1697–1753 (2011).

[16] E. Balkovsky, A. Fouxon, and V. Lebedev, "Turbulence of polymer solutions," Phys. Rev. E **64**, 056301 (2001).

[17] Y. Jun and V. Steinberg, "Polymer concentration and properties of elastic turbulence in a von Karman swirling flow," Phys. Rev. Fluids **2**, 103301 (2017).

[18] V. Steinberg, "Scaling relations in elastic turbulence," Phys. Rev. Lett. **123**, 234501 (2019).

[19] C. A. Browne and S. S. Datta, "Elastic turbulence generates anomalous flow resistance in porous media," Sci. Adv. **7**, eabj2619 (2021).

[20] T. T. Perkins, D. E. Smith, and S. Chu, "Direct observation of tube-like motion of a single polymer chain," Science **264**, 819 (1994).

[21] N. Tyagi and B. J. Cherayil, "The relaxation dynamics of single flow-stretched polymers in semidilute to concentrated solutions," J. Chem. Phys. **154**, 024907 (2021).

[22] E. S. Shaqfeh, "The dynamics of single-molecule DNA in flow," J. Non-Newtonian Fluid Mech. **130**, 1 (2005).

[23] P. LeDuc, C. Haber, G. Bao, and D. Wirtz, "Dynamics of individual flexible polymers in a shear flow," Nature **399**, 564 (1999).

[24] A. Fouxon and V. Lebedev, "Spectra of turbulence in dilute polymer solutions," Phys. Fluids **15**, 2060 (2003).

[25] S. Berti, A. Bistagnino, G. Boffetta, A. Celani, and S. Musacchio, "Two-dimensional elastic turbulence," Phys. Rev. E **77**, 055306 (2008).

[26] F. Cruz, R. Poole, A. Afonso, F. Pinho, P. Oliveira, and M. Alves, "Influence of channel aspect ratio on the onset of purely-elastic flow instabilities in three-dimensional planar cross-slots," J. Non-Newtonian Fluid Mech. **227**, 65 (2016).

[27] H. Garg, E. Calzavarini, and S. Berti, "Statistical properties of two-dimensional elastic turbulence," Phys. Rev. E **104**, 035103 (2021).

[28] E. S. Shaqfeh, "Purely elastic instabilities in viscometric flows," Annu. Rev. Fluid Mech. **28**, 129 (1996).

[29]T. Burghelea, E. Segre, and V. Steinberg, "Elastic turbulence in von Karman swirling flow between two disks," Phys. Fluids **19**, 053104 (2007).

[30]S. J. Haward, G. H. McKinley, and A. Q. Shen, "Elastic instabilities in planar elongational flow of monodisperse polymer solutions," Sci. Rep. **6**, 33029 (2016).

[31]X. Shi and G. F. Christopher, "Growth of viscoelastic instabilities around linear cylinder arrays," Phys. Fluids **28**, 124102 (2016).

[32]A. Soulies, J. Aubril, C. Castelain, and T. Burghelea, "Characterisation of elastic turbulence in a serpentine micro-channel," Phys. Fluids **29**, 083102 (2017).

[33]G. Yao, J. Zhao, H. Yang, M. A. Haruna, and D. Wen, "Reynolds number effect on drag control via spanwise wall oscillation in turbulent channel flows," Phys. Fluids **31**, 085108 (2019).

[34]S. S. Datta, A. M. Ardekani, P. E. Arratia, A. N. Beris, I. Bischofberger, J. G. Eggers, J. E. López-Aguilar, S. M. Fielding, A. Frishman, M. D. Graham, J. S. Guasto, S. J. Haward, S. Hormozi, G. H. McKinley, R. J. Poole, A. Morozov, V. Shankar, E. S. G. Shaqfeh, A. Q. Shen, H. Stark, V. Steinberg, G. Subramanian, and H. A. Stone, "Perspectives on viscoelastic flow instabilities and elastic turbulence," arXiv:2108.09841 [physics.flu-dyn] (2021).

[35]R. van Buel and H. Stark, "Characterizing elastic turbulence in the three-dimensional von Kármán swirling flow using the Oldroyd-B model," Phys. Fluids **34**, 043112 (2022).

[36]L. Casanellas, M. A. Alves, R. J. Poole, S. Lerouge, and A. Lindner, "The stabilizing effect of shear thinning on the onset of purely elastic instabilities in serpentine microflows," Soft Matter **12**, 6167–6175 (2016).

[37]A. M. Howe, A. Clarke, and D. Giernalczyk, " Flow of concentrated viscoelastic polymer solutions in porous media: Effect of M W and concentration on elastic turbulence onset in various geometries," Soft Matter **11**, 6419–6431 (2015).

[38]D. Kawale, E. Marques, P. L. Zitha, M. T. Kreutzer, W. R. Rossen, and P. E. Boukany, "Elastic instabilities during the flow of hydrolyzed polyacrylamide solution in porous media: Effect of pore-shape and salt," Soft Matter **13**, 765 (2017).

[39]X. Chen, H. Marschall, M. Schäfer, and D. Bothe, "A comparison of stabilisation approaches for finite-volume simulation of viscoelastic fluid flow," Int. J. Comput. Fluid Dyn. **27**, 229 (2013).

[40]H.-C. Tseng, "A revisitation of White−Metzner viscoelastic fluids," Phys. Fluids **33**, 057115 (2021).

[41]K. Tatsumi, Y. Takeda, K. Suga, and K. Nakabe, "Turbulence characteristics and mixing performances of viscoelastic fluid flow in a serpentine micro-channel," J. Phys.: Conf. Ser. **318**(9), 092020 (2011).

[42]Y. Jun and V. Steinberg, "Power and pressure fluctuations in elastic turbulence over a wide range of polymer concentrations," Phys. Rev. Lett. **102**, 124503 (2009).

[43]A. Malm and T. Waigh, "Elastic turbulence in entangled semi-dilute DNA solutions measured with optical coherence tomography velocimetry," Sci. Rep. **7**, 1186 (2017).

[44]R. Lindken, M. Rossi, S. Große, and J. Westerweel, "Micro-particle image velocimetry (μPIV): Recent developments, applications, and guidelines," Lab Chip **9**, 2551 (2009).

[45]S. J. Beresh, "Time-resolved particle image velocimetry," Meas. Sci. Technol. **32**, 102003 (2021).

[46]A. Schröder and C. E. Willert, *Particle Image Velocimetry: New Developments and Recent Applications* (Springer Science & Business Media, 2008), Vol. 112.

[47]A. Groisman and V. Steinberg, "Elastic turbulence in curvilinear flows of polymer solutions," New J. Phys. **6**, 29 (2004).

[48]B. Qin and P. E. Arratia, "Characterizing elastic turbulence in channel flows at low Reynolds number," Phys. Rev. Fluids **2**, 083302 (2017).

[49]S. J. Muller, R. G. Larson, and E. S. Shaqfeh, "A purely elastic transition in Taylor-Couette flow," Rheol. Acta **28**, 499 (1989).

[50]T. Burghelea, E. Segre, and V. Steinberg, "Validity of the Taylor hypothesis in a random spatially smooth flow," Phys. Fluids **17**, 103101 (2005).

[51]G. I. Taylor, "The spectrum of turbulence," Proc. Roy. Soc. London, Ser. A **164**, 476 (1938).

[52]G. Berkooz, P. Holmes, and J. L. Lumley, "The proper orthogonal decomposition in the analysis of turbulent flows," Annu. Rev. Fluid Mech. **25**, 539 (1993).

[53]E. De Angelis, C. M. Casciola, V. S. L'vov, R. Piva, and I. Procaccia, "Drag reduction by polymers in turbulent channel flows: Energy redistribution between invariant empirical modes," Phys. Rev. E **67**, 056312 (2003).

[54]K. D. Housiadas, A. N. Beris, and R. A. Handler, "Viscoelastic effects on higher order statistics and on coherent structures in turbulent channel flow," Phys. Fluids **17**, 035106 (2005).

[55]P. Gutierrez-Castillo and B. Thomases, "Proper orthogonal decomposition (POD) of the flow dynamics for a viscoelastic fluid in a four-roll mill geometry at the Stokes limit," J. Non-Newtonian Fluid Mech. **264**, 48 (2019).

[56]P. Holmes, J. L. Lumley, G. Berkooz, and C. W. Rowley, *Turbulence, Coherent Structures, Dynamical Systems and Symmetry* (Cambridge University Press, 2012).

[57]J. L. Lumley, *Transition and Turbulence* (Elsevier, 1981), pp. 215–242.

[58]B. Podvin and Y. Fraigneau, "A few thoughts on proper orthogonal decomposition in turbulence," Phys. Fluids **29**, 020709 (2017).

[59]K. Taira, S. L. Brunton, S. T. Dawson, C. W. Rowley, T. Colonius, B. J. McKeon, O. T. Schmidt, S. Gordeyev, V. Theofilis, and L. S. Ukeiley, "Modal analysis of fluid flows: An overview," AIAA J. **55**, 4013 (2017).

[60]P. J. Schmid, D. S. Henningson, and D. Jankowski, "Stability and Transition in Shear Flows. Applied Mathematical Sciences, Vol. 142," Appl. Mech. Rev **55**, B57 (2002).

[61]L. Sirovich, "Turbulence and the dynamics of coherent structures. I. Coherent structures," Q. Appl. Math. **45**, 561 (1987).

[62]A. Chatterjee, Curr. Sci. **78**, 808 (2000), available at https://www.jstor.org/stable/24103957.

[63]API, *API Recommended Practice 63 (RP63)* (API, 1990).

[64]A. Clarke, A. M. Howe, J. Mitchell, J. Staniland, and L. A. Hawkes, "How viscoelastic-polymer flooding enhances displacement efficiency," SPE J. **21**, 0675 (2016).

[65]P. Shakeri, M. Jung, and R. Seemann, "Scaling purely elastic instability of strongly shear thinning polymer solutions," Phys. Rev. E **105**, L052501 (2022).

[66]H. A. Barnes, J. F. Hutton, and K. Walters, *An Introduction to Rheology* (Elsevier, 1989), Vol. 3.

[67]O. Maklad and R. Poole, "A review of the second normal-stress difference; its importance in various flows, measurement techniques, results for various complex fluids and theoretical predictions," J. Non-Newtonian Fluid Mech. **292**, 104522 (2021).

[68]J. L. White and A. B. Metzner, "Development of constitutive equations for polymeric melts and solutions," J. Appl. Polym. Sci. **7**, 1867–1889 (1963).

[69]T. Burghelea and V. Bertola, *Transport Phenomena in Complex Fluids* (Springer, 2020), Vol. 598.

[70]Y. Xia and G. M. Whitesides, "Soft lithography," Annu. Rev. Mater. Sci. **28**, 153–184 (1998).

[71]M. Olsen and R. Adrian, "Out-of-focus effects on particle image visibility and correlation in microscopic particle image velocimetry," Exp. Fluids **29**, S166 (2000).

[72]J. Westerweel, "Fundamentals of digital particle image velocimetry," Meas. Sci. Technol. **8**, 1379 (1997).

[73]Y. Son, "Determination of shear viscosity and shear rate from pressure drop and flow rate relationship in a rectangular channel," Polymer **48**, 632–637 (2007).

[74]P. D. Gennes, "Coil-stretch transition of dilute flexible polymers under ultrahigh velocity gradients," J. Chem. Phys. **60**, 5030 (1974).

[75]S. J. Haward, C. C. Hopkins, and A. Q. Shen, "Stagnation points control chaotic fluctuations in viscoelastic porous media flow," Proc. Natl. Acad. Sci. **118**, e2111651118 (2021).

[76]J. Beaumont, N. Louvet, T. Divoux, M.-A. Fardin, H. Bodiguel, S. Lerouge, S. Manneville, and A. Colin, "Turbulent flows in highly elastic wormlike micelles," Soft Matter **9**, 735 (2013).

[77]M. Grilli, A. Vázquez-Quesada, and M. Ellero, "Transition to turbulence and mixing in a viscoelastic fluid flowing inside a channel with a periodic array of cylindrical obstacles," Phys. Rev. Lett. **110**, 174501 (2013).

[78]P.-G. D. Gennes, "Reptation of a polymer chain in the presence of fixed obstacles," J. Chem. Phys. **55**, 572 (1971).

112

[79]L. Ducloué, L. Casanellas, S. J. Haward, R. J. Poole, M. A. Alves, S. Lerouge, A. Q. Shen, and A. Lindner, "Secondary flows of viscoelastic fluids in serpentine microchannels," Microfluid. Nanofluid. **23**, 33 (2019).

[80]R. Poole, A. Lindner, and M. Alves, "Viscoelastic secondary flows in serpentine channels," J. Non-Newtonian Fluid Mech. **201**, 10 (2013).

[81]B. Knight and L. Sirovich, "Kolmogorov inertial range for inhomogeneous turbulent flows," Phys. Rev. Lett. **65**, 1356 (1990).

[82]L. Guglielmini, R. Rusconi, S. Lecuyer, and H. A. Stone, "Three-dimensional features in low-Reynolds-number confined corner flows," J. Fluid Mech. **668**, 33–57 (2011).

Effect of viscoelasticity on displacement processes in porous media

M. Jung[1,2], **Authors:** P. Shakeri[1,2], and R. Seemann[1,2]

[1]Experimental Physics, Saarland University, 66123 Saarbrücken,Germany

[2]Max Planck Institute for Dynamics and Self-Organization, 37077 Göttingen, Germany

Author contributions:

Planning the experiments, conducting the research, and analyzing the experimental results were performed by M. Jung and P. Shakeri. The simulations were performed by P. Shakeri. The article was written by P. Shakeri, M. Jung and R. Seemann. The research work was directed by R. Seemann.

Abstract:

Improving the displacement efficiency of capillary entrapments in porous media by adding high molecular weight polymers to the invading phase has various industrial applications, from enhanced oil recovery to soil remediation. Apart from an increased viscosity contrast compared to regular water flooding, the flow of viscoelastic polymer solutions exhibits unstable flow behavior even at small Reynolds numbers, which can lead to an additional displacement mechanism of the capillary entrapments. In this work, we employ a microfluidic approach to unravel the underlying physics and mechanism of this enhanced pore scale displacement. To this end, we show that the major complex topological flow features in a typical porous medium can be mimicked by a flow geometry consisting of a single capillary entrapment connected to two symmetric serpentine channels. This design excludes the effect of viscous stresses and allows direct focus on displacement processes driven solely by elastic stresses. We show that the unique viscoelastic fluid features, such as the significant storage and release of elastic stresses and first normal stress difference, combined with the flow geometry, lead to purely elastic instability and secondary flow, which in turn provide the stresses necessary to overcome the capillary threshold and displace the capillary entrapment.

frontiers | Frontiers in Physics

Effect of viscoelasticity on displacement processes in porous media

Michael Jung[1,2][*][†], Pegah Shakeri[1,2][†] and Ralf Seemann[1,2]

[1]Experimental Physics and Center for Biophysics, Saarland University, Saarbrücken, Germany, [2]Max Planck Institute for Dynamics and Self-Organization, Göttingen, Germany

Improving the displacement efficiency of capillary entrapments in porous media by adding high molecular weight polymers to the invading phase has various industrial applications, from enhanced oil recovery to soil remediation. Apart from an increased viscosity contrast compared to regular water flooding, the flow of viscoelastic polymer solutions exhibits unstable flow behavior even at small Reynolds numbers, which can lead to an additional displacement mechanism of the capillary entrapments. In this work, we employ a microfluidic approach to unravel the underlying physics and mechanism of this enhanced pore scale displacement. To this end, we show that the major complex topological flow features in a typical porous medium can be mimicked by a flow geometry consisting of a single capillary entrapment connected to two symmetric serpentine channels. This design excludes the effect of viscous stresses and allows direct focus on displacement processes driven solely by elastic stresses. We show that the unique viscoelastic fluid features, such as the significant storage and release of elastic stresses and first normal stress difference, combined with the flow geometry, lead to purely elastic instability and secondary flow, which in turn provide the stresses necessary to overcome the capillary threshold and displace the capillary entrapment.

1 Introduction

Displacement processes in porous media are ubiquitous in a variety of natural settings and technical applications Pinder and Gray [1]; Blunt [2]; Singh et al. [3]; Bear and Verruijt [4]. At low flow rates, i.e., at sufficiently small capillary numbers (ratio of viscous to capillary forces) the advance of an invading fluid sweeping out an immiscible defending fluid is governed by the wettability of the porous medium Zhao et al. [5]; Jung et al. [6]; Singh et al. [3]. Thus, these displacement processes are mainly controlled by geometrical properties, i.e., the pore-throat size distribution. This typically leads to ramified displacement patterns, where large portions of the defending fluid remain trapped by capillary forces. For an invading wetting fluid these entrapments of the defending fluid are preferentially located at the center of pores or throats, while for intermediate to non-wetting invading fluids the residual defending fluid commonly remains trapped at narrow gaps and dead ends, or spreads as films Zhang et al. [7]; Emami Meybodi et al. [8]. A schematic sketch to illustrate the different types of capillary entrapment is given in Figure 1. Mobilization of these capillary entrapments in porous media is important in soil remediation Zhong et al. [9]; Smith et al. [10]; Cao et al. [11]; Ghosh et al. [12]; Philippe et al. [13], cleaning filtration membranes Li et al. [14]; Salama [15], and enhanced oil recovery Muggeridge et al. [16].

115

Regardless of the wettability of the porous medium, an increase of the viscosity of the invading fluid, i.e., increasing the capillary number, leads to a suppression of capillary fingers. Therefore, a more homogeneous flow profile and consequently an improved sweep efficiency is achieved when increasing the viscosity of the invading fluid Lenormand et al. [17]. Furthermore, experiments using inelastic fluids as invading phase reveal that an increased capillary number results in breakup of large entrapments of the defending fluid Krummel et al. [18], while entrapments in smaller pores with large capillary pressure threshold are barely affected Lacey et al. [19]. However, theoretical and experimental studies Zhang et al. [7]; Buchgraber et al. [20]; Afsharpoor et al. [21]; Nilsson et al. [22]; Clarke et al. [23]; Mitchell et al. [24]; Parsa et al. [25] show that the remaining saturation of the defending fluid is often distinctly lower than expected after invasion by a viscoelastic polymer solution with high molecular weight compared to inelastic invading fluids even at the same viscosity and capillary number Huifen et al. [26]; Qi et al. [27]; Salmo et al. [28]. This implies that, apart from the increased capillary number, an additional driving mechanism must be active to reduce the residual saturation caused by the invasion of viscoelastic fluids. Although it is meanwhile a consolidated hypothesis that the improvements of the sweep efficiency by viscoelastic polymer flooding can be attributed to the elastic properties of such fluids, the underlying fundamental mechanisms remain obscure Urbissinova et al. [29]; Clarke et al. [30]; Rock et al. [31]. Various displacement mechanisms were proposed in the literature including a strip-off of oil films attached to pore walls caused by an apparent slip length Beaumont et al. [32]; Wei et al. [33], reducing the effective permeability of porous media by polymer retention Ekanem et al. [34]; Zhu et al. [35], mobilization of oil entrapments by an apparent shear-thickening effect as a consequence of purely elastic instability Clarke et al. [23]; Mitchell et al. [24]; Xie et al. [36]; Clarke et al. [30]; Kawale et al. [37]; Browne and Datta [38], as well as breakup, and pulling effects originating from normal stress differences that remove oil from dead ends Zhang et al. [7]; Lima et al. [39]; Wang et al. [40]; Fan et al. [41]. However, displacement processes in natural porous media might be affected by some if not by all the listed mechanisms, yet it remains an open question which mechanism prevails to (re-) mobilize capillary entrapments.

Due to the opacity and inherent complexity of porous media such as soil, rock, or filter membranes, direct observation of the underlying mechanisms of mobilization of capillary entrapments is generally challenging. Therefore, it is necessary to develop simplified model systems that mimic the characteristic features of the rather complex flow of viscoelastic polymer solutions in random porous media. To address these issues, microfluidic model systems raised interest among researchers Galindo-Rosales et al. [42]; Browne et al. [43]; Kumar et al. [44]. Several experimental and numerical studies have been focused on basic designs representing simplified porous media such as straight channels embedded with single cylinders Hemingway et al. [45]; Qin and Arratia [46]; Qin et al. [47], uniform or random post arrays Khomami and Moreno [48]; Ichikawa and Motosuke [49]; Haward et al. [50]; Walkama et al. [51], a single pore formed by four disks De et al. [52]; Gillissen [53], and converging-diverging channels Ekanem et al. [54]; Galindo-Rosales et al. [55]; Kumar et al. [56]; Ekanem et al. [57]. However, even in the simplest designs used so far, description of viscoelastic flow is still very complex due to a wide distribution of flow velocity (and consequently shear rate) caused by the non-constant cross-section of flow pathways in these geometries. Estimating accurate *in-situ* shear rates is particularly important for viscoelastic polymer solutions with concentrations above their overlap concentration c^* because their rheological properties are strongly shear dependent. Therefore, a reliable evaluation of their flow characteristics requires the approximation of an accurate characteristic shear rate. To avoid this issue, alternative designs such as serpentine channels can be employed which are still capable of representing essential features of porous media such as tortuosity. Serpentine channels are particularly advantageous because their constant cross-section allows a single characteristic shear rate $\dot{\gamma}$ to be assigned to the entire geometry, which facilitates the description of viscoelastic flows.

In this work, we used a microfluidic approach to experimentally investigate the displacement mechanism for the mobilization of capillary entrapments by viscoelastic polymer solutions in the semi-dilute regime, where viscosity and relaxation time are shear dependent. To tackle this question effectively, we first performed a series of displacement experiments in a quasi-two-dimensional porous medium with various Newtonian and non-Newtonian fluids to separate the effects of viscosity and elasticity. In order to focus on the influence of elastic stresses and eliminate the influence of viscosity on the displacement process, we employed a single capillary entrapment enclosed by two symmetrical serpentine channels and varied the degree of elasticity by using polymer solutions with different concentration and molecular weight. To exclude inertial effects, all experiments were performed at low Reynolds numbers, i.e., Re < $O(10^0)$.
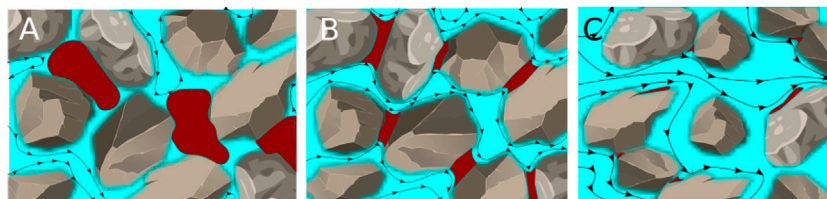

FIGURE 1
Sketch of potential types of capillary entrapments for water wet grains **(A)**, intermediate wet grains **(B)**, and oil wet grains **(C)**. The invading water phase is colored blue, whereas the defending oil phase is colored red. The arrows indicate the path lines of the invading fluid.
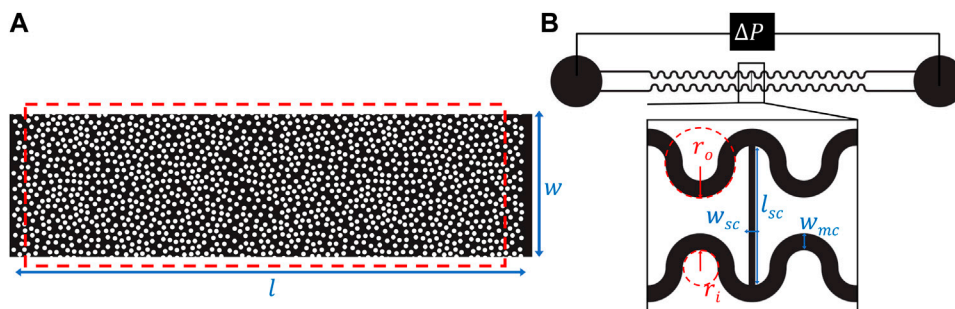
116

FIGURE 2
Sketches of the employed microfluidic geometries: **(A)** Random arrangement of about 1,400 cylinders with a diameter $d \approx 0.032$ mm, and a height $h_1 \approx$ 0.030 mm. The array has the lateral dimensions of $l = 3.5$ mm and $w = 1$ mm, The red box indicates the field of view; **(B)** Two symmetric serpentine channels with a width $w_{mc} = 0.125$ mm that are connected by a perpendicular side channel with a width of $w_{sc} = 0.050$ mm and a length of $l_{sc} = 1$ mm. The inner and outer radii of curvature of the serpentine channels were $r_i = 0.125$ mm and $r_o = 0.250$ mm. The height h_2 of the microfluidic channels was approximately 0.045 mm.

2 Materials and methods

2.1 Microfluidic setup

Two different microfluidic geometries were employed in this study and are shown in Figure 2. In order to model a porous medium, we considered a random array of about 1,400 mono-disperse cylinders and a porosity of $\phi = 0.7$ [Figure 2A]. The cylinders had a diameter $d \approx$ 0.032 mm, a height $h_1 \approx 0.030$ mm and an average center-to-center distance of (0.027 ± 0.013) mm. The field of view had a width and length of 1 mm, respectively 3 mm, resulting in a pore-volume (PV) of $6.3 \cdot 10^{-11}$ m³. To explore the sole impact of elasticity and to rule out the effects of viscous forces on the displacement mechanism, a single-pore geometry was designed which included two identical serpentine channels with a width $w_{mc} = 0.125$ mm that were connected by a perpendicular side channel with a width $w_{sc} = 0.050$ mm, as sketched in Figure 2B. The dimensions of the serpentine channels and the side channel were chosen to ensure entrapment of the defending fluid in the side channel by capillary forces. The devices for both designs were made from the UV-curable glue NOA 83H (Norland optical adhesive). They were fabricated using standard soft lithographic methods; details of device fabrication are described elsewhere Jung et al. [6]; Shakeri et al. [58].To conduct the microfluidic experiments, both types of devices were placed on an inverted microscope (MeF3, Reichert-Jung) equipped with ×2 and ×4 magnification to observe the flow in the porous medium and single-pore geometry, respectively. The illumination was done with a LED light source in transmission. Images were captured using a 16 bit sCMOS camera (PCO Panda 4.2) at a maximum frame rate of 40 fps at full resolution of (2048 × 2048) pixels. The corresponding pixel resolution with respect to the applied magnification was 1.5 μm/pixel for the porous medium and 0.7 μm/pixel for the single-pore geometry. All experiments were conducted at room temperature of $(20 \pm 1)°$C. To enable fluid injection at a controlled volumetric flow rate, the inlet of the microfluidic device was connected to a high-precision, pulsation-free syringe pump (neMESYS, Cetoni GmbH). Both microfluidic geometries were first fully saturated with dodecane. Then, the respective invading fluid was injected at a constant flow rate for the displacement experiments with the random post array. In the case of the single-pore geometry, the initial condition was established

by slowly injecting the invading fluids, removing all the oil from the serpentine channel and leaving the oil entrapment in the connecting side channel. Once this situation was established, the flow rate was stepwise increased until complete desaturation of the side channel was achieved. The maximum Reynolds number in all experiments was in the order of Re ~ $\mathcal{O}(10^0)$ and thus effects of inertia on the flow could be neglected. Besides, in all experiments, the outlet was connected to a fluid reservoir located at the same level as the microfluidic device to avoid back pressure due to gravity. To measure the hydrodynamic pressure difference along the single-pore geometry, a board-mounted differential pressure sensor (26PC series, Honeywell) was placed between the inlet and outlet as sketched in Figure 2B.

2.2 Working fluids

As non-Newtonian working fluids, we used aqueous solutions of the polyelectrolytes Flopaam 3630 ($M_{w,3630} \approx 18.7$ MDa, SNF Floerger), Flopaam 3330 ($M_{w,3330} \approx 6.5$ MDa, SNF Floerger), and Xanthan gum ($M_{w,Xanthan} \approx 15$ MDa Holzwarth [59], Sigma Aldrich) that are industrially used as viscosifier Sorbie [60]; Mahajan et al. [61]. Polymers of the Flopaam series are synthetic, partially hydrolyzed polyacrylamides (HPAM, 30% hydrolysis) with very flexible polymer chains, while Xanthan gum is a rather stiff polysaccharide produced from simple sugars in a fermentation process by adding *Xanthomonas campestris* bacteria Sorbie [60]. The sample solutions with different polymer concentrations were diluted from their respective stock solutions using 17 mM NaCl-solution following standard protocols Shakeri et al; [58,62]. The salt concentration was rather in the low-salt limit and not sufficient to screen all charges of the polyelectrolytes Dobrynin et al; [63]. By applying the Huggins—Kraemer method Mezger [64], we determined the overlap concentrations to be $c^\star_{3630} \approx 82$ ppm, $c^\star_{3330} \approx 137$ ppm, and $c^\star_{Xanthan} \approx 91$ ppm, respectively. The prepared concentrations of 1,000 ppm (0.1 w%) and 2,000 ppm (0.2 w%) of Flopaam 3630, 1,300 ppm (0.13 w%) and 2,500 ppm (0.25 w%) of Flopaam 3330, and 2,000 ppm (0.2 w%) of Xanthan gum were at least 10 times larger than the respective overlap concentration $c^\star$, to assure that the solutions were in the semi-dilute entangled regime. As Newtonian reference cases, we used purified water, as well as 67 w% and 85 w% aqueous glycerin
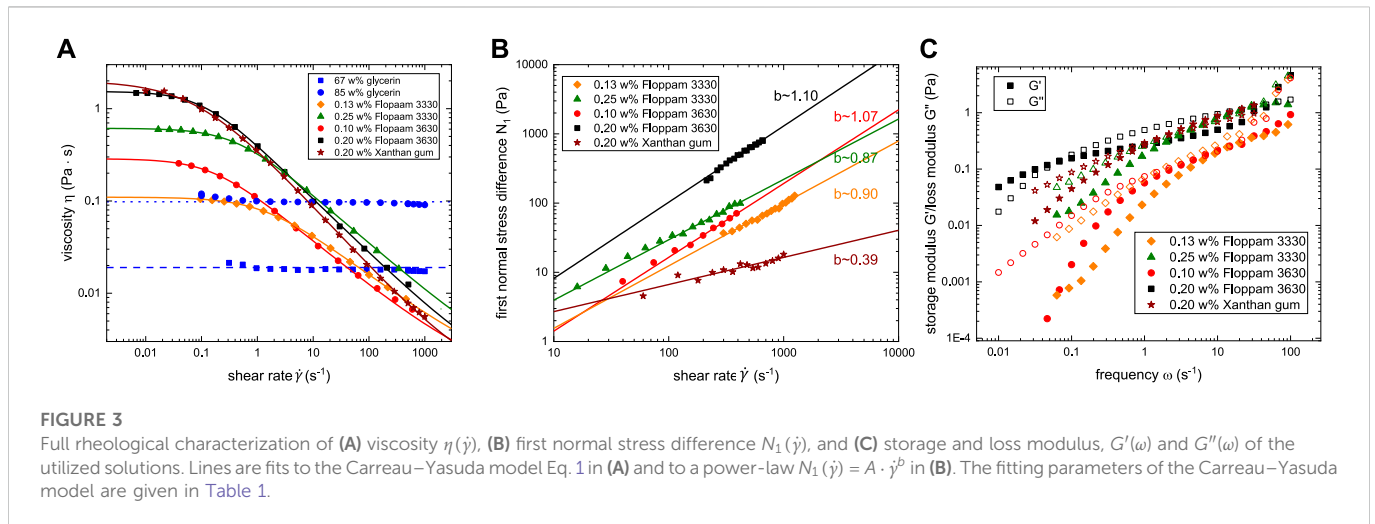
117

FIGURE 3
Full rheological characterization of **(A)** viscosity $\eta(\dot\gamma)$, **(B)** first normal stress difference $N_1(\dot\gamma)$, and **(C)** storage and loss modulus, $G'(\omega)$ and $G''(\omega)$ of the utilized solutions. Lines are fits to the Carreau–Yasuda model Eq. 1 in **(A)** and to a power-law $N_1(\dot\gamma) = A \cdot \dot\gamma^b$ in **(B)**. The fitting parameters of the Carreau–Yasuda model are given in Table 1.

TABLE 1 Fitting parameters of Carreau–Yasuda model for viscosity Eq. 1: η_0 is the zero-shear viscosity; Λ is a characteristic time; a is a transition control factor; and n is the power law exponent associated with the degree of shear-thinning. η_∞ was fixed to the solvent viscosity 0.001 Pa·s for all used polymer solutions.

Polymer	η_0 [Pa·s]	Λ [s]	a	n
0.13 w% Flopaam 3330	0.109 ± 0.001	0.72 ± 0.02	0.87 ± 0.01	0.54 ± 0.01
0.25 w% Flopaam 3330	0.612 ± 0.003	2.37 ± 0.16	0.99 ± 0.04	0.47 ± 0.01
0.10 w% Flopaam 3630	0.287 ± 0.003	6.43 ± 0.25	0.99 ± 0.04	0.50 ± 0.01
0.20 w% Flopaam 3630	1.535 ± 0.011	9.33 ± 0.81	1.07 ± 0.05	0.41 ± 0.02
0.20 w% Xanthan gum	1.863 ± 0.173	13.27 ± 1.53	0.83 ± 0.10	0.38 ± 0.01

TABLE 2 Density (ϱ) measured by a pycnometer (Blaubrand, Brand GmbH), as well as interfacial tension (σ) determined by pendant drop method, and advancing (θ_{adv}) and receding contact angle (θ_{rec}) of the utilized combinations of invading fluids and dodecane determined by sessile drop needle-in method using the contact angle measurement device (OCA 25, DataPhysics). It should be noted that the addition of HPAM, respectively Xanthan gum (XG) to water did neither alter the interfacial tension nor the wettability.

Invading fluid	ϱ [g/cm³]	σ [mN/m]	θ_{adv} [°]	θ_{rec} [°]
purified water	1.00 ± 0.01	50 ± 1	125 ± 4	< 20
water with HPAM/XG	1.00 ± 0.01	50 ± 1	125 ± 4	< 20
67 w% glycerin	1.18 ± 0.01	32 ± 1	125 ± 4	< 20
85 w% glycerin	1.22 ± 0.01	29 ± 2	125 ± 4	< 20

(Grüssing GmbH) solutions. A full rheological characterization of the utilized solutions including steady shear step measurements to determine the shear viscosity $\eta(\dot\gamma)$ and the first normal stress difference $N_1(\dot\gamma)$ as well as small amplitude frequency sweep tests to determine the storage modulus $G'(\omega)$ and the loss modulus $G''(\omega)$ were performed using a rotational rheometer (HAAKE MARS 40, Thermo Scientific) and the results are shown in Figure 3.

The defending fluid in all experiments, dodecane (Merck), has a constant dynamic viscosity of $\eta_{dodecane}$ = 1.4 mPa·s at room temperature of (20 ± 1)°C. Dodecane was initially filtered three times in a column of aluminum oxide powder (Al_2O_3, Sigma Aldrich) to remove any potential surface-active contaminants. To increase the optical contrast of the fluids in the microfluidic device, 0.5 w% of the non-surface-active dye oil-red-o (Sigma Aldrich) was added to the purified dodecane. The properties of the used fluid combinations are summarized in Table 2.

For visualization of flow path lines, 0.01 w% green fluorescent particles (2 μm, FluoroMax, Thermo Fisher) were added to the aqueous phase and imaged via fluorescence microscopy (Axiophot, Zeiss, equipped with a filter cube appropriate for excitation and emission wavelength of 475/40 nm and 530/50 nm, respectively). We have confirmed that the addition of the particles did not affect the physical or rheological properties of the utilized fluids.

2.3 Viscoelastic fluid model and dimensionless numbers

As presented in Figure 3, the studied polymer solutions exhibited strong shear-thinning viscosity $\eta(\dot\gamma)$ and a non-quadratic first normal stress difference $N_1(\dot\gamma)$. Such fluids can commonly be described by the constitutive White–Metzner (WM) fluid model Bodiguel et al. [65]; Soulies et al; [66]; Casanellas et al; [67]. In this work, we applied the WM-model to describe the rheological properties and consequently to compute the relevant dimensionless numbers. Fundamentals of the WM-model can be found elsewhere Macosko [68]; Barnes et al; [69]; Burghela and Bertola [70]; White and Metzner [71]; Tseng [72]. The supporting computational fluid dynamics (CFD) simulations in this work were based on an imaginary shear-thinning fluid having the same fitting parameters for the shear-thinning viscosity, but no elasticity component, using a generalized Newtonian fluid model ANSYS [73].

To represent the shear dependent total viscosity $\eta(\dot\gamma)$ of the polymer solutions, we employed the Carreau–Yasuda model:

$$\eta(\dot\gamma) - \eta_\infty = (\eta_0 - \eta_\infty)\left[1 + (\Lambda\dot\gamma)^a\right]^{\frac{n-1}{a}} \qquad (1)$$

Here η_0 and η_∞ are the zero-shear viscosity and viscosity at infinite shear rates, respectively, Λ is a characteristic time, n is the power law

118

exponent associated with the degree of shear-thinning, and a is a transition control factor. The shear dependent relaxation time $\lambda(\dot{\gamma})$ was calculated from the shear viscosity, $\eta(\dot{\gamma})$, and the first normal stress difference, $N_1(\dot{\gamma})$:

$$\lambda(\dot{\gamma}) = N_1(\dot{\gamma}) \Big/ 2[\eta(\dot{\gamma}) - \eta_\infty]\dot{\gamma}^2 \qquad (2)$$

The complex shear modulus $G(\omega)$ can be computed from the generalized Maxwell model $G(\omega) = G'(\omega) + iG''(\omega)$, where $G'(\omega)$ and $G''(\omega)$ are given by Eqs 3, 4. The discrete relaxation time spectrum λ_k and the corresponding shear moduli G_k were obtained by fitting the experimentally measured $G'(\omega)$ and $G''(\omega)$ data in Figure 3C to these equations with $N = 4$ elements. In this context, G_0 is the largest shear modulus corresponding to the smallest relaxation time Shakeri et al. [62].

$$G'(\omega) = \sum_{k=1}^{N} G_k \frac{(\lambda_k \cdot \omega)^2}{1 + (\lambda_k \cdot \omega)^2} \qquad (3)$$

$$G''(\omega) = \sum_{k=1}^{N} G_k \frac{\lambda_k \cdot \omega}{1 + (\lambda_k \cdot \omega)^2} \qquad (4)$$

To estimate the degree of elasticity during flow of the polymer solutions, several dimensionless numbers can be calculated within the framework of the White–Metzner model. The Deborah number De is defined as the ratio of the polymer relaxation time to a characteristic residence time in the flow:

$$De = \frac{\eta(\dot{\gamma})\,U}{G_0\,\mathcal{R}}, \qquad (5)$$

here $\mathcal{R}$ is the minimum radius of the curved streamlines and U is the average velocity. The Weissenberg number Wi is defined as the ratio of elastic stresses to the shear stress $\tau = 2\,\eta(\dot{\gamma})\,\dot{\gamma}$, and thus given by

$$Wi = \frac{N_1(\dot{\gamma})}{2\,\eta(\dot{\gamma})\,\dot{\gamma}}. \qquad (6)$$

Based on these two dimensionless numbers, the stress ratio M can be calculated by Morozov and van Saarloos [74]; Pakdel and McKinley [75]; McKinley et al. [76]; Shakeri et al. [62].

$$M = \sqrt{De\,Wi} = \sqrt{\frac{\eta(\dot{\gamma})\,U}{G_0\,\mathcal{R}}\,\frac{N_1(\dot{\gamma})}{2\,\eta(\dot{\gamma})\,\dot{\gamma}}}. \qquad (7)$$

The stress ratio M is of particular interest, since exceeding a critical value M_{crit} characterizes the onset of purely elastic instability, i.e., an unstable flow of viscoelastic fluids at low Reynolds numbers. The value of M_{crit} depends on the particular geometry, the type, and concentration of the polymer and salt in the solution, as well as on the type of solvent, and is commonly in the range of 1–6 Morozov and van Saarloos [74]; Yao et al. [77].

3 Results and Discussion

3.1 Displacement processes in a random post array

Exploring the impact of viscoelastic fluid properties on displacement processes in porous media requires to disentangle the effects of viscosity and elasticity. To this aim, we conducted a series of

experiments employing three Newtonian fluids with different viscosity (water, 67w% and 85w% glycerin solution), a shear-thinning inelastic Xanthan gum solution (0.2w%), and a shear-thinning highly elastic HPAM solution (0.2w% Flopaam 3630) as invading fluids, displacing dodecane at a constant applied volumetric flow rate. The evolving displacement patterns, as well as the configuration of the remaining saturation of the defending fluid after injecting 200 PV and 1,200 PV of the invading fluid, are shown in Figure 4.

Prior to the experiments presented in this section, we experimentally determined a critical capillary number $Ca_{crit} \approx 10^{-4}$ as an upper threshold for purely capillary dominated displacement for our specific microfluidic design, and for the advancing contact angle of $\theta_{adv} = (125 \pm 4)°$ for all used invading fluids. The capillary number was approximated by $Ca = (\eta(\dot{\gamma})\,U)/\sigma$, where $\eta(\dot{\gamma})$ is the shear dependent viscosity and U is the average velocity. The shear rate was approximated by $\dot{\gamma} = U/\sqrt{k\,\phi}$ Berg and van Wunnik [78]; Browne and Datta [38]. Here, the average velocity was calculated by $U = Q/(A\,\phi)$, where Q is the flow rate, A the cross-section of the channel, ϕ the porosity, and k the absolute permeability. The absolute permeability of the microfluidic device $k = U \cdot \eta/(-dp/dx) \approx 1.59 \cdot 10^{-11}\,\text{m}^2$ was calculated from Darcy law. The pressure gradient (dp/dx) was computed *via* CFD simulation of water flooding (here it was assumed that the permeability is constant for a specific porous medium and does not depend on the type of invading fluid De et al. [52]). The applied flow rate was set to $Q = 4\,\mu\text{L/min}$ in all experiments, and the capillary number was varied by varying the viscosity of the invading fluid.

Figure 4A shows the evolution of the displacement pattern for water displacing dodecane at a capillary number of $Ca_{water} \approx 8 \cdot 10^{-6}$. The observed displacement fronts appeared to be branched and followed the geometrical most favorable pathways, indicating that the displacement is fully capillary dominated. Further injection of 200 PV and 1,200 PV of water in Figures 4B, C had no impact on configuration of the remaining saturation. Experiments using 67w% glycerin solution as invading fluid and hence increasing the capillary number to $Ca_{glycerin_{67}} \approx 5 \cdot 10^{-5}$, exhibited no significant influence on the initial evolution of the displacement pattern in Figure 4D compared to water. This is expected as the applied capillary number was still below the critical threshold that was determined to $Ca_{crit} \approx 10^{-4}$ for this system. However, injection of 200 PV and 1,200 PV of 67w% glycerin solution in Figures 4E, F led to a reduction in the maximum size of the entrapments and hence to a lower remaining saturation of the defending fluid compared to water invasion. This observation is in line with the fact that by increasing the capillary number, the maximum size of the entrapments is controlled by the competition of viscous to capillary forces Krummel et al. [18]. Further increase of the capillary number above Ca_{crit} by invasion of 85w% glycerin solution $(Ca_{glycerin_{85}} \approx 3 \cdot 10^{-3})$, viscous forces of the invading fluid gain importance. As visible in Figure 4G, the formation of capillary fingers was suppressed and the front advance was more compact. Injection of 200 PV of 85w% glycerin solution led to a reduction in size of the entrapments in Figure 4H. However, injection of 1,200 PV of 85w% glycerin solution in Figure 4I had no visible impact on the configuration of the remaining saturation since the capillary pressure threshold to mobilize small entrapments is seemingly too large to overcome. After benchmarking the Ca dependent displacement behavior in our porous model geometry for Newtonian fluids, we address now potential deviations of the displacement pattern by
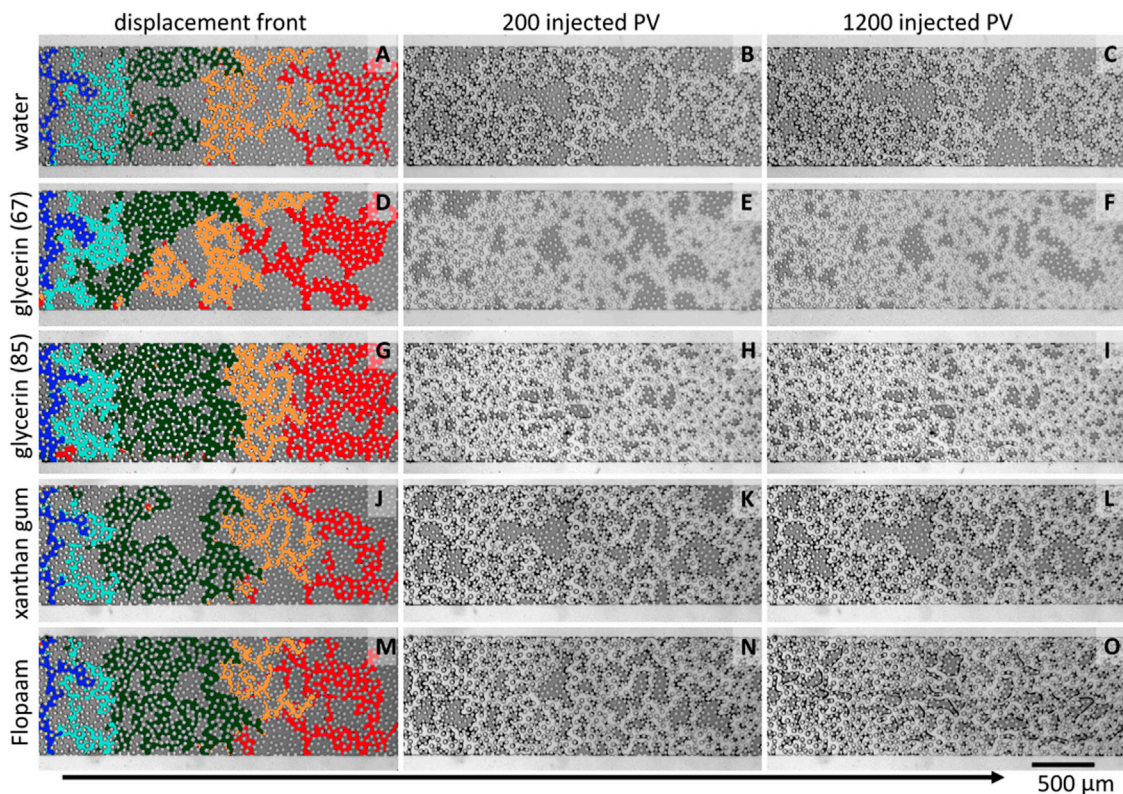
119

FIGURE 4
Snapshots of the displacement pattern for **(A–C)** water ($Ca_{water} = 8 \cdot 10^{-6}$), **(D–F)** 67 $w\%$ glycerin ($Ca_{glycerin_{67}} = 5 \cdot 10^{-5}$), **(G–I)** 85 $w\%$ glycerin ($Ca_{glycerin_{85}} = 3 \cdot 10^{-3}$), **(J–L)** 0.20 $w\%$ Xanthan gum ($Ca_{Xanthan} = 9 \cdot 10^{-5}$), and **(M–O)** 0.20 $w\%$ Flopaam 3630 ($Ca_{HPAM} = 8 \cdot 10^{-5}$). The first column shows a compiled image of the displacement patterns for about 0.05 PV (dark blue), 0.15 PV (bright blue), 0.30 PV (green), 0.45 PV (orange), and 0.60 PV (red) of the invading fluid. The second and third column show displacement pattern for 200 PV, and 1,200 PV of the invading fluid. As indicated by the arrow, the main flow direction was from left to right.

invasion of non-Newtonian fluids. Invasion of the shear-thinning inelastic Xanthan gum solution at $Ca_{Xanthan} \approx 9 \cdot 10^{-5}$ led initially to a branched displacement pattern with large entrapments in Figure 4J. Compared to invasion by the Newtonian invading fluids in Figures 4A, D, no impact of the shear-thinning property on the evolution of the front was detectable for slow invasion processes. Since all experiments involving non-Newtonian fluids as invading fluids were performed at very low capillary numbers, a strong influence of the shear-thinning properties of the polymer solutions on the morphology of the displacement front is not expected De et al; [79]; Mitchell et al; [24]. Similar to the displacement experiment with water, injection of 200 PV and 1,200 PV of Xanthan gum solution in Figures 4K, L had no significant impact on configuration of the remaining saturation. This finding is particularly remarkable because the corresponding capillary number was even slightly larger than in the experiments with 67w% glycerin solution, in which a reduction of entrapments was observed. This could be explained by the fact that the strong shear-thinning viscosity of Xanthan gum solution dampens the impact of viscous forces when the inlet pressure increases during the continuous injection. Employing the viscoelastic HPAM solution as invading fluid at $Ca_{HPAM} \approx 8 \cdot 10^{-5}$, we observed again a branched evolution of the displacement pattern in Figure 4M. Analogous to the case of Xanthan gum, invasion of 200 PV HPAM solution did not significantly alter the configuration of the remaining saturation in Figure 4N. In contrast, a

substantially different displacement pattern was observed after injecting 1,200 PV of Flopaam 3630 [Figure 4O]. Large entrapments have been broken up and only small ones at the smallest throats remain. A zoomed-in view of the displacement process can be seen in the time series for Xanthan gum and Flopaam 3630 in Figure 5 and the corresponding movies in the Supplementary material Video S1. While the fluid–fluid interfaces of the Xanthan gum/dodecane interfaces were stable throughout the experiment, the Flopaam/dodecane interfaces began to fluctuate after a certain time. These fluctuations seemed to cause the large entrapments to break up and eventually be displaced completely.

To investigate the causes of the observed fluctuations, we visualized the path lines of the invading fluid by adding fluorescent particles to the aqueous phase. Figure 6 illustrates the path lines of the invading 85 $w\%$ glycerin solution, panel (a), respectively of the viscoelastic HPAM solution, panel (b), displacing dodecane [movies in Supplementary material Video S2]. Despite the similar viscosity of the invading fluids for both experiments, the path lines appeared to be distinctly different. Viscoelastic flow in Figure 6B featured crossing path lines, semi three-dimensional effects, and fluctuations of the fluid–fluid interfaces of the entrapped oil, which were absent for the inelastic flow in Figure 6A. A possible explanation for the observed unstable flow can be the occurrence of purely elastic instability. This instability is a unique feature in viscoelastic flow at low Reynolds
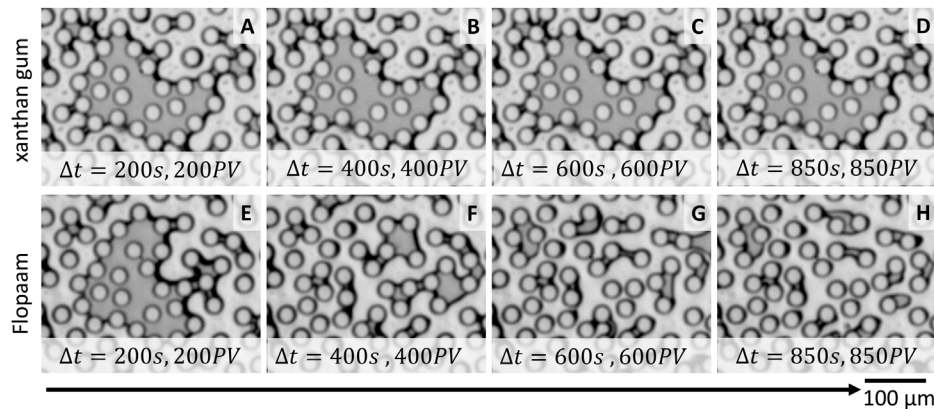
120

FIGURE 5
Time series of optical images of a capillary entrapment displaced by 0.20 *w%* Xanthan gum **(A−D)**, and 0.20 *w%* Flopaam 3630 **(E−H)**. As indicated by the arrow, the main flow direction was from left to right.
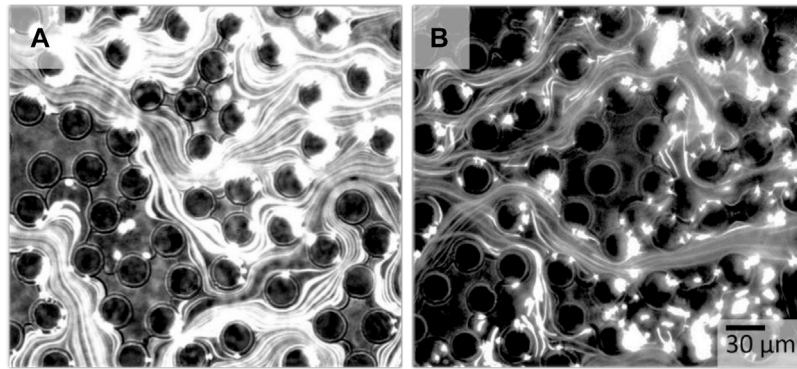

FIGURE 6
Path lines obtained by fluorescence microscopy for an invading Newtonian glycerin solution, respectively viscoelastic polymer solution displacing dodecane. In **(A)** the Newtonian glycerin solution follows symmetrical the tortuous path lines of the porous medium, whereas the viscoelastic HPAM solution exhibits asymmetric and even crossing path lines in **(B)**, which represents an unsteady flow.

numbers, and it is linked to the molecular behavior of the polymers in solution Shaqfeh [80]; Groisman and Steinberg [81,82]. Such viscoelastic highly flexible polymers are strongly deformable. Specially at high shear rates, their deformation during the flow is strongly anisotropic. This anisotropic deformation causes anisotropic distribution of elastic stresses in 3D. The difference of the stress components in the observation plane, i.e., in x- and y-direction, causes a first normal stress difference N_1 acting in the out-of-plane direction. If the ratio of N_1 to the shear stress τ exceeds a critical stress ratio McKinley et al. [76]; Pakdel and McKinley [75]; Morozov and van Saarloos [74]; Shakeri et al. [62], the base flow becomes unstable and strongly fluctuating fluid–fluid interfaces are caused. Since the stress distribution of Newtonian fluids is isotropic and solutions of the rather stiff Xanthan gum do not develop a significant first normal stress difference N_1, the base flow and consequently the fluid–fluid interfaces remained stable for inelastic fluids.

However, precise quantification of the contribution of elastic and viscous stresses, e.g., by computing the stress ratio M, Eq. 7, for flow of semi-dilute polymer solutions in porous media, is challenging for two major reasons. First, from a rheological point of view, due to the shear-thinning viscosity and relaxation time of the polymer solution in this concentration regime, and non-uniform distribution of shear rate in the porous media, defining a characteristic viscosity and relaxation time is not straightforward. Second, the complex flow geometry makes it difficult to estimate the radius of curvature of the streamlines $\mathcal{R}$, since a single flow path curvature can not be assigned to the entire geometry. Besides, the occurrence of purely elastic instability lead to an increased flow resistance, i.e., increased apparent viscosity Shaqfeh [80]; Groisman and Steinberg [81,83]; Kawale et al. [37]; Shakeri et al. [58]; Browne and Datta [38]; Datta et al. [84]. Therefore, a distinct separation of viscosity- and elasticity-related effects is unfeasible employing a random arrangement of posts as representative for porous media.

3.2 Flow properties of porous media

It is well known that increasing the viscosity of the invading fluids leads to an improved displacement efficiency. By comparing the
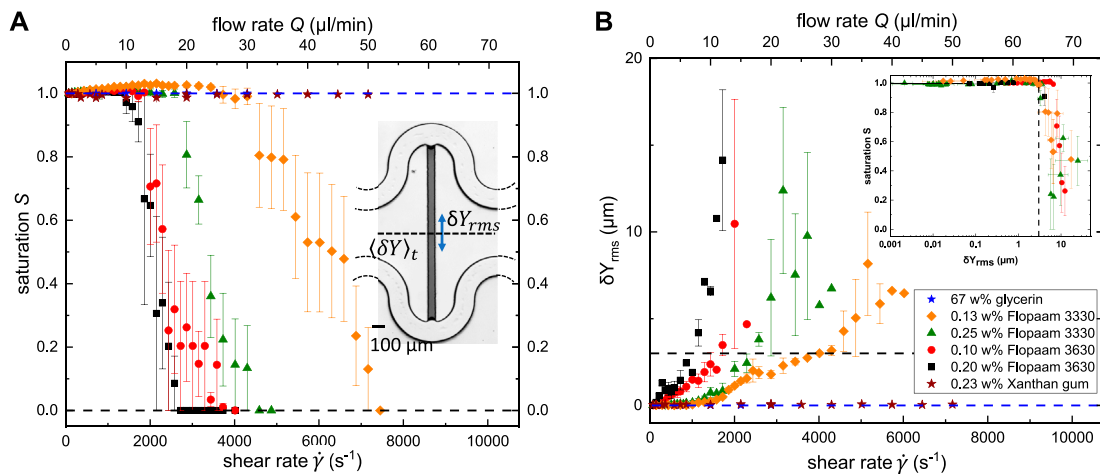
121

FIGURE 7
(A) Remaining oil saturation *S* in the side channel, and **(B)** root-mean-square (rms) of δY_{rms} as function of the applied flow rate (top) and corresponding shear rate (bottom). The insets display an optical image of microfluidic geometry in **(A)**, and the remaining oil saturation *S* as a function of δY_{rms} in **(B)**. The dashed line in **(B)** indicates the strength of fluctuation of $\delta Y_{rms} \approx 3\,\mu m$ required to trigger the mobilization of the entrapped oil. The symbols in **(A)** and **(B)** represent experimental data for 67 *w%* glycerin (blue star), 0.13 *w%* Flopaam 3330 (orange diamond), 0.25 *w%* Flopaam 3330 (green triangle), 0.10 *w%* Flopaam 3630 (red circle), 0.20 *w%* Flopaam 3630 (black square), and 0.20 *w%* Xanthan gum (brown star).

displacement pattern resulting from an invasion with Xanthan gum, respectively Flopaam in the previous section, we observed, that elasticity driven interfacial fluctuations contribute as well to an increased displacement. However, since the turbulent flow related to the observed fluctuations leads also to an increase of an apparent viscosity, it is *per se* not possible to differentiate the effects of these increased apparent viscosity and the fluctuations due to their interconnected nature. Hence, to decompose these combined contributions, we needed to design a more simplified model system, which is still capable to mimic the characteristic flow features in porous media, such as the mixed distribution of flow types. Thus, in order to construct such a model system, we must start by identifying the characteristic flow features in porous media. In fact, flow in porous media is composed of an interplay of regions of shear flow in the vicinity of solid walls, as well as of extensional regions of converging–diverging flows away from the walls and at stagnation points at the front and rear poles of obstacles in a flow James [85]; Kawale et al. [37]; De et al. [86]; Poole [87]; Mokhtari et al. [88]. De et al. De et al. [86] performed direct numerical simulations to determine the flow type distribution for invasion of a viscoelastic fluid in a randomized porous medium assembled by bi-disperse disks. In their simulations, the pore structure triggered tortuous flow paths that enforce the polymers to undergo repetitive contraction and expansion. De et al. observed a predominance of shear dominated flow regions for the full range of the considered Deborah numbers, while the extent of extensional regions was further reduced at higher degree of elasticity. Moreover, in this numerical study, it was proven that the largest normal stress differences in a porous medium were generated in a shear dominated flow region rather than in extensional regions. The primary importance of shear flow has also been confirmed in other works, where it has been demonstrated that the normal stress differences responsible for an increased pressure gradient are mainly generated in shear dominated regions De et al. [52]; Ekanem et al. [54], and most of the energy of viscoelastic stresses

is dissipated in these regions De et al. [86]; Gillissen [53]. In summary, the elastic nature of the polymer fluid is more pronounced when coupled with the extensional nature of the flow field Kawale et al. [37]; Walkama et al. [51]; Haward et al. [50]; Ichikawa and Motosuke [49], however extensional flow is not essential to observe elasticity-induced flow instabilities. In fact, the most important feature is tortuosity, i.e., curved path lines that cause a sufficiently strong first normal stress difference of viscoelastic fluids. Thus, serpentine channels with constant cross-section are suitable model systems for porous media. Viscoelastic flow in serpentine channels is very well characterized in the literature and are straightforward to be described Soulies et al. [66]; Zilz et al. [89]; Shakeri et al. [90]; Poole et al. [91]; Ducloué et al. [92].

3.3 Displacement of single capillary entrapment

As previously discussed, serpentine channels are well suited to mimic tortuous flow in porous media, while the perpendicular side channel connecting the two serpentine channels of our microfluidic geometry represents the location for capillary entrapment of the defending fluid [Figure 2B]. The symmetry of the serpentine channels, in conjunction with a shared inlet and outlet, ensures equal viscous pressure at both ends of the side channel. Hence, our microfluidic model system corresponds to a single capillary entrapment in a porous medium, where the effect of elastic stresses at the fluid interfaces can be isolated from the effects of viscous stresses. In the following experiments, we studied the impact of the degree of elasticity of the invading fluid on the displacement mechanism of the capillary entrapment. To this aim, we used as invading fluids four different viscoelastic HPAM solutions (i.e., for two different molecular weights and two concentrations each), an inelastic shear-thinning Xanthan gum solution, and a high viscous
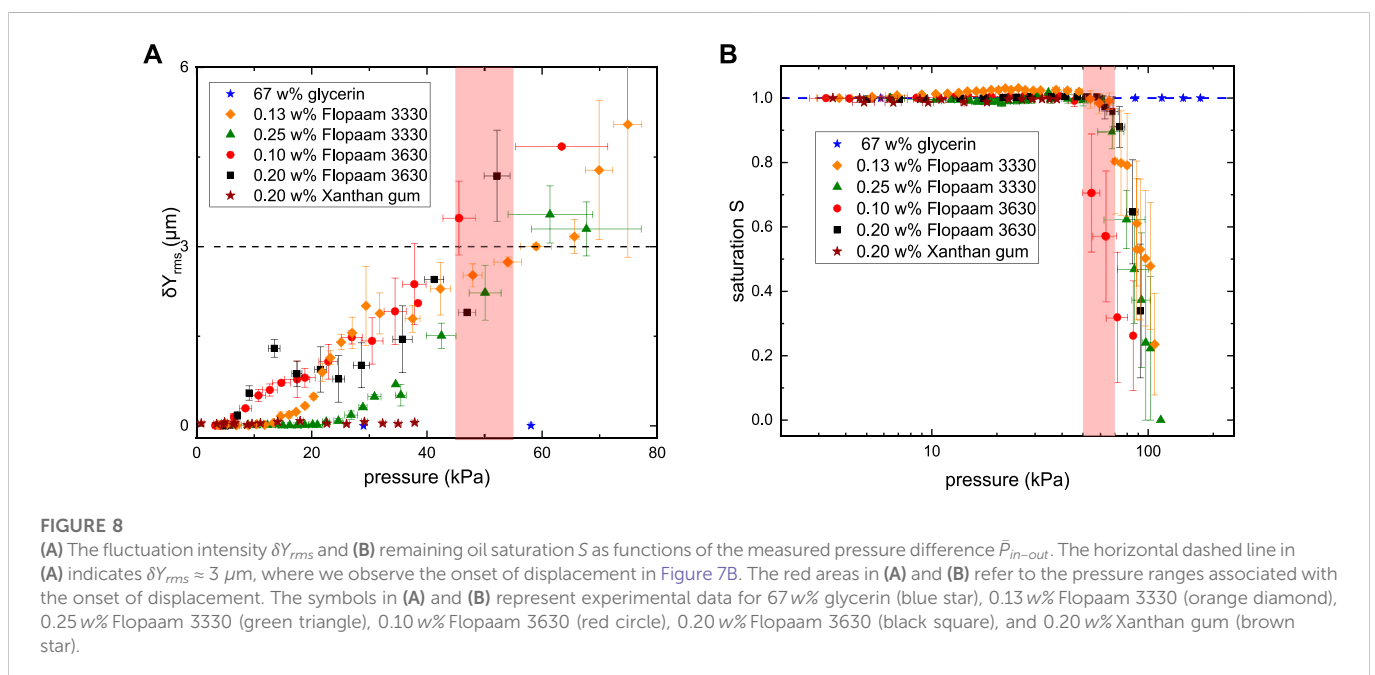
122

TABLE 3 Overview of the experimentally preset flow rate Q_{crit}, the ratio of polymer concentration to overlap concentration c/c^*, the approximate shear rate $\dot{\gamma}_{crit}$ determined from **Figure 9,** and critical stress ratio M_{crit} at the onset of purely elastic instability computed from **Eq. 7.**

Polymer	c/c^*	Q_{crit} [$\mu l/min$]	$\dot{\gamma}_{crit}$ [s^{-1}]	M_{crit}
0.13 *w%* Flopaam 3330	≈ 10	14.0 ± 0.2	2006 ± 28	5.32 ± 0.27
0.25 *w%* Flopaam 3330	≈ 18	12.0 ± 0.2	1719 ± 28	4.24 ± 0.21
0.10 *w%* Flopaam 3630	≈ 12	2.5 ± 0.2	358 ± 28	4.06 ± 0.20
0.20 *w%* Flopaam 3630	≈ 24	2.0 ± 0.2	286 ± 28	3.99 ± 020

Newtonian glycerin solution. We initially saturated the single-pore geometry with dodecane, and subsequently stepwise increased the flow rate of the invading fluid. The experiments were stopped either when a complete removal of the oil phase from the perpendicular side channel was observed, or a maximum Reynolds number in the order of 10^0 was reached to avoid any contribution from inertia. To study the interactions between the flow in the serpentine channel and the entrapment at the side channel, we captured time series of the area shown in the inset of Figure 7A at each applied flow rate. To ensure that a fully developed steady-state flow was established while recording fluid–fluid interface fluctuations, we used the simultaneously measured pressure signal as a reference and started recording at each flow rate after the pressure reached a stable plateau. The saturation S of the oil in the side channel and the fluctuating motion of the fluid–fluid interface could be extracted from the recorded time series. The corresponding results are plotted in Figure 7 as a function of shear rate, which was approximated by $\dot{\gamma} = 4Q/(\pi r^3)$ with the equivalent radius of $r = \sqrt{(W\,H)/\pi}$ Son [93]. Even though this approach neglects the slightly non-parabolic flow profile of shear-thinning fluids and does not account for a possible apparent wall-slip effect of non-Newtonian fluids, we have previously shown that this approximation is sufficiently accurate for the employed serpentine channels Shakeri et al; [62]. The saturation S in

Figure 7A was defined as the area of the oil column at the end of each recording step, normalized by the area of the oil column in the first step. Desaturation was initiated once the fluid—fluid interface was depinned from the edges of the side channel and $S < 1$. It should be mentioned that for increasing shear rates, the menisci of the trapped oil column get more bulged towards the serpentine channel. This effect led to saturation values which are slightly larger than one. Interfacial motion was described quantitatively based on the motion of the center of mass, δY, of the entrapped oil column. To quantify the strength of the interfacial motion, we calculated the root-mean-square δY_{rms} for each shear rate and plotted the results in Figure 7B. For $\delta Y_{rms} > 0.015\,\mu m$ (i.e., for δY_{rms} values exceeding the noise level of the experimental setup), optically visible motion of the fluid–fluid interface was clearly detectable and increased with the shear rate. At the lowest applied shear rate of $\dot{\gamma} \approx 72\ s^{-1}$, the fluid–fluid interface was stationary for all utilized invading fluids. When solutions of glycerin or Xanthan gum were employed as the invading phase, the fluid–fluid interface remained stationary across the full range of applied shear rates. Accordingly, no oil displacement was observed from the side channel despite the rather high viscosity of these solutions [Figure 7A]. However, when a viscoelastic polymer solution was injected, the fluid–fluid interface began to wobble above a certain shear rate. The intensity of this wobbling motion increased monotonically as the shear rate was further increased. The corresponding shear rates at which wobbling was initially detected were significantly lower for polymers with higher molecular weight, while they were rather independent of concentration, cf. Table 3. Eventually, displacement of the entrapped oil phase from the side channel was initiated for all utilized HPAM solutions when the fluid–fluid interface fluctuations were sufficiently intense at $\delta Y_{rms} \approx 3\,\mu m$ [dashed horizontal line in the inset of Figure 7B].

Simultaneously with the optical recordings, we measured the corresponding pressure drop $\Delta P(t) = \langle P \rangle_t + \Delta P'(t)$ across the serpentine channels, where $\langle P \rangle_t = \bar{P}_{in-out}$ is the time averaged steady-state mean value, and $\Delta P'(t)$ is a fluctuating component of the pressure. For the viscoelastic HPAM solutions, the strength

FIGURE 8
(A) The fluctuation intensity δY_{rms} and **(B)** remaining oil saturation S as functions of the measured pressure difference $\bar{P}_{in-out}$. The horizontal dashed line in **(A)** indicates $\delta Y_{rms} \approx 3\,\mu m$, where we observe the onset of displacement in Figure 7B. The red areas in **(A)** and **(B)** refer to the pressure ranges associated with the onset of displacement. The symbols in **(A)** and **(B)** represent experimental data for 67 *w%* glycerin (blue star), 0.13 *w%* Flopaam 3330 (orange diamond), 0.25 *w%* Flopaam 3330 (green triangle), 0.10 *w%* Flopaam 3630 (red circle), 0.20 *w%* Flopaam 3630 (black square), and 0.20 *w%* Xanthan gum (brown star).
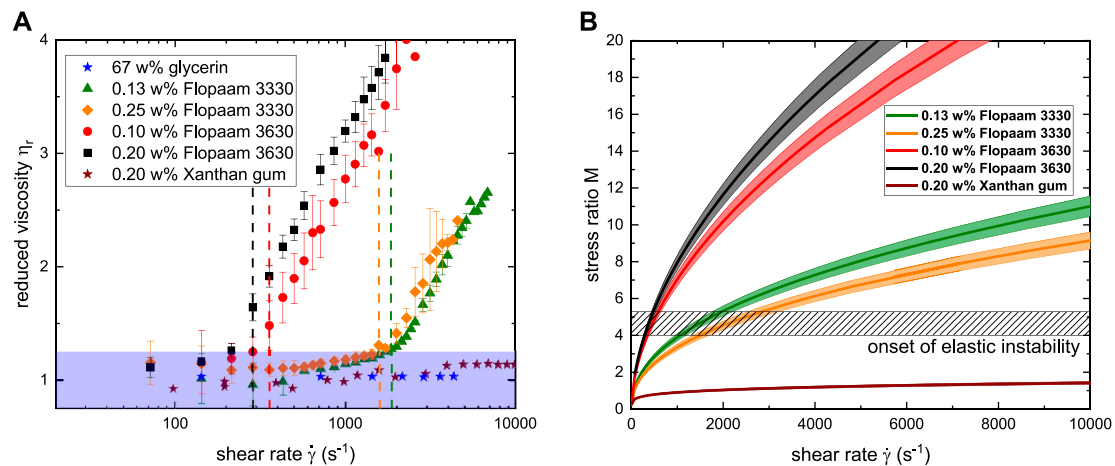
123

FIGURE 9
(A) Reduced viscosity η_r and **(B)** stress ratio M as function of shear rate $\dot{\gamma}$. The symbols in **(A)** represent data for 67 $w\%$ glycerin (blue star), 0.13 $w\%$ Flopaam 3330 (orange diamond), 0.25 $w\%$ Flopaam 3330 (green triangle), 0.10 $w\%$ Flopaam 3630 (red circle), 0.20 $w\%$ Flopaam 3630 (black square), and 0.20 $w\%$ Xanthan gum (brown star). The blue area in **(A)** indicates a laminar base flow where $\eta_r < 1.15$. The dashed vertical lines in **(A)** as well the shaded area in **(B)** indicate the onset of purely elastic instability.

of fluctuations of the fluid–fluid interface δY_{rms} raised monotonic with the measured pressure $\bar{P}_{in-out}$ [Figure 8A]. Interestingly, the required strength of fluctuations $\delta Y_{rms} \approx 3\,\mu m$ to overcome the capillary pressure that keeps the entrapment in place was achieved at a similar pressure $\bar{P}_{in-out} \approx 50$ kPa for all HPAM solutions, independent of polymer type and concentration. However, since there was no displacement in case of the inelastic invasion of glycerin and Xanthan gum solutions, during the entire range of the experiments, it is evident that the magnitude of the pressure, $\bar{P}_{in-out}$, cannot drive the displacement. Instead, the displacement mechanism can be explained with respect to the fluctuating component of the pressure, $\Delta P'(t)$, in the serpentine channels Shakeri et al. [58].

To examine the underlying mechanism that caused the fluctuations, we converted $\bar{P}_{in-out}$ to an apparent viscosity $\eta_{app}(\dot{\gamma}) = \tau(\dot{\gamma})/\dot{\gamma}$, where the shear stress in a serpentine channel was approximated by $\tau = (\Delta P\, H\, W)/(2L(W + H))$ Machado et al. [94]. Comparison of the apparent viscosity $\eta_{app}(\dot{\gamma})$ with the extrapolated bulk viscosity values $\eta(\dot{\gamma})$ from Figure 3 revealed that, above a critical shear rate $\dot{\gamma}_{crit}$, the apparent viscosity $\eta_{app}(\dot{\gamma})$ deviated from $\eta(\dot{\gamma})$. Figure 9A shows the reduced viscosity $\eta_r(\dot{\gamma}) = \eta_{app}(\dot{\gamma})/\eta(\dot{\gamma})$ as function of the shear rate $\dot{\gamma}$ for all studied polymer solutions. We identified the critical shear rate $\dot{\gamma}_{crit}$ at the onset of instability when the reduced viscosity exceeds 1.15 cf. Table 3. The value of 1.15 was chosen to ensure that the reduced viscosity η_r clearly exceeds our experimental accuracy. In general, a reduced viscosity significantly larger than one is a signature of turbulent flow. Since the maximum Reynolds number in our experiments was on the order of Re ~ $\mathcal{O}(10^0)$, potential inertial contributions to the observed increase in flow resistance could be safely neglected. This is confirmed by the fact that no increased reduced viscosity was detected for the inelastic Xanthan gum and glycerin solutions. Hence, the increase of the reduced viscosity η_r for the four HPAM-solutions was associated with purely elastic instability at low Reynolds numbers Browne and

Datta [38]; Groisman and Steinberg [81]. Moreover, the occurrence of purely elastic instability is also reflected by the stress ratio M. In the utilized serpentine channels, we detected the onset of instability for $M \gtrsim 4$, cf. Figure 9B, in line with reported values in literature for similar geometries Pakdel and McKinley [75]; McKinley et al. [76]; Shakeri et al. [62]. However, in case of the two Flopaam 3330 solutions, the wobbling motion started already at shear rates well below $\dot{\gamma}_{crit}$ [Figure 7B]. This suggests that the unstable base flow due to purely elastic instability is not the only explanation for the observed fluctuating interfaces.

In fact, the observed interfacial fluctuations prior to the onset of purely elastic instability were also affected by elastic secondary flows, i.e., flows in the cross-stream direction that are much weaker than the flow in the main flow direction Ducloué et al. [92]; Yao et al. [77]; Poole et al. [91]. In this particular geometry, these types of secondary flows result from the difference between the curvatures of the inner and outer bends of the serpentine channel, where the gradient of the first normal stress difference N_1 arises Shakeri et al. [58]. Consequently, a so–called "Hoop stress" emerges and drives the viscoelastic fluid towards the inner bends at the top and bottom of the serpentine channel, where N_1 is the largest. The fluid is then pushed back to the outer part of the serpentine channel at the center plane to complete formation of counter-rotating vortices in the out-of-plane cross-section of the channel. Such elastic secondary flows are present for all applied shear rates in the case of viscoelastic flow, and their strength is expected to increase almost linearly with the applied shear rate for a laminar base flow Zilz et al. [89]. Even though secondary flows occur in the cross-sectional plane perpendicular to the plane of observation and therefore cannot be directly observed with conventional planar microscopy, secondary flow structures can be indirectly sensed by their influence on the flow paths as previously done by, e.g., Groisman and Steinberg [83]; Zilz et al. [89]; Machado et al. [94]; Shakeri et al. [58]. To visualize these secondary flow structures, we added fluorescent particles to the 0.10 $w\%$ Flopaam 3630 solution, as well as to the 0.25 $w\%$ Flopaam 3330 solution and
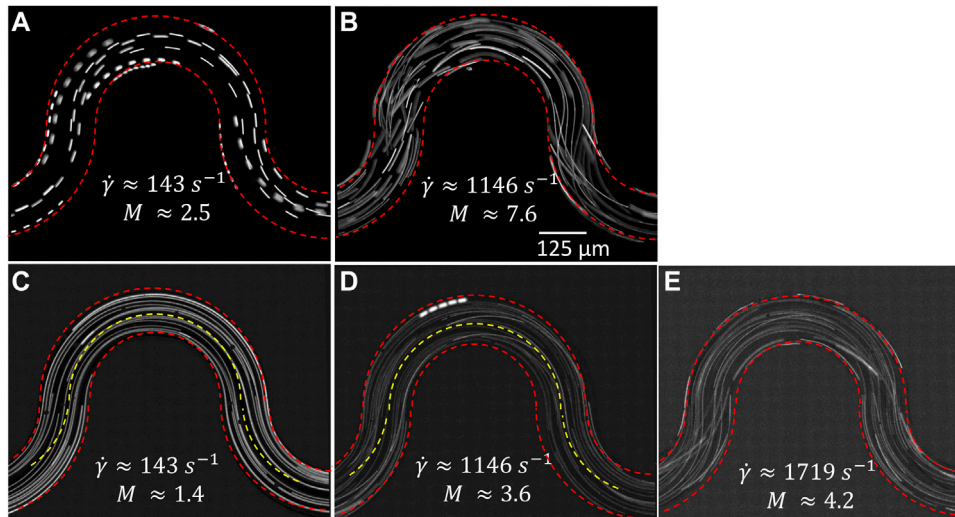
124

FIGURE 10
Path lines obtained by fluorescence microscopy for 0.10 *w%* Flopaam 3630 at **(A)** $\dot{\gamma} \approx 143$ s^{-1} and **(B)** $\dot{\gamma} \approx 1146$ s^{-1}, and 0.25 *w%* Flopaam 3330 at **(C)** $\dot{\gamma} \approx 143$ s^{-1}, **(D)** $\dot{\gamma} \approx 1146$ s^{-1} and **(E)** $\dot{\gamma} \approx 1719$ s^{-1}. The red dashed lines indicate the boundary of the serpentine channels. The yellow dashed lines in **(C)** and **(D)** indicate the center line of the channel as a guide to the eye rates to highlight the evolution from laminar to turbulent flow.

captured the path lines by fluorescence microscopy at shear rates below and above the critical shear rates $\dot{\gamma}_{0.10\ w\%,3630} \approx 358$ s^{-1} and $\dot{\gamma}_{0.25\ w\%,3330} \approx 1719$ s^{-1}, cf. Figure 10. At $\dot{\gamma} \approx 143$ s^{-1} in Figure 10A and Figure 10C, we observed a fully laminar flow, in which the path lines follow the curvature of the serpentine channels. At $\dot{\gamma} \approx 1146$ s^{-1} in Figure 10D, still below the critical shear rate for this solution but corresponding to experiments where we detected already mild interfacial fluctuations, we observe a slight shift of the path lines towards the inner bend of the serpentine channel. At and above the onset of purely elastic instability, at $\dot{\gamma} \approx 1146$ s^{-1} in Figure 10B and $\dot{\gamma} \approx 1719$ s^{-1} in Figure 10E, we observed crossing path lines, and semi three-dimensional effects that were very similar to the observed path lines for highly viscoelastic flow in porous media in Figure 6B.

The contribution of secondary flows to the fluctuations of the fluid–fluid interface in Figure 7B can be further investigated by subjecting the recorded position data δY to power spectral density (PSD) analysis. Figure 11A displays the PSD analysis of δY extracted from the optical images of 0.25 *w%* Flopaam 3330. At the lowest shear rate $\dot{\gamma} \approx 72$ s^{-1}, we observed a plateau, indicating that the fluid–fluid interface remained stationary. At $\dot{\gamma} \approx 716$ s^{-1}, i.e., below $\dot{\gamma}_{crit}$, the PSD curve exhibited still a plateau-like shape although interfacial fluctuations were already optically sensed at this shear rate [Figure 7B]. At further increased shear rates, close to $\dot{\gamma}_{crit} \approx 1576$ s^{-1} and above, a power-law decay $\sim f^{-\beta}$ was observed with two distinct exponents, β_L and β_H, at lower and higher ranges of frequencies. At higher frequencies from 2 Hz to 20 Hz, an exponent β_H in the range of 3–4 is valid. This exponent observed over at least one decade in the frequency domain is commonly reported for turbulent flows originated from the purely elastic instability of dilute polymer solutions Groisman and Steinberg [83], and theoretically derived by Fouxon et al. Fouxon and Lebedev [95] and later Steinberg et al. Steinberg [96] for an Oldyod-B fluid. At lower frequencies from 0.2 Hz to 2 Hz, a smaller exponent β_L in the range of 1–2 exist.While this
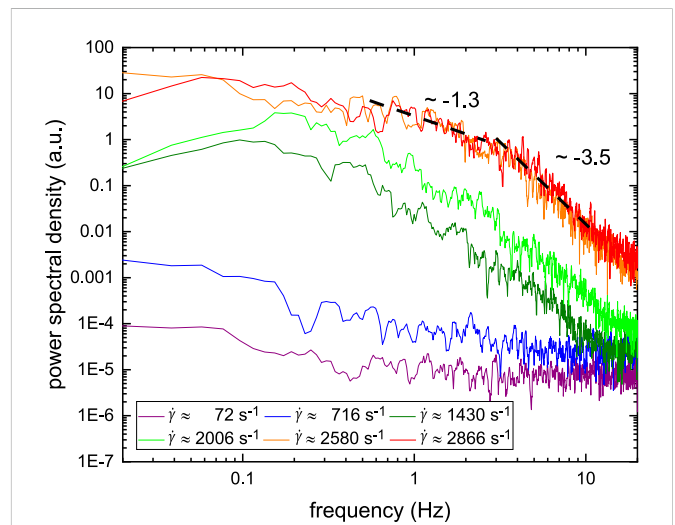

FIGURE 11
PSD analysis of vertical fluctuation of the center position δY of 0.25 *w%* Flopaam 3330 for various shear rates above and below the critical shear rate $\dot{\gamma}_{crit} \approx 1719$ s^{-1} for this solution.

exponent is in a similar range to the Kolmogorov scale 5/3 for inertia-induced turbulence Kolmogorov et al. [97], we can rule this out since the experiments were conducted at small Reynolds numbers. Similar observations were reported for the PSD analysis of the center-of-mass fluctuations of entrapped oil droplets, and pressure fluctuations in viscoelastic flow in porous media, but remained so far unexplained Mitchell et al. [24]; Kawale et al. [37]. We believe that the two distinct exponents can be explained in view of the flow structure underlying the turbulent flow, namely the short-range elastic instability and the elastic secondary flow. In fact, the high range of frequencies from 2 Hz

125

to 20 Hz, correspond to relatively small-scaled fluctuations, originating from purely elastic instability. On the other hand, the lower range of frequencies, from 0.2 Hz to 2 Hz, is associated with relatively large flow structure of the secondary flow. This explanation is supported by our previously published work, which provided a structural analysis of viscoelastic turbulent flow in serpentine channels Shakeri et al. [90]. Applying the proper orthogonal decomposition method on velocity fluctuations obtained by particle image velocimetry of viscoelastic flow in a serpentine channel, we demonstrated that in fact, secondary flows are the dominant feature that contribute to the kinetic energy in viscoelastic flows at high shear rates, but still low Re numbers. When the flow of viscoelastic fluids becomes turbulent, it is reasonable to assume that the stretching of polymers intensifies and hence the evolution of normal stress differences gets amplified. Therefore, the purely elastic instability has an amplifying effect on the secondary flow structures. Thus, the combination of these two elasticity driven phenomena has a synergistic effect on providing the force required to destabilize the interfaces and mobilize the capillary entrapments.

4 Conclusion

In this work, we investigated the underlying mechanism that leads to an improved mobilization of capillary entrapments in porous media by invasion of viscoelastic polymer solutions. To this aim, we conducted a series of displacement experiments employing various Newtonian and non-Newtonian fluids to separate the effects of viscosity and elasticity on the displacement process. While entrapments in large pores were mainly affected by an increased viscosity ratio between the invading and defending fluids, entrapments at small throats with high capillary pressure remained unaffected as long only the capillary number was varied. A distinct behavior was observed during the invasion of viscoelastic polymer solutions, where the fluid–fluid interfaces began to fluctuate. Moreover, small entrapments were affected and were eventually displaced by viscoelastic polymer flooding. However, due to the complexity of flow in porous media, a clear separation of viscosity and elasticity related effects is not straightforward. To tackle this problem, we focused on a single entrapment enclosed by two symmetric serpentine channels that allowed us to study elasticity driven fluctuations while eliminating the influence of viscous forces. We have found out that these fluctuations are caused by a synergetic effect of secondary flows and purely elastic instability generated by a first normal stress difference N_1. The randomness of these fluctuations lead to a symmetry-breaking of the flow paths and is consequently the ultimate cause for the observed mobilization of capillary entrapments in our single-pore geometry. Since in flow in porous media, curved path lines are as well a dominant feature, a similar mechanism is responsible for an enhanced displacement process. However, to address how other features present in the flow in porous media such as elongational flow contribute to the displacement process is an interesting task for future research.

References

1. Pinder GF, Gray WG. *Essentials of multiphase flow and transport in porous media*. Hoboken, NJ: John Wiley & Sons (2008). doi:10.1002/9780470380802

Data availability statement

The raw data supporting the conclusions of this article will be made available by the authors, without undue reservation.

Author contributions

MJ designed the experiments, performed research, and analyzed the experiments. PS designed the experiments, performed research, analyzed the experiments, and conducted simulations. RS acquired funding and directed the research. All authors (MJ, PS, and RS) discussed the results and wrote the manuscript.

Funding

Acknowledgments

Conflict of interest

The authors declare that the research was conducted in the absence of any commercial or financial relationships that could be construed as a potential conflict of interest.

Publisher's note

All claims expressed in this article are solely those of the authors and do not necessarily represent those of their affiliated organizations, or those of the publisher, the editors and the reviewers. Any product that may be evaluated in this article, or claim that may be made by its manufacturer, is not guaranteed or endorsed by the publisher.

Supplementary material

The Supplementary Material for this article can be found online at: https://www.frontiersin.org/articles/10.3389/fphy.2023.1099073/full#supplementary-material

2. Blunt MJ. *Multiphase flow in permeable media: A pore-scale perspective*. Cambridge: Cambridge University Press (2017). doi:10.1017/9781316145098

3. Singh K, Jung M, Brinkmann M, Seemann R. Capillary-dominated fluid displacement in porous media. *Annu Rev Fluid Mech* (2019) 51:429–49. doi:10.1146/annurev-fluid-010518-040342

4. Bear J, Verruijt A. *Modeling groundwater flow and pollution*, 2. Dordrecht, Holland: Springer Science & Business Media (1987). doi:10.1007/978-94-009-3379-8

5. Zhao B, MacMinn CW, Juanes R. Wettability control on multiphase flow in patterned microfluidics. *Proc Natl Acad Sci* (2016) 113:10251–6. doi:10.1073/pnas.1603387113

6. Jung M, Brinkmann M, Seemann R, Hiller T, Sanchez de La Lama M, Herminghaus S. Wettability controls slow immiscible displacement through local interfacial instabilities. *Phys Rev Fluids* (2016) 1:074202. doi:10.1103/PhysRevFluids.1.074202

7. Zhang L, Yue X, Guo F. Micro-mechanisms of residual oil mobilization by viscoelastic fluids. *Pet Sci* (2008) 5:56–61. doi:10.1007/s12182-008-0009-1

8. Emami Meybodi H, Kharrat R, Wang X. Study of microscopic and macroscopic displacement behaviors of polymer solution in water-wet and oil-wet media. *Transport in porous media* (2011) 89:97–120. doi:10.1007/s11242-011-9754-5

9. Zhong L, Oostrom M, Wietsma T, Covert M. Enhanced remedial amendment delivery through fluid viscosity modifications: Experiments and numerical simulations. *J Contaminant Hydrol* (2008) 101:29–41. doi:10.1016/j.jconhyd.2008.07.007

10. Smith MM, Silva JAK, Munakata-Marr J, McCray JE. Compatibility of polymers and chemical oxidants for enhanced groundwater remediation. *Environ Sci Techn* (2008) 42:9296–301. doi:10.1021/es800757g

11. Cao S, Bate B, Hu J, Jung J. Engineering behavior and characteristics of water-soluble polymers: Implication on soil remediation and enhanced oil recovery. *Sustainability* (2016) 8:205. doi:10.3390/su8030205

12. Ghosh J, Tick GR, Akyol NH, Zhang Y. A pore-scale investigation of heavy crude oil trapping and removal during surfactant-enhanced remediation. *J Contaminant Hydrol* (2019) 223:103471. doi:10.1016/j.jconhyd.2019.03.003

13. Philippe N, Davarzani H, Colombano S, Dierick M, Klein P-Y, Marcoux M. Experimental study of the temperature effect on two-phase flow properties in highly permeable porous media: Application to the remediation of dense non-aqueous phase liquids (dnapls) in polluted soil. *Adv Water Resour* (2020) 146:103783. doi:10.1016/j.advwatres.2020.103783

14. Li L, Xu G, Yu H. Dynamic membrane filtration: Formation, filtration, cleaning, and applications. *Chem Eng Techn* (2018) 41:7–18. doi:10.1002/ceat.201700095

15. Salama A. On the dynamics of a meniscus inside capillaries during imbibition and drainage processes: A generalized model, effect of inertia, and a numerical algorithm. *Phys Fluids* (2021) 33:082104. doi:10.1063/5.0061415

16. Muggeridge A, Cockin A, Webb K, Frampton H, Collins I, Moulds T, et al. Recovery rates, enhanced oil recovery and technological limits. *Phil Trans R Soc A: Math Phys Eng Sci* (2013) 372:20120320. doi:10.1098/rsta.2012.0320

17. Lenormand R, Touboul E, Zarcone C. Numerical models and experiments on immiscible displacements in porous media. *J Fluid Mech* (1988) 189:165–87. doi:10.1017/S0022112088000953

18. Krummel AT, Datta SS, Münster S, Weitz DA. Visualizing multiphase flow and trapped fluid configurations in a model three-dimensional porous medium. *AIChE J* (2013) 59:1022–9. doi:10.1002/aic.14005

19. Lacey M, Hollis C, Oostrom M, Shokri N. Effects of pore and grain size on water and polymer flooding in micromodels. *Energy & Fuels* (2017) 31:9026–34. doi:10.1021/acs.energyfuels.7b01254

20. Buchgraber M, Clemens T, Castanier LM, Kovscek A. A microvisual study of the displacement of viscous oil by polymer solutions. *SPE Reservoir Eval Eng* (2011) 14:269–80. doi:10.2118/122400-PA

21. Afsharpoor A, Balhoff MT, Bonnecaze R, Huh C. Cfd modeling of the effect of polymer elasticity on residual oil saturation at the pore-scale. *J Pet Sci Eng* (2012) 94(95):79–88. doi:10.1016/j.petrol.2012.06.027

22. Nilsson MA, Kulkarni R, Gerberich L, Hammond R, Singh R, Baumhoff E, et al. Effect of fluid rheology on enhanced oil recovery in a microfluidic sandstone device. *J Non-Newtonian Fluid Mech* (2013) 202:112–9. doi:10.1016/j.jnnfm.2013.09.011

23. Clarke A, Howe AM, Mitchell J, Staniland J, Hawkes L, Leeper K. Mechanism of anomalously increased oil displacement with aqueous viscoelastic polymer solutions. *Soft matter* (2015) 11:3536–41. doi:10.1039/c5sm00064e

24. Mitchell J, Lyons K, Howe AM, Clarke A. Viscoelastic polymer flows and elastic turbulence in three-dimensional porous structures. *Soft Matter* (2016) 12:460–8. doi:10.1039/C5SM01749A

25. Parsa S, Santanach-Carreras E, Xiao L, Weitz DA. Origin of anomalous polymer-induced fluid displacement in porous media. *Phys Rev Fluids* (2020) 5:022001. doi:10.1103/PhysRevFluids.5.022001

26. Huifen X, Demin W, Junzheng W, Fanshun K. Elasticity of hpam solutions increases displacement efficiency under mixed wettability conditions. In: SPE Asia Pacific Oil and Gas Conference and Exhibition. APOGCE (2004). p. 103–10. doi:10.2523/88456-ms

27. Qi P, Ehrenfried DH, Koh H, Balhoff MT. Reduction of residual oil saturation in sandstone cores by use of viscoelastic polymers. *SPE J* (2017) 22:447–58. doi:10.2118/179689-PA

28. Salmo IC, Sorbie KS, Skauge A. The impact of rheology on viscous oil displacement by polymers analyzed by pore-scale network modelling. *Polymers* (2021) 13:1259. doi:10.3390/polym13081259

29. Urbissinova TS, Trivedi JJ, Kuru E. Effect of elasticity during viscoelastic polymer flooding: A possible mechanism of increasing the sweep efficiency. *J Can Pet Techn* (2010) 49:49–56. doi:10.2118/133471-PA

30. Clarke A, Howe AM, Mitchell J, Staniland J, Hawkes LA. How viscoelastic-polymer flooding enhances displacement efficiency. *SPE J* (2016) 21:0675–87. doi:10.2118/174654-PA

31. Rock A, Hincapie RE, Tahir M, Langanke N, Ganzer L. On the role of polymer viscoelasticity in enhanced oil recovery: Extensive laboratory data and review. *Polymers* (2020) 12:2276–43. doi:10.3390/polym12102276

32. Beaumont J, Bodiguel H, Colin A. Drainage in two-dimensional porous media with polymer solutions. *Soft Matter* (2013) 9:10174–85. doi:10.1039/c3sm51480c

33. Wei B, Romero-Zerón L, Rodrigue D. Oil displacement mechanisms of viscoelastic polymers in enhanced oil recovery (eor): A review. *J Pet Exploration Prod Techn* (2014) 4:113–21. doi:10.1007/s13202-013-0087-5

34. Ekanem EM, Rücker M, Yesufu-Rufai S, Spurin C, Ooi N, Georgiadis A, et al. Novel adsorption mechanisms identified for polymer retention in carbonate rocks. *JCIS Open* (2021) 4:100026. doi:10.1016/j.jciso.2021.100026

35. Zhu S, Zhang S, Xue X, Zhang J, Xu J, Liu Z. Influencing factors for effective establishment of residual resistance factor of polymer solution in porous media. *J Polym Res* (2022) 29:210–0. doi:10.1007/s10965-022-03066-7

36. Xie C, Xu K, Mohanty K, Wang M, Balhoff MT. Nonwetting droplet oscillation and displacement by viscoelastic fluids. *Phys Rev Fluids* (2020) 5:063301. doi:10.1103/PhysRevFluids.5.063301

37. Kawale D, Marques E, Zitha PL, Kreutzer MT, Rossen WR, Boukany PE. Elastic instabilities during the flow of hydrolyzed polyacrylamide solution in porous media: Effect of pore-shape and salt. *Soft Matter* (2017) 13:765–75. doi:10.1039/c6sm02199a

38. Browne CA, Datta SS. Elastic turbulence generates anomalous flow resistance in porous media. *Sci Adv* (2021) 7:eabj2619. doi:10.1126/sciadv.abj2619

39. Lima NM, Avendaño J, Carvalho MS. Effect of viscoelasticity on oil displacement in a microfluidic porous medium. *J Braz Soc Mech Sci Eng* (2022) 44:144–10. doi:10.1007/s40430-022-03435-9

40. Wang D, Wang G, Wu W, Xia H, Yin H. The influence of viscoelasticity on displacement efficiency–from micro to macro scale. In: *SPE annual technical conference and exhibition*. Anaheim, California: Society of Petroleum Engineers (2007). doi:10.2118/109016-MS

41. Fan JC, Wang FC, Chen J, Zhu YB, Lu DT, Liu H, et al. Molecular mechanism of viscoelastic polymer enhanced oil recovery in nanopores. *R Soc Open Sci* (2018) 5:180076. doi:10.1098/rsos.180076

42. Galindo-Rosales FJ, Campo-Deaño L, Sousa PC, Ribeiro VM, Oliveira MS, Alves MA, et al. Viscoelastic instabilities in micro-scale flows. *Exp Therm Fluid Sci* (2014) 59:128–39. doi:10.1016/j.expthermflusci.2014.03.004

43. Browne CA, Shih A, Datta SS. Pore-scale flow characterization of polymer solutions in microfluidic porous media. *Small* (2020) 16:1903944. doi:10.1002/smll.201903944

44. Kumar M, Guasto JS, Ardekani AM. Transport of complex and active fluids in porous media. *J Rheology* (2022) 66:375–97. doi:10.1122/8.0000389

45. Hemingway E, Clarke A, Pearson J, Fielding S. Thickening of viscoelastic flow in a model porous medium. *J Non-Newtonian Fluid Mech* (2018) 251:56–68. doi:10.1016/j.jnnfm.2017.11.002

46. Qin B, Arratia PE. Characterizing elastic turbulence in channel flows at low Reynolds number. *Phys Rev Fluids* (2017) 2:083302–14. doi:10.1103/PhysRevFluids.2.083302

47. Qin B, Salipante PF, Hudson SD, Arratia PE. Flow resistance and structures in viscoelastic channel flows at low re. *Phys Rev Lett* (2019) 123:194501. doi:10.1103/PhysRevLett.123.194501

48. Khomami B, Moreno LD. Stability of viscoelastic flow around periodic arrays of cylinders. *Rheologica Acta* (1997) 36:367–83. doi:10.1007/BF00396324

49. Ichikawa Y, Motosuke M. Viscoelastic flow behavior and formation of dead zone around triangle-shaped pillar array in microchannel. *Microfluidics and Nanofluidics* (2022) 26:44–12. doi:10.1007/s10404-022-02549-9

50. Haward SJ, Hopkins CC, Shen AQ. Stagnation points control chaotic fluctuations in viscoelastic porous media flow. *Proc Natl Acad Sci* (2021) 118:e2111651118. doi:10.1073/pnas.2111651118

51. Walkama DM, Waisbord N, Guasto JS. Disorder suppresses chaos in viscoelastic flows. *Phys Rev Lett* (2020) 124:164501. doi:10.1103/PhysRevLett.124.164501

52. De S, Kuipers JA, Peters EA, Padding JT. Viscoelastic flow past mono- and bidisperse random arrays of cylinders: Flow resistance, topology and normal stress distribution. *Soft Matter* (2017) 13:9138–46. doi:10.1039/c7sm01818e

53. Gillissen JJJ. Viscoelastic flow simulations through an array of cylinders. *Phys Rev E* (2013) 87:023003. doi:10.1103/PhysRevE.87.023003

54. Ekanem EM, Berg S, De S, Fadili A, Bultreys T, Rücker M, et al. Signature of elastic turbulence of viscoelastic fluid flow in a single pore throat. *Phys Rev E* (2020) 101:042605. doi:10.1103/PhysRevE.101.042605

55. Galindo-Rosales FJ, Campo-Deaño L, Pinho FT, Van Bokhorst E, Hamersma PJ, Oliveira MS, et al. Microfluidic systems for the analysis of viscoelastic fluid flow phenomena in porous media. *Microfluidics and Nanofluidics* (2012) 12:485–98. doi:10.1007/s10404-011-0890-6

56. Kumar M, Aramideh S, Browne CA, Datta SS, Ardekani AM. Numerical investigation of multistability in the unstable flow of a polymer solution through porous media. *Phys Rev Fluids* (2021) 6:033304–39. doi:10.1103/PhysRevFluids.6.033304

127

57. Ekanem EM, Berg S, De S, Fadili A, Luckham P. Towards predicting the onset of elastic turbulence in complex geometries. *Transport in Porous Media* (2022) 1–18. doi:10.1007/s11242-022-01790-8

58. Shakeri P, Jung M, Seemann R. Effect of elastic instability on mobilization of capillary entrapments. *Phys Fluids* (2021) 33:113102. doi:10.1063/5.0071556

59. Holzwarth G. Molecular weight of xanthan polysaccharide. *Carbohydr Res* (1978) 66:173–86. doi:10.1016/S0008-6215(00)83250-4

60. Sorbie K. *Polymer-improved oil recovery*. Dordrecht, Netherlands: Springer Netherlands (2013). doi:10.1007/978-94-011-3044-8

61. Mahajan S, Yadav H, Rellegadla S, Agrawal A. Polymers for enhanced oil recovery: Fundamentals and selection criteria revisited. *Appl Microbiol Biotechnol* (2021) 105:8073–90. doi:10.1007/s00253-021-11618-y

62. Shakeri P, Jung M, Seemann R. Scaling purely elastic instability of strongly shear thinning polymer solutions. *Phys Rev E* (2022) 105:L052501. doi:10.1103/PhysRevE.105.L052501

63. Dobrynin AV, Colby RH, Rubinstein M. Scaling theory of polyelectrolyte solutions. *Macromolecules* (1995) 28:1859–71. doi:10.1021/ma00110a021

64. Mezger T. *The rheology handbook: For users of rotational and oscillatory rheometers*. Hannover, Germany: Vincentz Network (2020). doi:10.1515/9783748603702

65. Bodiguel H, Beaumont J, Machado A, Martinie L, Kellay H, Colin A. Flow enhancement due to elastic turbulence in channel flows of shear thinning fluids. *Phys Rev Lett* (2015) 114:028302–5. doi:10.1103/PhysRevLett.114.028302

66. Soulies A, Aubril J, Castelain C, Burghelea T. Characterisation of elastic turbulence in a serpentine micro-channel. *Phys Fluids* (2017) 29:083102. doi:10.1063/1.4996356

67. Casanellas L, Alves MA, Poole RJ, Lerouge S, Lindner A. The stabilizing effect of shear thinning on the onset of purely elastic instabilities in serpentine microflows. *Soft Matter* (2016) 12:6167–75. doi:10.1039/c6sm00326e

68. Macosko CW. *Rheology principles, measurements, and applications*, 86. New York, NY: Wiley VCH (1994).

69. Barnes HA, Hutton JF, Walters K. *An introduction to rheology*, 3. Amsterdam, Netherlands:: Elsevier (1989).

70. Burghelea T, Bertola V. *Transport phenomena in complex fluids*, 598. Cham, Switzerland: Springer (2020). doi:10.1007/978-3-030-35558-6

71. White JL, Metzner AB. Development of constitutive equations for polymeric melts and solutions. *J Appl Polym Sci* (1963) 7:1867–89. doi:10.1002/app.1963.070070524

72. Tseng H-C. A revisitation of white-metzner viscoelastic fluids. *Phys Fluids* (2021) 33:057115. doi:10.1063/5.0049132

73. ANSYS. *Ansys polyflow user's guide*. Canonsburg, PA: ANSYS inc. (2020). ANSYS Polyflow User's guide 2020 R1.

74. Morozov AN, van Saarloos W. An introductory essay on subcritical instabilities and the transition to turbulence in visco-elastic parallel shear flows. *Phys Rep* (2007) 447:112–43. doi:10.1016/j.physrep.2007.03.004

75. Pakdel P, McKinley GH. Elastic instability and curved streamlines. *Phys Rev Lett* (1996) 77:2459–62. doi:10.1103/PhysRevLett.77.2459

76. McKinley GH, Pakdel P, Öztekin A. Rheological and geometric scaling of purely elastic flow instabilities. *J Non-Newtonian Fluid Mech* (1996) 67:19–47. doi:10.1016/S0377-0257(96)01453-X

77. Yao G, Zhao J, Yang H, Haruna MA, Wen D. Effects of salinity on the onset of elastic turbulence in swirling flow and curvilinear microchannels. *Phys Fluids* (2019) 31:123106. doi:10.1063/1.5120459

78. Berg S, van Wunnik J. Shear rate determination from pore-scale flow fields. *Transport in Porous Media* (2017) 117:229–46. doi:10.1007/s11242-017-0830-3

79. De S, Krishnan P, van der Schaaf J, Kuipers J, Peters E, Padding J. Viscoelastic effects on residual oil distribution in flows through pillared microchannels. *J Colloid Interf Sci* (2018) 510:262–71. doi:10.1016/j.jcis.2017.09.069

80. Shaqfeh ES. Purely elastic instabilities in viscometric flows. *Annu Rev Fluid Mech* (1996) 28:129–85. doi:10.1146/annurev.fl.28.010196.001021

81. Groisman A, Steinberg V. Elastic turbulence in a polymer solution flow. *Nature* (2000) 405:53–5. doi:10.1038/35011019

82. Groisman A, Steinberg V. Stretching of polymers in a random three-dimensional flow. *Phys Rev Lett* (2001) 86:934–7. doi:10.1103/PhysRevLett.86.934

83. Groisman A, Steinberg V. Elastic turbulence in curvilinear flows of polymer solutions. *New J Phys* (2004) 6:29. doi:10.1088/1367-2630/6/1/029

84. Datta SS, Ardekani AM, Arratia PE, Beris AN, Bischofberger I, McKinley GH, et al. Perspectives on viscoelastic flow instabilities and elastic turbulence. *Phys Rev Fluids* (2022) 7:080701. doi:10.1103/PhysRevFluids.7.080701

85. James DF. N1 stresses in extensional flows. *J Non-Newtonian Fluid Mech* (2016) 232:33–42. doi:10.1016/j.jnnfm.2016.01.012

86. De S, Kuipers JA, Peters EA, Padding JT. Viscoelastic flow simulations in model porous media. *Phys Rev Fluids* (2017) 2:053303–21. doi:10.1103/PhysRevFluids.2.053303

87. Poole RJ. Three-dimensional viscoelastic instabilities in microchannels. *J Fluid Mech* (2019) 870:1–4. doi:10.1017/jfm.2019.260

88. Mokhtari O, Latché J-C, Quintard M, Davit Y. Birefringent strands drive the flow of viscoelastic fluids past obstacles. *J Fluid Mech* (2022) 948:A2. A2. doi:10.1017/jfm.2022.565

89. Zilz J, Poole RJ, Alves MA, Bartolo D, Levaché B, Lindner A. Geometric scaling of a purely elastic flow instability in serpentine channels. *J Fluid Mech* (2012) 712:203–18. doi:10.1017/jfm.2012.411

90. Shakeri P, Jung M, Seemann R. Characterizing purely elastic turbulent flow of a semi-dilute entangled polymer solution in a serpentine channel. *Phys Fluids* (2022) 34:073112. doi:10.1063/5.0100419

91. Poole R, Lindner A, Alves M. Viscoelastic secondary flows in serpentine channels. *J Non-Newtonian Fluid Mech* (2013) 201:10–6. doi:10.1016/j.jnnfm.2013.07.001

92. Ducloué L, Casanellas L, Haward SJ, Poole RJ, Alves MA, Lerouge S, et al. Secondary flows of viscoelastic fluids in serpentine microchannels. *Microfluidics and Nanofluidics* (2019) 23:33. doi:10.1007/s10404-019-2195-0

93. Son Y. Determination of shear viscosity and shear rate from pressure drop and flow rate relationship in a rectangular channel. *Polymer* (2007) 48:632–7. doi:10.1016/j.polymer.2006.11.048

94. Machado A, Bodiguel H, Beaumont J, Clisson G, Colin A. Extra dissipation and flow uniformization due to elastic instabilities of shear-thinning polymer solutions in model porous media. *Biomicrofluidics* (2016) 10:043507. doi:10.1063/1.4954813

95. Fouxon A, Lebedev V. Spectra of turbulence in dilute polymer solutions. *Phys Fluids* (2003) 15:2060–72. doi:10.1063/1.1577563

96. Steinberg V. Scaling relations in elastic turbulence. *Phys Rev Lett* (2019) 123:234501. doi:10.1103/PhysRevLett.123.234501

97. Kolmogorov AN, Levin V, Hunt JCR, Phillips OM, Williams D. Dissipation of energy in the locally isotropic turbulence. *Proceed R Soci. Lond Ser. A: Math. Phy. Sci.* (1991) 434:15–7. doi:10.1098/rspa.1991.0076

128